

4D Geophysical Monitoring of Hydrogeological Precursors to Landslide Activation

Andrew James Merritt

Submitted in accordance with the requirements for the degree of
Doctor of Philosophy

The University of Leeds

School of Earth & Environment

April, 2014

Intellectual Property and Publication Statement

The candidate confirms that the work submitted is his/her own, except where work which has formed part of jointly-authored publications has been included. The contribution of the candidate and the other authors to this work has been explicitly indicated below. The candidate confirms that appropriate credit has been given within the thesis where reference has been made to the work of others.

This copy has been supplied on the understanding that it is copyright material and that no quotation from the thesis may be published without proper acknowledgement.

The right of Andrew James Merritt to be identified as Author of this work has been asserted by him in accordance with the Copyright, Designs and Patents Act 1988.

© 2014 The University of Leeds and Andrew James Merritt

Publications

Chapter 3 is based on work published in:

A.J. Merritt, J.E. Chambers, W. Murphy, P.B. Wilkinson, L.J. West, D.A. Gunn, P.I. Meldrum, M. Kirkham & N. Dixon (2013), *3D ground model development for an active landslide in Lias mudrocks using geophysical, remote sensing and geotechnical methods*, *Springer Landslides*, DOI: 10.1007/s10346-013-0409-1, ISSN: 1612-5118.

J.E. Chambers & P.B. Wilkinson provided 3D electrical resistivity tomography data (models) and candidate performed all processing, analysis and interpretations on all geophysical datasets. Author performed high resolution geophysical field surveys, and processed and analysed the results. M. Kirkham performed laboratory core resistivity measurements and author analysed and interpreted results.

I partly contributed content or presented the following publications at conferences:

Gunn, D.A., Chambers, J.E., Hobbs, P.R.N., Ford, J.R., Wilkinson, P.B., Jenkins, G.O., **Merritt, A.J.** 2013. Rapid observations to guide the design of systems for long-term monitoring of a complex landslide system in the Upper Lias clays of North Yorkshire, UK. **QJEGH**. DOI: 10.1144/qjegh2011-028

Chambers, JE, Gunn, DA, Wilkinson, PB, Meldrum, PI, Haslam, E, Holyoake, S, Kirkham, M, Kuras, O, **Merritt, A.J**, Wragg, J. 2013. 4D Electrical Resistivity Tomography monitoring of soil moisture dynamics in an operational railway embankment. Near Surface Geophysics. Doi: 10.3997/1873-0604.2013002

Merritt, A.J., Chambers, J.E., Murphy, W., Wilkinson, P.B., West, L.J., Gunn, D., Dixon, N. 2013. An integrated approach to ground model development: geophysical, remote sensing and geotechnical methods. EGU2013 Conference Talk, Vienna, Austria. Session: NH3.5.

Merritt, A.J., Chambers, J.E., Murphy, W., West, L.J. 2011. Shallow landslide structure and seasonal soil moisture loading by three-dimensional electrical resistivity tomography. Student Session Poster presentation. EAGE Near-Surface Geophysics Conference 2011, Leicester, UK.

Acknowledgements

This research has been a collaboration between members of the University of Leeds, Geomechanics Research Group and the Geophysical Tomography Team at British Geological Survey (BGS). The members of the Geomechanics Research Group who have assisted me in my research are Drs William Murphy and Jared West. Acting as Lead University Supervisor, William Murphy oversaw my development as a researcher and Engineering Geologist and imparted his wisdom throughout, particularly in Chapter 3 when developing the ground model. Jared West principally instructed on the laboratory experimentation (Chapter 5) part of the project but also contributed his vast experience of engineering geological laboratory testing to make sure my analysis was watertight throughout.

Members of the Geophysical Tomography Team (GT) who have contributed to my research include Jonathan Chambers (PhD Project Initiator), Paul Wilkinson & Sebastian Uhlemann. The geophysical monitoring equipment used by the project and which provided field geophysical data was developed and maintained by this group.

Jonathan Chambers has been both a mentor and an advisor, having spent considerable time with me in the field explaining the finer points of the geophysical elements of the project. In addition, his advice getting the geophysical laboratory analysis off the ground was invaluable. Sebastian Uhlemann and Paul Wilkinson helped me considerably with the technical, modelling element of the project and supported me throughout. They performed all geophysical model inversions and also modelled the results of my field and laboratory physical properties. They both also acted as a fountain of knowledge about both general physics and mathematical modelling, and contributed Matlab code to convert geophysical results into usable products.

This project was part funded by a BUFI Scholarship and University of Leeds Student Scholarship.

I would formally like to thank my three supervisors, William Murphy, Jonathan Chamber and Jared West for their advice and support during the course of the research project. In addition I would also wish to thank them for their friendship, I take three friends away from this project.

Abstract

If the effects of landslides are to be mitigated and avoided then the causes of landslide activations – and re-activations – must be better understood. The most common subsurface property change in the lead up to rainfall-triggered landslide activation is the moisture content of slope material and associated pore water pressure rises and/or consistency changes.

Landslide early warning systems have been developed which observe and monitor characteristic slope properties in advance of activation and give advanced warning of imminent slope displacement. This PhD thesis analyses and presents the results of a four and a half year monitoring campaign of a periodically active inland landslide by – among other methods – a geoelectrical monitoring system called Automated time-Lapse Electrical Resistivity Tomography (ALERT). The ALERT system was trialled on a landslide system located within the Early Lias of North Yorkshire and the suitability of the system for landslide monitoring assessed.

The products of the geophysical monitoring campaign range from discrete resistance measurements on the landslide to a four-dimensional, high-temporal resolution dataset which is interpreted in terms of hydrogeological processes. Temperature corrected resistance results of the geoelectrical monitoring system reveal that the system responds very well to rises and falls in piezometric levels and seasonal trends of soil desiccation during warmer, drier months and crack annealing and slope soil moisture accumulation in response to wetter periods. The existence of threshold slope moisture contents, and hence electrical resistances/resistivities, above which the slope activates are not observed in resistance/resistivity results most probably due to the complex nature of the landslide system, the system resolution and a number of physical slope processes taking place. However, trends in precursory soil moisture dynamics during the period leading up to earthflow activation are apparent in temperature corrected resistance results.

Time-lapse model resistivity was converted to gravimetric moisture content through laboratory calibration of soil electro-petrophysical properties of each active lithological formation. Seasonal moisture content trends confirm system sensitivity to slope moisture content. However, lower moisture contents than were observed in the field indicate the need for higher

resolution, *intra*-landslide ERT data to make the hydrogeology of landslides more apparent.

Table of Contents

Intellectual Property and Publication Statement	2
Acknowledgements	4
Abstract	5
Table of Contents	7
List of Tables	11
List of Figures	13
Chapter 1 Project Introduction & Structure	22
1.1 Project Motivation & Aims	22
1.2 Thesis Structure	23
Chapter 2 Literature Review	25
2.1 Introduction	25
2.2 Landslides	25
2.3 Electrical Resistivity Tomography on Landslide Systems.....	32
2.3.1 Electrical Properties of Earth Materials	32
2.3.2 Electrical Resistivity Tomography (ERT)	36
2.4 Electrical Resistivity Tomography for Landslide Ground Model Development	43
2.5 Time-Lapse Electrical Resistivity Tomography of Landslide Systems and Hillslope Processes	46
2.6 Summary	49
Chapter 3 Ground Model Development of Field Site	51
3.1 Site Background.....	52
3.1.1 Geology.....	52
3.1.2 Previous Investigations	53
3.2 Methodology.....	54
3.2.1 Surface Characterisation.....	57
3.3 Subsurface Characterisation	58
3.3.1 Three-Dimensional Electrical Resistivity Tomography	58
3.3.2 Core Logging & Index Testing.....	59
3.3.3 Borehole Inclinator	60
3.3.4 Core Resistivity & Cation Exchange Capacity	60
3.4 Results	61
3.4.1 Surface Expression	61

3.4.2 Rates & Distribution of Movement	64
3.4.3 Soil Structure & Types.....	68
3.4.4 Soil Properties.....	71
3.4.5 Volumetric Resistivity Imaging (3D ERT)	75
3.5 Ground Model Development	80
3.6 Conclusion	85
Chapter 4 Methodology for slope monitoring.....	87
4.1 Monitoring Techniques	87
4.1.1 Real Time Kinematic (RTK) -GPS Monitoring of Peg Positions	90
4.1.2 Temperature.....	94
4.1.3 Rainfall	97
4.1.4 Evapotranspiration	99
4.1.5 Piezometry	101
4.2 Landslide Monitoring by Automated time-Lapse Electrical Resistivity Tomography	103
4.2.1 ALERT System at Hollin Hill.....	103
4.2.2 Data Acquisition	106
4.3 Data Processing.....	106
4.3.1 Interpolating electrode position from surveying peg array positions.....	110
4.3.2 Temperature Correcting Transfer Resistances	114
4.3.3 Inversion and Modelling of ERT monitoring data.....	117
4.3.4 Post-Inversion Temperature Correction of Time-Lapse ERT.....	120
4.3.5 Partitioning of Three-Dimensional ERT Model Domain ...	121
4.3.6 Conversion of time-lapse model resistivity to time- lapse volumetric images of moisture content	122
4.4 Discussion.....	124
Chapter 5 Geophysical–Geotechnical Property Relationships	125
5.1 Introduction	125
5.2 Laboratory determination of resistivity – moisture content relationship of undisturbed cores	126
5.2.1 Core sample preparation.....	126
5.2.2 Laboratory procedure	131
5.2.3 Undisturbed cores resistivity results	140
5.2.4 Measurement quality assessment.....	148

5.3 Modelling of electrical resistivity – moisture content relationship.....	151
5.4 Waxman-Smit Modelling	154
5.4.1 Waxman-Smits and Porosity	158
5.4.2 Waxman-Smits Modelling Results.....	158
5.4.3 Waxman-Smits Modelling Error.....	163
5.5 Soil Moisture Content , Matric Suction and Resistivity	167
5.5.1 Methodology.....	168
5.5.2 Soil Moisture Retention Results	171
5.6 Discussion.....	172
5.7 Conclusion	179
Chapter 6 Geoelectrical Observation of Landslide Hydrogeological Processes	181
6.1 Rainfall and piezometry monitoring results.....	181
6.1.1 Rainfall	181
6.1.2 Piezometry	184
6.1.3 Environmental Input Correlations	188
6.1.4 Weekly averaged air temperature	189
6.2 Transfer Resistance	189
6.2.1 Transfer Resistance Results	190
6.3 Temperature Corrected Transfer Resistance	195
6.3.1 Temperature Corrected Transfer Resistance Results	196
6.3.2 Temperature Corrected Transfer Resistance of 2012 Landslide Activation	205
6.3.3 Temperature Corrected Resistance and Piezometry Correlations.....	216
6.4 Time-lapse tomography results.....	217
6.4.1 Time-Lapse Model Resistivity & GMC Results.....	218
6.4.2 Time-lapse Volumetric Images of Gravimetric Moisture Content	226
6.4.3 Matric Suctions.....	229
6.5 Discussion.....	229
6.6 Suitability of ERT monitoring of slow-moving earthflows	243
6.7 Conclusion	246
Chapter 7.....	248
Recommendations & Guidelines for geoelectrical monitoring of landslides	248

Acronyms & Abbreviations	252
References.....	253
Appendix A Data Processing Performance	270
Appendix B Standardised Model Inversion Parameters	272
Appendix C Resistivity Model Inversion Misfit Errors	274
Appendix D Time-Lapse Temperature Corrected Resistance Maps using Baseline Average of 2010 Surveys.....	276

List of Tables

Table 2.1. Electrical resistivities of a range of common earth materials (Telford, 1990).....	34
Table 2.2. Typical cation exchange capacities of common clay minerals (After Carroll, 1959)	36
Table 3.1. X-ray diffraction analysis of six soil samples from BH7 which show the mineralogical composition of geological formations represented at the Hollin Hill field site.....	72
Table 4.1. RTK-GPS measurement of baseline survey peg positions. Coordinate System: OSGB36.....	90
Table 4.2. Dates of GPS surveys of peg positions at Hollin Hill	91
Table 4.3. Depths of temperature sensors of field site installed temperature sensor array.....	94
Table 4.4. Fitted parameters from subsurface temperature modelling of three temperature sensor arrays installed at the site, plus, a combined model for data from all three sensor locations. Misfit error between model and measured data is presented as %RMS.....	96
Table 4.5. Periods when ALERT system was not providing data due to malfunction.	106
Table 4.6. Combination of model inversion types and time-lapse damping factors.	119
Table 5.1. (left) Electrode arrangement for each electrical measurement orientation.	134
Table 5.3. Results of geometric factor laboratory measurements. Columns headed with A, B, E and F represent the four orientations of electrode measurements.	141
Table 5.4. Averaged geometric factors applied to laboratory electrical resistance measurements.....	141
Table 5.5. Waxman-Smits Equation modelling and fitting parameters for Trough 1.....	156
Table 5.6. Waxman-Smits Equation modelling and fitting parameters for Trough 2.....	156
Table 5.7. Waxman-Smits Equation modelling and fitting parameters for Trough 3.....	156
Table 5.8. Waxman-Smits Equation modelling and fitting parameters for Trough 4.....	157
Table 5.9. Waxman-Smits Equation modelling and fitting parameters for Trough 5.....	157

Table 5.10. Waxman-Smits Equation modelling and fitting parameters for Trough 6.....	157
Table 5.11. Waxman-Smits Equation modelling and fitting parameters for Trough 6 (resistance measurements affected by sample cracking are removed).	157
Table 5.12. Root-mean-square error, percentage root-mean-square error and correlation between laboratory measured resistivity and empirically modelled resistivity by Waxman-Smits equation. Error and correlation results for measurement orientations A and B for both 5cm and 1cm square arrays. Error and correlation results refer to modelling performed on the average of two orientations (A & B) for each square array... 	164
Table. 6.1. Calculations of hillslope runoff modelled from US Soil Conservation Service Method (1972).....	233

List of Figures

Figure 2.1. Landslide classification scheme (www.bgs.ac.uk)	27
Figure 2.2. Map of North Yorkshire annotated with major landslides. (Map generated by DigiMap)	31
Figure 2.3. Diagram Adapted from Revil et al., (1997) and Leroy et al., (2004).....	35
Figure 2.4. Current flow from a single point source electrode (After Kearey, 1991).....	37
Figure 2.5. Layout of field equipment for a 2D ERT survey using the wenner array (from Loke, 2002).....	39
Figure 3.1. Geological map of the study area, and inset large scale map. Geological mapping, BGS © NERC. Contains Ordnance Survey data © Crown Copyright and database rights 2013. (Merritt et al., 2013).....	53
Figure 3.2. Plan view of study site, annotated with lithological boundaries (dashed white lines), positions of GPS pegs (orange points), borehole locations (light blue points) and areas of high- and low-resolution ERT surveys (low-res array: red rectangle, high-res array: purple rectangle). Orange and lilac lines indicate positions of interpreted profiles presented as Figures 3.13 & 3.16 respectively. Coordinate system is British National Grid (BNG). Illustration of study site based upon an aerial photograph © UKP/Getmapping Licence No. UKP2006/01.....	56
Figure 3.3. Geomorphology Map of Hollin Hill field site produced from an airborne LiDAR dataset, visualised using GeoVisionary stereographic software package and presented using ArcGIS10. The top of the slope is towards the north of the map, with the base towards the south; coordinate system used is BNG. (Taken from Merritt et al., 2013).....	63
Figure 3.4. Annotated geomorphology map showing locations of pegs presented in figures 3.5 and 3.6.	64
Figure 3.5. Landslide activity from RTK-GPS monitoring of surface-installed survey peg array of eastern region of Hollin Hill landslide system. NB. Different peg displacement scale axes on each plot, the top graph displays larger displacements compared to the lower.	66
Figure 3.6. Landslide activity from RTK-GPS monitoring of surface-installed survey peg array of western region of Hollin Hill landslide system.....	66
Figure 3.7. Graphical representation of landslide activity by peg displacement	67

Figure 3.8. Images of shear surfaces and structural contact between earthflow and earthslide within Borehole 7.....	69
Figure 3.9. Interpreted core logs including particle size analyses, moisture content, cation exchange capacity, core resistivity and inclinometer data of boreholes: BH1, BH5 & BH7. Taken from Merritt et al., (2013).....	70
Figure 3.10. Atterberg limit a-line plot showing results for soil samples from BH5 & BH7. A-line plot presents results as plasticity versus liquid limit and shows plasticity of soil samples.....	71
Figure 3.11. Core resistivity laboratory measurements versus corresponding cation exchange capacity of core samples from borehole BH5 and BH7. Coloured points represent different structural zones from interpreted borehole logs (Figure 3.9).....	73
Figure 3.12. a.) (left) 3D volumetric image of resistivity from the low-resolution ERT survey (red rectangle on base map, Fig. 3.2.). Geological boundaries are marked with a white dashed line and formation names with white text. b.) (right) Height of model cell (z-axis) versus resistivity for low-resolution ERT survey and shows distribution of lithological formations at Hollin Hill.....	76
Figure 3.13. 2D ERT profile extracted from low-resolution 3D ERT survey. Profile runs parallel (approximately north-south) with y-axis and includes BH7. Rotational shear surfaces are represented by black dashed lines. Orientation and location of 2D ERT profile is indicated by an orange profile line on the basemap, Fig.3.2.	77
Figure 3.14. a.) (top) 3D volumetric image of resistivity from the high-resolution ERT survey (purple rectangle on the basemap, Figure 3.2.) A white dashed line indicates the boundary between WMF and SSF and two red points indicate borehole locations. b.) (below) displays the higher resistivity zone at 40% opacity and maintains the lower resistivity earthflow at 100% opacity. N.B. Low resistivity features at the base of the image are likely to be artefacts of the inversion process associated with regions of very low sensitivity (and hence resolution).	79
Figure 3.15. Annotated profile through high-resolution ERT survey whose location is indicated by a lilac profile line on basemap (Fig.3.2.) White lines represent flow surfaces with arrows indicating relative flow direction. The interpreted borehole log of BH7 shows structure of landslide system by landslide deposit type.	80
Figure 3.16. Ground model of the Hollin Hill study site based on geophysical, geomorphological and geotechnical investigations.	83

Figure 4.1. Hollin Hill basemap showing extent of landslide deposits, locations of field site sensors and extents of permanently-installed 3D ERT arrays.....	89
Figure 4.2 a.) (Upper left) Layout of monitoring pegs at Hollin Hill (NB. Five rows of nine pegs) b.) (Upper right) Local peg positions (after assigning local eastings and northings relative to Peg 1). c.) (lower left) Local eastings and local northings rotated to lie along x- and y- planes.....	92
Figure 4.3. Rotation of localised grid to be along the line of electrode and peg arrays.....	93
Figure 4.4. Plots of recorded temperature data and modelled temperature results at four depths (0.1m, 1.0m, 2.5m & 5.35m) from temperature sensor array T1 during a 2 year period.....	97
Figure 4.5. Position of rain gauge at Hollin Hill field site (white cylinder on roof of green enclosure).....	98
Figure 4.6. Location of piezometer wells in relation to boreholes	102
Figure 4.7. Piezometer casing installation diagram. Dashed: bedrock; blue: level logger; grey: cement-bentonite grout; stippled: sand.....	102
Figure 4.8 a.) (top left) ALERT System installed at Hollin Hill; green secure housing contains monitoring system, batteries and communication modem. To the west of the instrumentation housing is a pole with attached solar panels and wind turbine. b.) (top right) Inside the system housing; two black boxes are the ALERT system, wooden box positioned on the housing floor contains two batteries and the silver box to the right of the housing is a methanol fuel cell (installed ~October 2012). c.) (bottom left) Communication modem and SIM card for uploading data acquisition schedules and downloading survey results. d.) Stainless steel electrode with multicore cable attached before being inserted 0.1 m into the subsurface. Note, accurate electrode positioning by tape measure and later RTK-GPS location measurement.	104
Figure 4.9. Locations of automated time-lapse ERT electrode array. Along with electrode number and line number labels.	105
Figure 4.10. Schematic diagram of data collection, processing and presentation of electrical resistivity (ALERT) monitoring data ...	108
Figure 4.11. Example of interpolation of electrode positions from sparse array of GPS monitored survey peg positions.....	114
Figure 4.12. Diagram of the temperature correction of field transfer resistance measurements by 1D layered resistivity model.....	117
Figure 4.13. ERT survey dates and types of inversion performed.....	118

Figure 4.14. Temperature model calibrated from Hollin Hill temperature sensor array and applied to 40Ωm homogeneous half space. Model results presented as electrical resistivity and temperature distribution.	120
Figure 4.15. Domain partition; a 3D resistivity survey and the domain partitioned by geological formations, Whitby Mudstone Formation, Staithes Sandstone Formation & Redcar Mudstone Formation.....	122
Figure 4.16. Converting time-lapse model resistivity to volumetric gravimetric moisture content.....	123
Figure 5.1. a) (left). Removal of core from plastic bag and depth measurement of extracted sample. b) (right). Once sample to be extracted is located a hacksaw is used to separate the sample from the core.....	127
Figure 5.2. First incision into soil core. Tape Measure used to measure position of second incision	128
Figure 5.3. a) (left). Both incisions made, core is now ready to be lifted out of the temporary core holder and placed into the soil troughs, ready to be transported to the laboratory. b) (right). Sample about to be lifted out of the temporary core holder. Note the saw guide, a thin gap between two sections of the grey, plastic core holder.....	128
Figure 5.4. a.) (left) Empty trough with lid. b.) (right) Trough with soil sample inserted.....	129
Figure 5.5. a.) (left) Transferring core to soil trough at the BGS core store at Keyworth. b.) (right) Extracted half core about to be placed into plastic trough	129
Figure 5.6. Location and depth of soil samples selected for laboratory electrical resistivity measurement	130
Figure 5.7. Electrical circuit diagram of circuit board and pre-amplifier	131
Figure 5.8. a). Laboratory equipment used to make resistivity measurements on troughed soil samples extracted from field site and include: 5 cm square array electrode holder, guide and electrodes. b.) 1 cm square array electrodes are shown along with their indicated soil penetration depth. N.B. 1 cm electrodes are not shown in measurement position.....	133
Figure 5.9. Laboratory electrical resistance measurement equipment during resistance measurement.	133
Figure 5.10 (right) Position of each electrode site of the electrode holder to make the four point electrical measurement.....	134
Figure 5.11. a.) Resistance measurements made by 5 cm (left) and b.) 1 cm (right) square array. Yellow numbers, 1-4, represent four electrode sites. 'Electrode' labels point to one of four electrode sites used to perform resistance measurement.....	138

Figure 5.12. Orientation of electrical measurements relative to sample bedding.....	139
Figure 5.13. a) Cell geometric factor determination for 5 cm and Figure 5.13. b) 1 cm electrode arrays. A, B, E and F represent the four electrode orientations for each resistance measurement along with linear best fit trend line. Plotted in semi-log space.	142
Figure 5.14. Electrical resistivity results at a range of gravimetric moisture contents for trough 1 soil sample. Error bars, see Section 5.2.4.	144
Figure 5.15. Electrical resistivity results at a range of gravimetric moisture contents for trough 2 soil sample. Error bars, see Section 5.2.4	145
Figure 5.16. Electrical resistivity results at a range of gravimetric moisture contents for trough 3 soil sample. Error bars, see Section 5.2.4	145
Figure 5.17. Electrical resistivity results at a range of gravimetric moisture contents for trough 4 soil sample. Error bars, see Section 5.2.4	146
Figure 5.18. Electrical resistivity results at a range of gravimetric moisture contents for trough 5 soil sample. Error bars, see Section 5.2.4	146
Figure 5.19. Electrical resistivity results at a range of gravimetric moisture contents for trough 6 soil sample. Error bars, see Section 5.2.4	147
Figure 5.20. Resistivity percentage measurement error performed on Trough 1.	150
Figure 5.21. Resistivity percentage measurement error performed on Trough 2.	150
Figure 5.22. Resistivity percentage measurement error performed on Trough 3.	150
Figure 5.23. Resistivity percentage measurement error performed on Trough 4.	150
Figure 5.24. Resistivity percentage measurement error performed on Trough 5.	151
Figure 5.25. Resistivity percentage measurement error performed on Trough 6.	151
Figure 5.26. Effect of porosity on Waxman-Smits Model Curves.....	158
Figure 5.27 a). Trough 1 electrical resistivity – gravimetric moisture content model relationship for 5cm electrode array. b). Trough 1 electrical resistivity – gravimetric moisture content model relationship for 1cm electrode array Modelled by Waxman-Smits Equation.	159

Figure 5.28 a). Trough 2 electrical resistivity – gravimetric moisture content model relationship for 5cm electrode array.	
b). Trough 2 electrical resistivity – gravimetric moisture content model relationship for 1cm electrode array Modelled by Waxman-Smits Equation.	160
Figure 5.29 a). Trough 3 electrical resistivity – gravimetric moisture content model relationship for 5cm electrode array.	
b). Trough 3 electrical resistivity – gravimetric moisture content model relationship for 1cm electrode array Modelled by Waxman-Smits Equation.	161
Figure 5.30 a). Trough 4 electrical resistivity – gravimetric moisture content model relationship for 5cm electrode array.	
b). Trough 4 electrical resistivity – gravimetric moisture content model relationship for 1cm electrode array Modelled by Waxman-Smits Equation.	161
Figure 5.31 a). Trough 5 electrical resistivity – gravimetric moisture content model relationship for 5cm electrode array.	
b). Trough 5 electrical resistivity – gravimetric moisture content model relationship for 1cm electrode array Modelled by Waxman-Smits Equation.	162
Figure 5.32 a). Trough 6 electrical resistivity – gravimetric moisture content model relationship for 5cm electrode array and including model excluding crack affected measurements.	
b). Trough 6 electrical resistivity – gravimetric moisture content model relationship for 1cm electrode array Modelled by Waxman-Smits Equation.	163
Figure 5.33. Percentage RMS error of modelled results from measured resistivity results using measurement orientation A. Presented are model errors associated with both 5cm and 1cm square arrays.	165
Figure 5.34. Percentage RMS error of modelled results from measured resistivity results using measurement orientation B. Presented are model errors associated with both 5 cm and 1 cm square arrays.	166
Figure 5.35. Percentage RMS error of modelled results from mean averaged laboratory measured trough resistivity data. Averaged resistivity of the two orientations A and B for each square array size. Presented are model errors associated with both 5 cm and 1 cm square arrays.	166
Figure 5.36. a) (left) Pressure plate apparatus as setup during soil moisture retention curve experiments. b) (top right) Pressure regulation gauge reading 40 PSI. c) (bottom right) Water level measuring burette for determining when soil moisture equilibrium is reached. Note: the marker pen lines indicating previous water levels while reaching equilibrium.	170

Figure 5.37. Soil moisture retention curve of two earthflow samples, extracted from Hollin Hill soil cores. a) BH7,1.30 m, and b) BH5, 0.40 m.	172
Figure 6.1. Rainfall data for Hollin Hill field site. Presented are both weekly total rainfall and weekly cumulative rainfall. Weekly effective rainfall is presented and was modelled using Hargreaves evapotranspiration model.	182
Figure 6.2. a.) Piezometric levels within eastern earth flow deposits throughout monitoring period at Hollin Hill field site. Locations and depths of piezometers are displayed in Chapter 4 and are relative to AoD. b.) Piezometric levels within western earth flow deposits throughout monitoring period at Hollin Hill field site.	187
Figure 6.3. Rolling averaged effective rainfall and piezometric levels at Hollin Hill.	188
Figure 6.4. Plan of electrode locations and resistance measurement dipole locations. Annotated on the plan are the locations of dipole centres of resistance measurements analysed within this chapter.	190
Figure 6.5. Transfer resistances extracted from ALERT monitoring campaign between 07/2008 and 02/2013. Data pertainto Line 1 of monitoring array and are from western earthflow region of landslide system.	191
Figure 6.6. Transfer resistances extracted from ALERT monitoring campaign between 07/2008 and 02/2013. Data pertainto Line 5 of monitoring array and are from eastern earthflow region of landslide system.	193
Figure 6.7. Time-lapse temperature corrected transfer resistance ratio measurements of dipoles located within the western earth flow deposits along Line 1. Resistance measurements are normalised to 13/07/2008 baseline survey. Locations of measurement dipoles are shown on Figure 6.4 and resistance results are plotted along with piezometry and rainfall data.	198
Figure 6.8. Time-lapse temperature corrected transfer resistance measurements of dipoles located within eastern earth flow deposits along Line 5. Locations of measurement dipoles are shown on Figure 6.4.	202
Figure 6.9. Geographic location of resistance maps (left). Outline of survey area indicated by red rectangle and to the right of geographic map is the baseline resistance map to scale.	206
Figure 6.10. Time-lapse temperature corrected transfer resistance measurements of dipoles plotted as resistance map. Locations of measurement dipoles are shown on initial survey.	209

Figure 6.11. Time-lapse temperature corrected transfer resistance measurements of dipoles located within western earth flow deposits along Line 1. Time period between 06/2011 and 02/2013 plotted as lead up to earthflow activation at 08/2012. Locations of measurement dipoles are shown on Figure 6.4.	212
Figure 6.12. Time-lapse temperature corrected transfer resistance measurements of dipoles located within western earth flow deposits along Line 5. Time period between 06/2011 and 02/2013 plotted as lead up to earthflow activation at 08/2012. Locations of measurement dipoles are shown on Figure 6.4.	215
Figure 6.13. Comparison between temperature corrected resistance and western piezometer level.....	216
Figure 6.14. a) (left) Block diagram showing model partitioning of the low resolution resistivity model domain. Shown are the three geological formations present, WMF, SSF and RMF, as well as three landslide regions examined in detail, Slump, eastern and western flow deposits. The area imaged is shown in 6.13b, right.....	218
Figure 6.15. Time lapse model resistivity results from the western earth flow region of the landslide system (green region in Figure 6.14).....	221
Figure 6.16. Time lapse model resistivity results from the eastern flow region of the landslide system (orange region in Figure 6.14).....	225
Figure 6.17. Selection of volumetric images of gravimetric moisture content for the period between 06/2011 and 05/2013 and leading up to earth flow activation 08/2012.	227
Figure 6.18. Four-dimensional volumetric image of gravimetric moisture content ratio of the low resolution array. Originated from time-lapse constrained model inversions.....	228
Figure 6.19. Response of electrical resistivity monitoring results to both subsurface processes and landslide activation. Sand flow exists within western earthflow.	235
Figure 6.20. Schematic describing less responsive nature of resistivity measurements at higher gravimetric moisture contents.	238
Figure 6.21. 2D ground model describing recommended relationship between dimensions of flows and resolution and size of model cells.....	244
Figure 6.22. 2D ground model describing activation mechanism of slow-moving, shallow earthflows of the Hollin Hill landslide system, North Yorkshire.....	245
Appendix A. Which member of the collaboration performed each of the major data processing tasks.	271

Appendix B. Model Inversion parameters as applied for all model cell inversions of Hollin Hill ERT surveys.....	273
Appendix C. Model Inversion Misfit Errors for Movement Corrected ERT Inversions	275
Appendix D. Time-Lapse Temperature Corrected Resistance Maps using Baseline Average of 2010 Surveys.....	276

Chapter 1

Project Introduction & Structure

1.1 Project Motivation & Aims

Landsliding in the UK was thrust into the limelight in 2012 with several high profile events taking place such as the Burton Bradstock rock fall and the Hatfield Colliery slump , both of which resulted in either loss of life or severe damage to infrastructure. If similar events and landslide reactivations are to be mitigated and avoided then the causes of landslide activation must be understood. One way of developing a better understanding of landslide activation events is by monitoring subsurface changes in the lead up to activation. The most common change in the subsurface that leads to landslide activation is the movement of water and associated moisture content variations. If characteristic hill slope conditions, for example water pressure changes or exceeding consistency limits (plastic or liquid limits) can be observed in advance of activation then early warning of imminent slope displacement may be possible.

Previous landslide warning systems e.g. the USGS Alert system have relied on rainfall as a proxy for moisture content, but direct observation of water in the ground is preferable. In recent years monitoring of landslide processes by geoelectrical methods has become more common (Suzuki et al., 2001; Lebourg et al., 2005; Jomard et al., 2006; Friedel et al., 2006). They reveal that time-lapse electrical resistivity tomography is a useful tool to observe hydrogeological processes; however, their studies lasted a short time-frame and compare few tomograms. Therefore, a geophysical imaging system in which the progressive wetting of the ground in response to rainfall leading to saturation and then sliding would seem to be a useful approach to explore for forecasting imminent landslide movement.

In this thesis the results of one such long-term landslide monitoring system is described and the capability of this method to observe landslide precursory processes is assessed. The main aim of this project was to

assess the suitability of a geoelectrical monitoring method for observing the moisture content changes in landslide systems that act as precursors to movement. The technique was trialled on an inland slow moving shallow landslide system located in North Yorkshire. A shallow landslide was chosen so that it would be responsive to relative short term rainfall events. The product of the geophysical monitoring campaign is a four-dimensional, high-temporal resolution dataset which is interpreted in terms of hydrogeological processes. The outcomes of the field investigation are used to develop new guidelines for the implementation of geoelectrical monitoring of landslides and highlight what additional information is required for any future deployments to be successful.

1.2 Thesis Structure

The project aim is divided into several objectives. The first objective, presented in Chapter 2, is to present key concepts and evaluate the current state-of-the-art surrounding geoelectrical monitoring of landslides. In this chapter a brief description of landslides is given, with greater emphasis then placed on mechanics of the types of landslide present at the field site investigated by this project. Electrical properties of earth materials are described, as is the geophysical method utilised by this research project, Electrical Resistivity Tomography (ERT). The Literature Review is concluded by covering the use of ERT both for site characterisation and as a landslide monitoring technique.

Secondly, the assessment of the capacity of three dimensional electrical resistivity tomograms (3D ERT) to be incorporated into the development of landslide ground models was investigated in Chapter 3. This material was published in a paper in the journal *Landslides*.

Chapter 4 sets out the implemented geophysical monitoring data processing routes and provides explanation of each processing step. In this Chapter the manipulation of field geophysical monitoring results along with auxiliary datasets is described.

The next Chapter of the thesis, Chapter 5, catalogues the laboratory analysis of core samples, performed to make the conversion of raw field

geophysical monitoring results to other presentation formats possible. The conversion of raw field resistance measurements required, amongst other things, calibration of soil resistivity – moisture content relationships through laboratory experiments.

The penultimate Chapter, Chapter 6, identifies landslide property trends in time-lapse resistivity monitoring data. Monitoring results are presented in several formats and include unprocessed raw resistance monitoring data, to inverted model resistivity results converted to gravimetric moisture content, through soil laboratory calibration. In Chapter 6 the suitability of the monitoring technique is evaluated for its ability to observe hydrogeological precursors to landslide activation and include *inter alia* volumetric images of moisture content.

The outcomes of the monitoring results of this investigation feed into a series of new guidelines and recommendations (Chapter 7) for the future implementation of geoelectrical monitoring of landslides.

Chapter 2 Literature Review

2.1 Introduction

An insight is provided in this chapter into relevant literature and basic theoretical concepts for the project, in particular for landslide characterisation and ground model development, as described in Chapter 3, and for laboratory calibration of electrical properties of field site geological formations, in Chapter 5. It should be noted that the theory behind data manipulation and processing of time-lapse ERT results are covered in Chapter 4, the Methodology Chapter, and although relevant information may be touched on in this chapter, it is not covered in detail.

Landslides are classified and the types relevant to the project described in detail. This is followed by a short overview of the application of geoelectrical methods for investigation of landslides. An in depth explanation of how electrical resistivity tomography (ERT) works and how it has been applied to investigate landslide systems is covered. Finally, ERT monitoring is presented, as are several examples of its application to better understand landslide processes.

2.2 Landslides

This project is centred on better understanding the hydrogeological triggers to landsliding, therefore Section 2.2 is aimed at informing the reader about landslide classification and mechanics, trigger mechanisms and failure events in the geographical region of North Yorkshire.

Landslides are a form of mass movement process and are generally defined as the “movement of a mass of rock, debris or earth down a slope” (Cruden, 1991; Varnes, 1978) and the term describes, inland, coastal and submarine landslides. Many landslide classification schemes exist, therefore Varnes (1978) attempted to standardise classification so that slope instability events can be described succinctly and unambiguously.

There are five types of landslide movement (shown in Figure 2.1) these are; fall, topple, slide, flow and spread and can occur within both bedrock or engineering soil. Landslides in engineering soil are further divided into two groups depending on dominant soil grain size (Cruden et al., 1996). A landslide within a soil with 80% or more particles smaller than 2mm is prefixed as *earth*, whereas a *debris* material has between 20% and 80% coarser material. Landslides taking place within rock are prefixed as *rock*. Further detail about the manner in which the landslide behaves when active is described in terms of landslide: state, distribution and style. The landslide studied in this research project is a slow moving earthslide-earthflow, with the latter being the most active region of the landslide.

Precipitation is one of the major landslide triggering mechanisms and temporal landslide activity is often associated with seasonal rainfall patterns (Van Asch et al., 1999). If sufficient rainfall data is present along with precisely dated landslide events then critical daily rainfall thresholds and antecedent rainfall amounts that trigger slope instability can be determined. This can be performed with good results if carried out for more or less homogeneous areas with only a single type of landslide (Terlien et al., 1996). In more convoluted landslide systems a distinct threshold is less easily achieved. This is due to the movement pattern and landslide types being related to entirely different meteorological threshold conditions. Shallow landslides generally develop slips between 1-2 m depth and it is the infiltration of rain water, unsaturated percolation and rapid water table rise that typically trigger this type of landslide (Haneberg et al., 1994). Shallow landslide failure occurs along a slip plane when moisture content is close to saturation due to rainfall accumulation, resulting in dissipation of matric suctions and considerable reduction of soil strength (Tu et al., 2009; Van Asch et al., 1999). Two types of moisture flow take place in a landslide system, matrix flow and bypass flow and the relationship between the two is an important aspect of understanding landslide triggering mechanisms.

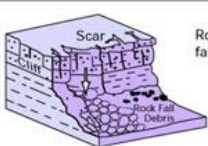
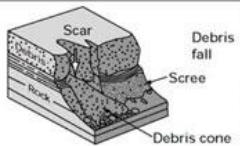

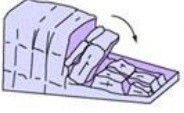
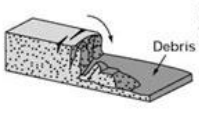
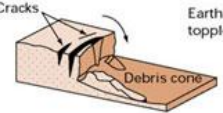

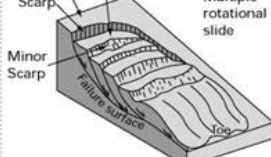
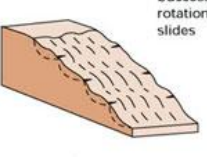
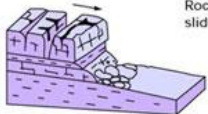


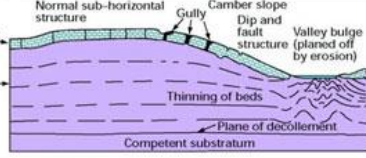

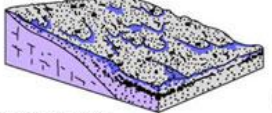
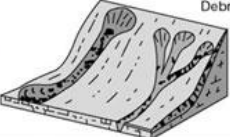


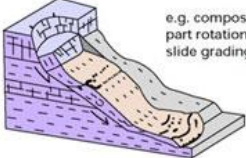
Material		ROCK	DEBRIS	EARTH
Movement type	FALLS	 <p>Scar Rock fall Rock Debris</p>	 <p>Scar Debris fall Rock Scree Debris cone</p>	 <p>Scar Earth fall Fine soil Rock Colluvium Debris cone</p>
	TOPPLES	 <p>Rock topple</p>	 <p>Debris topple Debris cone</p>	 <p>Cracks Earth topple Debris cone</p>
SLIDES	Rotational	 <p>Single rotational slide (slump) Failure surface</p>	 <p>Crown Head Scarp Multiple rotational slide Minor Scarp Failure surface Log</p>	 <p>Successive rotational slides</p>
	Translational (Planar)	 <p>Rock slide</p>	 <p>Debris slide</p>	 <p>Earth slide</p>
SPREADS	 <p>Cap rock Normal sub-horizontal structure Gully Camber slope Dip and fault structure Valley bulge (planned off by erosion) Thinning of beds Plane of decollement Competent substratum</p> <p>e.g. cambering and valley bulging</p>			 <p>Earth spread</p>
FLOW	 <p>Solifluction flows (Periglacial debris flows)</p>	 <p>Debris flow</p>	 <p>Earth flow (mud flow)</p>	
COMPLEX	 <p>e.g. Slump-earthflow with rockfall debris</p>		 <p>e.g. composite, non-circular part rotational/part translational slide grading to earthflow at toe</p>	

Figure 2.1. Landslide classification scheme (www.bgs.ac.uk)

Earthflows

Broadly speaking, two types of earthflow landslide exist, one is rapid, fluid charged, cohesion-less and shears along a thick zone of distributed shear. Most rapid earthflows take place in highly sensitive clay deposits, quick clays (Lefebvre., 1996) and often in response to intense, flash, rainfall events. These highly sensitive clays possess very low post failure shear strengths and result in very long runouts (Karlsrud et al., 1985). The other is very slow

to slow moving earthflow, they are common in plastic, fine grained highly weathered clay rich soils and distinctly drier than their rapid equivalent (Cruden et al., 1996).

Slow moving earthflows

This type of mass movement is typically found in temperate and tropical climates, and forms wherever clay or weathered clay-bearing rocks crop out (Baum et al., 1993) and are pervasive in rapidly eroding landscapes. Slow moving earthflows generally occur within fine grained marine-derived soils dominated by plastic silt or clay. Atterberg limits (plastic and liquid limits) vary between flow deposits however almost consistently fall between moderate and high plasticity. Shear strengths of earthflow deposits are soft to stiff and have a low sensitivity (Baum et al., 1993). The locations of shallow landslides correlate with soil depth, drainage area, topography, intense rainfall and loss of vegetation (Montgomery et al., 1994; Schmidt et al., 2001). The controls on slow earthflow spatial distribution must be understood to assess their contribution to erosion, landscape morphology and hazard analysis. These controls are geological, biological, climatic and topographic in nature (Kelsey et al., 1978; Bovis et al., 1985; Iverson et al., 1985; Mackay et al., 2011). Morphologically, these deposits have a teardrop shape and appear bulbous in plan view and elongate in the direction of down slope movement (Keefer et al., 1983). Very slow to slow moving earthflows travel at less than 13m per month (Cruden et al., 1996). Owing to the ephemeral nature of earthflow active periods, earthflow-prone landscapes are frequently imprinted with characteristically subtle landslide features such as head scarps, toes and multiple, deflated and eroded earthflow lobes at various stages of dormancy (Bovis et al., 1992). Several authors have identified the preference of slow earthflows on south facing hill slopes (Putnam et al., 1940; Kelsey et al., 1978) in fact, the landslide investigated in this project has a south facing aspect.

The majority of slow earthflows move primarily by sliding along discrete basal and lateral slip surfaces at residual strength (Hutchinson et al., 1971; Skempton, 1985; Keefer et al., 1989; Fleming et al., 1989), with a small fraction of internal shear deformation. Wasowski et al (1998) used borehole

inclinometry to show that the majority of flow displacement takes place by sliding along shear surfaces. Lateral boundaries of flows resemble strike-slip faults and form in conjunction with flank ridges. Shear zones are composed of low permeability clay layers that are weaker than both adjacent ground and landslide material, these clay layers also act to isolate the earthflow from adjacent lithologies. Shear surfaces are often pre-existing features such as buried soil horizons or former topographic surfaces and some appear to form due to mechanical enrichment of existing clay as a by-product of earthflow movement (Picarelli et al., 1998).

Savage et al., (1986) modelled slow earthflow displacement by assuming a Coulomb plastic material subjected to pore pressure and predicted normal fault scarps – in the zone of depletion – due to stretching and thrust faults – in the zone of accumulation – associated with shortening processes. Longitudinal deformation takes place within flow deposits, stretching taking place in the upslope and shortening in the downslope part of the flow (Fleming et al., 1993).

Slow earthflows respond quickly to hydrologic input and can be easily correlated with accelerations in earthflow activation and acceleration (Coe et al., 2003), thus implying that basal shear surfaces respond quickly to positive pore water pressures. This type of landslide is particularly prone to long term instability and commonly reactivate during periods of above average effective rainfall, as well as disturbing processes such as earthquakes (Skempton et al., 1985). Increasing water content of flow deposits increases the unit weight and therefore the driving stresses that encourage slope failure. By increasing soil moisture content, pore water pressures increase, causing a decrease in soil effective shear strength and reduction of shearing resistance available to be mobilised. Pore pressure fluctuations and shear surface roughness influence the rate of earthflow displacement (Iverson, 2000; Coe et al., 2003). Earthflow thickness is often a function of the depth of the weathering profile and depth to competent bedrock, therefore bedrock weathering rate may limit earthflow activity (Mackay et al., 2011).

Much of current research into slow moving earthflows centres on observing small scale movement patterns over seasonal or annual monitoring periods, however, little research focusses on the triggering mechanisms – precipitation, temperature, topographic loading and toe erosion – and their interaction with landscape geomorphological processes on the decadal scale (Mackay et al., 2009). Despite earthflow movement at a given location being episodic and accounting for a small area of landscape, they can deflate a basin source region of material far quicker than average regional erosion rates (Kelsey et al., 1978).

Interferometric synthetic radar along with aerial photographs have been used to identify and characterise over 150 previously unknown slow moving earthflows in the creeping portion of the San Andreas Fault, California (Schiengross et al., 2013). 75% of these landslides occur within 2 km of the fault trace activation occurs seasonally in response to winter rainfall on hill slopes of between 20° and 40°. Similar landslides are much less frequent away from the fault trace and are therefore attributed to fault-induced rock weakening taking place, increasing landslide susceptibility. Similarly to this investigation they attempt to understand triggering mechanisms leading to activations within their landscape system.

Landsliding in Lias Group of the Lower Jurassic of North Yorkshire

Nationally, the landslide density within Lower Jurassic is 21 landslides per 100 km², in the York area this is a factor of four higher. The density of inland landslides per 100km² in North Yorkshire as a whole is 5.91 (Jones et al., 1994). The Whitby Mudstone Formation of the Upper Lias is estimated to be mantled by landslides across 51% of its nationwide outcrop (Jones et al., 1994) However, this is only 4% within the York area according to Foster et al., 2007.

Landslides within the Lias Group account for approximately 50% of all landslides occurring within the District of York (Foster et al., 2007) and are typically shallow failure mechanisms, with slumps and flows the most numerous. Landsliding within Whitby Mudstone Formation are the most frequent in the York area and are often associated with the overlying Dogger Formation of the middle Jurassic, a local aquifer unit.

According to Foster et al (2008), who details the extent of landsliding in North Yorkshire, the main controls on landsliding in North Yorkshire are lithology, stratigraphy, topography and weathering. Landsliding appears to be concentrated in areas underlain by weak mudstone units such as Redcar Mudstone, Whitby Mudstone and Oxford Clay Formations. In particular, it is the Redcar Mudstone and Whitby Mudstone Formations, which outcrop at Hollin Hill which are the most prone to landsliding in North Yorkshire (Foster et al., 2008). In addition, the order in which formations are positioned, the stratigraphy, has an effect on landslide activation, for example where local aquifer units overlie weak mudstone formations.

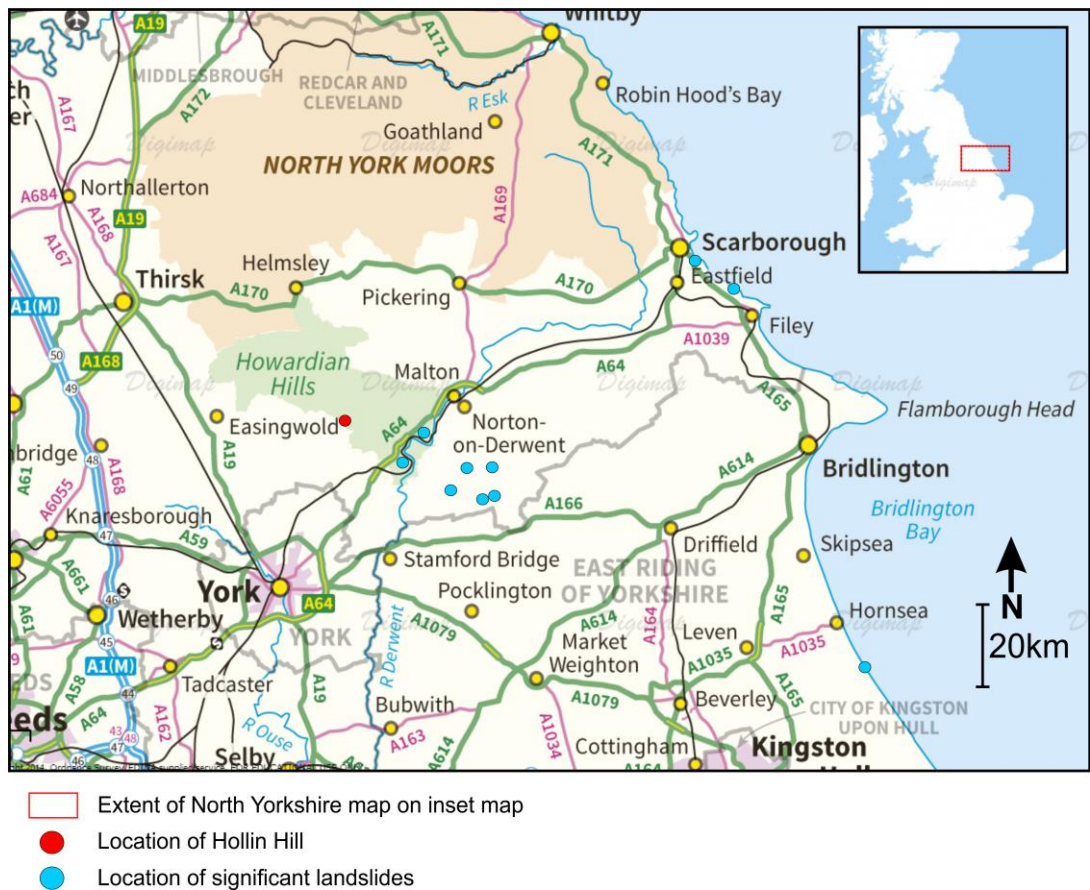


Figure 2.2. Map of North Yorkshire annotated with major landslides. (Map generated by DigiMap)

Figure 2.2 above highlights the locations of some of the most well-known and extensive landslide systems in North Yorkshire, these include, Knipe Point, Holbeck Hall, Acklam, Uncleby, Kirby Underdale, Leavening Brow, Birdsall Brow, Low Hutton, Crambe and Hollin Hill (Jenkins et al., 2006).

2.3 Electrical Resistivity Tomography on Landslide Systems

Electrical resistivity tomography is a geoelectrical tool used to image the subsurface distribution of electrical properties. It is also the principal investigative tool of this project. Described in Section 2.3 are the physical principles of resistivity surveying and modelling techniques which are utilised in this investigation. As well as the current state-of-art of electrical resistivity monitoring.

2.3.1 Electrical Properties of Earth Materials

Electrical current propagates through geological materials such as rock and minerals in three ways: electronic, electrolytic and dielectric conduction. Electronic conduction takes place through a material such as a metal, which contains free electrons. By comparison, in electrolytic conduction current is carried by ions within an electrolyte such as a salty brine. Dielectric conduction takes place in poor conductors whereby, under the influence of an external varying electric field electrons are slightly displaced with respect to their nuclei, thus separating negative and positive charges (dielectric polarisation) and results in the production of an electrical current (Telford., 1990).

Electrical resistance, R , (units: ohms, Ω) is the ability of an object to resist the flow of an electrical current. The resistance of a cylinder of homogeneous material (i.e. of constant cross section) is given in terms of an applied current, I , (units: Amperes; A) through the material and the measured resultant potential difference, V , (units: Volts; V) across it. Hence,

$$R = V/I$$

Equation 2.1. Ohm's Law for electrical resistance of a homogeneous material

The resistance of a material is a function of the cross section of the material and is observed as potential difference across the specimen. A more useful measure of a materials ability to resist electrical current flow is resistivity, ρ , (Units: Ωm or $1\Omega\text{m}^2/\text{m}$) which is a bulk property of the material, and therefore does not vary with the shape of the material. For a cuboid of

material of length, l , and cross sectional area, A , its electrical resistivity, ρ , is described

$$\rho = R \cdot \frac{A}{L} = \frac{V}{I} \cdot \frac{A}{L} = \frac{1}{\sigma} = \frac{E}{J}$$

Equation 2.2. Electrical resistivity of a cuboid of material.

Where, E is the electric field strength, $E = V/L$, (Units: Volts per metre, V/m) and J is the current density, $J = I/A$, (Units: Amperes per metre²). Conversion of resistance to resistivity requires the integration of the geometry of the electrical measurement (A/L) and is referred to as the geometric factor, K . The inverse of resistivity is conductivity, σ (Units: S/m Siemens per metre). The resistivities of many abundant rock types are presented in Table 2.1 along with several at various moisture contents.

Methods of current conduction

The electrical resistivity of earth materials is the physical property which shows the greatest variation relative to other physical properties of the Earth (Telford., 1990), ranging over 20 orders of magnitude. A conductor is defined as a material that possesses a resistivity less than $10^{-5} \Omega\text{m}$, conversely, an insulator has a resistivity greater than $10^7 \Omega\text{m}$ and semiconductors lie between these two extremes.

Certain minerals such as native metals, e.g. copper, gold and graphite, conduct current via the passage of electrons (electronic conduction). However, most rock forming minerals, such as quartz and feldspar are insulators or possess negligible conductivities (Keller et al., 1966), therefore electrical current is carried through a rock most often by the passage of ions in pore waters (Kearey, 1991), i.e. by electrolytic rather than electronic conductivity.

Table 2.1 presents the typical ranges of resistivities exhibited by many sedimentary and igneous rock types, considerable overlap can be seen, and consequently it is very difficult to identify rock types based solely on this property.

The conductivity of porous rocks, electrolytic conductors, is strongly dependent on volume and arrangement of pore space, but even more importantly by the conductivity and amount of water contained within these pore spaces (see Table 2.1). An empirical formula called Archie's Law, published in 1942, describes the effective resistivity of an electrolytic conductor such as a porous rock. The application of Archie's Law (Archie, 1942) to model resistivity as a function of saturation is covered in more detail in Chapter 5.

Common Rock Types	Resistivity range (Ωm)
Granite porphyry	4.5×10^3 (wet) - 1.3×10^6 (dry)
Gabbro	$10^3 - 10^6$
Slates	$6 \times 10^2 - 4 \times 10^7$
Consolidated shales	$20 - 2 \times 10^3$
Conglomerates	$2 \times 10^3 - 10^4$
Sandstones	$1 - 6.4 \times 10^8$
Limestones	$50 - 10^7$
Unconsolidated wet clay	20
Clays	1 - 100
Common Sedimentary Rock Types with moisture content	
Siltstones (54 % H ₂ O)	1.5×10^4
Siltstones (38 % H ₂ O)	5.6×10^8
Coarse sandstone (39 % H ₂ O)	9.6×10^5
Coarse sandstone (18 % H ₂ O)	10^8
Medium sandstone (100 % H ₂ O)	4.2×10^3
Medium sandstone (10 % H ₂ O)	1.4×10^8

Table 2.1. Electrical resistivities of a range of common earth materials (Telford, 1990).

Pore waters contain dissolved salts and in the presence of an electric field conduction occurs through this electrolyte much more effectively than through rock minerals which are commonly poor electrical conductors and are classified as insulators. The resistivity of a liquid electrolyte is dependent on the species of ion present, their concentrations and mobilities (Keller et al., 1966).

There exist unbalanced charges on the surfaces of certain mineral crystals, this permits these minerals to sorb ions onto their surfaces in an exchangeable state. These surfaces appear to locally possess charge which attracts water molecules and ions of the opposite charge in the Stern Layer.

However, the charge imbalance at the negative mineral surface is not perfectly balanced by the compensating Stern Layer and so an additional layer known as the Electrical Diffuse Layer is formed through the attraction of partially mobile ions that are surrounded by water molecules to counterbalance this slight charge imbalance. These partially mobile ions surrounded by water molecules are known as hydration shells or free electrolyte, and the combination of the Electrical Diffuse Layer and the Stern Layer forms the Electrical Double Layer (Revil et al., 1997; Pride, 1994; Leroy et al., 2004).

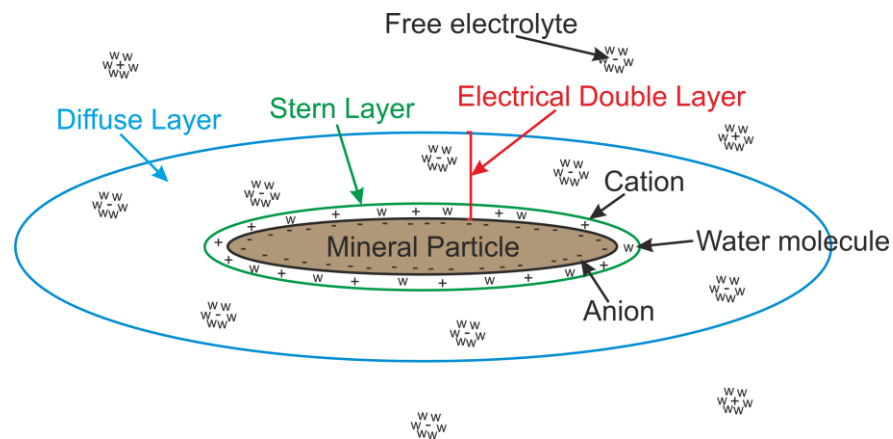


Figure 2.3. Diagram Adapted from Revil et al., (1997) and Leroy et al., (2004).

Clay minerals such as Illite and Smectite are examples of minerals that possess a negative charge imbalance on their surfaces (Figure 2.3). Their plate-like mineral grain structure gives them a large surface area on which to sorb ions and water molecules relative to other minerals. In the presence of an electrical field, for example while an electrical resistivity tomography survey is being performed, current can be transmitted within the Electrical Double Layer (EDL). This process is particularly significant within the Electrical Diffuse Layer as water-surrounded partially mobile ions are able to move in the direction of the applied electrical field. The process of mobile ions transporting electrical charge near the surface of clay minerals (the matrix) acts to reduce the resistivity of clay containing lithologies and contributes a second mechanism of electrical current flow in the subsurface, the first being within the pore fluid electrolyte, carried by free electrolytes outside of the EDL.

Clay minerals are particularly efficient at sorbing exchangeable ions because of their small particle size and resulting large surface area relative to coarser grained lithologies. Many species of clay minerals exist and have many different crystal lattice structures, and therefore produce different strengths of bonds between internal clay layers. Some clay species are capable of attracting more charge than others, therefore a range of ion sorbtion capabilities are exhibited. The clay mineral species' ability to sorb exchangeable ions on to their mineral surfaces is called the cation exchange capacity (CEC). Table 2.2. displays the range of CEC values of the most common clay mineral species. Similarly to Archie's Law which models resistivity as a function of saturation for clean sands (i.e. conduction only through the pore fluid), there exists a model for geological materials with non-negligible clay and shale contents (i.e. conduction through the pore fluid and EDL). The Waxman-Smit model is implemented during this investigation and is described in more detail in Chapter 5.

Clay Mineral	CEC (meq/100g)
Kaolinite	3-15
Halloysite 2H ₂ O	5-10
Halloysite 4H ₂ O	40-50
Montmorillonite-group	70-100
Illite	10-40
Vermiculite	100-150
Chlorite	10-40
Glaucosite	11-20+
Palygorskite-group	20-30
Allophane	~70

Table 2.2. Typical cation exchange capacities of common clay minerals (After Carroll, 1959)

2.3.2 Electrical Resistivity Tomography (ERT)

ERT is a geophysical investigation tool which can be deployed to provide information about subsurface resistivity distribution in either 2- or 3- dimensions. This method works by injecting an electrical current, an artificial, galvanic source, into the subsurface and measuring the resulting potential difference at the surface (Kearey, 1991). By far the most common way to

perform this test is by using a four point measurement, comprising two injecting current electrodes and two electrodes to measure the resulting potential difference.

Electrical Theory

Electrical resistivity surveys are performed to inform about subsurface resistivity distribution and are done by making electrical measurements on the ground surface. The fundamental physical law exploited by resistivity surveying is Ohm's Law which describes the flow of current in the ground (Loke, 2002). Consider a single current electrode on the surface of a medium of uniform resistivity, ρ , as shown in Figure 2.4 and described previously.

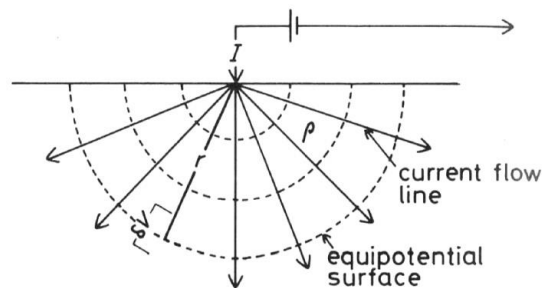


Figure 2.4. Current flow from a single point source electrode (After Kearey, 1991)

Electrical current flows radially away from the current source so as to maintain a constant current distribution along hemispherical shells centred on the point source, thus the current density $J = I/2\pi r^2$, where I is the injected current and r is the distance from the point source. Hemispherical shells mark surfaces of constant voltage and are often called equipotential surfaces. To determine the potential (V_r) at any point within the homogeneous half space the following equation is applied:

$$V_r = \frac{\rho I}{2\pi r}$$

Equation 2.1. Electrical potential at any point within a homogeneous half space

Rearranged in terms of ρ , we get the following

$$\rho = \frac{2\pi rV}{I}$$

Equation 2.2. Electrical resistivity at any point within a homogeneous half space

If the ground is homogeneous then resistivity (true resistivity) will remain constant and independent of electrode spacing and surface location. However, when inhomogeneities exist resistivity is a function of measurement location. Any resistivity measurement is therefore termed apparent resistivity (ρ_a) and is a function of the electrical properties of the material surveyed. If an electrical measurement is performed on a series of geological layers of different true resistivities then the apparent resistivity will be a bulk average of the true resistivity of the layers. The general equation to describe apparent resistivity made by a four point measurement and in terms of potential difference (ΔV) for any electrode position is:

$$\rho_a = \frac{2\pi\Delta V}{I \left\{ \left(\frac{1}{r_A} - \frac{1}{r_B} \right) - \left(\frac{1}{R_A} - \frac{1}{R_B} \right) \right\}}$$

Equation 2.3. Apparent resistivity for any electrode configuration (Kearey, 1991)

And where, r_A , r_B , R_A and R_B are distances between the arrangement of current and potential electrodes. By laterally traversing this four point electrode measurement of resistivity and taking repeat measurement an understanding of lateral resistivity distribution is developed. Separating the electrodes by a greater distance increases the depth of investigation, therefore, allowing a picture of spatial subsurface resistivity distribution to be built up. In homogenous ground the depth of current flow increases with increasing electrode spacing and places practical limitations on survey size and attainable depths (Kearey, 1991).

Field Resistivity Measurement

Two-dimensional ERT surveys are carried out using a number of electrodes, usually 25 or more, connected to a resistivity meter system via multi-core cable (Loke, 2002). A typical 2D ERT survey layout is shown in Figure 2.5 and details the arrangement of electrodes and the sequence of electrical

measurements when performing an ERT field survey, using the wenner array type.

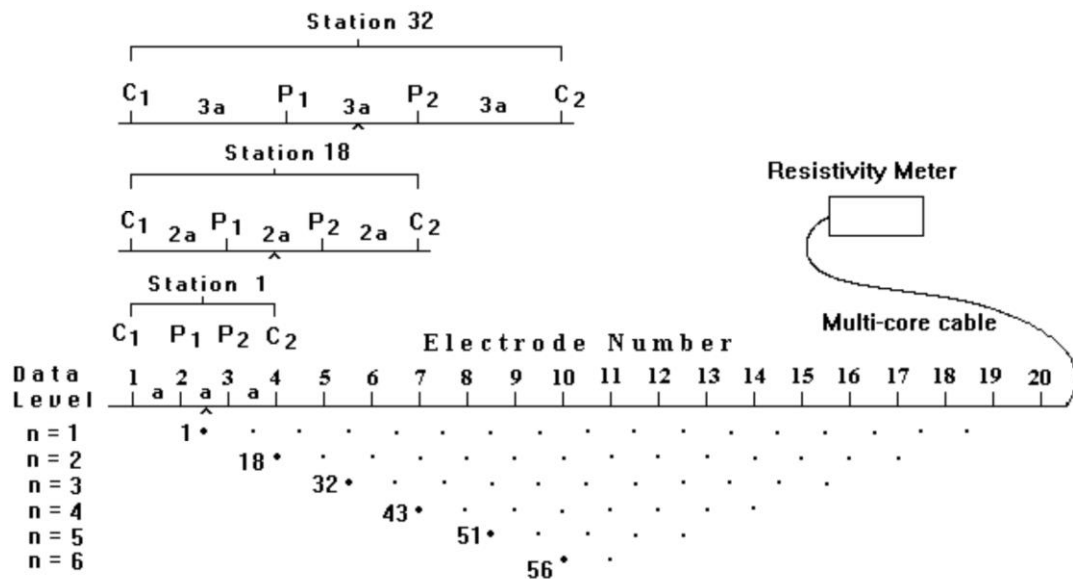


Figure 2.5. Layout of field equipment for a 2D ERT survey using the wenner array (from Loke, 2002)

The sequence of electrical measurements as well as the array type and amount of current to inject for each survey is transferred from a laptop in the form of a command file to the internal microprocessor built into the resistivity meter. The switching unit controls which electrodes inject current and which measure potential (Loke, 2002). Once all cables are laid out and take-outs are connected to electrodes via clips the multi-core cables are connected to the data acquisition unit and switching unit ready to begin taking electrical measurements.

The manner in which electrodes are positioned relative to one-another is known as the array type, and in practice three array types are most commonly used, these are; the wenner array, schlumberger array and dipole-dipole array. The wenner array has electrodes oriented C1,P1,P2,C2 and is highly sensitive to vertical changes in resistivity below the centre of the array. However, it is less sensitive to lateral, horizontal resistivity changes and for example is sensitive to sills and sedimentary structures. Conversely to the wenner array, the dipole-dipole array is highly sensitive to horizontal subsurface resistivity changes and is therefore highly suited to mapping vertical structures such as igneous dykes and cavities. Dipole-

dipole is frequently used in resistivity and IP surveys because of its low EM coupling effect (Loke, 2002). The electrodes of the dipole-dipole array are positioned C2,C1,P1,P2. Schlumberger array is similar to the wenner array as electrodes are positioned in the same orientation, with C1,P1,P2,C2. This hybrid of the wenner array has slightly better horizontal coverage compared to wenner array. However, its horizontal coverage is narrower than the dipole-dipole array.

The first step of a resistivity tomography survey (using the wenner array as an example) is to take all the electrical measurements using adjacent electrodes as current and potential electrodes. Following performing all measurements of $a=1$, electrical measurements are made using every other electrode, or of $a=2$ (Figure 2.4). This process is repeated until all resistance measurements have been taken and often a maximum of $n=6$ is adhered to. Electrical measurements are performed in a systematic order so as to minimise the effects of electrode polarisation which can hinder the quality of resistance measurements. Reciprocal measurements are often taken and are used as a measure of data quality with a reciprocal error of 5% or 10% often being used as an arbitrary cut-off between good and bad data (Dahlin et al., 1998).

Three-dimensional ERT surveys can be performed in a number of ways. In this investigation resistivity monitoring results were attained by category four type (according to Loke's classification) of 3D data acquisition. This means that several parallel 2D lines were performed and inverted together to produce a 3D model of subsurface resistivity. Loke, (2002) advises that if category 4 data is attained then the distance between parallel resistivity lines should not be more than the electrode spacing. This investigation has line spacing a factor of two greater than the electrode spacing. Although Chambers et al (2002) and Gharibi et al (2005) suggest that a line separation of two electrode spacings is acceptable.

Field measurements of apparent resistivity are bulk measurements of a volume of the subsurface and 2D profiles of apparent resistivity can be plotted by spatially aligning each measurement at the mid-point between measurement electrodes and assuming an arbitrary depth (e.g. median

depth of investigation (Edwards, 1977)). This method produces pseudosections and although these can be useful, say if apparent resistivity mapping, they do not provide the most accurate measure of subsurface resistivity distribution. Pseudosection contouring method gives a good approximate picture of true subsurface resistivity distribution but often give a distorted picture because different electrode arrays, such as Wenner, dipole-dipole arrays, would give different shaped anomalies.

Electrical Resistivity Modelling

The field measured resistivity of the subsurface is not true subsurface resistivity but an apparent resistivity, or a resistivity value that is the resistivity of a homogeneous ground that will give the same resistivity value for the same electrode arrangement (Loke, 2002). A mathematical inverse problem is solved to determine the subsurface distribution of resistivity from measurements of apparent resistivity made at the surface. Inverse modelling of resistivity datasets seeks to find a subsurface model that gives a similar response to observed apparent resistivity field measurements. Therefore, the model produces an idealised mathematical representation of the subsurface resistivity distribution which most agrees with field apparent resistivity measurements, within certain restrictions and limits. The model has a set of model parameters that are the physical quantities we want to estimate from the observed field data (Loke, 2002).

The inverse problem is solved in four stages, firstly a forward model is commenced starting from a homogeneous half-space. Then, the homogeneous half-space is adjusted by creating synthetic apparent resistivities which are then compared to measured field data. Apparent resistivities are then adjusted and the model iteratively improved so as to minimise the difference between the forward model and field data. The modelling process then ceases when the model has a sufficient fit with field data.

The software used in this investigation Loke's Res3DINV uses a cell-based method of assigning model parameters and resistivity values to the subsurface. The model parameters are the resistivity values of the model cells and the data are the observed, apparent resistivity data. A finite-

difference (Dey et al., 1979) or finite-element (Silvester et al., 1990) forward modelling approach provides the mathematical link between these two values and is optimised in an iterative manner to minimise the sum of least-square error between model parameters and data (Day-Lewis et al., 2002). Where the initial model is very poor the parameter change vector might change in a very unrealistic manner, this is overcome by implementing a Marquardt-Levenberg modification to the Gauss-Newton equation (Loke, 2002). A modification is added to the Gauss-Newtonian least-squares equation by introducing a smoothness-constraint to the model which buffers the spatial roughness of the model. These smoothness constraints are termed either smooth, or L1, or robust (blocky), L2 inversion methods.

Time-lapse Inversion Modelling Constraints on Resistivity Models

Any form of geophysical monitoring campaign is principally undertaken to image the changes in subsurface properties or conditions with time. Geophysical monitoring has been widely performed to study environmental and engineering problems. Electrical resistivity tomography is now commonly used to estimate hydrogeological properties, since the method is sensitive to fluid injection (Slater et al., 2000). Repeat ERT can be carried out to detect temporal and spatial changes of the subsurface (Rosqvist et al., 2010). The most common approach to time-lapse ERT monitoring is to invert a series of surveys independently and compare time-lapse images post-inversion. However, interpretation of ground condition evolution may be contaminated by inversion artefacts resulting from measurement error (Kim, 2005). Kim et al., (2009) proposed a four-dimensional least-squares inversion algorithm which provides subsurface images when subsurface properties are constantly changing. This was done by defining the subsurface medium in both space and time (space-time domain). Incorporating the time-domain into the inversion process permits the entire 4D monitoring dataset to be inverted using just one inversion process. Inversion artefacts are minimised between surveys by introducing regularisation into the time-domain. The approach to minimising erroneous noise in electrical resistivity monitoring data during the inversion process utilised by the inversion modelling software, Res3DINV, also involves a 4D simultaneous inversion route. This inversion software also uses a least-

squares method of subsurface modelling but applies a roughness filter (damping factor) which acts to minimise model cell property variation between surveys in both time and space (Loke et al, 2011). A spatial roughness filter constrains model resistivity in the x,y and z axes and similarly, another filter – a temporal roughness filter – minimises changes between the same model cell in subsequent surveys.

$$[J_i^T R_d J_i + \lambda_i (W^T R_m W + \alpha M^T R_t M)] \Delta r_i = J_i^T R_d g_i - \lambda_i (W^T R_m W + \alpha_i M^T R_t M) r_{i-1}$$

Equation 2.4. Inversion optimisation method with time and space constraints (Kim et al., 2009)

The linearised smoothness-constrained least-squares optimisation method is described in terms of model parameters and measured data in Equation 2.4. Where, the Jacobian matrix, J , contains the sensitivities of the measurements with respect to the model parameters. λ is the damping factor vector and g the data misfit vector. r_{i-1} is the model resistivity for the previous iteration while Δr_i is the change of model resistivity between iterations. While, W introduces the spatial roughness filter and R_m and R_d are weighting matrices used so that data misfit and model roughness vectors carry equal weights in the L1-norm inversion (Loke et al., 2003). Incorporating temporal roughness constraints involves the use of a difference matrix, M , applied across time models and a temporal damping factor, α . The higher the value of α , results in time-lapse inverted models being more similar to one another, at the expense of a higher data misfit and model roughness. The method described here can successfully recover temporal changes in the resistivity in a noisy, three-dimensional ERT monitoring data set.

2.4 Electrical Resistivity Tomography for Landslide Ground Model Development

Upon initiation of the project it became apparent that a ground model had to be developed for the site in order to best interpret the bulk of the monitoring datasets from the site. This Section therefore presents how ERT has been applied to develop a geological model so that I could adapt and build on their collective effectiveness.

In the last decade, electrical resistivity tomography (ERT) has become a standard geophysical imaging technique for environmental and engineering investigations (Reynolds, 2011) and is routinely implemented to locate the failure surfaces within landslide systems (Jongmans, 2007). The method can be effectively applied to ground investigation due to its sensitivity to lithological variation, principally, quartz and clay content, but also water content and pore-fluid conductivity (Telford et al., 1990). When applied to landslides, ERT is implemented to highlight lithological variations and boundaries, as well as geological discontinuities such as faults, drainage channel systems and other structural features (Lebourg et al., 2005). Because ERT provides indirect subsurface information, it is most appropriately applied alongside other techniques for calibration and validation.

Two-dimensional electrical resistivity tomography is extensively applied to landslide investigation due to its capacity to model landslide geometries such as body thickness, lateral extent and position of slip surfaces in a number of varying geological settings, ranging from the earthflows of Varco D'Izzo and Super Sauze to the Quesnel Forks debris slides (Perrone et al., 2004; Lapenna et al., 2003; Godio et al., 2006; Jomard et al., 2007; Sass et al., 2008; Schmutz et al., 2009; Colangelo et al., 2008; Bichler et al., 2004). In contrast, three-dimensional ERT (3D-ERT) is rarely implemented to investigate landslide systems; this could be attributed to several factors, principally the additional field and processing effort that is required relative to 2D ERT. However, for complex 3D structures, which landslides typically are, a fully volumetric 3D approach is more appropriate. A number of examples of 3D landslide studies exist in the literature, a brief summary of the most relevant is provided below.

A 3D resistivity survey was performed at a coastal setting by Udphuay et al., (2012). They implemented 3D ERT to assess the vulnerability of a cliff section in Normandy to cliff collapse. The various formations present – identified based on variable resistivity response – were assigned different mass movement potentials, despite the presence of extreme topography and cultural signals.

Heincke et al (2010) studied The Åknes rockslide in western Norway using a combined 3D geoelectrical and seismic tomographic approach. Seismic low velocity zones coincident with low resistivity anomalies were associated with drained (air-filled) and water-filled parts of tension cracks. Low-velocity and low-resistivity anomalies are explained by elongated tension cracks that are dry close to the surface and water-saturated at greater depths and correspond to tension cracks previously located and mapped in the region.

Pyroclastic cover material subject to debris-flow processes were investigated through high-resolution 3D resistivity surveys by Di Maio et al (2011) in the Sarno Mountains of Campania Region, Southern Italy. These landslides are periodically triggered by heavy rainfall events, hence, subsurface water content distribution is a key factor influencing the stability of the investigated lithologies. Laboratory determined petrophysical relationships were used to determine subsurface soil moisture content from ERT images.

A semi-empirical approach to slope stability analysis of pyroclastic cover material was proposed by Di Maio et al (2012). They introduced a geophysical factor of safety in terms of in-situ electrical resistivity and slope angle. They outlined the benefits of applying 3D ERT, a volumetric geophysical technique to assess slope stability as opposed to conventional physical analyses whose input parameters are determined through point-sample testing and laboratory tests performed on small volume soil samples, which are unrepresentative of the wider slope.

The La Clapiere landslide in the South East French Alps is responsible for large-volume mass movement of metamorphic bedrock. Lebourg et al., (2005) applied 2D, 3D and 4D ERT to investigate the rupture processes taking place within deep seated landslides. The investigation successfully located the principal slipping surface of La Clapiere landslide as well as the draining system in terms of identifying vertical draining structures and perched water table in superficial moraine deposits.

2.5 Time-Lapse Electrical Resistivity Tomography of Landslide Systems and Hillslope Processes

Presented in this Section is a description of several uses of ERT monitoring for the purpose of better understanding hillslope processes and also landslide internal dynamics. There is no exact scheme for exactly how to apply time-lapse ERT in the context of imaging environmental conditions, therefore care has been taken to order the research paper summaries included in this Section in as informative an order as possible. The summary Section of this Chapter (2.6) highlights how this project advances the current state-of-art in terms of ERT monitoring of hill slopes.

Due to the infancy of the application of the monitoring technique, very few examples of ERT monitoring of active landslide systems are published within literature. The examples that do exist offer very limited actual monitoring, as the majority offer only comparison between several differential resistivity images. Accounting for the effect that variation in seasonal subsurface temperature distribution has only been considered in a small number of projects. In addition to describing time-lapse resistivity applied to landslide systems, research into hill slope moisture dynamics by time-lapse ERT are also highlighted due to considerable overlap between the two research areas.

Descloitres et al 2008 studied sandy soil moisture dynamics using a combination of artificial sprinkler, electrical resistivity tomography and tensiometers to measure soil electrical properties as a function of rainfall infiltration and associated soil tensions. Their results feed nicely into our investigation, they found repeat electrical resistivity tomography results were sensitive to rainfall infiltration and evaporation within the vadose layer. Through application of Archie's Law they ascertained that small changes in porosity lead to large variations in modelled soil saturation; a 15% change in porosity causing a 40% resistivity change. They therefore opted to remove porosity effects from their analysis by utilising resistivity ratio as it is only affected by the electrical conductivity of pore fluid (pore fluid EC) and saturation. Similarly, Schwartz et al., (2008) studied field-scale soil moisture dynamics by applying a modified form of Archie's law – that accounts for

considerable clay content – to convert time-series 2D electrical resistivity profiles to 2D profiles of soil moisture profiles. The conversion was calibrated using a combination of Time-Domain Reflectometry (TDR) and pore water conductivity using an exchangeable cation proxy. While, Binley et al 2002 observed aquifer recharge processes using ERT and borehole radar and was able to track the migration of wetting and drying fronts as they percolated downwards in the vadose zone.

This investigation converted electrical resistivity field measurements to moisture content using Waxman-Smit equation which is presented in terms of gravimetric moisture content and not volumetric moisture content or soil saturation both of which are affected by non-constant porosity (described in detail in Chapter 4). When working with resistance, resistance ratios are analysed in place of total resistance.

Archie's Law is not applicable in this investigation as it can only be used for granular geological materials with negligible clay mineral content. Instead, a solution came from Chambers et al (2013), who studied subsurface soil moisture dynamics of a section of earth embankment that is an operational railway. They applied a different model that accounts for the additional electrical conductivity provided by shale bearing rocks (Waxman-Smit, 1968; Cassiani et al., 2009). Their investigation of a section of engineered transport infrastructure slopes visualised resistivity changes and gravimetric moisture content variation associated with rainfall-induced soil moisture wetting and drying events.

Seasonal subsurface temperature distribution was modelled by both Chambers et al (2013) and Brunet et al (2010) who both applied a similar method of fitting the heat equation (Cannon, 1984) to recorded temperature sensor data from several depths within the temperature-affected ground. Where the two differ however is the temperature to which they normalise resistivity measurements. Brunet et al (2010) opted to normalise resistivity to 25 °C, whereas Chambers et al (2013) proposed that normalising to mean air temperature is a more suitable method.

Brunet et al (2010) performed a regional evaluation of electrical resistivity monitoring for the purpose of assessing water deficit of a small plot in the

south of France. By performing one survey every month over a ten month period and using an array of 48 electrodes, each 0.5 m apart, they produced 2D time-lapse resistivity profiles and also 1D averaged volumetric moisture content plots through resistivity-moisture content laboratory calibration, and modelled using Archie's Law. Interpretation of ERT profiles and moisture content plots were complex due to the many different factors affecting electrical resistivity: porosity, temperature, pore water resistivity and water content. High resolution time-lapse resistivity monitoring observed catchment and hillslope processes on an artificially irrigated hillslope the Italian Central Alps (Cassiani et al., 2009). Their 3D resistance ratio images showed water migrating the unsaturated zone through preferential flow paths and through fracture flow. Later, they produced 1D profiles of soil moisture content as they converted model resistivity to volumetric moisture content by suitably adopting Waxman-Smits equation. In order to calibrate Waxman-Smit several parameters must be defined by laboratory testing and include, cation exchange capacity, soil bulk density, and pore fluid conductivity (Glover et al., 2000; Brovelli et al., 2005). Pyroclastic rocks potentially subjected to rainfall-induced, debris-flow type landslides were investigated in terms of their model resistivity differences between two surveys, one in Autumn, the other in Spring (Di Maio et al., 2011). Soil saturation was plotted as depth slices and was compared between the two surveys, as Archie's Law was again applied to laboratory calibrate electro-petrophysical relationships (soil saturation-resistivity). Considerable rise in water table occurred in the Spring survey into the lithological layer directly overlying a permanently saturated pyroclastic layer. Resistivity monitoring can therefore be used to assess transient soil saturation as a result of seasonal rainfall trends both of which are debris-flow activation trigger mechanisms.

While Friedel et al., (2006) applied a similar method, they primarily wanted to investigate use of 3D ERT to characterise a landslide endangered slope. Their investigation also implemented time-lapse imaging of a slope to compare the resistivity response of a silt layer during 'dry' and 'wet' periods. This could lead to resistivity tomography being used to inform about rainfall-induced landslides on slopes steeper than the soil's angle of internal friction, where the effect of suction plays a major part in stabilising the slope. The

electrical resistivity tomography array utilised comprised 50 electrodes, placed 0.5 m apart, and measurements were controlled using the Geotom of Geolog system. Groundwater flow within a landslide-slope area is imaged by 2D resistivity monitoring over a period of 42 days, in the Central Kyushu region of Japan (Suzuki et al., 2001). By presenting resistivity monitoring data in several formats, including 2D profiles of resistivity, percentage change in resistivity (%) and as 1D apparent resistivity sounding, rainfall infiltration was tracked and a conceptual hydrogeological model produced. Suzuki et al (2001) also modelled the effect that varying porosity has on the electrical resistivity – soil saturation modelled relationship that Archie's Law predicts.

The understanding of the structure of the large, deep-seated La Clapiere landslide system in South East French Alps was improved using 3D-ERT, which characterised its geometry, as well as ascertain the locations and nature of principle slip surfaces and vertical drainage system (Lebourg et al., 2005; Jomard et al., 2006). In addition, groundwater evolution was observed percolating in shearing zones and along rock discontinuities over a six month period within three repeat 2D-ERT surveys of La Clapiere. Repeat 2D-ERT surveys were displayed as electrical resistivity profiles – utilising a 2m electrode spacing – but were not performed during landslide activity and were not temperature corrected. They also highlighted the sensitivity of ERT to identifying the importance of different flow paths, such as deep flow, perched water table flow to landslide displacement acceleration.

2.6 Summary

This investigation draws on current literature and combines their collective successes to advance the area of geophysical monitoring of landslide processes. This area is advanced in several ways:

1. Monitoring a periodically active landslide system, as all examples of landslide monitoring in literature study either endangered slopes, or suspended/inactive landslide systems.
2. By performing a long-term investigation of a periodically active landslide processes using 3D time-lapse resistivity tomography (3D-ERT).

3. Monitoring a periodically active landslide at high temporal resolution over a long period compared to investigations existing in literature. The total number of 3D-ERT surveys included in this project significantly exceeds even the most thorough of known previous projects.
4. Accounting for subsurface physical processes which act to mask hydrogeological processes. An example being seasonal subsurface temperature distribution.
5. Accounting for the anomalies that arise while monitoring a dynamic, constantly evolving, natural system. An example being changing resistivity measurement geometries as a result of electrode mobilisation.
6. Observing resistance monitoring results after different levels of post-processing to assess which is the most informative at the landslide system associated with this project. The literature review highlighted the range of ways in which resistivity monitoring results are plotted. Here, monitoring results are presented in a number of ways, from 1D temporal 'point' resistance measurements to 3D volumetric resistivity and moisture content images.

Chapter 3

Ground Model Development of Field Site

The aim of this chapter is to develop and present the results of ground model development through an integrated 3D geophysical and geotechnical approach for the Hollin Hill landslide system (and is published in Springer, International Consortium on *Landslides*; Merritt et al., 2013). The methodology for landslide ground model development is outlined and its effectiveness critically assessed. The study site has been the focus of a previous geophysical reconnaissance investigation (Chambers et al., 2011).

The focus of this site investigation is on the most effective geoelectrical method of the previous study and apply it to develop a detailed landslide ground model. Site-scale 3D ERT surveys, presented in Chambers et al (2011) are accompanied by additional, high-resolution, volumetric 3D ERT images of the most active regions of the landslide. High-resolution ERT results are integrated with detailed core logging and direct calibration of field ERT survey results. These data were correlated with petrophysical laboratory analysis of samples and geomorphological map production by air photo interpretation.

ERT surveys are presented at different resolutions to display the internal structure of the landslide system and display the improved detail afforded by higher resolution imaging. Here, new high-resolution ERT images of the most active area of the landslide system are interpreted alongside lower resolution ERT images (Chambers et al., 2011) and together informed the creation of detailed core logs. Laboratory analyses were integrated to establish relationships between the measured resistances, other electrical properties and lithologies of the key formations (i.e. WMF and SSF). Surface and subsurface observations of movement are used to indicate the distribution and rate of slip and the location of shear surfaces. The latest Digital Elevation Model (DEM) data generated from airborne LiDAR was analysed alongside aerial photographs using GeoVisionary, an immersive 3D graphical visualisation software package, designed to allow the user to

undertake virtual fieldwork in which even subtle geomorphologic features can be identified (Jordan et al., 2009). This combination of high resolution surface and subsurface data was used here to develop a ground model.

In this chapter, previous investigations are used as a basis for further advances in landslide characterisation. This improved understanding will be used to understand temporal and spatial landslide hydrogeological processes using the time-lapse ERT (presented in Chapter 6).

3.1 Site Background

The research area is located 6 km west of the market town of Malton, North Yorkshire, UK (see Figure 3.1, image inset). The field site itself is located on a south-facing slope used as pasture land. It is bounded to the north, south and east by hedged arable land and by mature woodland to the west. Figure 3.1 is an overview map, which shows the geology of the field site and surrounding area.

Beyond the base of the field site hill slope is a wide topographic embayment called Sheriff Hutton Carr, to the south of which is a ridge composed of Lower Jurassic formations. During the Devensian much of Northern Britain was covered in a thick ice sheet. Sheriff Hutton Carr was the site of an ice-marginal lake, responsible for depositing lacustrine material in the lowland between Hollin Hill slope and the ridge (Ford, in press).

3.1.1 Geology

The slope is composed of four geological formations of Lower and Middle Jurassic Age. The base of the Hollin Hill slope is composed of Redcar Mudstone Formation (RMF) and marks the oldest formation at the field site. This is overlain by Staithes Sandstone Formation (SSF) which gives way to Whitby Mudstone Formation (WMF), with Dogger Formation (DGF) capping the hill slope (geological map, Figure 3.1). Dogger Formation (a calcareous sandstone and local aquifer) is the lowermost formation of the Ravenscar Group of the Middle Jurassic and has an erosional base over most of the Yorkshire Basin (Powell, 1984; Rawson et al., 1995).

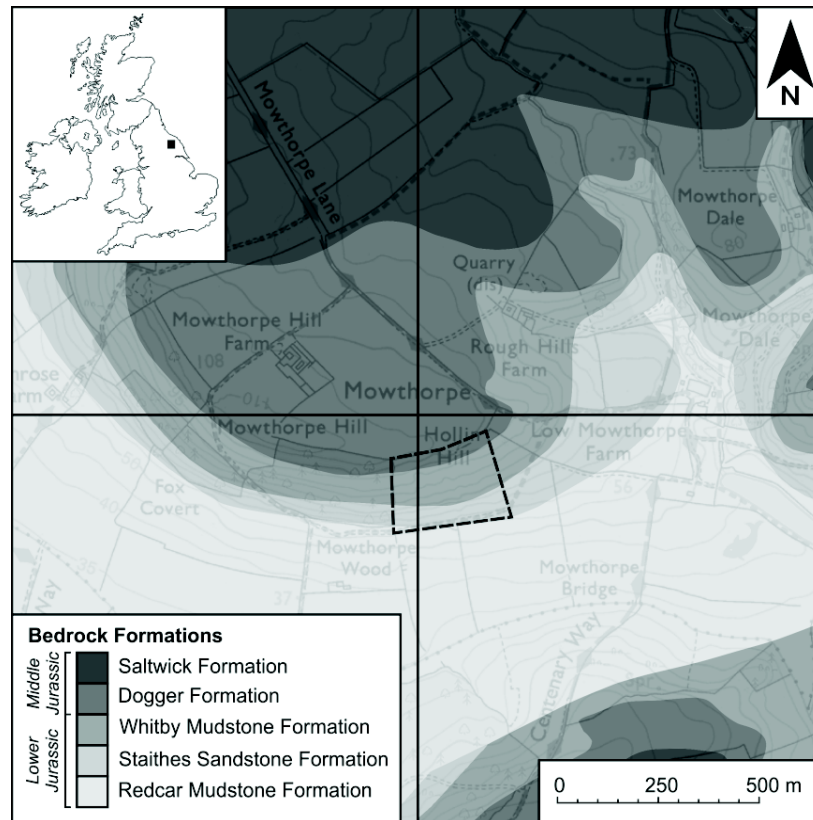


Figure 3.1. Geological map of the study area, and inset large scale map. Geological mapping, BGS © NERC. Contains Ordnance Survey data © Crown Copyright and database rights 2013. (Merritt et al., 2013). Black dashed lines represent the geographical limits of the field site.

Lias Group formations – in particular WMF – are prone to slope instability (Jones et al., 1994; Foster et al., 2007). The study site covers an area of roughly 450m by 200m, and a change in elevation of approximately 50m from the base to the top of the slope (mean slope angle of 12°), and contains a complex landslide system that exhibits a variety of landslide types and activity. The landslide system extends many hundreds of metres along the hill slope beyond the limits of the study site and has been previously described using Cruden and Varnes (1996) classification as ‘a *slow to very slow moving multiple earth slide – earth flow*’ (Chambers et al., 2011).

3.1.2 Previous Investigations

Previous investigations at the site are reviewed in Chambers et al., 2011 and include site reconnaissance using several geoelectrical geophysical methods including 2D and 3D ERT, self-potential profilings, mapping and tomography, and mobile resistivity mapping. Large scale, low resolution 3D

ERT, which extends from beyond the head scarp of the slump to the toe of this slump-flow landslide system reveals the site-scale structure of the site. It shows the near horizontal attitude (dipping $\sim 5^\circ$ to the north) and the resistivity response of the three geological formations which outcrop at the site.

Very near surface features and properties were revealed by mobile resistivity mapping using an automated profiling technique developed by Geocarta SA which produces a map of apparent resistivity variation. This technique is sensitive to soil property variations such as texture, stoniness, clay content and depth to bedrock.

Ground water movement was investigated through implementation of self-potential profiling, mapping and 3D SP tomograms whose sensitivity to subsurface streaming potentials reveal the nature of infiltration and drainage into formations at the site, in particular the granular, silty sand of SSF (Chambers et al., 2011).

3.2 Methodology

The site was characterised through an integrated approach, one which drew upon many available datasets and included methods which investigate the surface, such as remote sensing, and intrusive sampling and 3D ERT being vital examples (Merritt et al., 2013). Results of the integrated approach are presented in the form of a ground model and implement geophysical, geotechnical and remote sensing investigative techniques. In broad terms, surface geomorphology was mapped and interpreted through visualisation of airborne LiDAR and aerial photography. Subsurface internal landslide structure was ascertained by core logging of drilled samples and 3D volumetric electrical resistivity tomography, 3D ERT, which was deployed at several scales and resolutions, and are described in section 3.3.1. High resolution ERT images of the most active area of the landslide are interpreted in combination with detailed core logs and laboratory geotechnical and geophysical analyses. Furthermore, petrophysical relationships were developed between electrical and physical formation properties and were applied to aid calibration and interpretation of 3D ERT

results. Petrophysical tests were used to establish the relationship between measured resistivity and the key formations; Whitby Mudstone (WMF) and Staithes Sandstone Formations (SSF) (see Chapter 5).

Distribution and rate of slope movements and location of principal slip surfaces are identified through surface and subsurface observations. The latest Digital Elevation Model (DEM) data generated from airborne LiDAR is analysed alongside aerial photographs. It is the combination of high-resolution surface and subsurface data that is used here to develop a landslide ground model of the Hollin Hill landslide system.

A site plan and aerial photograph of the field site is presented as Figure 3.2, and shows the locations of installed monitoring equipment such as extent of 3D ERT arrays, borehole locations (Boreholes 1, 5 & 7) and of the major geological formation boundaries which crop out at the site.

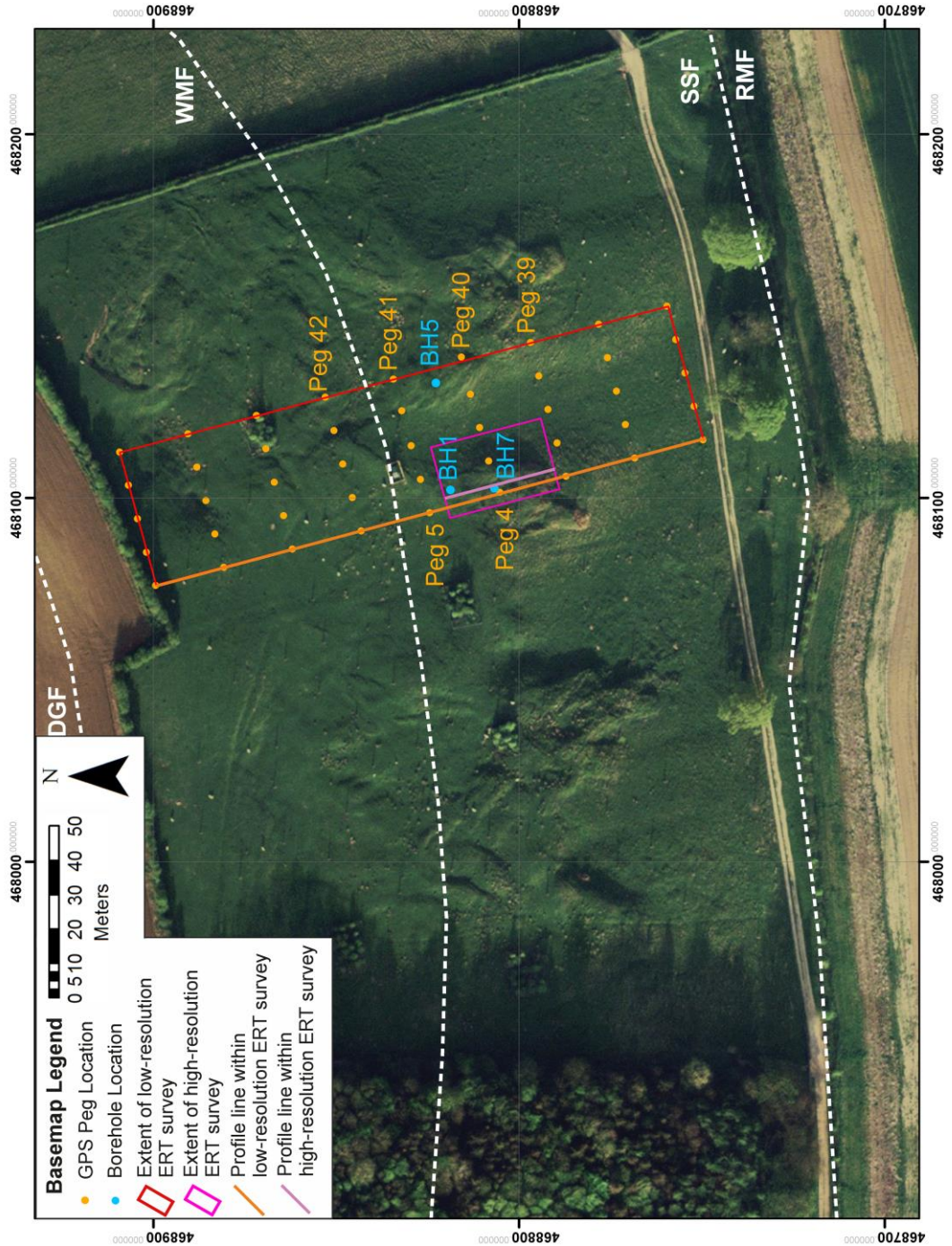


Figure 3.2. Plan view of study site, annotated with lithological boundaries (dashed white lines), positions of GPS pegs (orange points), borehole locations (light blue points) and areas of high- and low-resolution ERT surveys (low-res array: red rectangle, high-res array: purple rectangle). Orange and lilac lines indicate positions of interpreted profiles presented as Figures 3.13 & 3.16 respectively. Coordinate system is British National Grid (BNG). Illustration of study site based upon an aerial photograph © UKP/Getmapping Licence No. UKP2006/01

3.2.1 Surface Characterisation

Geomorphology

Light Detection and Ranging (LiDAR) optical remote sensing methods are implemented to produce high-resolution Digital Elevation Models (DEMs). An airborne LiDAR survey of Hollin Hill was performed January 2011, and GeoVisionary 3D Stereographic Software System used to visualise the resulting survey dataset. Virtual field reconnaissance software is capable of visualising high-resolution spatial data containing geomorphologic features, such as changes and breaks in slope, which can be digitised directly onto the 3D DEM. LiDAR and aerial photographs were performed on the same flight. The geomorphological map produced at Hollin Hill shows the distribution of landslide features, breaks in slope and other landforms throughout the field site.

Virtual fieldwork by visualising the DEM with an aerial photograph drape of the field site and surrounding areas – the model extended along the slope in easterly and westerly directions – was initially performed by picking out slope features such as changes or breaks in slope and sag ponds, and annotating them directly on to the DEM. Thus, creating a georeferenced shape file (.shp) that could be imported directly into ArcGIS10 to be interpreted and presented. Once all surface features were picked and catalogued in ArcGIS10 these geomorphological features were interpreted in terms of landslide type, activity and distribution. Identified landslide features include, main and secondary scarps, back tilted blocks (indicative of slumping), head, crown and toes.

GPS Survey of Peg Positions

A series of 45 surveying pegs were inserted approximately 0.3m into the top soil at the field site in a rectangular-shaped grid as shown on the base map (Figure 3.2). By periodically surveying the position of each peg over four and a half years it has been possible to determine both the landslides active regions and rate of movement. The most active regions and movement history during the monitoring period (March 2008 to February 2013) were identified. The Leica System 1200 RTK-GPS (Real-Time Kinematic-Global Positioning System) was used to make repeat measurements of pegs

installed at the field site. Accuracy of the system in kinematic mode (receiving real-time position corrections) is up to 10mm (rms) horizontally and 20mm vertically.

3.3 Subsurface Characterisation

Core logging of percussion drilled samples, associated index testing and laboratory analysis, were combined with the three-dimensional electrical resistivity tomography. By performing index testing and additional laboratory sample analysis it is possible to calibrate 3D ERT images – which suffer the issue of non-uniqueness – in terms of geological formation and internal structure. The results of index testing and laboratory sample analysis is also implemented as a confirmatory tool when linking borehole logs to volumetric ERT images.

3.3.1 Three-Dimensional Electrical Resistivity Tomography

Low-resolution

Electrical resistivity tomography was performed on the landslide at two scales. The large-scale survey covered a region of the landslide system from the crown to beyond the landslide foot and toe, and is represented by the red rectangular area on the base map (Figure 3.2). Electrode spacing was 4.75m along-line and 9.5m between lines, covering an area of 38 x 147.25m. Data was acquired using the AGI Supersting R8 electrical resistivity survey system. Measurements of potential were made using a dipole-dipole configuration, with dipole sizes of 4.75, 9.5, 14.25 and 19 m ($a = 1-4$) and dipole sizes (n) of 1 to $8a$. A complete set of reciprocal measurements was utilised for data quality assessment and editing (Dahlin et al., 2004; Wilkinson et al., 2012).

High-resolution

The higher resolution ERT survey imaged an active flow lobe at a level of resolution closer to that of landslide heterogeneity (i.e. sub-metre rather than metre scale). A similar measurement configuration was employed, dipole-dipole, with dipole sizes of 1.0, 2.0, 3.0 and 4.0m ($a = 1 - 4$) and n of 1 to $8a$. Higher-resolution was achieved for the second survey by decreasing the

electrode spacing of the second ERT survey by a factor of 5 to one metre along-line spacing and two metres between survey lines. Survey location is shown on the basemap, Figure 3.2. A total 28 lines were performed, eleven- 31m length surveys parallel to y-axis and seventeen- 20m surveys perpendicular to the y-axis which were combined to produce a fully three-dimensional resistivity dataset. The high resolution survey covered an area of 31m by 20m using a grid of 32 by 21 electrodes.

Error Management of ERT surveys

Dipole-dipole measurements of resistance are made by four-point measurement, with two current and two potential electrodes. The reciprocal measurement (ρ_r) of the transfer resistance (ρ_n) is made by interchanging the current and potential dipoles. The Reciprocal Error for a given four-point measurement of resistance is defined as the percentage standard error in the average resistance measurement (average of transfer and reciprocal measurements) and is calculated:

$$|e| = 100 \times |\rho_n - \rho_r| / (\rho_n + \rho_r)$$

Equation 3.1. Reciprocal percentage error calculation

Chambers et al (2011) reports the error handling method and values utilised for the large-scale ERT survey. The higher-resolution ERT survey of the flow region 92.9% of measurements had a reciprocal error of less than 1% and so, all data points greater than 1% reciprocal error were removed before inversion. After editing a total of more than 8700 transfer resistance data points were inverted and an acceptable model convergence was achieved within four iterations of 1.83% mean absolute misfit error.

3.3.2 Core Logging & Index Testing

During October 2009 a drilling campaign was undertaken using the Dando Terrier geotechnical percussion drilling rig and a total of eight boreholes advanced to a depth of between 5m and 7m. The decision was made to focus attention on the most active part of the landslide system within the field site, which exhibited the freshest landslide features (a sharp crown and main scarp and lightly vegetated flow deposits).

Three of the eight boreholes performed during the drilling campaign at Hollin Hill were logged to BS5930 (British Standards Institution, 1999) and index tested to BS1377 (British Standards Institution, 1993). Cores selected for logging and geotechnical index testing were subjected to the following: particle size distribution (fines content by x-ray sedigraph), moisture content and shear strength by hand vane. Also, a series of Atterberg Limit tests were performed, to give an insight into the consistency and behaviour of the WMF and SSF at various moisture contents (Head, 2006). X-ray diffraction (XRD) analysis was used to investigate clay mineralogy. Particle size distribution analyses were performed every 0.5m until a lithology change was reached, in that case a PSD was performed either side of the lithological boundary. The positions of boreholes selected for logging and geotechnical index testing are shown on the field site basemap, Figure 3.2, with Boreholes 1 (BH1) and 7 (BH7) located on the western lobe and Borehole 5 (BH5) on the eastern lobe. Boreholes were interpreted based on the results of detailed core logging, high-resolution core photographs and index testing into landslide deposit type and stable, *in-situ* material. Therefore, the 1-dimensional structure of the landslide system is known at three discrete regions, these interpreted core logs. Four divisions were used to classify the core in terms of lithology and internal structure; agricultural top soil, flow deposits, rotational slump blocks and *in situ* Staithes Sandstone Formation.

3.3.3 Borehole Inclinometer

Borehole inclinometer measurements were made using an ITMSOIL vertical inclinometer system at boreholes BH1, BH5 and BH7, during 2009. Displacement readings were taken every 0.5m within the casing to determine the depth, direction and magnitude of slip surface displacement over time. Inclinometer survey dates are presented on Figure 3.9.

3.3.4 Core Resistivity & Cation Exchange Capacity

Laboratory measurements of soil resistivity were made on core from BH5 and BH7, with the aim of aiding the differentiation between units and formations. The cores were halved using a purpose-made rock core cutting saw by making an axial cut, along the full length of each one-metre core run. At 0.1 metre spacing a Decagon 5TE soil moisture and bulk electrical

conductivity (EC) probe was inserted into the half core and bulk EC measured for the whole length of cores BH5 and BH7. The results of core resistivity measurements are presented (Figure 3.9) along with the interpreted borehole logs in order to show the variation in electrical resistivity between soil units at Hollin Hill.

A series of 32 soil core samples from BH5 and BH7 were tested for CEC and a plot of core resistivity – measured using Decagon 5TE soil moisture sensor (described above) – versus CEC produced. These tests were used to differentiate between the major geological formations on the basis of lithological properties (i.e. CEC) and resistivity, thereby establishing petrophysical relationships to aid the interpretation of the 3D resistivity images.

3.4 Results

3.4.1 Surface Expression

The geomorphology map of Hollin Hill is shown in Figure 3.3. To the north of the site, an abrupt increase in slope angle, highlighted by positive and negative break in slope, indicates the presence of the main scarp along with associated crown cracks as the landslide continues to retrogress northward. The backwards tilt of the head of the landslide is suggestive of slumping. The main scarp can be traced east-west across the site, however it is the north-east region that was seen to be most active. Fresh, shallow slumps (shear surface at ~0.5m) to the north-east are taking place alongside less active and more extensive, deeper-seated (shear surface at between 3.0m and 5.0m) and more laterally extensive slumps. Traversing south from the main scarp and beyond the fresh, shallow slumps are a series of five or six subtle pairs of positive and negative breaks in slope. Each pair is separated by near-horizontal or slightly back tilted ground surface and are indicative of rotated slump blocks. The number of slumps present across the landslide system appears to vary in the mid-hill slope region of the system. Evidence of differing slump movement patterns is apparent between the eastern and western slumps. The eastern region of the site has more visible fresh slumps than the west suggesting that the eastern area experiences slump activation

more frequently and recently when compared to the west of the site. Slumps to the west appear less frequently active due to their lack of fresh surfaces and more weathered, degraded appearance and morphology.

The patterns of movement at the site transform further south as approximately parallel breaks in slope give way to curved breaks in slope. The change in surface expression is attributed to a change in landslide type as slumping seen in the mid- to upper- regions of the slope gives way to flowing, with several flows being active simultaneously. There are four regions of the landslide system where flows have developed and overridden slumped material. Each lobe of flow deposits is composed of previously slumped material and is comprised of several smaller flows, moving on multiple shear planes, which together form four distinct zones of accumulation throughout the field site. The zone of depletion of the landslide system lies between the main scarp to the north and the flow deposits further to the south. Above the two most easterly flow deposit lobes exists an area of relatively flattened and smoothed hill slope, this area is supplying displaced material to the currently active flow lobes.

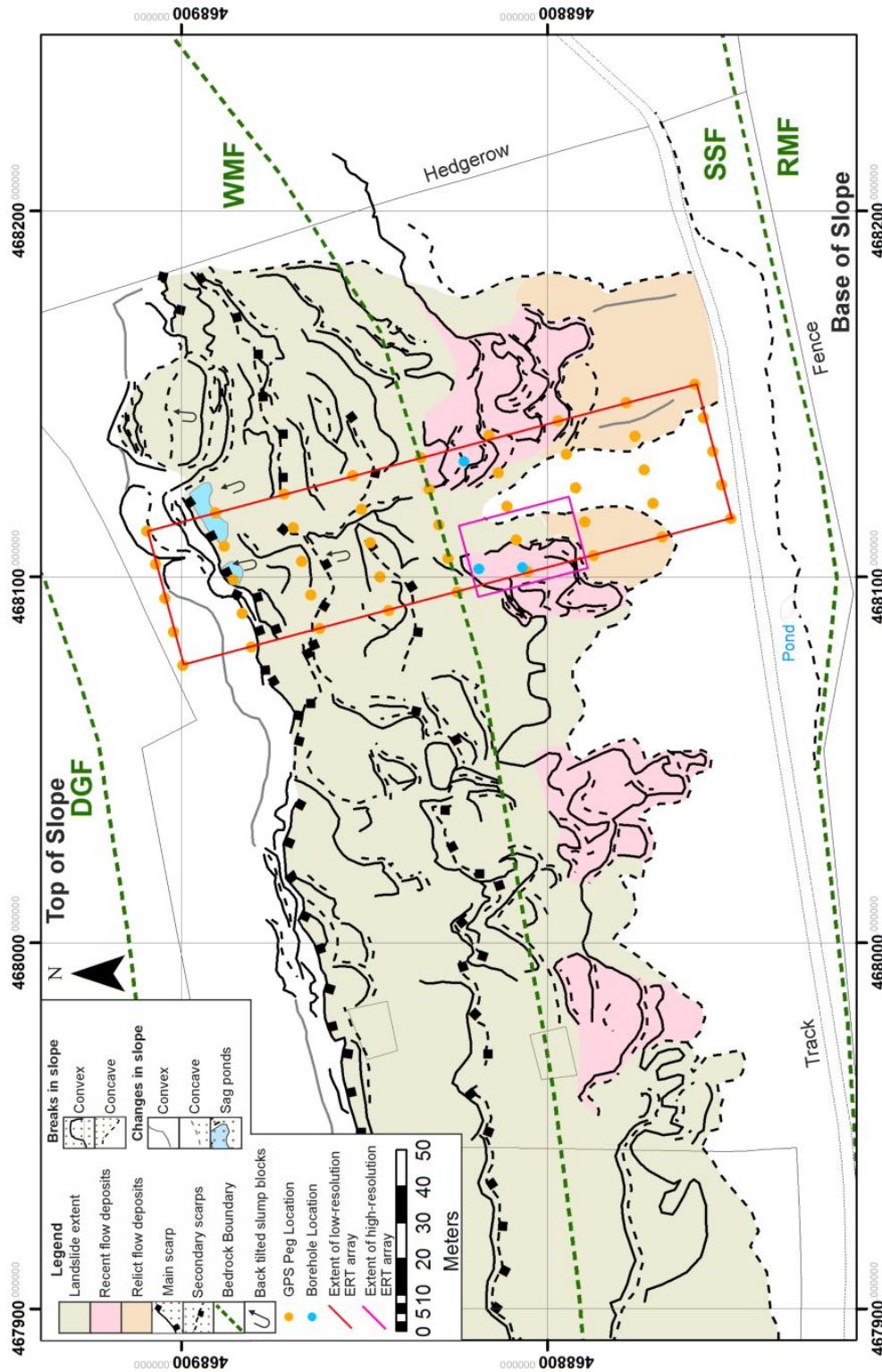


Figure 3.3. Geomorphology Map of Hollin Hill field site produced from an airborne LiDAR dataset, visualised using GeoVisionary stereographic software package and presented using ArcGIS10. The top of the slope is towards the north of the map, with the base towards the south; coordinate system used is BNG. (Taken from Merritt et al., 2013)

3.4.2 Rates & Distribution of Movement

The landslide was separated into two regions to make graphical presentation of results more straightforward and the locations of pegs is shown in Figure 3.4. The results of the GPS survey are presented in Figures 3.5 and 3.6, which show marker peg movement during the monitoring period. Figure 3.5 displays peg movement results for pegs located in the eastern region of the landslide system, whereas Figure 3.6 displays movements in the western region of the system. Peg displacements are graphically summarised in Figure 3.7.

Typical rates of movement are in the order of a few tens of centimetres per year (0.1m yr^{-1}) and are restricted to small areas towards the front of the earth flow lobes, with many of the marker pegs remaining static.

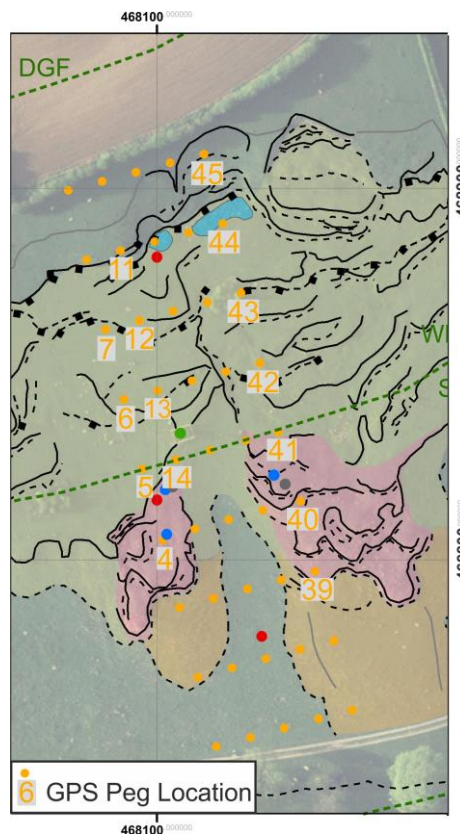


Figure 3.4. Annotated geomorphology map showing locations of pegs presented in figures 3.5 and 3.6.

Figure 3.5 shows peg displacement for pegs located in the east of the peg survey grid. Pegs 39, 40 and 42 of the flow region of the landslide system show displacement straight away with the pegs moving 0.2m, 0.1m and

0.1m respectively between 08/2008 and 04/2009. Several other pegs – 41 & 43 – show small amounts of movement (less than 0.05m) however these are very small movements and could be related to precision of the RTK-GPS system. Displacements appear to stop between April and October 2009 as survey pegs are shown to not be moving between these dates. Pegs 39 and 40 of the earthflow region displace 0.2m and 0.1m respectively between October 2009 and June 2010. Monitoring data from the next ~20 months reveal that the landslide was suspended before pegs 39, 40 and 42 once again begin to show evidence of slope activation during March or April 2012 as they move slowly until peg 39 – located at the foot of the landslide – moves more rapidly, covering 0.4m between July 2012 and November 2012.

Peg 40 located centrally within the earth flow region begins to move more rapidly between October 2012 and November 2012. Peg 42 moves extremely slowly between April 2012 and November 2012 at a seemingly constant rate of 0.15m over 8 months, it then moves more rapidly from November onwards, displacing 0.3 m in little over 3 months (November 2012 until February 2013). The survey pegs located higher up slope within the slump region of the landslide system show inactivity throughout the monitoring campaign and move very little, if at all, between August 2008 and November 2012, a period during which time the earth flow region shows several activation phases. From November 2012 onwards, until the end of the monitoring period, pegs 42, 43, 44 and 45 can be seen to activate suddenly, moving up to 0.7m in 3 months. Peg 45, located at the back scarp/crown of the landslide slump system displaces over 3.5m during the 3 month period. The fact that the earthflows activate several months before the slumps begin to show movement highlights the sequential nature of the eastern region of the landslide system.

Displacement of pegs located on the west side of the landslide system is presented in Figure 3.6. It is immediately apparent that the western side of the GPS-monitored survey peg array has a more simple displacement history. Between the commencement of peg monitoring in August 2008 until March 2008, only peg 4 can be seen to displace during this period, by 0.45m. All other pegs remain inactive during this period and all pegs – peg 4 included – show no activity between March 2008 and November 2012, over

a 4 year period. It should be noted that although not obvious, pegs 4 and 5 may show a small amount of displacement between April 2012 and November 2012, moving up to 0.1 m. From November 2012 onwards, pegs 4, 5, 7, 12, 13 and 14 of both the western flow region and slump region activate, by moving ~0.2m.

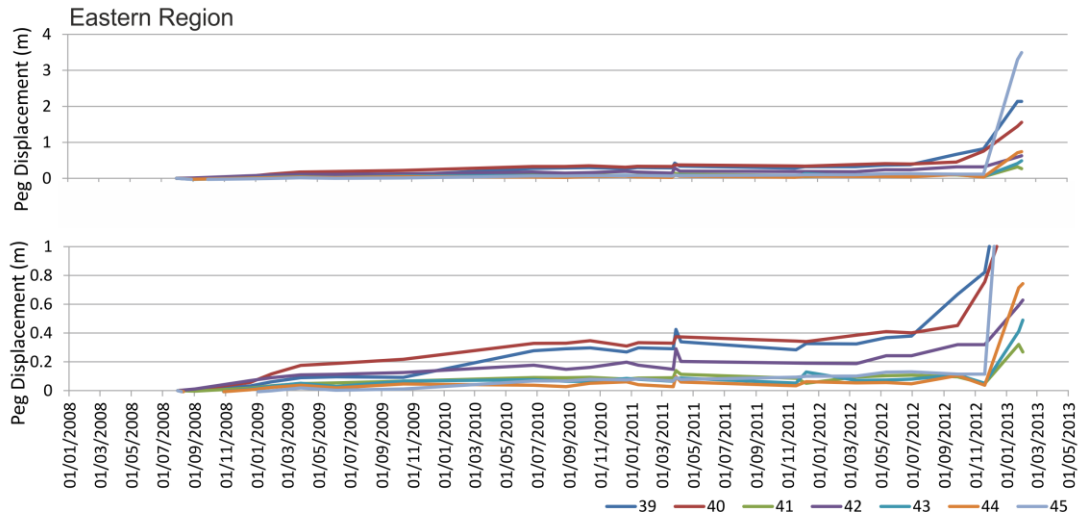


Figure 3.5. Landslide activity from RTK-GPS monitoring of surface-installed survey peg array of eastern region of Hollin Hill landslide system. NB. Different peg displacement scale axes on each plot, the top graph displays larger displacements compared to the lower.

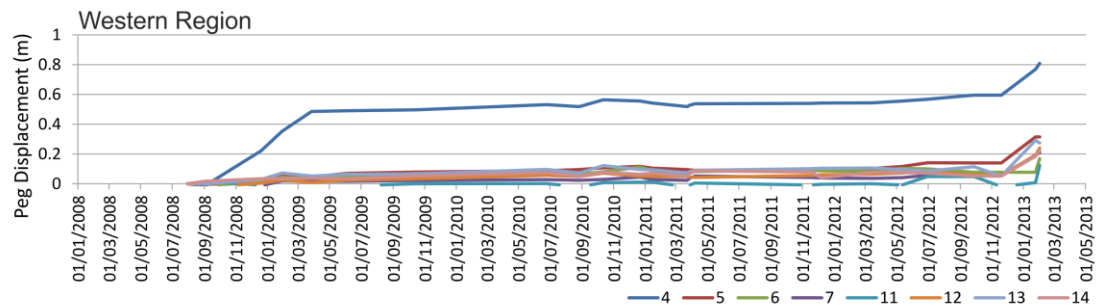


Figure 3.6. Landslide activity from RTK-GPS monitoring of surface-installed survey peg array of western region of Hollin Hill landslide system. Beyond January 2013, until the end of peg monitoring pegs 6 and 11 also activate. The seemingly instantaneous activation of both flow and slump regions of the landslide highlights the complex nature of this side of the landslide system.

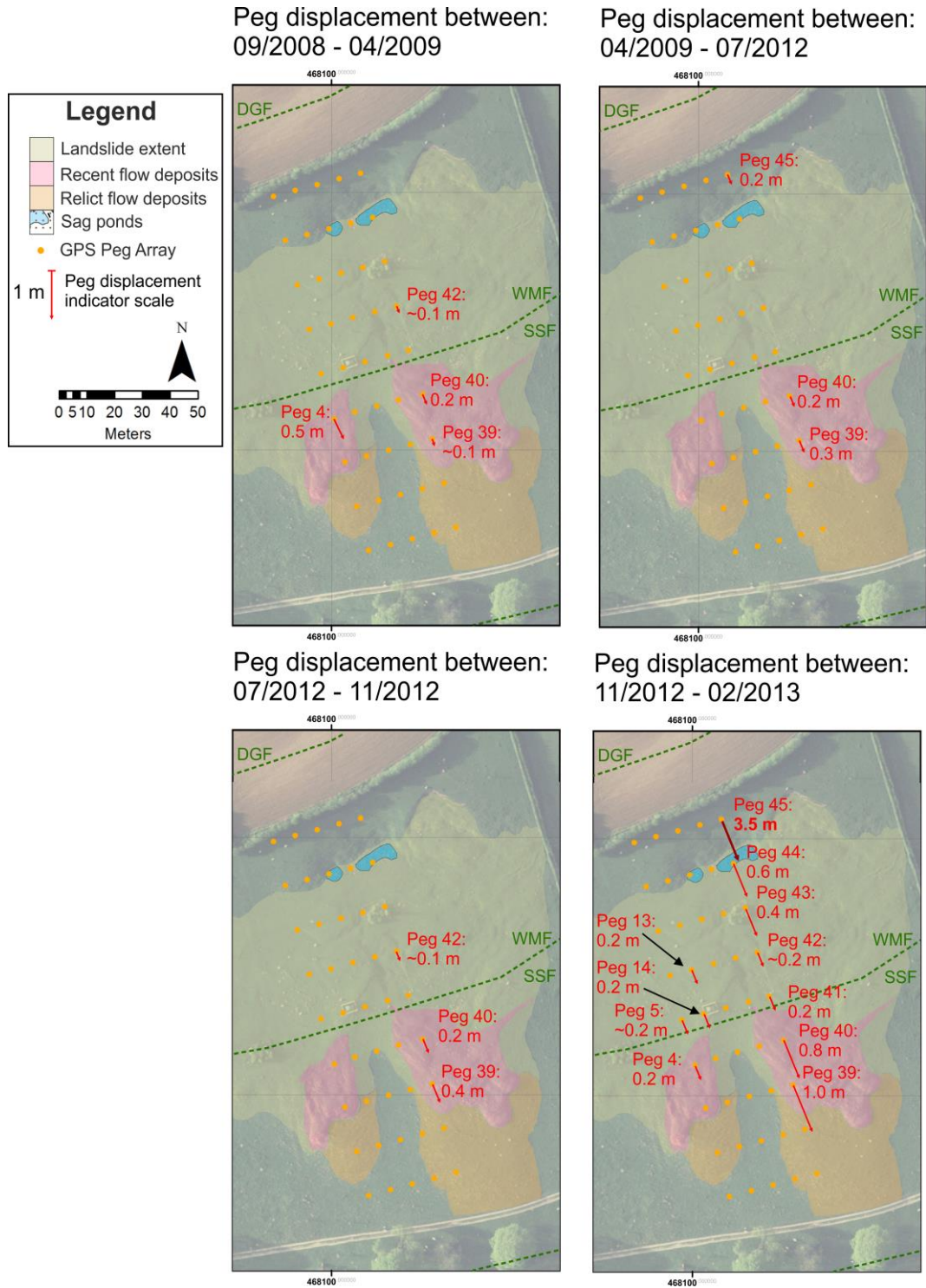


Figure 3.7. Graphical representation of landslide activity by peg displacement
Borehole Inclinator

Inclinometer data (Figure 3.9) produced over a period of two months in 2009 (Oct-Dec 2009) at BH7 and a period of twelve months (Jan-Dec 2009) at BH1 show that the active slip surface of the flow lobes is at between 1.0m and 1.5m depth, indicating that the same flow lobe is moving at the two

locations. Maximum shear surface displacements during the period of investigation by inclinometer at BH1 and BH7 are 25mm and 15mm respectively. BH5 inclinometer records show that a small amount of movement within the slumped deposits took place (2 mm of displacement), along with movement between 0.5m and 1.0m depth during the 2009 period of monitoring.

3.4.3 Soil Structure & Types

The results of core logging, index, resistivity and CEC testing from BH1, BH7 and BH5 are shown in Figure 3.9. These indicate that below the top soil layer are three principal soil units.

The uppermost layer is composed of several flow deposits, each separated by narrow slip surfaces. BH7 and BH1 are both interpreted as comprising six flow deposits, in which inclinometer data indicates that movement is occurring along shear planes between 1.0m and 1.5m (see Figure 3.9). Flow shear planes were identifiable by core logging due to the existence of thin yellowish-brown clay layers, often found in conjunction with organic-rich horizons, decayed rootlets underlain by mottled grey, gleyed clay zones. Flow deposits of BH1 and BH7 show similarities in their particle size distributions as their upper 0.7m is dominated by clay- and silt-sized material, below this depth, until the contact with slump deposits is reached at 3.1m, sand-sized material dominates. Core photographs presented in Figure 3.8 show the appearance of shear surfaces in borehole 7.

With increased depth the clay-dominated and sand-dominated flow deposits give way to a series of slump deposits. Slump deposits at BH1 and BH7 are distinctly heterogeneous interbeds of gravelly silty clay and clayey sandy silt being the most common soil types. Three slip surfaces are present in all three boreholes and are identifiable in soil core due to the existence of gravel-sized rip-up clasts, mostly composed of sub-angular, iron-stained clasts of sandstone. Where the formation is silt dominated shear surfaces exist as thin silt/clay rich layers, 0.1m in thickness. At greater depths, at 5.20m and 4.90m in BH7 and BH1 respectively the base of the slump deposits exist and the top of *in-situ* Staithes Sandstone Formation is reached. In the core, SSF is a firm to hard light olive grey to yellowish brown

micaceous sandy clayey silt with occasional nodules of ironstone and siltstone. Inclinator records show that no movement within slumped material took place within BH1 and BH7 during the period of monitoring.

The lithologies present within BH5, located on the eastern most flow lobe, follow a similar sequence to boreholes 1 and 7; a thin layer of top soil, followed by a series of clay-dominated flow deposits, three slump deposits and *in-situ* Staithes Sandstone Formation. Flow deposit thickness is 0.5m thicker in borehole 5 (3.5 m) than boreholes 1 and 7 (3.0m) located on the other investigated lobe, the second lobe to the east. Inclinator records show two active shear planes, between 0.5m and 2.0m, within flowed material, and between 4.0m and 4.5m within slump deposits.

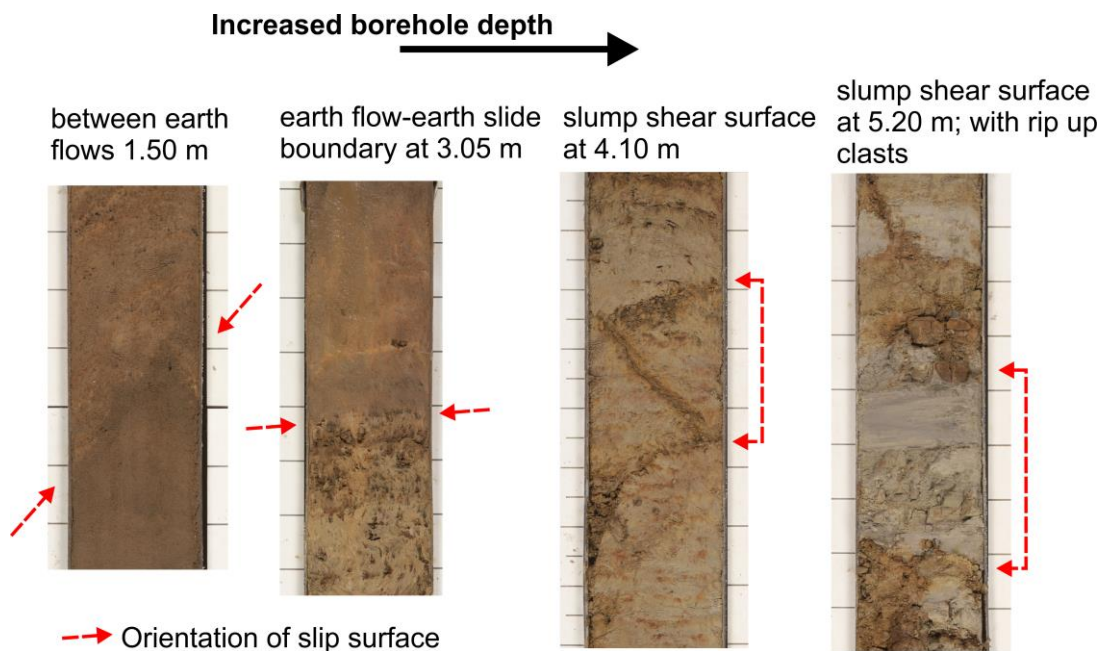


Figure 3.8. Images of shear surfaces and structural contact between earthflow and earthslide within Borehole 7.

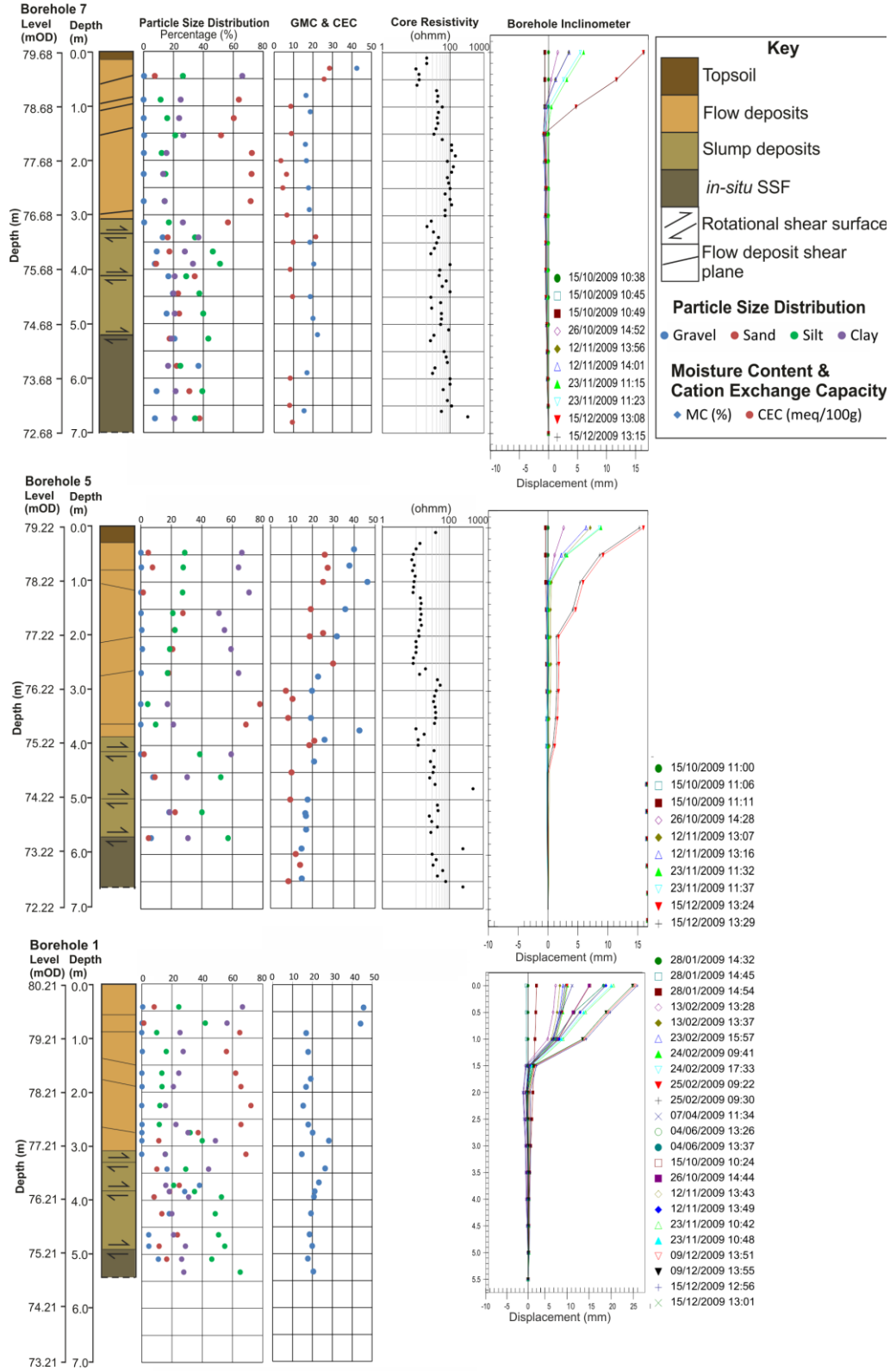


Figure 3.9. Interpreted core logs including particle size analyses, moisture content, cation exchange capacity, core resistivity and inclinometer data of boreholes: BH1, BH5 & BH7. Taken from Merritt et al., (2013)

3.4.4 Soil Properties

Clay content and mineralogy

The plasticity index and liquid limit of the unstable formations were determined and results presented in a plasticity plot, Figure 3.10. The results show that WMF consistently has a high to very high plasticity with all points plotting below the A-line indicating that the formation behaves in a silt-like manner. Whereas SSF has a lower liquid limit, plasticity index and plasticity compared to WMF, and is attributed to SSF having a higher silt and/or sand content.

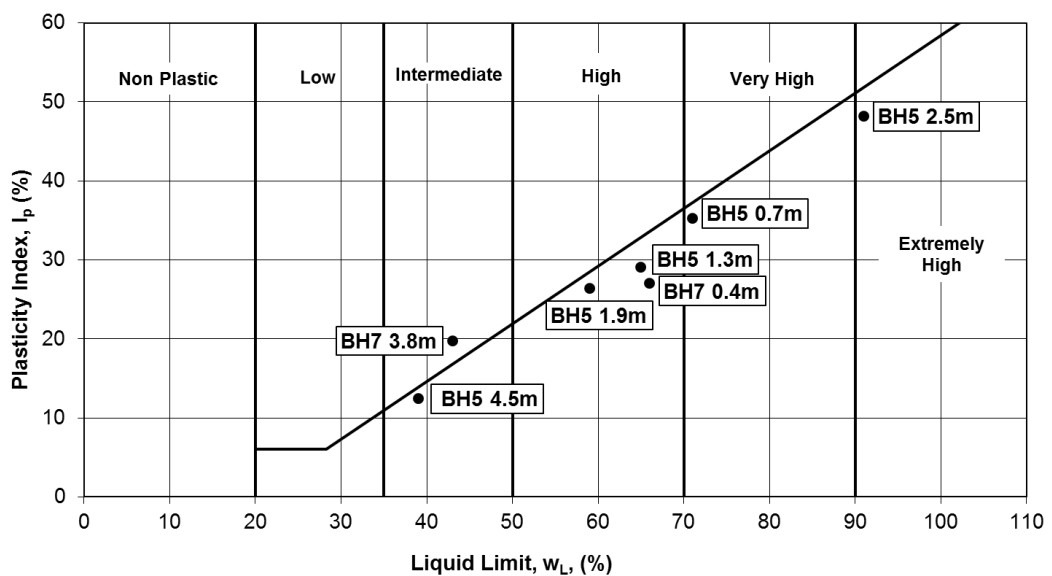


Figure 3.10. Atterberg limit a-line plot showing results for soil samples from BH5 & BH7. A-line plot presents results as plasticity versus liquid limit and shows plasticity of soil samples.

Clay mineralogy, determined from XRD analysis of material recovered from BH7, is summarised in Table 3.1. Clay contents vary from more than 50% to less than 6%, with illite-smectite and kaolinite represented. The sample of the slip surface within SSF – at 5.2m – has a higher Illite-Smectite content (26.6%) compared to other SSF-derived samples. Samples from 4.35m, 5.2m and 5.7m have a chlorite content of between 3.7 and 7.4%, which could be a result of natural presence of the mineral in the rock and/or the slip surface acting as a conduit for clay minerals, transported by groundwater flow or rainfall infiltration. Comparison of the XRD and CEC results (i.e.

Figure 3.9 and Table 3.1) shows a consistent correspondence between high illite-smectite contents and CECs, demonstrating that CEC is a good indicator of clay content at this site. Organic material worked into geological materials also raises the material's cation exchange capacity. Therefore, those CEC tested samples located near earthflow shear surfaces may have higher cation exchange capacities than those samples tested from mid-earthflow, due to additional CEC contributed by soil and organic horizons.

Depth (m)	Soil Desc.	Quoted as %									Total
		Quartz	Albite	Microcline	Calcite	Dolomite	Mica	Illite-smectite	Kaolinite	Chlorite	
0.4 m	Flow	18.4	5.4	4.8	0.0	0.0	16.2	33.4	21.6	0.0	99.8
1.9 m	Flow	81.0	4.5	5.1	0.2	0.5	2.1	3.5	2.2	0.0	99.2
3.55 m	Slump	40.8	15.0	5.1	0.0	0.0	6.0	17.0	15.9	0.0	99.8
4.35 m	Slump	35.4	11.7	5.9	0.0	0.0	7.8	16.6	16.4	3.7	97.4
5.2 m	<i>Slump: shear surface</i>	32.9	9.9	5.8	0.0	0.0	4.3	26.6	11.2	7.4	98.1
5.70 m	<i>In-situ SSF</i>	39.4	11.0	6.3	0.0	0.0	9.6	14.4	10.9	4.7	96.3

Table 3.1. X-ray diffraction analysis of six soil samples from BH7 which show the mineralogical composition of geological formations represented at the Hollin Hill field site.

Soil Cation Exchange Capacity – resistivity relationships

By plotting resistivity – determined by soil conductivity probe in the laboratory – of the cored samples versus their cation exchange capacity of 32 samples from various depths throughout BH5 and BH7 it is possible to differentiate between the formations present based solely on their electrical properties. Figure 3.11 presents cored soil resistivity versus CEC in semi-log space and shows the presence of two clustered groups of results. The first cluster of results shows a range of electrical resistivities and CEC values of between 28-115ohmm and 7-14meq/100g and corresponds to sand flow deposits, slumped material and *in-situ* SSF and are represented on the resistivity-CEC plot as red, green and orange points respectively. The second cluster produced resistivities and CEC values of between 8-14ohmm and 25-30meq/100g respectively. This cluster is composed of WMF-derived flow deposits as low resistivity and high CEC values are indicative of clay-rich material.

Located between cluster 1 and 2 are five data points which do not clearly belong to either the SSF or WMF clusters, and are attributed to clay rich layers located towards the top of SSF-derived slump deposits. In addition, two data points from clay flow material (BH5, 1.5m & 2.0m) also plot between the cluster and are attributed to a WMF derived flow deposit with a higher sand content (~20% sand) relative to the clay flow cluster (~5% sand).

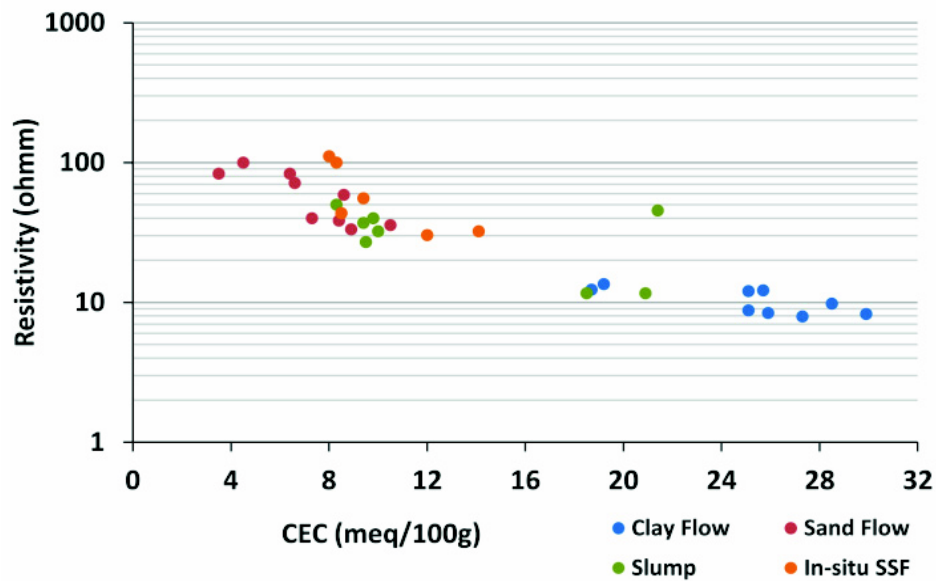


Figure 3.11. Core resistivity laboratory measurements versus corresponding cation exchange capacity of core samples from borehole BH5 and BH7. Coloured points represent different structural zones from interpreted borehole logs (Figure 3.9)

Soil Resistivity

Borehole 7 is seen to contain several zones of varying resistivities and good correlation exists between the various lithological and structural units found within the core (Figure 3.9). A thin layer of top soil exists from the surface to a depth of 0.2m with a resistivity of 20Ωm. The first clay-dominated flow exists between the top soil and 0.7 m depth, has a core resistivity of 10Ωm and CEC value of 25-27meq/100g. Beyond the first flow deposit are a further three flows which have similar resistivities ranging between 40Ωm and 60Ωm, where the flow deposits are met by an abrupt increase in resistivity at 1.6m. At this depth the clay-dominated flow deposits give way to sand-dominated flows along with associated resistivity increase to between 70Ωm

and 120 Ω m (Figure 3.9). CEC results for this series of sandy flows are consistently lower than those of the clay flows at around 6meq/100g. The boundary between flow and slump deposits is marked by a decrease in resistivity at 3.0m depth from ~100 Ω m to between 20 and 60 Ω m and with it comes a distinct change in lithology, as fines content increases from 30% to 70%. The resistivity of the slump deposits and *in-situ* SSF extending from 4.0m to 7.0m (termination of borehole) show a range of values between 30 Ω m and 100 Ω m. This 3 m section of the borehole is composed of soil and weak rock layers along with an assortment gravels and sands. Despite the lithological variety shown by the slump and *in-situ* SSF cation exchange capacity remains constantly between 8-10meq/100g within this depth range.

Borehole 5 contains a thicker layer of clay-dominated flow deposits – ascertained through particle size analyses – and core resistivity measurements are persistently low from beyond the top soil (0.3m) to the boundary with the rotational slump deposits at 3.9m depth. Resistivity remains at 10 Ω m from 0.3m until 2.7m where it steps out for one-metre to 35 Ω m, between 2.7m and 3.7m depth. Cation exchange capacity measurements within the clay flows between 0.3m and 2.8m vary between 19 and 30meq/100g. Between 2.7m and 3.7m the CEC is between 8 and 10meq/100g and coincides with a sand-dominated flow deposit possessing reduced clay content. The lowermost flow deposit and the uppermost slump deposit are located between 3.7m and 4.1m depth and show a resistivity and CEC of 10-20 Ω m and 20meq/100g respectively.

Slump deposits show an almost consistent resistivity from 4.1m to 5.7m which marks the contact with *in-situ* SSF and are between 25 Ω m and 45 Ω m, a much narrower range when compared to borehole 7. Core resistivity of *In-situ* SSF gradually increases with depth from 30 Ω m at 6.0m depth to 80 Ω m at 6.5m. Two high resistivity outliers of over 250 Ω m exist within *in-situ* SSF and are attributed to thin layers of weak siltstone. Between 4.1m and 6.5m the CEC measurement varies consistently between 9 and 14meq/100g.

Resistivity measurements made on soil cores show a range of values. This is due to the lithological variation within each soil type, which manifests as layers of more or less resistive material in core resistivity measurements.

Accumulation and dissipation of soil moisture content also contribute to resistivity variability in subsurface material and varies both spatially and temporally within the subsurface.

3.4.5 Volumetric Resistivity Imaging (3D ERT)

Low resolution

The result of the large-scale ERT surveys of the landslide system is presented in Figure 3.12. Three geological formations are present and are distinguished from one another by their relative differences in model resistivity. High relative resistivities are expressed as warm colours such as browns, oranges and yellows, whereas relatively low resistivities appear blue and green. The low resistivity formation present at the top of the slope (z-axis, 100m) is WMF and has a resistivity of 10-20 Ω m. Borehole derived measurement of resistivity of the soil core samples recorded a resistivity of between 10 and 20 Ω m (Fig. 3.9). Clay-dominated flows can be seen between 0.2m and 0.7m at BH7 and BH1, and 0.3 m and 2.7m at BH5. These resistivity values are in agreement with results of ERT surveys, thus confirming the presence and extent of clay-dominated flows, WMF derived, within both the survey and field site. This is the main formation which supplies material to form the flow lobes at Hollin Hill. The higher resistivity SSF is sandwiched between two low resistivity (blue) formations. When compared with WMF and RMF, SSF has a wider range of model resistivities, between 40 and 120 Ω m. Again, borehole derived measurement of resistivity show similarity with ERT survey results as SSF exhibits core sample resistivities ranging between 30 and 100 Ω m (see Fig. 3.9).

The stepped nature of the boundary between RMF with SSF in Figure 3.12 is an artefact of the inversion process and increased size of model blocks with depth. The more resistive regions of the tomogram are where the SSF crops out at the surface, this occurs towards the base of the slope, at the southern limits of the surveyed area. The uppermost ~4m of Staithes Sandstone has relatively high resistivities in the order of 70-120 Ω m, below this layer the resistivity of the formation is lower at around 40 Ω m.

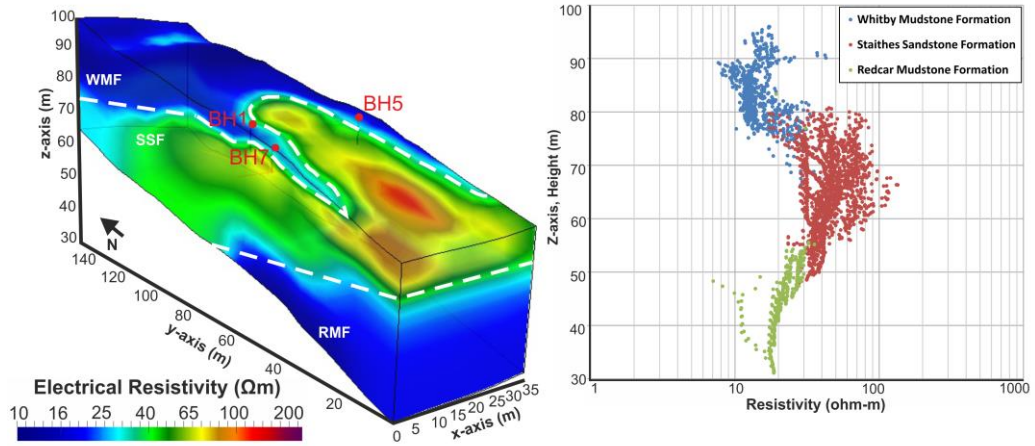


Figure 3.12. a.) (left) 3D volumetric image of resistivity from the low-resolution ERT survey (red rectangle on base map, Fig. 3.2.). Geological boundaries are marked with a white dashed line and formation names with white text. b.) (right) Height of model cell (z-axis) versus resistivity for low-resolution ERT survey and shows distribution of lithological formations at Hollin Hill.

This unsaturated and free-draining layer is subjected to seasonal soil moisture content variation as a result of evapotranspiration. Below this more resistive zone the Formation appear to be reasonably homogeneous with respect to electrical resistivity. Finally, placed stratigraphically below SSF is Redcar Mudstone Formation. RMF, similarly to WMF is a mudrock formation and has a model resistivity of 10-20Ωm. All three stratigraphical formations share a similar dip of between 5° and 10° to the North as can be seen from the layer boundaries in Figure 3.12. An annotated cross section – parallel with the y-axis – is shown in Fig. 3.13 and has the interpreted core log of BH7 superimposed to aid the positioning of the three main rotational slip surfaces. Slump shear surfaces were identified during core logging, however no geomorphological evidence, nor resistivity contrast exists within ERT survey images to suggest the exact orientation, length or form of these surfaces. The dearth of geomorphological evidence is due to the degradation of both the slumped SSF as a flow and the subsequent flowing of WMF up and over the SSF slumped material.

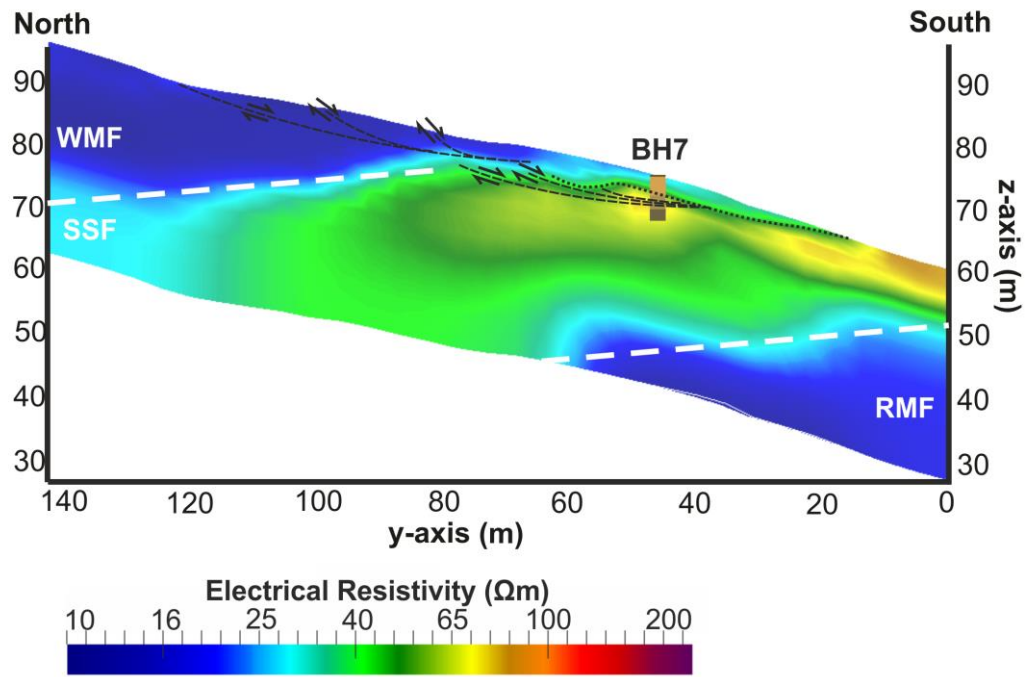


Figure 3.13. 2D ERT profile extracted from low-resolution 3D ERT survey. Profile runs parallel (approximately north-south) with y-axis and includes BH7. Rotational shear surfaces are represented by black dashed lines. Orientation and location of 2D ERT profile is indicated by an orange profile line on the basemap, Fig.3.2.

Rotational slip surfaces within WMF were matched with geomorphologic features picked out from LiDAR information and walkover survey. The material that composed the back scarp or slump block of that slump has since been activated, incorporated into a flow and deposited further down the slope. The boundary between the flow deposit of WMF – shown as a low resistivity (blue) mantle – with SSF-composed rotational slumps and *in-situ* SSF is clearly marked by a change in resistivity from 10-20Ωm (WMF) to 50-65ohmm (SSF) and also correlates well with the interpreted borehole log of BH7. Flow deposits appear to thin in a southerly direction and show a maximum thickness of ~5-6m. Two flow lobes can be seen in Figure 3.12 and form the two pointed features at the sides of the image as the unstable WMF flows down the slope over the underlying SSF.

The model cell height versus resistivity plot (Fig. 3.12, right) is used to illustrate the range of resistivity values for each lithological formation and acts as a guide, during ground model development, when applying ERT

results to inform the ground model regarding the spatial distribution of lithologies.

High resolution

Results of the high-resolution survey of the flow region are shown in Figure 3.14 along with the positions of BH1 and BH7. Figure 3.14 shows the flow region at a higher resolution than the large-scale survey presented in Figures 3.12 and 3.13, thus permitting the observation of additional subsurface features in the near-surface. Much of the surface is dominated by the blue coloured, lower resistivity unit which is composed of clay-dominated flow deposits of WMF. These flow deposits appear thinner in the high resolution survey and have a maximum thickness of 3m. In order to make the low-resistivity flow deposits more visible Figure 3.14 shows the blue flow deposits in 100% opacity but with the underlying units which possess higher resistivities at 50% opacity. From this figure the spatial distribution of the clay-rich, low resistivity flow deposit is clear, it thins towards its periphery like a thin veneer over the underlying formation. This is in agreement with borehole data which suggests that clay-dominated flows exist from the surface to a depth of 0.5m and 0.8m at BH7 and BH1 respectively. In the north of the survey area the clay-dominated, blue coloured, flow deposits appear thicker than to the south of the area.

This thickening of the blue unit is attributed to stacking of flow deposits over one another as the landslide system evolved. Directly below the clay-dominated flow deposits is a more resistive, tabular shaped unit with an electrical resistivity of between 80-120 Ωm . Boreholes 1 and 7 show that the lithology of the sand flow deposit is different to that seen elsewhere at the site, as the flows contain a greater sand content than WMF, *in-situ* SSF and slumped SSF. This alteration could be attributed to weathering processes or mechanical reworking while in flow as the finer material has been preferentially removed from the soil. The sand content of the sand flow is between 50-70% yet the rest of the formations present at the hill slope contain a relatively low proportion of sand. It is therefore uncertain as to provenance of this sand flow. However groundwater flow through WMF-composed flow, stripping it of its fines content seems the most credible.

Weathering can be discounted as a cause for increased sand content of the sand flow because the feature is relatively localised, weathering would have operated throughout the site.

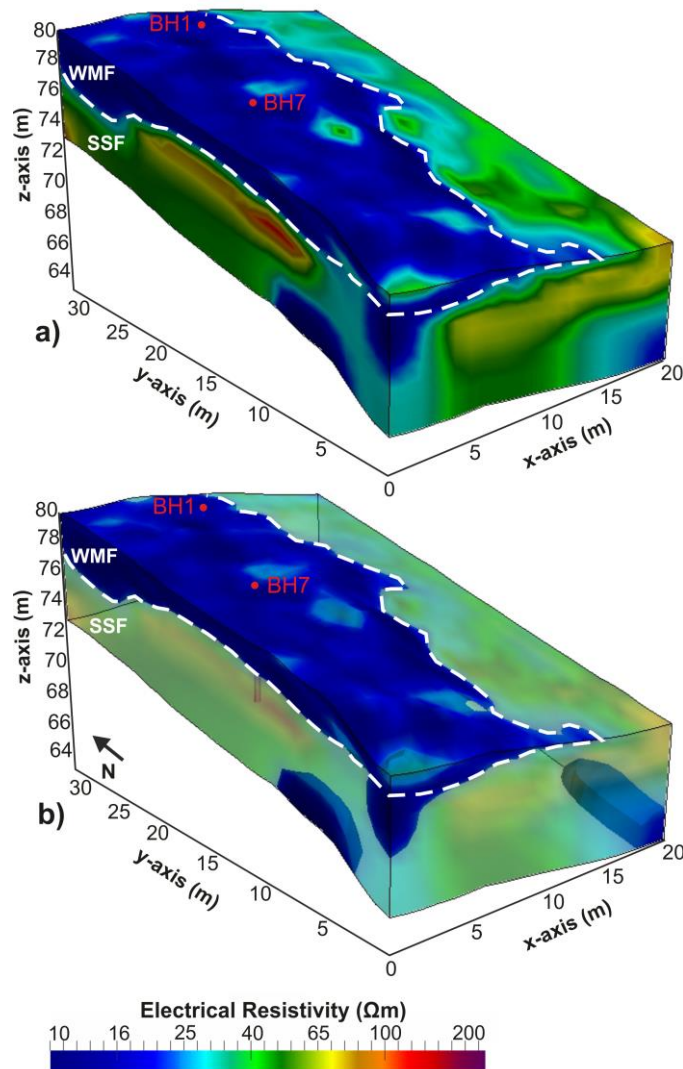


Figure 3.14. a.) (top) 3D volumetric image of resistivity from the high-resolution ERT survey (purple rectangle on the basemap, Figure 3.2.) A white dashed line indicates the boundary between WMF and SSF and two red points indicate borehole locations. b.) (below) displays the higher resistivity zone at 40% opacity and maintains the lower resistivity earthflow at 100% opacity. N.B. Low resistivity features at the base of the image are likely to be artefacts of the inversion process associated with regions of very low sensitivity (and hence resolution).

Figure 3.15 is a profile through the 3D volumetric image of model resistivity (Fig. 3.14) and is superimposed with interpreted borehole logs 1 and 7. Both 2D profiles offer good correlation with core logged data as all lithological and

structural boundaries are identifiable and well constrained. Figure 3.15 identifies a small resistivity difference between the sand flow and the rotational slump deposits which are composed of SSF. The resistivity is seen to reduce across the boundary between the flow and slump deposits from 80Ωm to 50Ωm.

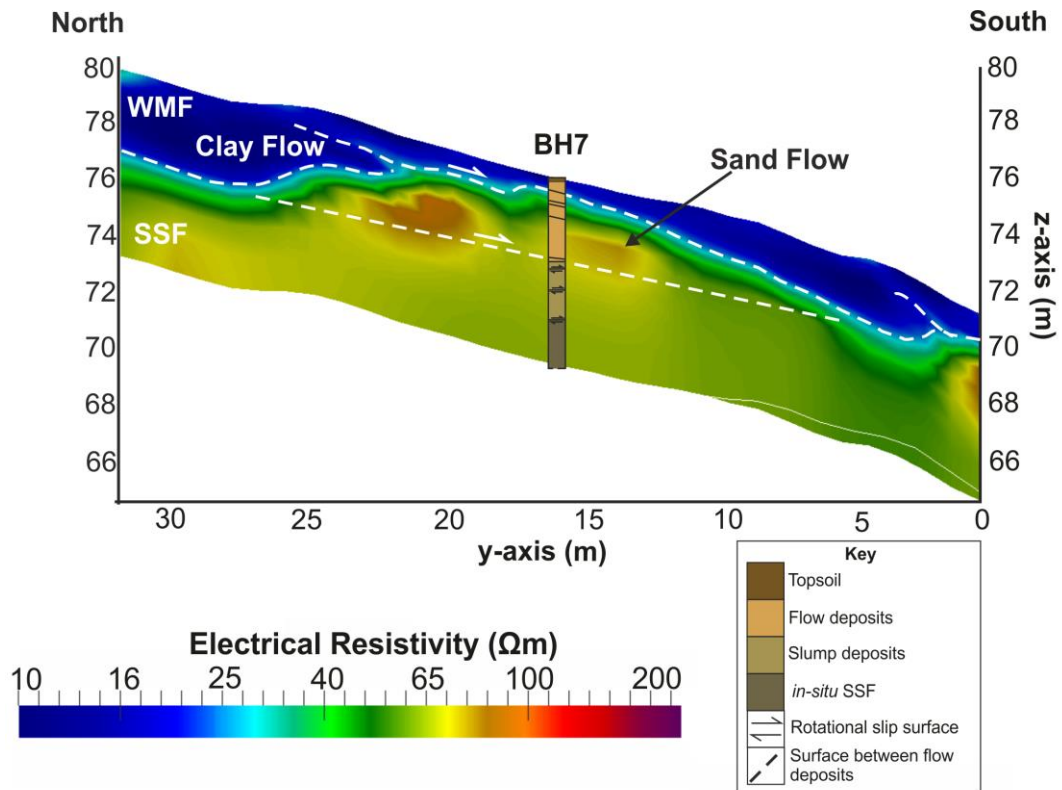


Figure 3.15. Annotated profile through high-resolution ERT survey whose location is indicated by a lilac profile line on basemap (Fig.3.2.) White lines represent flow surfaces with arrows indicating relative flow direction. The interpreted borehole log of BH7 shows structure of landslide system by landslide deposit type.

3.5 Ground Model Development

The ground model of Hollin Hill, which has been generated through the merging of results of many investigative methods, is presented as Figure 3.16. This section aims to provide a summary of the contribution that each method provided to the process of ground model development.

Surface characterisation was performed through the interpretation of airborne LiDAR remote sensing data. Remote sensing data permitted the

interpretation of surface morphology, breaks in slope, and as a result identification (and location) of landslide type, such as the back scarp and back-rotated blocks indicative of rotational slumping. Visualisation of airborne LiDAR and production of geomorphology map allowed the spatial distribution of landslides to be determined as a series of rotational slumps towards the top of the slope giving way to a number of flow deposits in the mid-slope region. By combining airborne LiDAR with aerial photography the resulting DEM can be used to identify which areas of the landslide are most recently active by looking for surface features such as partially vegetated slopes/areas and abrupt or smoothed breaks in slope.

Low resolution ERT determines the overall structure of the hill slope, at the formational scale, from beyond the back scarp to the relict flow deposits nearing the base of the slope. The low resolution ERT survey picked out three lithological formations present at the field site (WMF, SSF and RMF), identified the nature of the flow deposits positioned over SSF and determined the regional dip of the formations.

High resolution ERT was performed to gain more information about active flow deposits and in particular their internal structure and lateral persistence. High resolution surveying identified the resistivity contrasts which exist between flow deposits as a result of lithological variation. The blue, low resistivity uppermost flow deposits in contrast with deeper, higher resistivity flows. Core logging and index testing of boreholes performed at the field site shed further light on the reasons behind resistivity variation both between flow deposits and between lithological formations represented. ERT permits the interpolation of interpreted borehole information which can aid determining the landslide structure laterally.

Core logs were interpreted on the basis of mass movement type, so whether the soil cores were flow or slump deposits or *in-situ* material. The task of differentiating between flow deposits and slump deposits required identification of features associated with each deposit type, for example rotated bedding planes and presence of rip-up clasts is indicative of slumping. Slip surfaces associated with flow deposits were identified as thin (~5mm)

bands of light brown clay between layers of highly disturbed dark brownish grey silty, sandy clay or silty sand.

Analysis of core soil samples allowed core samples and ERT surveys to be correlated. For example, core resistivity measurements can be used as a confirmatory tool when interpreting ERT surveys. In order to differentiate between clay and sand flow deposits in the high resolution ERT survey core resistivity measurements were utilised. Core resistivity measurements were then related to particle size analyses, the resistivity variation could then be explained in terms of lithology. CEC versus core resistivity plot can inform about potential similarities in resistivities between lithological formations. In our example differentiating between sand flow, slump and *in-situ* SSF could be problematic and as a result any interpretation took this into account. For this reason the differentiation between *in-situ* SSF and slumped SSF was impossible and attributed to there being little to no lithological – and therefore electrical property – variation between the two. XRD results also indicate the mineralogical similarities between slumped and *in-situ* SSF, and dissimilarities with clay and sand dominated flows of WMF.

Implementation of peg displacement results along with ERT surveys and geomorphology studies made it possible to define active landslide regions, types of movement (flow or slump) and rate of displacement. With the addition of inclinometer results the active shear surfaces were identified and incorporated into the ground model.

Order of investigative technique application

If one were to implement the techniques utilised and described in detail during this investigation in the context of landslide site investigation and ground model development, performing the methods in the following order would give the most beneficial outcome. To characterise the surface expression, which may provide an indication of subsurface structure, the whole site both quickly and at high resolution, visualisation of either airborne or static LiDAR should be the first technique applied.

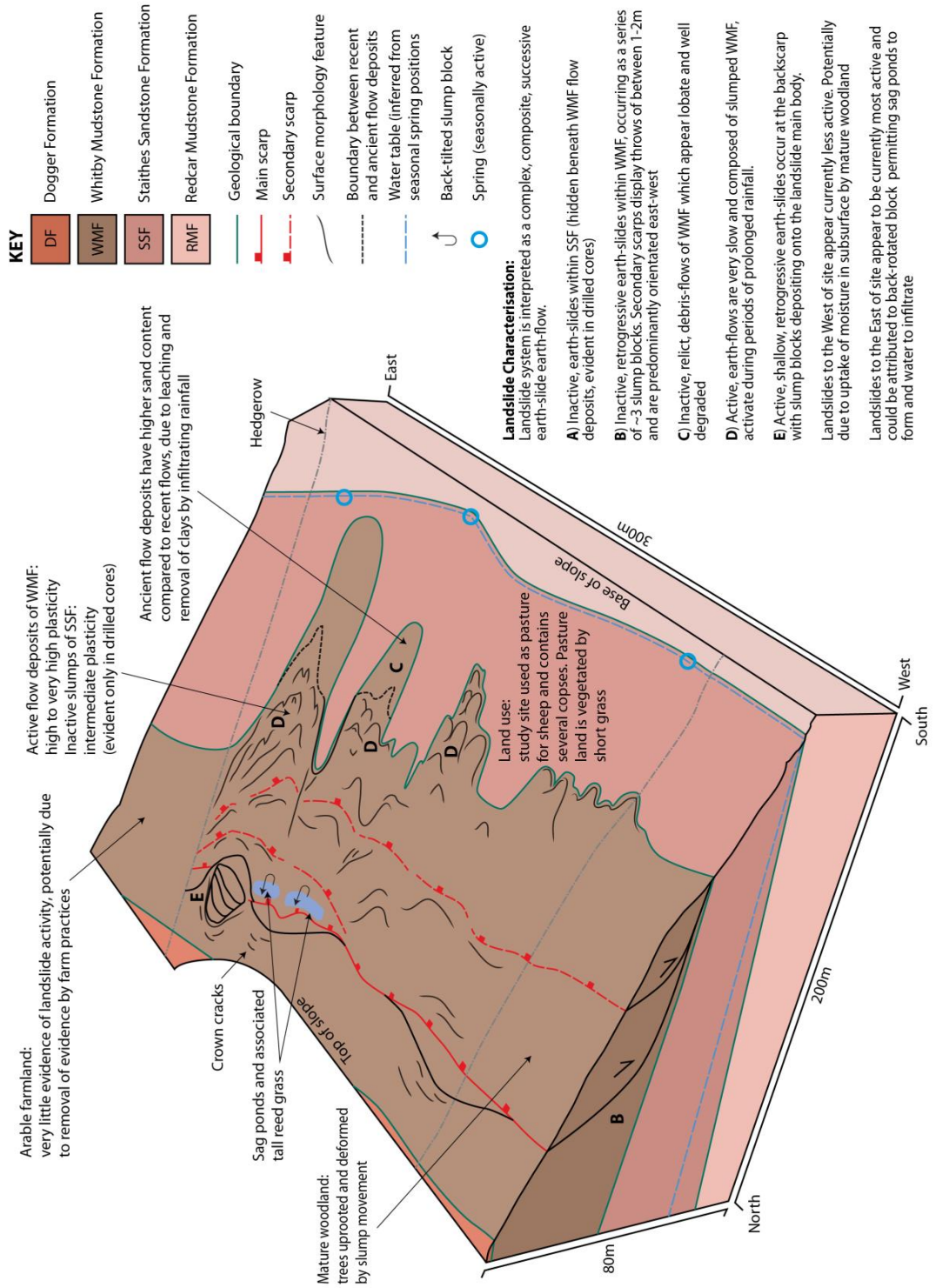


Figure 3.16. Ground model of the Hollin Hill study site based on geophysical, geomorphological and geotechnical investigations.

Upon gaining an insight into both surface expression and potential internal, subsurface feature, either several site-scale 2D ERT profile or 3D ERT volumetric image should be performed with the aim of ascertaining large-

scale subsurface features such as lithological boundaries. 3D ERT is preferred to several disparate 2D ERT surveys as the majority of geological features are three-dimensional in nature, therefore the former method is most appropriate and reduces the need for guess-work later on in the investigation. The two main draw backs of performing three dimensional ERT are that the method can be time-consuming relative to 2D ERT when surveying large areas of terrain, and pre-inversion data processing can be demanding if quality, intelligible survey notes are not available for reference. Once large scale ERT has been performed at the site, it would be wise to perform smaller scale ERT surveys of the areas of the landslide system which look either most active or may reveal the most structural information. The outcome of small scale ERT surveys should then dictate the direction of the intrusive investigation, i.e. where to drill and also which features could potentially be encountered. An ERT survey performed either in undisturbed landslide material or off the landslide system can act as a control and aid better understanding landslide physical properties such as soil desiccation.

Cores should firstly be analysed and interpreted in terms of lithology and later, in conjunction with core petrophysical and geotechnical information, such as cation exchange capacity, core resistivity and moisture content, as well as structural core observations be interpreted in terms of landslide deposit type (as is outlined in (3.4.3 and 3.4.4 of this chapter, see Figure 3.8). By linking core petrophysical, geotechnical and index testing information the process of interpreting 3D ERT surveys is more straightforward as any trends observed in field ERT surveys will be directly visible in core log results. Links can be identified between cation exchange capacity and respective core resistivity measurement, confirming that, differentiation between lithologies and deposit types can take place solely based on core electrical properties. This technique is most useful where formations have distinct differences in lithologies and therefore electrical properties, such as between sand- and clay-dominated formations.

Finally, performing these techniques in the order described above produces a detailed landslide ground investigation and subsequent ground model as each technique informs and directs the next technique to be utilised. It is generally good practise to start with surface characterisation through LiDAR

visualisation and geomorphological map production followed by subsurface characterisation through application of 3D geophysics and intrusive investigation.

3.6 Conclusion

Geoelectrical methods such as ERT can be usefully applied to landslide investigations where ground truth information is provided and where several lithological formations of contrasting resistivities exist within the area of interest. The investigation presented here informed to a high level of detail about subsurface conditions present within the hill slope by drawing upon many complementary information streams. Where one data set lacked the ability or resolution to inform about a feature or property another could be used to provide such information, an example being the inability of the large-scale ERT to differentiate between slumped and *in-situ* SSF, instead the positions of the slump shear surfaces in SSF were identified in core logs.

A key factor to be considered when designing a resistivity survey in the context of landslide investigation is the electrode spacing, as this has a profound effect on the resolution of the images returned. Resistivity images and profiles must be of a sufficient resolution and quality to permit the identification of the features of interest, in our case the individual flow deposits, which were only detectable at the high-resolution afforded by closer electrode spacings.

A detailed ground model was developed based on additional high resolution ERT information, remote sensing datasets and thorough interpretation of results from core logging, geotechnical testing and laboratory analysis of core samples. An integrated approach for ground model development, which takes into account both subsurface and surface investigative methods, is shown to improve the conclusions that can be drawn from a given site investigation. This is achieved by calibration of the geophysical results with direct physical property measurements of materials taken from the landslide and its environs. In particular, the use of 3D ERT at different spatial resolutions provides a means of volumetrically characterising the subsurface expression of both site scale (tens of metres) geological structure, and finer

(metre to sub-metre) scale earth-flow related structures, which were not effectively revealed by either the 1D information derived from discrete intrusive sampling, or the 2D surface data provided by remote sensing.

This section provides a detailed understanding of the structure of the Hollin Hill landslide system. This is essential further on in this project when analysing time-lapse 3D ERT monitoring results and interpreting the data in terms of landslide hydrogeological triggering mechanisms in Chapter 6. The next chapter (Chapter 4) describes the slope monitoring techniques implemented in this project and also the processing techniques and application of various datasets.

Chapter 4

Methodology for slope monitoring

A number of permanent monitoring systems are installed at the Hollin Hill field site, which record a range of physical and environmental parameters. The principal monitoring array comprises a grid of electrodes for 3D resistivity imaging, and is used to monitor temporal and spatial variations in subsurface geoelectrical properties. These subsurface properties can vary due to both environmental conditions and landslide-related physical activity. In this chapter the methodology underpinning the monitoring campaign at the field site is presented. Also covered are the processes applied to monitoring records to improve their suitability to observing and monitoring landslide hydraulic trigger mechanisms.

4.1 Monitoring Techniques

The landslide is instrumented with a permanently-installed large scale electrical resistivity tomography monitoring array and logger, referred to here as the Automated time-Lapse ERT (ALERT) system. It has been used to monitor the landslide since early 2008. The system has been deployed to take periodic measurements of subsurface electrical properties with the aim of linking trends in these electrical properties to landslide activation processes, in particular rainfall infiltration and soil moisture accumulation. However, landslide activation mechanisms cannot be studied and reported by installing only a geophysical monitoring array on the landslide; several other monitoring systems must also record information to validate and complement the geophysical monitoring data.

Temporal patterns of landslide movement must be known if geophysical data are to be interpreted in terms of landslide hydraulic precursors. An array of marker pegs (reference points) were therefore installed on the surface of the landslide and monitored manually by highly accurate RTK-GPS to record surface displacements. In addition to recording landslide movement this marker array can also be used to correct for geometry changes in the permanently-installed electrode array caused by ground movement.

ERT monitoring results are also corrected for the seasonal effect of subsurface temperature distribution, which potentially acts to mask the small soil moisture variations vital to the success of this investigation. Subsurface temperature distribution is recorded at several depths and at several locations at the field site. These data are modelled using an appropriate heat equation, and used to normalise all ERT model results to a constant subsurface temperature.

Two other sensors were installed to aid interpretation of the results of landslide geophysical monitoring; rain gauge and water level loggers installed in standpipe piezometers. The rainfall data was required to assess the frequency and quantity of water entering the subsurface, whilst water levels were monitored to assess likely pore pressure changes near failure surfaces.

The locations and extents of all sensors and monitoring arrays installed at the Hollin Hill field site are shown in Figure 4.1, the field site base map. The base map is presented in this chapter as an aerial photograph with the extents of landslide deposits draped over it. In addition, each sensor type is assigned a colour and a reference code, e.g. T1, temperature sensor 1; this aids identification of the whereabouts of each sensor. The two rectangles represent the extent of the permanently-installed large scale 3D ERT monitoring array (red coloured) and the extent of the one-off smaller scale 3D ERT survey (purple coloured) performed on the most active landslide region and presented in Chapter 3. Locations of interpreted boreholes (BH1, BH5 & BH7) are also presented on the base map, as are the locations of the array of 45 marker pegs, used to determine periods of landslide activity. The collection and processing for monitoring data was performed both by the Student and by colleagues at BGS and a chart displaying what is contained in Appendix A.

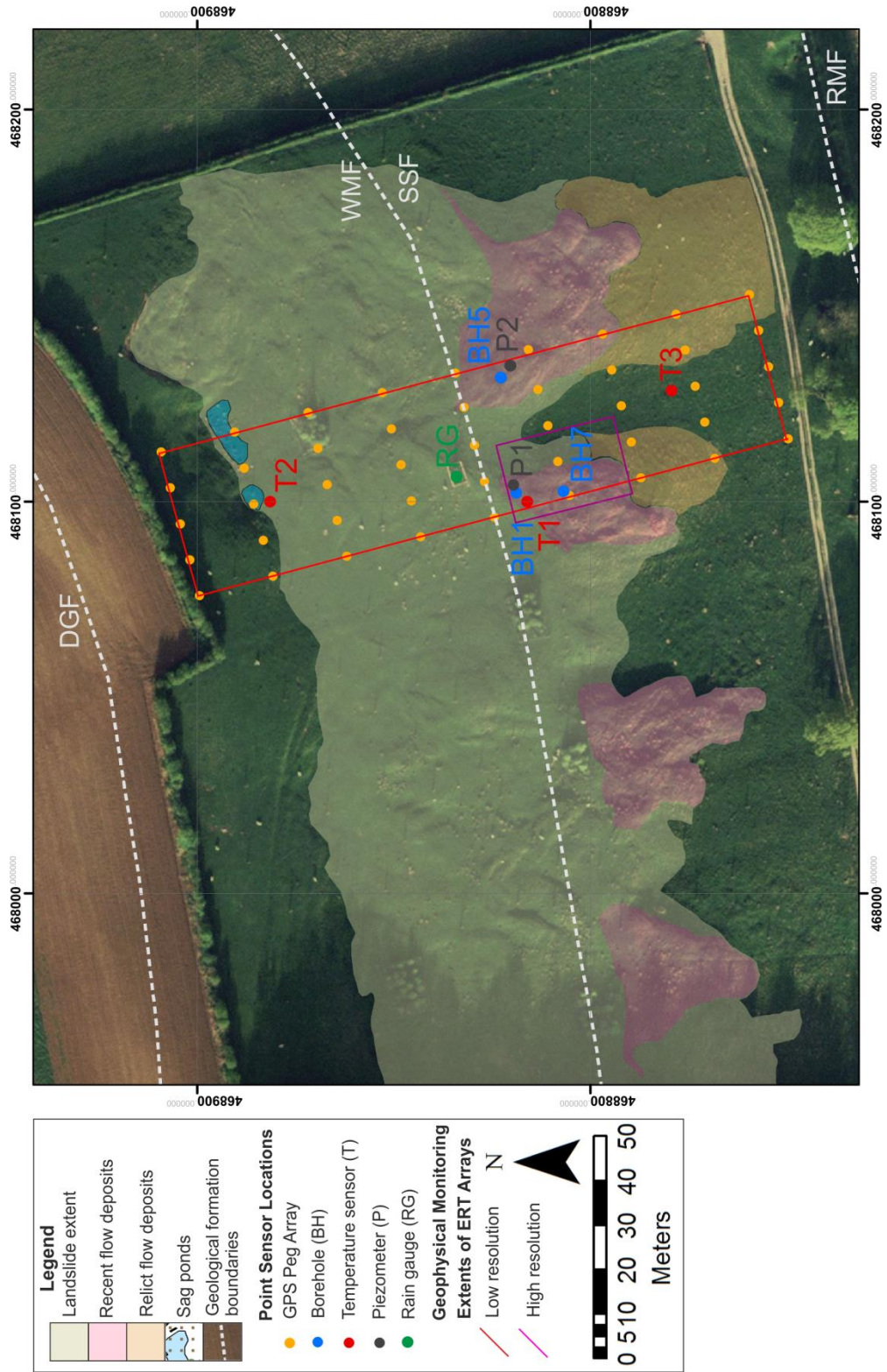


Figure 4.1. Hollin Hill basemap showing extent of landslide deposits, locations of field site sensors and extents of permanently-installed 3D ERT arrays.

4.1.1 Real Time Kinematic (RTK) -GPS Monitoring of Peg Positions

This section contains a description of how peg location RTK-GPS data were processed to determine peg movement between July 2008 and February 2013. The Leica VIVA GS12 Global Positioning System is used to fix the location of 45 pegs (5 rows of 9 pegs), positioned in a grid pattern throughout the area of interest of the landslide system at Hollin Hill. The pegs were installed in early 2008 and an initial baseline peg location data set was measured in 30th July 2008.

		Date 30/07/2008			
		Baseline Coordinates (m), BNG			
Peg No.	Easting	Northing			
45	468112.65	468909.26	22	468119.39	468810.79
44	468117.69	468890.59	21	468124.39	468792.08
43	468122.76	468871.87	20	468129.40	468773.34
42	468127.76	468853.09	19	468134.42	468754.63
41	468132.69	468834.39	18	468125.22	468752.16
40	468138.69	468815.93	17	468120.22	468770.89
39	468142.77	468796.96	16	468115.19	468789.58
38	468147.79	468778.24	15	468110.22	468808.30
37	468152.77	468759.54	14	468105.17	468827.01
36	468143.63	468757.11	13	468100.16	468845.64
35	468138.62	468775.81	12	468095.16	468864.39
34	468133.59	468794.58	11	468090.12	468883.16
33	468128.58	468813.30	10	468085.10	468901.94
32	468122.60	468835.59	9	468075.97	468899.41
31	468118.55	468850.66	8	468080.97	468880.73
30	468113.55	468869.34	7	468086.02	468862.03
29	468108.51	468888.13	6	468091.02	468843.23
28	468103.55	468906.81	5	468095.99	468824.49
27	468094.31	468904.37	4	468101.42	468805.73
26	468099.31	468885.62	3	468106.03	468787.15
25	468104.41	468866.92	2	468111.07	468768.35
24	468109.36	468848.23	1	468116.05	468749.69
23	468114.42	468829.48			

Table 4.1. RTK-GPS measurement of baseline survey peg positions. Coordinate System: OSGB36.

The coordinates of the baseline survey are found in Table 4.1. The GPS utilised during the investigation receives RTK correction data which acts to

improve the accuracy of surveyed positions by receiving real-time corrections from a single local reference station. This method permits sub-centimetre position accuracy.

Survey No.	Survey Date		
1	30/07/2008	13	23/03/2011
2	02/09/2008	14	28/03/2011
3	19/12/2008	15	07/04/2011
4	29/01/2009	16	17/11/2011
5	27/03/2009	17	07/12/2011
6	04/06/2009	18	14/03/2012
7	13/10/2009	19	11/05/2012
8	24/06/2010	20	29/06/2012
9	26/08/2010	21	27/09/2012
10	12/10/2010	22	19/11/2012
11	22/12/2010	23	24/01/2013
12	14/01/2011	24	01/02/2013

Table 4.2. Dates of GPS surveys of peg positions at Hollin Hill

All field surveyed GPS data points were imported into Leica Geo-office for processing and in particular converting to a uniform coordinate system and format. The coordinate system used in this investigation is OSGB36(02) and local grid format. In addition to each peg's Easting and Northing the standard deviation of peg position measurements is recorded, for data quality purposes.

Once the surveyed peg positions were exported from Leica Geo-office they were reformatted to make movement interpretation simpler. This was done in two stages, firstly the surveyed points are adjusted to local coordinates by making Peg 1 equal to $x = 0\text{m}$ and $y = 0\text{m}$. Figure 4.2a shows peg positions as they are within British National Grid and Figure 4.2b shows the peg positions converted to a local coordinates.

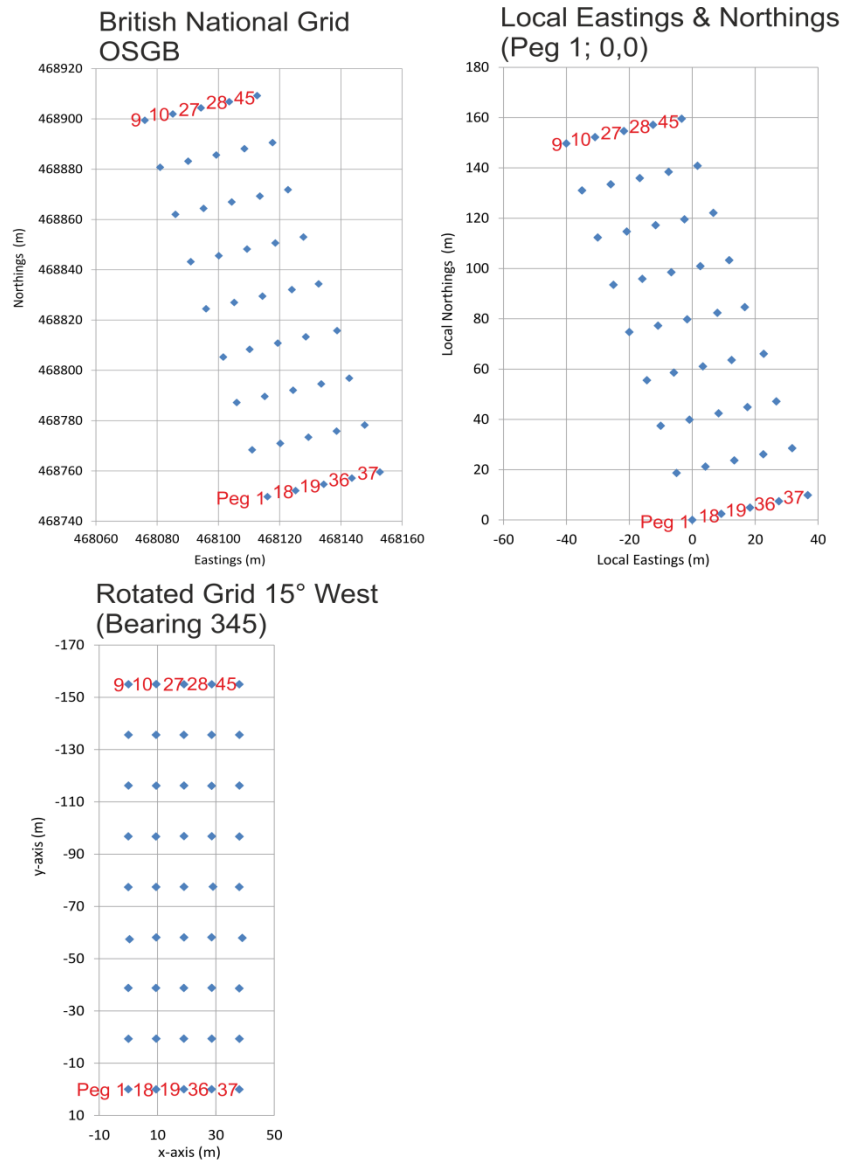


Figure 4.2 a.) (Upper left) Layout of monitoring pegs at Hollin Hill (NB. Five rows of nine pegs) b.) (Upper right) Local peg positions (after assigning local eastings and northings relative to Peg 1). c.) (lower left) Local eastings and local northings rotated to lie along x- and y- planes

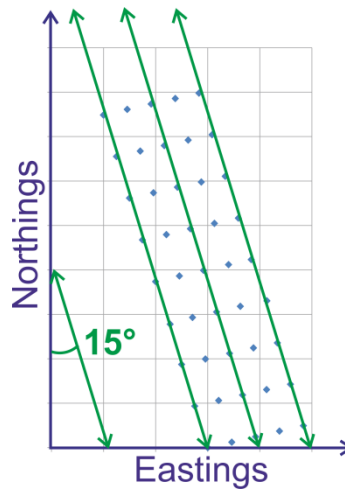


Figure 4.3. Rotation of localised grid to be along the line of electrode and peg arrays.

Rotation of peg position (Fig 4.3) is done by rotating the peg positions from their actual bearing of 345 to a new bearing 000 and is done so by applying the following equations

$$x = E \cdot \cos(15^\circ) + N \cdot \sin(15^\circ)$$

$$y = -E \cdot \sin(15^\circ) + N \cdot \cos(15^\circ)$$

Equation 4.1. Rotate local gridded peg positions (formerly GPS peg coordinates) to align with the five ERT survey lines, bearing 345°

By applying the two formulas the x- and y- components of movement can be easily related to movement parallel and perpendicular to the five lines of survey pegs. With the y-direction being parallel to peg and ERT survey lines and x-direction being perpendicular. Figure 4.2c shows the result of one such rotation, using the baseline 30/07/2008 as an example. The peg positions could be interpreted in terms of local coordinates, however the results would be difficult to interpret, as the lines of pegs are angled at 15 degrees to Grid North.

It is possible to determine peg movement between successive peg positions by subtracting subsequent surveys from the initial baseline (30/07/2008). Each peg can be represented through time by its position relative to that baseline.

Another, essential part of the investigation relates peg – and therefore electrode movement – with electrical resistivity variation induced by

electrode movement and was resolved using along-line measures of landslide movement.

4.1.2 Temperature

Subsurface temperature at the field site is monitored to correct geophysical monitoring datasets for the effect of subsurface temperature fluctuations. Air temperature is monitored to assist in the determination of evapotranspiration and effective rainfall. Subsurface temperature is monitored by a series of 14 sensors, located at three locations (lower-, mid- and upper-hillslope) throughout the slope (Figure 4.1). These three sensor clusters give discrete, point source temperature information from surface to a depth of 6.4m (Table 4.3).

T1		T2		T3	
	Depth [m]		Depth [m]		Depth [m]
Port 1	AIR	Port 1	0.10	Port 1	0.10
Port2	0.10	Port2	0.70	Port2	0.70
Port3	1.00	Port3	2.00	Port3	2.00
Port4	2.50	Port4	3.80	Port4	3.80
Port5	5.35	Port5	6.40	Port5	6.40

Table 4.3. Depths of temperature sensors of field site installed temperature sensor array.

Several breaks in temperature logging by temperature sensor exist due to technical issues such as data logger malfunction and defective temperature sensors. In both cases, logger or sensors were replaced at the next available opportunity, so as to minimise data gaps. Between 14/03/2012 and 31/12/2012 the data logger storing air temperature measurements failed, and so manual daily air temperature measurements were used to supplement the logger data.

The subsurface temperature sensors installed at Hollin Hill are RT-1 Rugged Soil Temperature Sensors (several were later replaced by 5TE Soil Moisture Sensor), air temperature is monitored by ECT Air Temperature Sensor, and all data was logged by EM50 Datalogger (Decagon Devices, USA).

Subsurface Temperature Modelling

Seasonal subsurface temperature variation greatly affects the resistivity response of the ground. To eliminate this effect on the resistivity response subsurface temperature was modelled.

Seasonal temperature changes in the subsurface can be described by Equation 4.2 (Brunet et al., 2010; Chambers et al., 2013) and is valid where temperature at the surface varies sinusoidally with a period equal to one year,

$$T(z, t) = T_{\text{mean}}(\text{air}) + Ae^{-\left(\frac{z}{d}\right)} \sin\left(\omega t + \varphi - \frac{z}{d}\right)$$

Equation 4.2. Model to describe subsurface seasonal temperature variation

where $T(z, t)$ is the subsurface temperature at day t and depth z , m, $T_{\text{mean}}(\text{air})$ is the mean yearly air temperature, °C, A is the yearly amplitude of the air temperature variation, °C, d is the characteristic depth of the temperature variation, m, φ is the constant phase offset, radians, and ω is the angular frequency ($2\pi/360$). The constant phase offset ensures that the maximum temperature at the surface occurs at the hottest part of the year. Whereas $(\varphi - z/d)$, the overall phase lag, describes that maximum temperature occurs later in time deeper in the subsurface relative to maximum surface temperature, because the heat has further to travel through the ground.

The characteristic depth highlights how quickly the temperature variation decreases with depth and is related to the thermal properties of the ground by the expression,

$$d = \sqrt{\frac{2k}{\omega\rho c}}$$

Equation 4.3. Characteristic depth, d , parameter of heat equation

where, k is the thermal conductivity ($\text{Wm}^{-1}\text{K}^{-1}$), ρ is density (kgm^3) and c is the specific heat capacity (JK^{-1}) at constant pressure.

Temperature data from all subsurface temperature sensors collected over a two year period, from Summer 2009 to Summer 2011 was used in the

modelling of subsurface seasonal temperature distribution. The data was fitted through the application of FindMinimum[] function in the Mathematica computational algebra package.

The fitted model determines all four parameters, T_{mean} , A , φ and d . Four models were produced, one for each of the three temperature sensor arrays, labelled T1, T2 and T3, and the final model combines temperature data from all three sensor locations. The fitted parameters from temperature modelling are presented in the Table 4.4.

Sensor Location	T_{mean} (°C)	A (°C)	d (m)	φ (rad)	%RMS
T1	9.81	14.62	2.073	-1.907	47.1
T2	9.992	15.62	1.968	-1.908	44.3
T3	10.253	16.49	2.697	-1.896	58.9
All	10.029	15.54	2.264	-1.907	48.0

Table 4.4. Fitted parameters from subsurface temperature modelling of three temperature sensor arrays installed at the site, plus, a combined model for data from all three sensor locations. Misfit error between model and measured data is presented as %RMS.

Raw temperature data recorded by all temperature sensors across all three sensor array locations are plotted alongside their fitted models are presented in Figure 4.4 and reveal very good correlation between the two. The blue points represent field temperature measurements from sensor arrays (T1) and red curves represent the fitted temperature model, Equation 4.2.

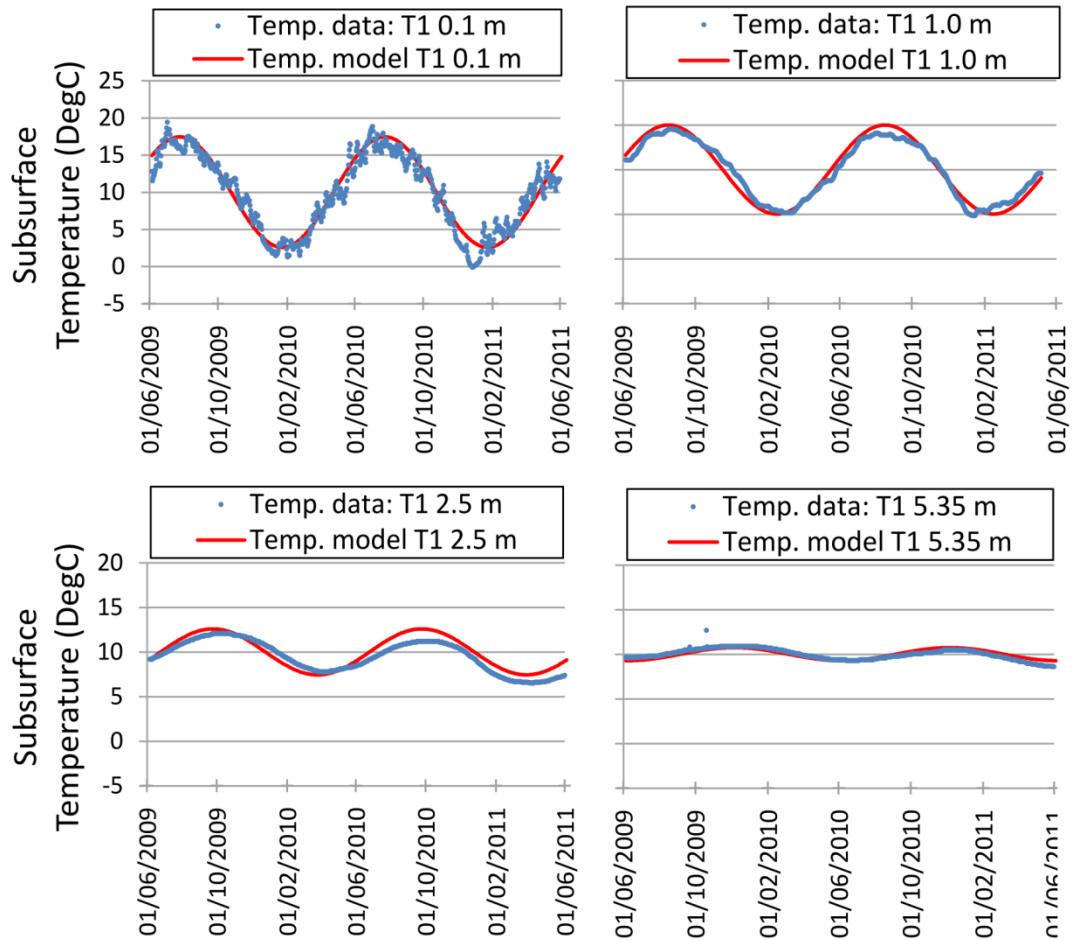


Figure 4.4. Plots of recorded temperature data and modelled temperature results at four depths (0.1m, 1.0m, 2.5m & 5.35m) from temperature sensor array T1 during a 2 year period.

4.1.3 Rainfall

Rainfall has been monitored at the research site to complement the results of the geoelectrical monitoring regime with soil moisture input information. Knowledge of rainfall is essential when investigating the processes taking place within moisture driven landslides as it gives quantitative information about moisture input, which are linked to water pressures and moisture content, into the landsliding system.

A tipping bucket rain gauge was installed at Hollin Hill on the flat roof of the monitoring system enclosure (Figure 4.5) on the 16th October 2008 (for location see Figure 4.1) and has been logging rainfall for the duration of the project with limited downtime during that period. The rain gauge's tipping bucket has a rainfall sensitivity of 0.2mm. The data logger attached to the

rain gauge was downloaded at roughly 3 monthly intervals and the data added to an excel file containing all the rainfall data to date.



Figure 4.5. Position of rain gauge at Hollin Hill field site (white cylinder on roof of green enclosure).

The principal tipping bucket became faulty and eventually failed on 05/07/2011 during the winter/spring 2011 and was replaced on 19/04/2012, rainfall data to fill the gap was provided by Mr Steve Gibson, the local farmer and landowner who keeps detailed weather logs. His weather station is located 400 m from the field site and the data is used in this investigation where only data gaps exist.

Every time the bucket of the rain gauge tips the data logger records a single, 0.2mm amount of rainfall. By summing the number of tips occurring daily and then multiplying by the capacity of the rainfall bucket the daily rainfall can is determined, thus giving a daily rainfall value in millimetres. However, the effects of evapotranspiration can be substantial during warmer, sunnier months and so the effects of evaporation potential and crop moisture uptake (transpiration) must be taken into account. Both processes act to reduce the amount of moisture entering the soil and reaching groundwater. Rainfall corrected for these processes is known as effective rainfall. Several models exist, offering varying degrees of accuracy and complexities, the Hargreaves Model (Hargreaves et al., 1985) was implemented for this investigation as it

offers good correlation with actual measures of evapotranspiration at temperate climates.

Rainfall results are presented in several formats including weekly rainfall and effective rainfall, as well as weekly cumulative and weekly cumulative effective rainfall. The aim of analysing rainfall in several formats is to compare each with variation in field resistivity – as well as volumetric images of gravimetric moisture content – to ascertain over which time period field resistivity responds to rainfall infiltration. Furthermore, rainfall is integrated along with piezometer, peg movement by RTK-GPS and soil electrical resistivity data sets in the interest of better understanding the interplay between rainfall infiltration, subsurface physical property variation and subsequent landslide activation.

4.1.4 Evapotranspiration

Hargreave's empirical formula to model potential evapotranspiration (ET_p) has taken several forms during its development from 1981 until 1985, in its most advanced iteration takes the form:

$$ET_p = 0.0023R_a(T + 17.8)\sqrt{T_{MAX} - T_{MIN}}$$

Equation 4.4. Hargreaves Formula for potential evapotranspiration (Hargreaves et al., 1985)

The formula is useful where only rudimentary climatic information is present, thus on occasions where the more advanced Penman-Monteith model (Penman, 1948; Monteith, 1965) cannot be implemented. The model is appropriately applied at Hollin Hill as it produces results that are referenced to grass. The field site is pasture land with a thin cover of grass, making Hargreaves suitable for use. Were the field site to be covered with crop, for example, wheat or barley then an additional parameter K_c , the crop coefficient would have to be implemented to account for the crop's differing water demand. Hargreaves requires only minimum, maximum and average air temperature (T_{max} , T_{min} and T , in °C) measured at the field site and the determination of total incoming extraterrestrial solar radiation (R_a , MJ m⁻² d⁻¹) for the latitude of the field site,

$$R_a = 15.392d_r(W_s \sin \varphi \sin \delta + \cos \varphi \cos \delta \sin w_s)$$

Equation 4.5. Total incoming extraterrestrial solar radiation, (R_a)

Where each component of the equation is defined as follows:

$$\delta = 0.4093 \sin \left(\frac{2\pi J}{365} - 1.405 \right)$$

Equation 4.6. Solar Declination in radians, (δ)

$$d_r = 1 + 0.033 \cos \left(\frac{2\pi J}{365} \right)$$

Equation 4.7. Relative distance between Earth and Sun, (d_r)

$$W_s = \arccos(-\tan \varphi \cdot \tan \delta)$$

Equation 4.8. Sunset hour angle in radians (W_s)

The final two components of the equation are latitude of field site, φ , (54°N in this case), and J , is the day of interest as Julian Day. It is possible to convert a given date to Julian day by applying the following formula

$$J = 367Y - \left(\frac{7 \left(Y + \frac{M+9}{12} \right)}{4} \right) \left(\left(\frac{3Y \left(\frac{9M}{7} \right)}{100} \right) + 1 \right) + \left(\frac{275M}{9} \right) + (D + 1721028.5)$$

Equation 4.9. Julian Day Number (Y=year, M=month & D=day)

Where, the date of interest is inputted to the equation as Y, year; M, month and D, day. Day zero corresponds to Noon (Greenwich Mean Time), 1st January 4713 BCE and is a continuous count of days since the start of the Julian Period.

Potential evapotranspiration at the Hollin Hill field site is determined using the Hargreaves model in mm per day (mm/day), which is subtracted from measured rainfall events, hence computing the daily effective rainfall at the field site. Effective rainfall is therefore the quantity of rain water that

recharges groundwater. As the processes being monitored at the field site are taking place over a larger time frame than *per diem*, weekly rainfall and weekly effective rainfall are deemed more appropriate and are applied throughout this project.

4.1.5 Piezometry

Two piezometers have been installed within boreholes (Figure 4.1 & 4.6) lined with plastic casing on the eastern and western flow lobes respectively. The casing is screened over the estimated depth interval of the failure plane on each lobe (Figure 4.7). The hole outside of the casing was backfilled with sand over the screened interval, and low permeability cement-bentonite grout above the screen interval. Water level changes therefore were used to indicate pore pressure changes in the vicinity of the slip planes. Piezometric level has been monitored at the field site between 24th September 2009 to present and a near complete record exists.

The most active slip surfaces are annotated on to Figure 4.7 and their depths are different to those displayed by inclinometer results on Figure 3.9 because the piezometer diagram accounts for topography variation between the piezometer well and borehole and assumes a near horizontal shear surface.

The Solinst Levellogger Junior Edge piezometer was chosen as it measures groundwater level and temperature at a frequency determined by the user, in our case a measurement is taken every seven minutes. Water level is determined by piezoresistive silicon with Hastelloy sensor pressure transducer which measures absolute pressure. To correct absolute pressure measured by submerged piezometers for atmospheric pressure an additional piezometer, stored at surface, logged barometric pressure and was subtracted from submerged pressures.

Pore fluid electrical conductivity (EC) is an essential parameter used during laboratory calibration of soil resistivity – moisture content curves (Chapter 5), an LTC Levellogger Junior – also capable of measuring fluid EC – replaced the piezometer of the eastern lobe at 2nd November 2011, providing a year of pore fluid conductivity data.

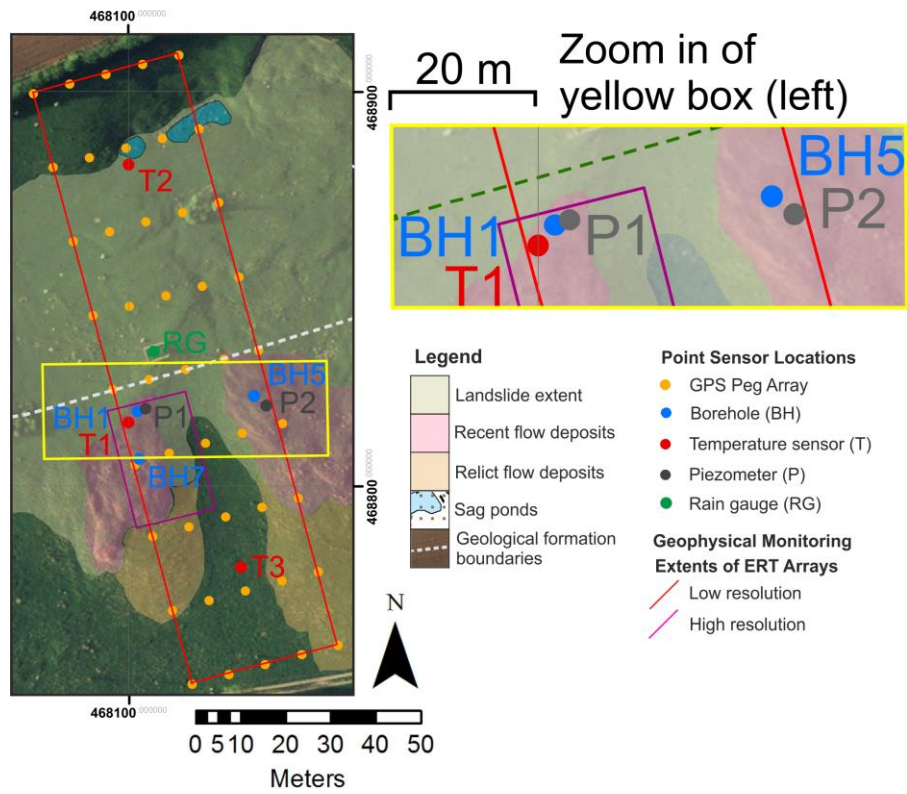


Figure 4.6. Location of piezometer wells in relation to boreholes

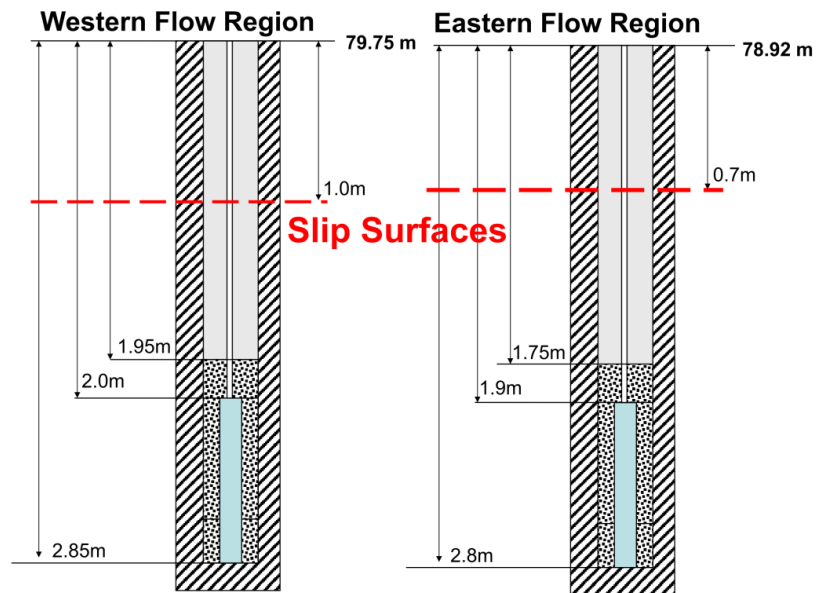


Figure 4.7. Piezometer casing installation diagram. Dashed: bedrock; blue: level logger; grey: cement-bentonite grout; stippled: sand.

Piezometers also measure temperature and is determined by Platinum RTD thermometer and have an accuracy of +/- 0.1°C.

It should be noted that during December 2012 the eastern piezometer became lodged at depth within its plastic casing as a result of landslide movement either trapping or severing the plastic casing at roughly 1.0m depth.

4.2 Landslide Monitoring by Automated time-Lapse Electrical Resistivity Tomography

The landslide system at Hollin Hill is monitored by a permanently-installed geoelectrical monitoring system called Automated time-Lapse ERT (ALERT) and the system was developed by the British Geological Survey (Ogilvy et al., 2009; Kuras et al., 2006; Wilkinson et al., 2010) and installed on the landslide early 2008, with the first resistance measurements taken 11/07/2008. The remotely configurable system can be interrogated by wireless telemetry from the office via GSM (GPRS or 3G) or wireless internet link (Figure 4.8c), via this link pre-programmed data acquisition schedules are uploaded and measurement results downloaded. The system is powered by high-capacity batteries which are recharged by wind-turbine, solar panels and a methanol fuel cell. ERT surveys were run in accordance with the pre-programmed schedule, and stored on the ALERT data logger before being downloaded to the office server for data analysis, processing, and 3D inversion (Ogilvy et al., 2009).

4.2.1 ALERT System at Hollin Hill

The ALERT system comprises permanently-installed stainless steel electrode arrays, arranged in five lines with each line made up of 32 electrodes, all located 0.1 m below the ground surface. All electrodes are connected to the ALERT acquisition instrument and logger via electrical cables. Electrode lines are orientated parallel to the general direction of landslide system displacement, 165°S (other direction: 345°N).

Figures 4.7a–d show the geoelectrical monitoring system as installed at Hollin Hill. The system instrumentation is all stored in the green, secure housing which is mounted on concrete hard standing (Figure 4.8a). Solar panels and wind turbine recharge the system batteries and are fixed to the tall, green pole, located to the west – left in the Figure 4.8a – of the housing.

Inside the housing are all the system components (Figure 4.8b) and include the stand-alone, black boxes of the ALERT system, into which all the cables connect, thus linking the electrode array (Figure 4.8d & 4.8b) with the acquisition system.



Figure 4.8 a.) (top left) ALERT System installed at Hollin Hill; green secure housing contains monitoring system, batteries and communication modem. To the west of the instrumentation housing is a pole with attached solar panels and wind turbine. b.) (top right) Inside the system housing; two black boxes are the ALERT system, wooden box positioned on the housing floor contains two batteries and the silver box to the right of the housing is a methanol fuel cell (installed ~October 2012). c.) (bottom left) Communication modem and SIM card for uploading data acquisition schedules and downloading survey results. d.) Stainless steel electrode with multicore cable attached before being inserted 0.1 m into the subsurface. Note, accurate electrode positioning by tape measure and later RTK-GPS location measurement.

The array of 160 electrodes (Figure 4.9) are laid out in a series of 5 parallel lines, with a distance of 4.75m between electrodes gives a total electrode line length of 147.25m. Five of these lines of electrodes are positioned

parallel and 9.5m apart, therefore the electrode lines extend laterally 38m and an area of 5600m² was imaged and monitored by time-lapse ERT at the field site.

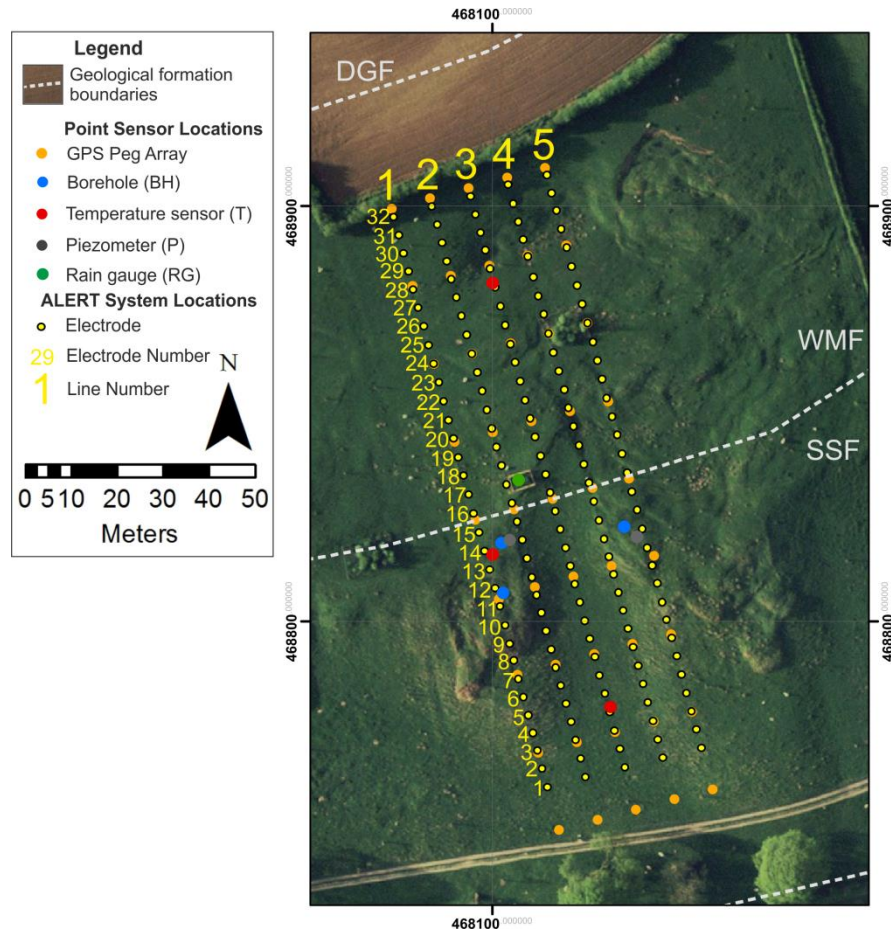


Figure 4.9. Locations of automated time-lapse ERT electrode array. Along with electrode number and line number labels.

By introducing nomenclature to identify each electrode within the 3D ERT survey array, the description of transfer resistance results is made much simpler. With that in mind the electrodes are identified in the following way. For any given electrode, the line along which the electrode is located is given first and ranges between 1 and 5. This is followed by the electrode number, from 1, indicating the 1st electrode, located at the base of the slope in the south, increasing to 32, which identifies the 32nd electrode, located at the top of the slope to the north. The electrode number is bracketed to minimise confusion, an example being, 3(16) represents electrode 16 of line 3.

4.2.2 Data Acquisition

Once the system was installed resistivity surveys took place according to a predefined measurement schedule. Command files contain information about the geoelectrical survey to be performed and contain information on the electrode measurement sequence, i.e. which are the current and potential electrodes, and other data acquisition parameters such as duty-cycle, number of stacks, measurement standard deviation and sampling windows. The generic system specification of the ALERT system is summarised in Ogilvy et al (2009). Raw ERT data are periodically transferred from the ALERT monitoring system to the BGS server, at Keyworth, where the data is accessed and downloaded to be processed, analysed and interpreted.

The geophysical monitoring campaign comprised 695 geophysical surveys of all five lines during the four years and nine months of monitoring equating to 1740 days of monitoring with ERT surveys performed on average every 2.5 days. There were several short periods when the ALERT system was not functioning correctly and as a result there are several periods during which no data is available. These periods of malfunction were rare and down periods are summarised in Table 4.5.

Malfunction Period		
	Start	End
1	22/07/2008	05/10/2008
2	16/06/2009	25/08/2009
3	08/03/2011	07/04/2011
4	28/07/2011	14/09/2011
5	09/12/2012	25/01/2013

Table 4.5. Periods when ALERT system was not providing data due to malfunction.

4.3 Data Processing

The results of the ERT monitoring campaign of the landslide system are processed and presented in a number of ways depending on the degree of additional processing needed to convert the data into several formats to be analysed and interpreted. The schematic diagram (Figure 4.10) shows the stages of data processing performed and the formats of output data. The

diagram is colour coordinated and broken down into three categories, the first (green boxes) highlight the measurement systems utilised, i.e. which raw data set is the starting block of the processing route.

The red boxes represent the processes applied to the raw data sets, how these datasets can be combined and in what order they are utilised. The final column of boxes, those purple in colour, summarise the outputs of each processing route. The interpretation of these outputs are presented in Chapter 6. The different routes are represented by the grey boxes on the far left of the diagram.

Processing Routes

The results of long term ERT monitoring of the Hollin Hill landslide were subjected to a range of processing techniques, ranging from simple extraction of transfer resistance data to more sophisticated correction of physical landslide processes and inversion modelling of raw transfer resistance data. Data processing route 1 was subjected to the fewest number of data processing techniques and is presented in the most 'raw' of formats; conversely, route 4 was subjected to the largest number of processing techniques and therefore required the largest number of processing stages.

Route 1 had only one process applied to it, raw transfer resistance data extraction, and was principally used as a 'look-see' to reveal data quality issues but also to display raw resistance data trends, i.e. those which may result from seasonal temperature.

Route 2 requires raw transfer resistance data extraction, which are then temperature corrected through the following techniques: interpolation of electrode positions (see 4.3.1), subsurface seasonal temperature distribution recording and modelling (both, 4.1.2) and temperature correction factor determination (4.3.2) and finally, its application to raw transfer resistance results to output temperature corrected resistance data.

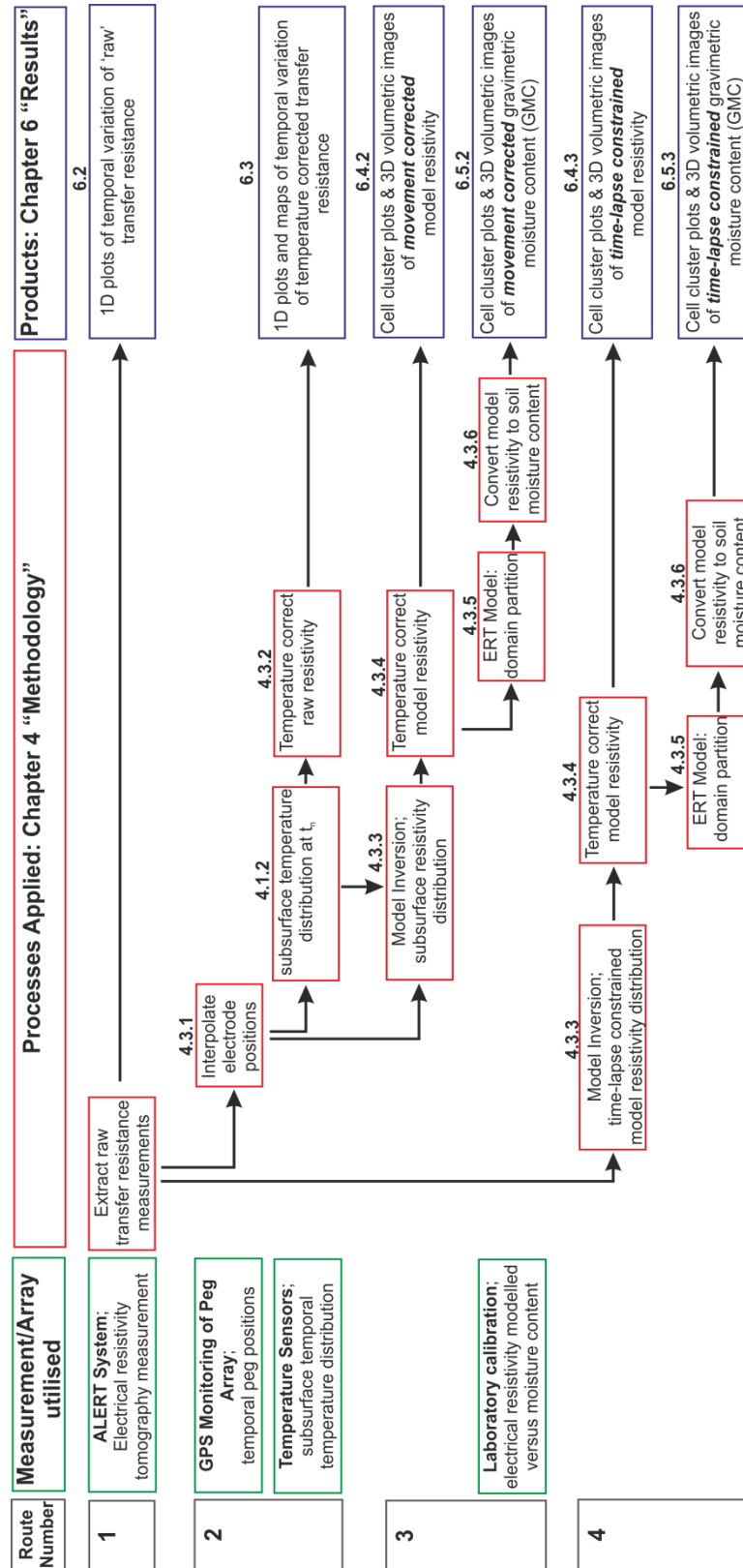


Figure 4.10. Schematic diagram of data collection, processing and presentation of electrical resistivity (ALERT) monitoring data

It is necessary to incorporate interpolated electrode locations into the process as their positions are required to determine the temperature

correction factor. There are two data outputs, presented in Chapter 6, of route 2, firstly, maps of temperature corrected resistance are produced, which show both spatial and temporal near surface resistance changes. Secondly, certain dipole measurements are extracted and plotted against time, thus revealing temperature corrected resistance variation throughout the monitoring campaign.

Route 3 and 4 follow very similar processing routes however the resistance monitoring data are inverted using different methods and routes. Both routes produce temperature corrected model resistivities of the investigated domain. Temperature correction is modelled and performed as laid out in sections 4.1.2 and 4.3.4 of this chapter. The main difference between the two routes is the manner in which the resistance monitoring data are inverted. Route three attempts to account for electrode movement pre-inversion through the interpolation of electrode positions (methodology outlined in Section 4.3.1). The inversion modelling software utilised in this investigation, Res3DINV, does not have the capability of inverting different resistivity measurement geometries between inversions and also incorporating time-lapse inversion constraints on inversion models. Therefore route 3 accounts for electrode movements between surveys but does not make use of time-lapse inversion constraint option available in Res3DINV. Following model inversion of resistance data the domain is partitioned into the three lithologies present within the domain (described in Section 4.3.5). Laboratory calibration of soil moisture-resistivity relationship of soil samples was performed and results are presented in Chapter 5. The electrical resistivity as a function of soil moisture content was modelled using an appropriate model (in this case Waxman-Smit equation, Chapter 5 & Section 4.3.6) and one calibration curve was applied to each lithological formation domain present at the field site. Application of calibration curves converts model resistivity images to GMC.

Route 4 follows the same order of processes, however, electrode movement is not interpolated pre-inversion, therefore, the assumption had to be made that electrodes did not move during the monitoring period being inverted. A caveat of this route is that ERT surveys performed when the landslide was active could not be inverted as electrodes would be displacing during this

period, resulting in incorrect measurement geometries. Only periods of landslide suspension were inverted using this route, and considering that the main aim of the research project is to observe hydrogeological precursors leading up to slope activation this is deemed a suitable investigative route and not flawed by the inability to account for electrode mobility. As with route 3, inverted resistivity monitoring models were converted to volumetric images of gravimetric moisture content through implementing laboratory calibrated resistivity-moisture content model curves (Chapter 5 & Section 4.3.6).

4.3.1 Interpolating electrode position from surveying peg array positions

Hollin Hill is instrumented with a series of 5 electrical resistivity survey lines, roughly running downslope and parallel to landslide movement. To understand the dynamics of the landslide system an array of 45 survey pegs were inserted into the land surface, positioned coincident with ERT survey lines, and has been monitored by highly accurate Real-Time Kinematic GPS (Leica Viva System). It should be noted that pegs are not co-located with electrodes.

Electrical resistivity tomography is increasingly being applied to both characterise and monitor landslide internal structure and physical property variation (Suzuki et al., 2001; Lebourg et al., 2005; Jomard et al., 2006). When the intention of investigation is to improve the understanding of landslide hydrogeological dynamics – such as those related to landslide activation – monitoring by ERT is not a straight forward task. Monitoring of landslide systems by electrical resistivity surveying requires known electrode positions as relative electrode position is a fundamental input when computing both apparent resistivity (using the geometric factor) and when modelling resistivity using a suitable software package such as Res2DINV, or in this case Res3DINV. Active landslide systems are dynamic natural phenomena and as a result the positions of buried electrodes do not remain constant as landslide displacements evolve through time. The exact positions of the electrodes are not known because they are buried at

approximately 0.1 m below land surface; therefore a method to derive the best-estimate of electrode positions is required.

Several methods to derive best-estimates of electrode positions have been proposed. Wilkinson et al (2010) predicts the movement of permanently installed electrodes on an active landslide by analysing electrical signatures which manifest as electrodes mobilise. Wilkinson et al (2010) found that movement artefacts over-print and obscure genuine time-lapse resistivity changes taking place in the subsurface. Their method is applied to predict electrode movement based on the time-lapse artefacts which appear as a result of changing electrode array geometry. This approach is has not been implemented for full 2D and 3D array monitoring, and so has not been used in this study.

Instead, we estimate electrode positions using the positions of a known set of reference points available at the field site. In the case of this investigation, the RTK-GPS monitored 45 survey peg array provide the necessary reference points (RPs).

Several approaches exist to derive electrode positions from movements of a known set of reference points (Uhlemann et al., 2013; Uhlemann et al., in press) and as a result attempt to avoid the considerable artefacts which would exist in time-lapse resistivity models. Deriving electrode positions from known reference points is the only option of determining electrode positions of the electrodes of the ERT monitoring array at Hollin Hill because the electrodes were buried during installation to protect the arrays from damage and due to strict planning regulations.

These approaches are described in Uhlemann et al (2013), and are briefly summarised here:

Velocity Approach (VA)

Movement of a set of reference points (RPs) from their initial positions (where P is the position of an RP) at time 0 (at $P_i(x, t_0)$) – in the case of this investigation the array of GPS monitored surveying pegs – to another position (at $P_i(x, t_n)$) at a future time n is divided into two directional movement vectors $dx(P_i, t_n)$ and $dy(P_i, t_n)$.

$$dx(P_i, t_n) = P(x, t_n) - P_i(x, t_0)$$

Equation 4.10. Determining directional movement vectors (dx)

To estimate the positions of electrodes between two reference points a linear interpolation of dx and dy to the initial electrode positions is applied. At a time n , the directional movement of an electrode along the x-axis is determined by

$$dx(E_i, t_n) = dx(P_i, t_n) + \left[(dx(P_{i+1}) - dx(P_i, t_n)) \cdot \frac{E_i(x, t_0) - P(x, t_0)}{P_{i+1}(x, t_0) - P(x, t_0)} \right]$$

Equation 4.11. Directional movement of an electrode at time n

The positions of the electrodes (E) at a time n , where initial electrode positions are known is estimated by applying the following equation

$$E_i(x, t_n) = E_i(x, t_0) + dx(E_i, t_n)$$

Equation 4.12. Position of electrode at time n

For times when no RP positions are known, electrode positions are interpolated by determining the velocities dv_x and dv_y from RP positions directly before and after the time of interest n .

General Approach (GA)

Three non-collinear points spanning a basis can be used to describe any point in a plane. The point of interest can be described

$$E(t_0) = S_u \cdot \vec{u} + S_v \cdot \vec{v} + S_n \cdot \frac{\vec{u} \cdot \vec{v}}{\|\vec{u} \cdot \vec{v}\|_2}$$

Equation 4.13. Electrode position at time t_0

Where S_u , S_v and S_n are weights and the final factor is the normalised normal vector which is perpendicular to \vec{u} and \vec{v} . If the positions of the three nearest RPs and the point of interest, here, an electrode ($E(t_0)$), are known the three weights S_u , S_v and S_n can be derived as well as the vectors u_0 and v_0 . The weights remain the same if we assume that the relative position of the electrode to the vectors \vec{u} and \vec{v} remain constant. Therefore, to calculate the new electrode position at time n , $E(t_n)$, the RP positions at time n are

used to determine u_n and v_n and are inputted into the equation above along with the three weights. To derive electrode positions for times when no RP positions are known, RP positions are derived by linear interpolation between times of known RP positions.

Uhlemann et al (in press) reports that the most accurate of the two methods to apply to interpolate electrode positions from a sparse number on reference points is the general approach, their comparison found the RMS error of the general approach to be substantially lower than that from the velocity approach, 0.0042 m compared to 1.12 m. For that reason the general approach is applied to interpolate electrode movement during this investigation.

The method described to interpolate electrode positions from a sparse number of reference points was applied in this geophysical investigation to generate an electrode location file for every field resistivity survey performed during the monitoring campaign. These files are termed '.geom' files and were incorporated into the 'pre-inversion' raw resistance data file which was later read into Res3DINV.

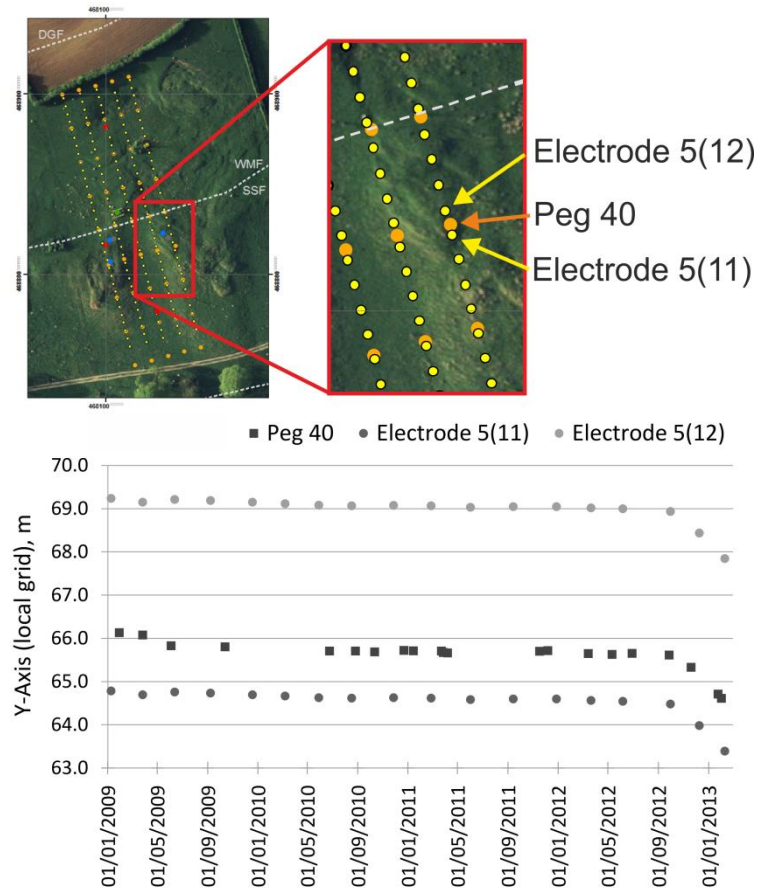


Figure 4.11. Example of interpolation of electrode positions from sparse array of GPS monitored survey peg positions.

As will be discussed in Section 4.3.2, these .geom files – which contain electrode position information – were also used when calculating temperature correction factor to correct transfer resistance results for the effects of temperature.

4.3.2 Temperature Correcting Transfer Resistances

Where time-lapse electrical resistivity data are being compared over a time duration longer than the time it takes for subsurface temperature to migrate through the subsurface, it is important to correct ERT results for the seasonal variation in subsurface temperature distribution. This is due to the effect that subsurface temperature variation has on the electrical properties of the subsurface, mainly its resistivity (ρ) or conductivity (σ). When the principal target of time-lapse resistivity surveying is to observe changes in subsurface electrical properties resulting from saturation or pore fluid conductivity the effects of subsurface temperature must be accounted for

(Hayley et al., 2010). Here, a temperature compensation method very similar to that used by Hayley et al (2010) is applied to measured transfer resistances in order to approximate transfer resistance with the effect of temperature removed. The method of temperature correcting time-lapse electrical resistivity data is a three stage process. Firstly, raw ERT data are inverted. The inversion results are then temperature corrected by adjusting to a temperature constant homogeneous half-space (sometimes referred to as a standard temperature equivalent model). This is achieved by determining the subsurface temperature distribution at time, n , from the Hollin Hill temperature model (4.1.2) and applying

$$\rho_T = \rho_h \cdot \frac{(1 + c(T_{MAT} - T_{MOD}))}{100}$$

Equation 4.14. Resistivity distribution within homogeneous half-space, determined in conjunction with subsurface temperature distribution model (see 4.1.2).

where, c is the percentage resistivity change per °C (standard assumption from Hayley et al (2007) is $c = -2.0^{\circ}\text{C}^{-1}$), and T_{MOD} is the modelled temperature of the subsurface as a function of depth and time. T_{MAT} is the temperature to which the model is normalised, in this investigation the mean air temperature. ρ_h is the resistivity of the uncorrected inverted half space and ρ_T is the temperature corrected resistivity after application of the temperature model.

The uncorrected and the temperature corrected models are then incorporated in a forward model simulation that determines the transfer resistances that would be measured from the two aforementioned models for the same measurement configuration. These forward models ascertain the values of R_h and R_{hc} for each survey. In this investigation a 1D temperature forward model was utilised, as opposed to Hayley et al (2010) which incorporates a 2.5D model, and was performed using Matlab (Ingeman-Nielson et al 2006). R_{hc} is calculated using a layered (i.e. 1D) resistivity inversion model, which is then temperature corrected using Equation 4.14. The model assumes a flat, horizontally layered resistivity and is obviously an approximation because the ground is not homogeneous (Figure 4.12).

Each transfer resistance measurement is temperature-corrected by the following equation

$$R_{tc} = \left(\frac{R_{hc}}{R_h} \right) \cdot R$$

Equation 4.15. Temperature correcting transfer resistance field measurements where R is the measured transfer resistance and R_{hc} is the temperature-corrected transfer resistance. The ratio (R_{hc}/R_h) is what corrects the resistance measurement. R_h is the transfer resistance that would be measured by that configuration on a homogeneous half-space of resistivity, ρ . R_{hc} is the transfer resistance that would be measured by the same configuration on the homogeneous half-space subjected to the Hollin Hill model temperature correction.

Very few examples of temperature correcting transfer resistance measurements exist in literature. The process of temperature correcting raw transfer resistance by applying a correction factor determined through temperature correcting model resistivity inversion results as developed by Hayley et al (2007) is applied here. As was highlighted above, electrode positions can shift between field resistivity surveys, therefore the process of accounting for electrode movement (presented in 4.3.1) was applied to locate measurement electrodes. Electrode positions were then passed to the 1D inversion program in order to get the most accurate model resistivity measurement. The inverted model was then converted to a temperature constant homogeneous half space and then divided by the original inversion model. This process was performed for each extracted dipole measurement and for every resistivity survey during the whole monitoring period. Therefore each extracted dipole measurement is individually temperature corrected as oppose to Hayley et al (2010) who determined the temperature correction factor once and applied the value to every subsequent extracted dipole measurement.

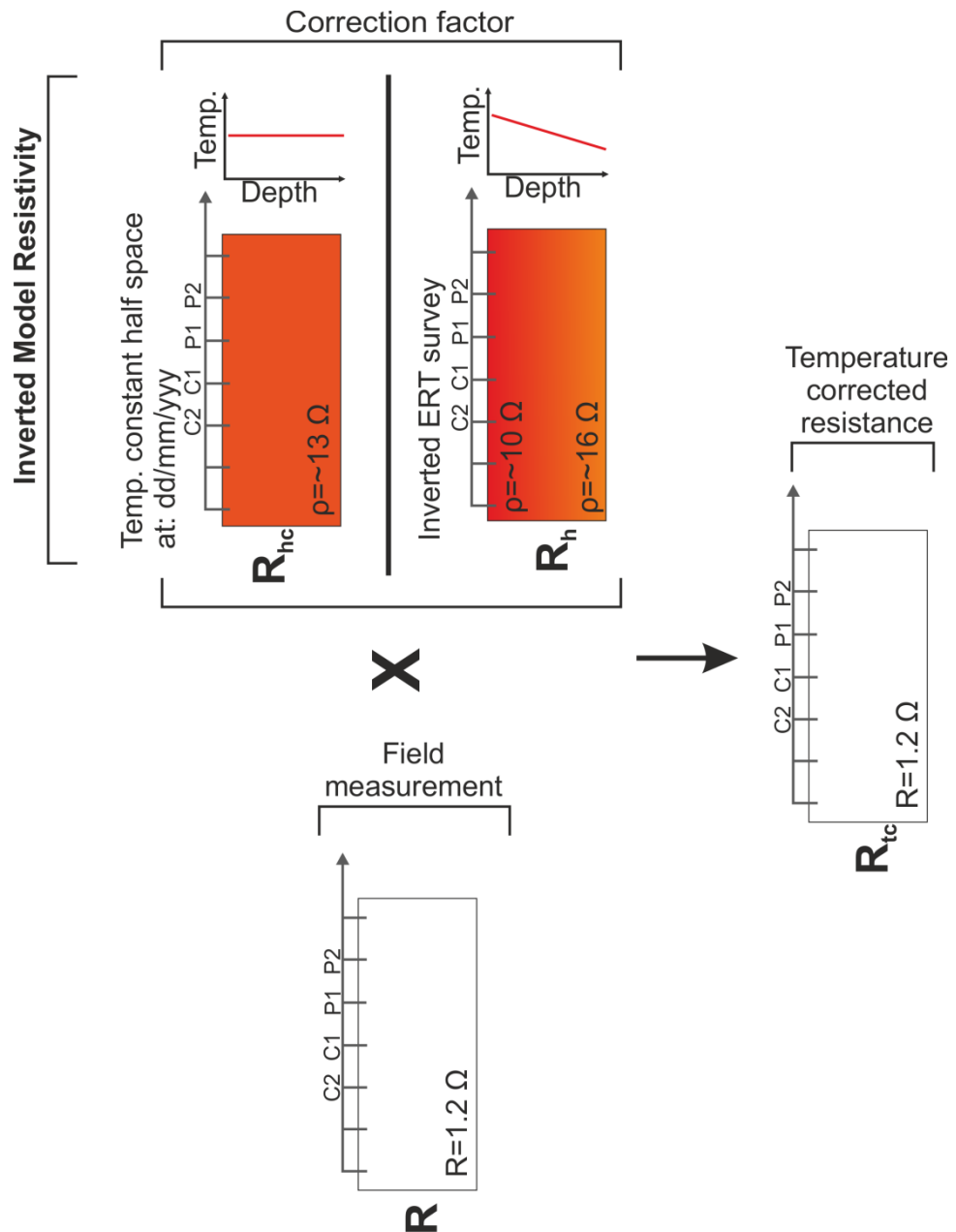


Figure 4.12. Diagram of the temperature correction of field transfer resistance measurements by 1D layered resistivity model

4.3.3 Inversion and Modelling of ERT monitoring data

Here, an explanation is given into the operations performed while converting time-lapse, field measured, raw, transfer resistance results into model resistivity monitoring results.

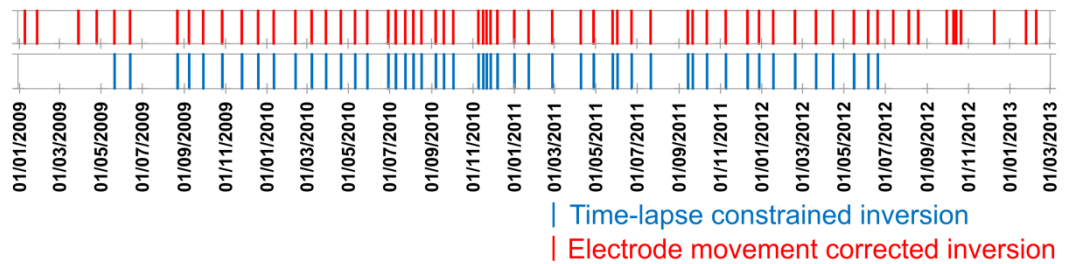


Figure 4.13. ERT survey dates and types of inversion performed.

Incorporating electrode mobility into resistivity modelling

As indicated in Figure 4.11 and section 4.3.1, an attempt was made to account for electrode movement during the landslide resistivity monitoring campaign by interpolating electrode movement from a known baseline of electrode locations and a sparse array of reference points (RPs). The next step in the processing route is the incorporation of interpolated electrode positions into each model inversion. Figure 4.13 reveals the dates of the 65 ERT surveys from the 4+ years monitoring period which were inverted, with each inversion including an individual set of electrode locations. Electrode positions were generated using a code written in Matlab by specifying only a date and the code outputs the complete electrode array geometry for the specified date and using both the general approach and velocity approach described in Section 4.3.1. Due to the lower RMS error associated with the general approach this approach was incorporated into the resistivity inversion models.

The 65 '.dat' files were passed to Res3DINV as a batch file and all therefore had identical inversion parameters throughout. By standardising inversion parameters any variations in the inversion results could not be attributed to varying the inversion parameters between surveys. The inversion parameters selected for this investigation are described in detail below.

Model Inversion Time-lapse Constraints

The method and benefits of applying time-lapse constraints to ERT monitoring data during the inversion modelling process is described in Section 2.2.2 of the Literature Review, Chapter 2. Here, only the implementation of the method is outlined.

Applying time-lapse constraints while modelling resistivity monitoring results restricts the time periods which can be inverted because the inversion modelling software utilised by this investigation, Res3DINV, lacks the capacity to apply both time-lapse constraints and vary the mesh geometries overtime. The intention of this project is to observe hydrogeological precursors to movement therefore only periods of landslide suspension were inverted with time-lapse constraints applied. The 50 ERT surveys inverted with time-lapse constraints were therefore selected from periods when the landslide system was suspended but do cover periods in the lead up to activation.

Several combinations of inversion type (either smooth, L1 or robust, L2) and degree of time-lapse damping were carried out to ascertain the effects of each of the variables on the resulting modelled resistivities. Model inversions were carried out with the following parameters

	Inversion type	Time-lapse damping factor
1	L1	0.2
2	L1	0.5
3	L1	1
4	L2	0.2
5	L2	0.5
6	L2	1

Table 4.6. Combination of model inversion types and time-lapse damping factors.

Observation of the results of each of the parameter combinations found that there was very little difference between the model resistivities computed by each combination. It was therefore decided to analyse only the smooth inversion with damping factor 0.2 in Chapter 6, the Results Chapter.

Inversion Parameterisation

Inversion parameters were, where possible, standardised throughout the modelling process of the investigation with the aim of making it possible to compare like-for-like, all inversion parameters are displayed in Appendix B.

4.3.4 Post-Inversion Temperature Correction of Time-Lapse ERT

Modelled seasonal temperature variation with depth is used to correct model resistivity results and the assumption that a 1°C increase in temperature results in a 2% decrease in resistivity (Hayley et al., 2007), hence

$$\rho_{MAT} = \rho_T \cdot (1 + \alpha(T_{MAT} - T_{MOD}))$$

Equation 4.16. Temperature correcting of model resistivity domains, from Hayley et al, (2007).

Where ρ_T is the electrical resistivity and is a function of date and depth, ρ_{MAT} is electrical resistivity at T_{MAT} , mean air temperature, T_{MOD} is the modelled subsurface temperature at the specific cell depth and α denotes the empirical coefficient that is often between 0.02 and 0.025°C⁻¹ (Hayley et al., 2007; Brunet et al., 2010), here α of 0.02°C⁻¹ is applied.

An understanding of both spatial and temporal subsurface temperature variation is needed if electrical resistivity models are to be corrected for the effect of subsurface temperature. This is achieved by normalising all model resistivity values to a common temperature, most often to an arbitrary temperature, for example 25 °C (Brunet et al., 2010), however in this investigation a temperature-constant homogeneous half-space normalised to mean air temperature (MAT is 10.03 °C) was used (Chambers et al., 2013).

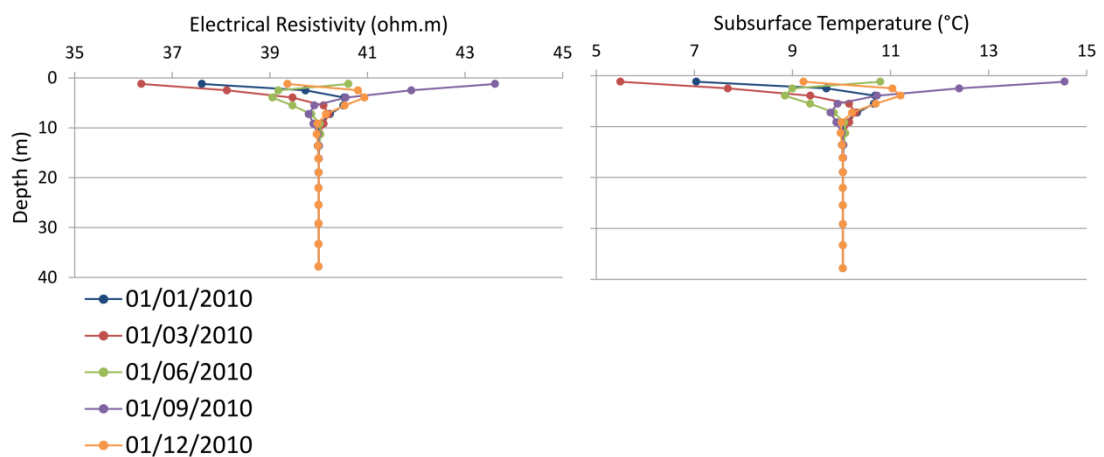


Figure 4.14. Temperature model calibrated from Hollin Hill temperature sensor array and applied to 40Ωm homogeneous half space. Model results presented as electrical resistivity and temperature distribution.

An example of how the degree to which seasonal subsurface temperature variation affects the electrical resistivity of a model half-space is given in Figure 4.14. Here, the temperature model fitted for the Hollin Hill field site is applied to a theoretical one-dimensional half space of 400m through application of the temperature correction equation from Hayley et al (2007) and the temperature and resistivity distributions plotted every 3 months over a one year period.

4.3.5 Partitioning of Three-Dimensional ERT Model Domain

In order to apply moisture-resistivity calibration curves to 3D volumetric images of resistivity it was necessary to partition the domain by each of the geological formations present at the field site. The process of partitioning the domain into the three geological formations underlying the field site involved interpreting a 3D ERT model in terms of geological formations based on electrical properties but also guided by intrusive data. This process was made easier as the low resolution ERT model was interpreted into three lithologies as part of the ground model development phase of research (Chapter 3). Paraview, a graphical data visualisation program, was used to visualise the 3D resistivity images and the 3720 cells which comprise the low resolution volumetric resistivity model were assigned a lithology, one of either Whitby Mudstone Formation (blue formation in Figure 4.15), Staithes Sandstone Formation (grey coloured) or Redcar Mudstone Formation (red coloured). This culminated in a .vts file, a paraview compatible file, being created which describes the formation associated with each model cell.

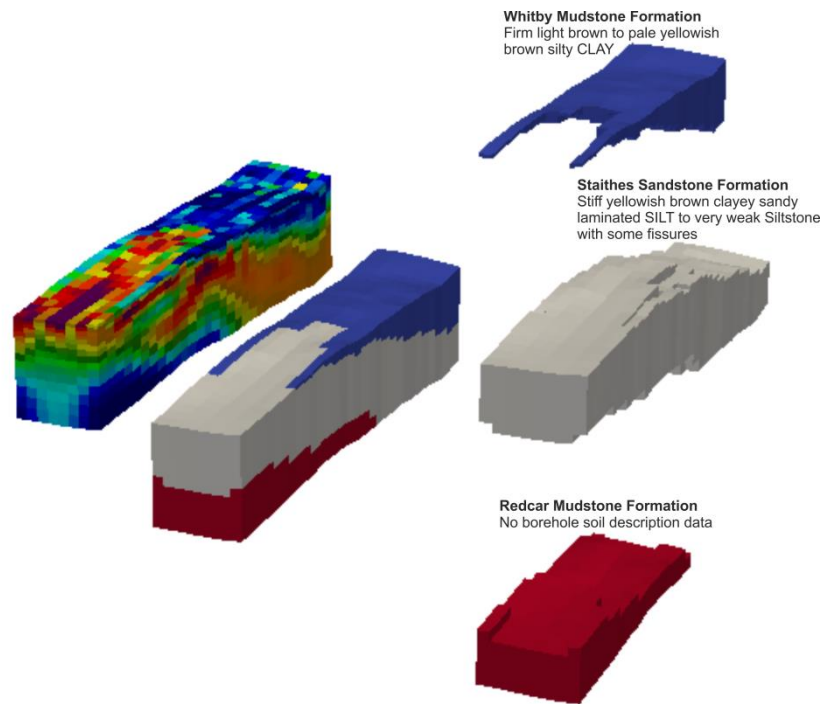


Figure 4.15. Domain partition; a 3D resistivity survey and the domain partitioned by geological formations, Whitby Mudstone Formation, Staithes Sandstone Formation & Redcar Mudstone Formation.

It was necessary to partition the domain by geological formation so that resistivity can be converted to gravimetric moisture content through the application of a modelled calibration curve to each model cell.

4.3.6 Conversion of time-lapse model resistivity to time-lapse volumetric images of moisture content

The final stage, and overall aim of this research is to convert field electrical resistivity monitoring measurements into 3D volumetric images of gravimetric moisture content. A code was prepared by colleagues at BGS that applies an electrical resistivity – gravimetric moisture content model curve to each of the three domain divisions, one pertaining to each of the three geological formations cropping out at Hollin Hill. The procedure is outlined graphically by Figure 4.16 and broadly details the four main steps required to go from taking multiple field ERT surveys to producing a final product which presents landslide properties as temporal gravimetric moisture content.

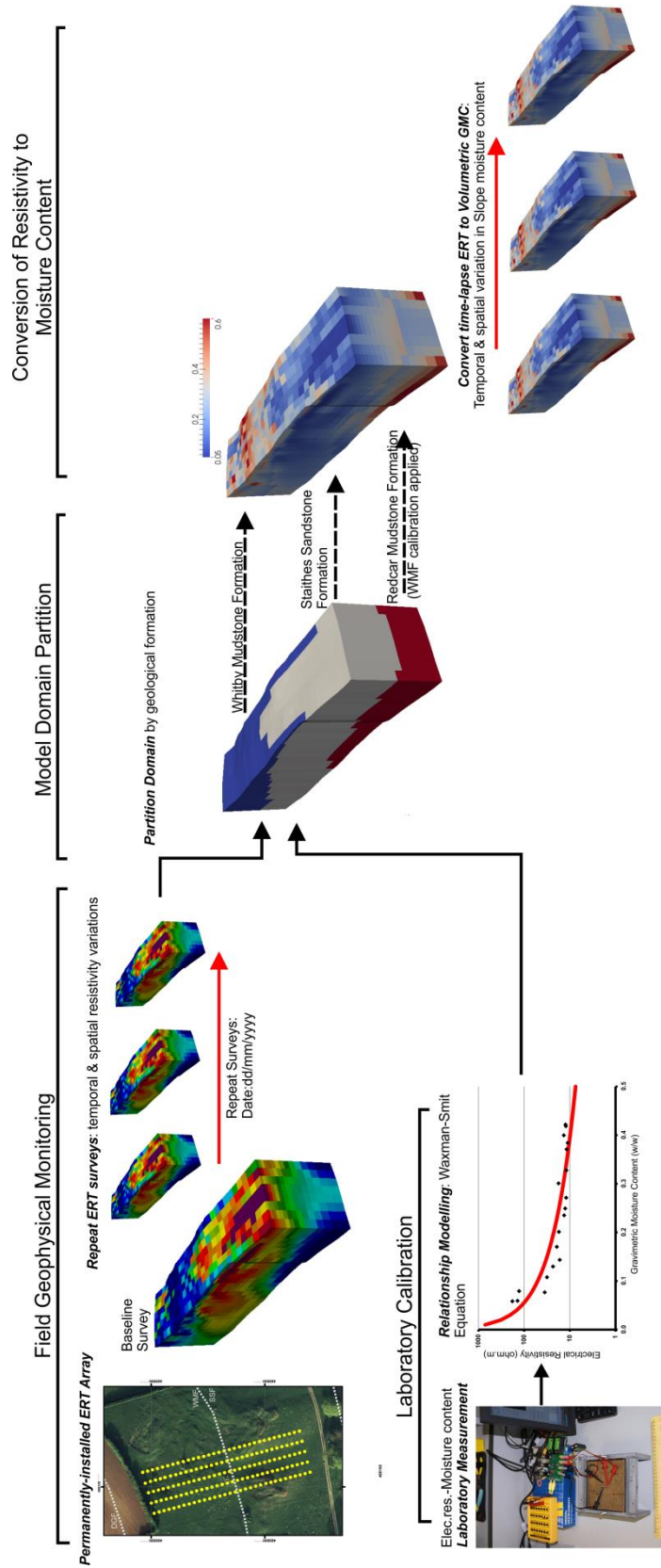


Figure 4.16. Converting time-lapse model resistivity to volumetric gravimetric moisture content.

It should be noted that laboratory calibration of Redcar Mudstone Formation (RMF) was not performed, as this formation is not subject to instability and is encountered at more than 15m depth within the model domain. For those reasons the added expense of coring to such depths was not deemed necessary. Two options therefore arose as to how to deal with Redcar Mudstone Formation within the model domain, either remove it completely (and have a non-rectangular domain), or to keep these cells composed of RMF and apply the Waxman-Smit model curve of a similar formation, i.e. that of Whitby Mudstone Formation to them. For ease of processing the decision was made to keep RMF composed regions of the model and apply the WMF model curve to RMF composed model cells.

4.4 Discussion

The methodology outlined in this chapter provides a practical solution for long-term geoelectrical monitoring of a dynamic physical system, such as a landslide system. What has been outlined attempts to overcome many of the challenges which arise while monitoring an intermittently active landslide system. The features of landslide systems which the methods described were devised to overcome include mobilisation of electrodes during monitoring, and seasonal variations in subsurface temperature distribution. Converting subsurface resistivity distribution into a more meaningful physical property – i.e. gravimetric moisture content – means that the hydrogeological precursors to landslide activation can be observed in a more understandable and relevant manner.

Chapter 5

Geophysical–Geotechnical Property Relationships

5.1 Introduction

If the results of landslide monitoring using geoelectrical methods are to be best understood they should be presented in a format that can be directly related to physical properties of landslide deposits. The results of landslide monitoring by time-lapse ERT are a series of either 2D profiles or, in the case of this investigation, 3D volumetric images of subsurface resistivity distribution (Loke, 1997; Chambers et al., 2013). To convert these volumetric images of subsurface resistivity to a more informative and relevant format, subsurface physical properties variations must be ascertained.

The moisture content of a natural soil is affected by climatic, seasonal and environmental factors such as rainfall amount and intensity, as well as evapotranspiration. Intense rainfall and rapid infiltration is widely accepted as one of the principal landslide triggers as slope materials tend to reduce in shear strength as they reach saturation (TRB, 1996; Bell, 2007) which can lead to landslide activation. ERT is sensitive to soil moisture content changes as a result of rainfall infiltrating the subsurface; thus potentially making ERT monitoring a useful tool when installed on a rainfall-induced landslide (Jongmans et al., 2007). However, the relationship between a soil's electrical properties and moisture content must be derived if field ERT monitoring results are to be presented in terms of subsurface moisture content variation.

Presented in this chapter is a methodology and results of the laboratory-based experimental measurement of electrical and geotechnical properties performed on samples extracted from the field site. Firstly, a series of laboratory electrical resistivity measurements are performed on landslide deposit material at various moisture contents, before an empirical, electropetrophysical model is applied to model the relationship between the two soil properties. The motive for this chapter is, ultimately, to derive the

electrical resistivity-moisture content relationship for each lithological formation present at the field site. Laboratory testing one-dimensional, discrete, point sampled landslide deposit samples and deriving the model parameters which – in Chapter 6 – can then be upscaled by directly applying them to volumetric, field-scale ERT monitoring results.

It is widely acknowledged that a major contributing factor in clay slope stability is the presence and strength of suctional forces acting within geological materials (Toll et al., 2011; Lourenco et al., 2009). The geological formation prone to instability episodes at Hollin Hill is the clay-dominated Whitby Mudstone Formation. This chapter also investigates the link between electrical resistivity and soil suctions of earthflow material by laboratory experimentation.

5.2 Laboratory determination of resistivity – moisture content relationship of undisturbed cores

A description of the soil resistivity – moisture content relationship determination for undisturbed samples from the field site is presented here, starting with an explanation of preparing cored samples for laboratory testing. Sample preparation is followed by an explanation of the laboratory measurement procedure, measurement error management, empirical modelling and results.

5.2.1 Core sample preparation

Sample Extraction

The cores extracted from Hollin Hill field site are 12 cm (0.12m) in diameter and were retrieved through percussion drilling, performed March 2010 using a Dando Terrier land drill (for details of drilling campaign see Chapter 3). The cores are stored and exist as half cores, held in place by the PVC sleeve into which the soils were originally intruded during drilling operations. The reason that the full cylindrical core is not available for testing is due to substantial, destructive, geotechnical tests being performed on the other half. These standard geotechnical index tests include moisture content and particle size analysis and result in sample disturbance and ultimate

destruction of any sedimentological fabric. The first stage of inserting the samples into the troughs involved opening the plastic bags, in which the cores have been stored since they were extracted from the subsurface in 2010. Cores were in turn removed from their storage bags and placed on a purpose built, temporary core holder in advance of being cut to size and removed from the parent core. The plastic, durable temporary core holder can be seen in Figures 5.1 and 5.2, supporting a core during several stages of preparation.



Figure 5.1. a) (left). Removal of core from plastic bag and depth measurement of extracted sample. b) (right). Once sample to be extracted is located a hacksaw is used to separate the sample from the core.

Care was taken at all stages of preparation to not damage the extracted samples, as any damage – fractures or chips – could greatly affect laboratory resistivity measurement.

Once locations of core samples to be extracted were finalised cutting was done by hand using a 30cm blade length hacksaw (Figure 5.2 & 5.3). A colleague was at hand at all times to minimise core movement/shaking and subsequent cracking due to the action of sawing.



Figure 5.2. First incision into soil core. Tape Measure used to measure position of second incision



Figure 5.3. a) (left). Both incisions made, core is now ready to be lifted out of the temporary core holder and placed into the soil troughs, ready to be transported to the laboratory. b) (right). Sample about to be lifted out of the temporary core holder. Note the saw guide, a thin gap between two sections of the grey, plastic core holder.

Sawing of the cores was at times difficult due to the sticky, cohesive nature of the often clayey soils. Care was taken when sawing granular, sandy material to prevent the walls of the freshly cut samples from collapsing after sawing (Figure 5.3). The task of sawing through the half soil cores was made easier as the temporary core holder includes a saw guide – a three

millimetre gap in the holder- to keep the saw straight, vertical and perpendicular to the cores edges (Figure 5.3b).

Transfer to Soil Trough

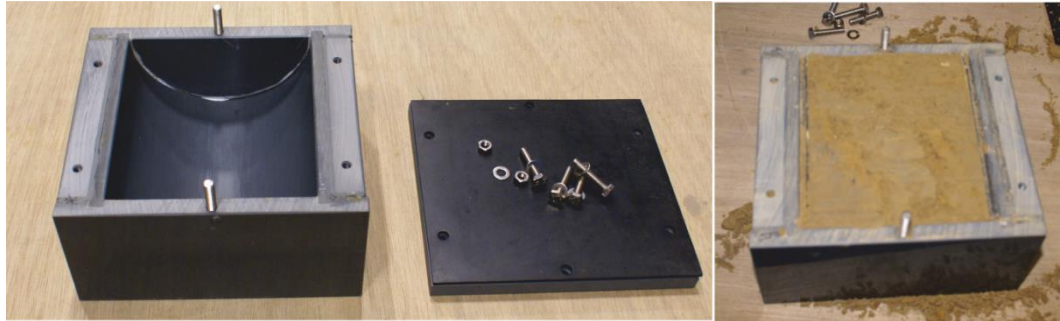


Figure 5.4. a.) (left) Empty trough with lid. b.) (right) Trough with soil sample inserted

Before cores are placed into the troughs (Figure 5.4), the troughs were thoroughly washed using hot and deionised water to remove any residues deposited during fabrication. Immediately after sawing the 13.7 cm (0.137 m) section of core was separated from the rest of his core by hand.

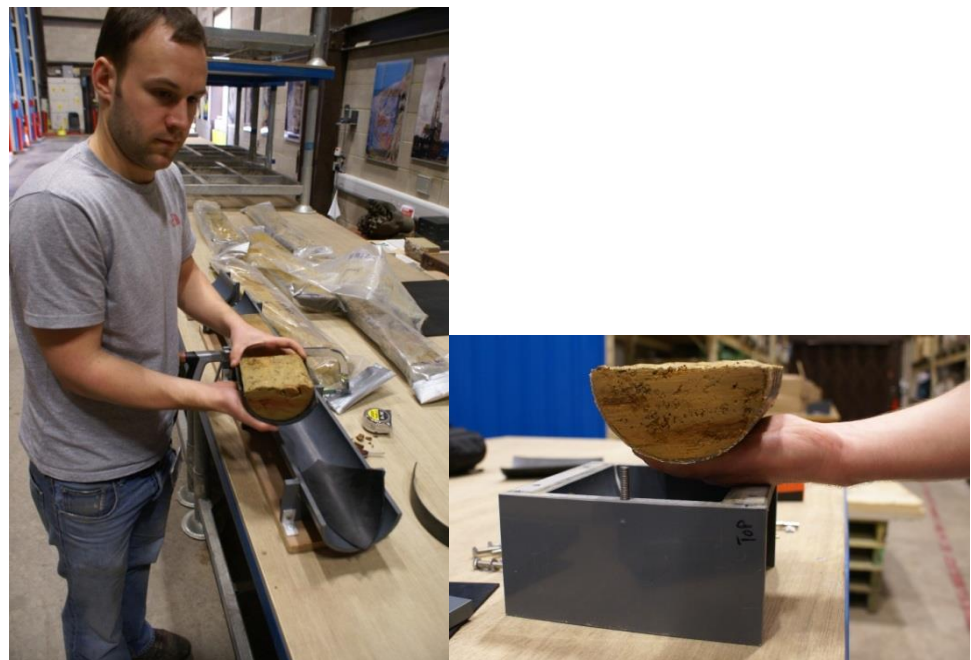


Figure 5.5. a.) (left) Transferring core to soil trough at the BGS core store at Keyworth. b.) (right) Extracted half core about to be placed into plastic trough
It was then lifted from the temporary core holder and carefully placed into one of the soil troughs, making sure that the soil was in no way damaged during the lifting process (Figures 5.4b, 5.5a & 5.5b). A total of six core troughs were fabricated from plastic to hold the short, 13.7cm length

samples of core during laboratory testing. The location, depth and description of each troughed soil sample is presented in Figure 5.6. Several factors were considered when deciding which soil samples should be transferred to trough and resistivity tested in the laboratory. After logging and interpreting the structure of each borehole, representative samples of the soil formations were selected. It was therefore decided to perform tests on both flowed, slumped and *in-situ* material of both Whitby Mudstone and Staithes Sandstone Formations.

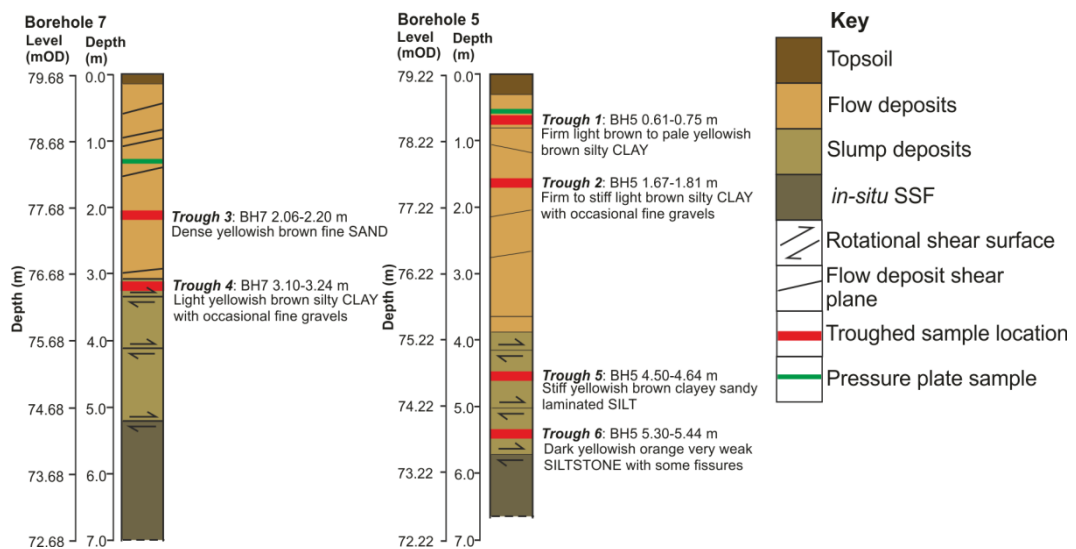


Figure 5.6. Location and depth of soil samples selected for laboratory electrical resistivity measurement

The decision as to where in the core to extract the 13.7cm (0.137m) sample, to perform resistivity experiments on was dictated by two factors. Firstly, the sample must be a fair representation of the whole formation, for example, sampling close to gradational boundaries was avoided, as was sampling non-pervasive, localised, structural features, such as shear surfaces. Secondly, samples were not taken from highly fractured, jointed or cracked regions, as this would make for inaccurate and unsuitable resistivity measurements. Joints and fractures whether naturally occurring, drill induced or formed during storage, within troughed samples would produce unrepresentative resistivity results because the empirical model implemented in this investigation (Waxman-Smit Equation) does not account for the aforementioned features. This selective avoidance of cracked or fractured regions does not constitute biased sampling as very few areas were pervasively affected by such features. In addition, an effort was made

to take samples which correspond to depths where soil cation exchange capacity (CEC) was previously measured through chemical testing at an external commercial laboratory (Alcontrol) and this was generally achieved, as all core samples were taken from within 0.3m of a CEC measurement.

5.2.2 Laboratory procedure

Laboratory Apparatus & Measurement

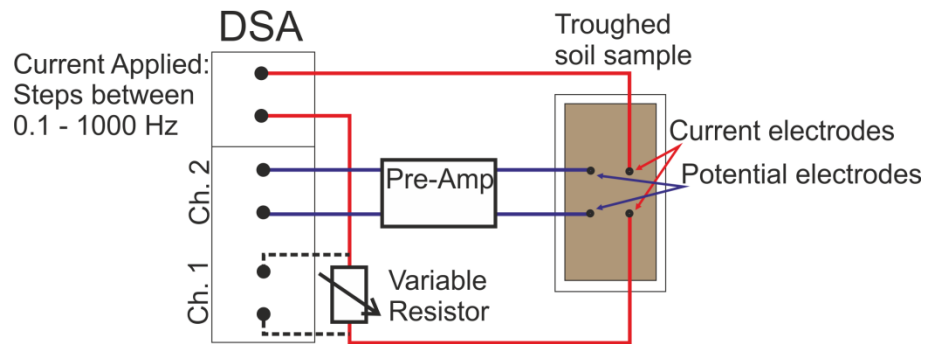


Figure 5.7. Electrical circuit diagram of circuit board and pre-amplifier

The accurate measurement of the electrical resistance of troughed soil samples (and saline solution during trough calibration) is measured using National Instruments NI-4461 circuit board (Figure 5.7) in association with preamplifier and variable resistor. The measurement instrument is set up for measurement by connecting two current and two potential electrodes, and works by measuring the potential difference between two electrodes while current is injected via the two current electrodes. Measurement of potential is made in the frequency-domain in the range of 1000Hz to 0.1Hz. A reference resistance is matched to the initial resistance of the cell (at 1000Hz) and a comparison is made between the measured waveform at the potential electrodes with that across the reference resistor. The waveform difference is recorded as decibel noise, dB, and the relationship between decibel noise and the initial cell resistance is a power law

$$\Omega_{(f_n)} = \Omega_{\text{Ref}} \times 10^{(N_{(f_n)}/20)}$$

Equation 5.1. Sample electrical resistance at frequency, $\Omega_{(f_n)}$, as a function of

cell resistance, Ω_{Ref} and magnitude of recorded noise, $N_{(f_n)}$.

Measurement of resistance is made using the square array measurement type (see Figure 5.8 & 5.9) and was chosen for practical reasons the electrodes can be placed directly into the open, upper surface of the half-core. Laboratory resistivity measurements were made using a very similar method utilised by Russell et al (2010) and were made using two measurement array sizes, a 5 cm (50mm) and a 1 cm (10mm) square array and a total of four measurements are made for each array size at each experimental stage. Two electrode array sizes were implemented to inform about the effects of sedimentary structure of varying scales. The main difference between the method utilised here and that used by Russell et al (2010) is that here, repeat measurements in each orientation were performed on undisturbed soil core samples, not reconstituted soil. The benefit of testing undisturbed samples is that variation in electrical properties attributed to sedimentary structure can be investigated.

Making Resistance Measurement

The electrode guide was positioned firmly over the trough to prevent electrode movement and resulting erroneous resistance measurements. To make sure the trough and electrode guide were correctly oriented at each test two star-symbols – one on the trough the other on the electrode guide – were aligned (Figure 5.8).

The electrode holder (Figure 5.8) was placed into the cut out of the electrode guide. Constant electrode penetration depth (how far the electrodes enter the saline solution or soil) was maintained throughout the resistance measurement. A slight taper (a point) was introduced to the electrode leading ends to reduce suction effects distorting the soils fabric when inserting or extracting the electrode housing from the soil sample. The depth that the electrode penetrates into the soil/saline solution must be maintained throughout geometric factor and subsequent soil moisture – resistivity experiments.

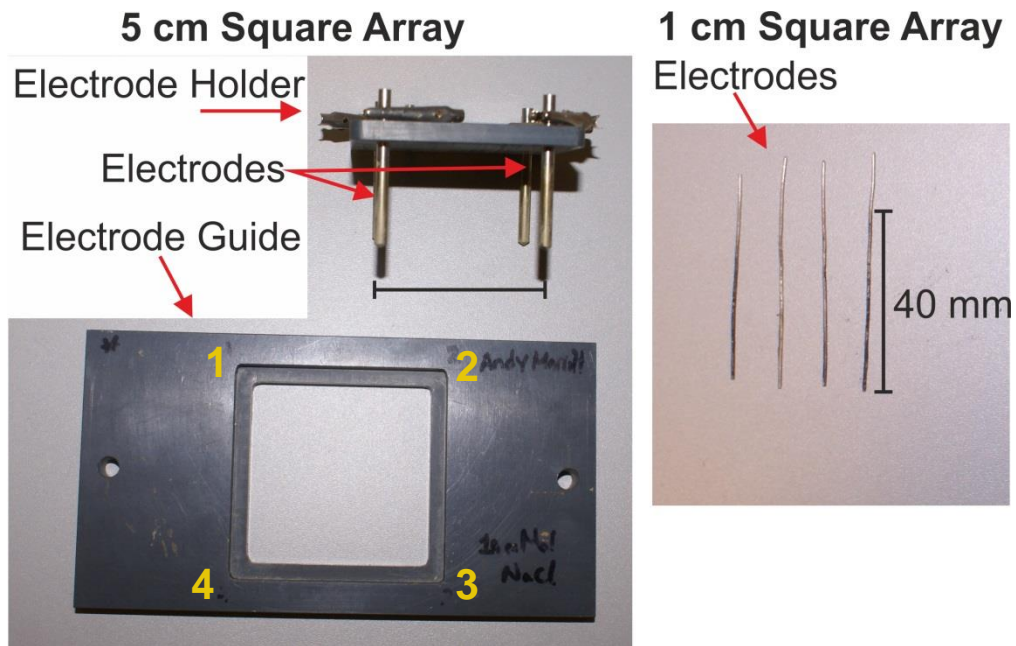


Figure 5.8. a). Laboratory equipment used to make resistivity measurements on trenched soil samples extracted from field site and include: 5 cm square array electrode holder, guide and electrodes. b.) 1 cm square array electrodes are shown along with their indicated soil penetration depth. N.B. 1 cm electrodes are not shown in measurement position.

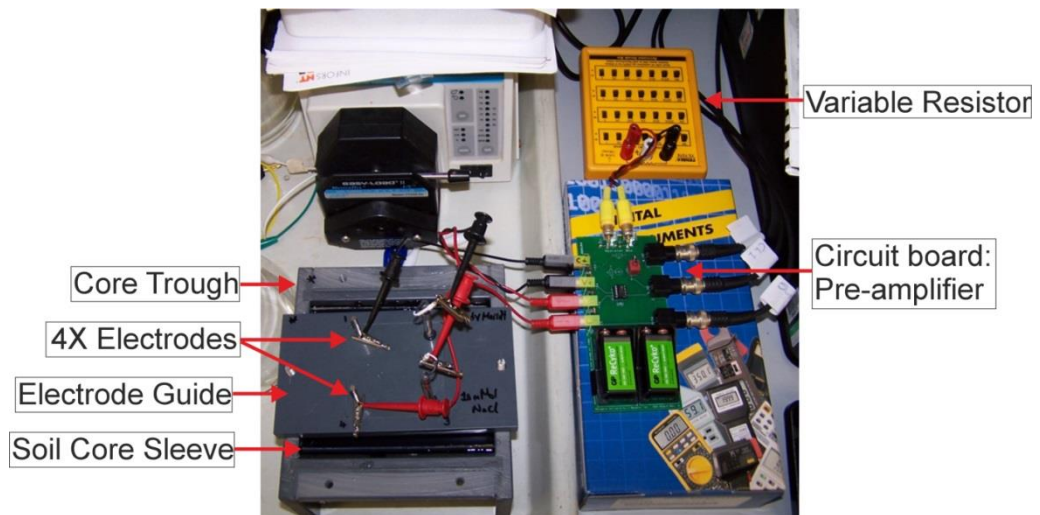


Figure 5.9. Laboratory electrical resistance measurement equipment during resistance measurement.

The four wires – two red and two black – from the circuit board and pre-amplifier are connected to the four electrodes by crocodile clips in the desired electrode arrangement. Electrodes are composed of two materials; 5cm array electrodes are composed of 4mm diameter stainless steel (grade 316) and penetrate 25mm and the 1cm array electrodes are composed of

2mm diameter silver alloy (Ag) and penetrate 40mm. Four electrode sites were labelled 1, 2, 3 and 4 and represent the four corners of the square-array electrode arrangement (Figure 5.8 & 5.9). At each of the four saline solution concentrations and for each array size a total of four electrical resistance measurements were made. This procedure produced two sets of resistance measurements along with a set of repeat electrical measurements, a summary of these electrode measurements is presented in Table 5.1 and Figure 5.10.

Electrode site	Electrode Arrangement			
	Initial		Repeat	
	A	B	E	F
1	C+	C-	C-	C+
2	P+	C+	P-	C-
3	P-	P+	P+	P-
4	C-	P-	C+	P+

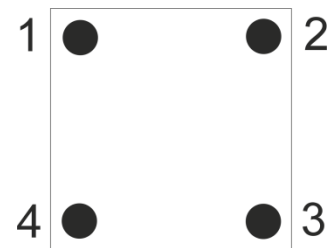


Table 5.1. (left) Electrode arrangement for each electrical measurement orientation.

Figure 5.10 (right) Position of each electrode site of the electrode holder to make the four point electrical measurement.

Electrode arrangements A, B, E and F correspond to the orientation and arrangement of current and potential electrodes during each resistance measurement. As can be seen in Table 5.1 electrode arrangement A and E have current and potential electrodes in the same orientation, however the polarities of each electrode is switched, thus making electrode arrangement E a repeat of A. Electrode arrangement B is repeated by arrangement F, however, B and F differ from A and E in that their current and potential electrodes are positioned at ninety degrees to each other. It is necessary to perform repeat measurements as a means of quantifying resistance measurement error.

Ready-prepared computer software produced in LabView is used to control injected current and record the resulting potential difference within a specified frequency range. The instrument outputs phase difference between sample and reference resistor, in mrad, and decibel noise magnitude, N , in dB, the latter being a key parameter when calculating sample resistance, Ω .

After opening the program IP final.exe (circuit board & pre-amplifier management software) several test parameters were input. These parameters include voltage (V), usually kept at 10V, and the measurement frequency range. The frequency range of the potential signal applied across the sample was 1000Hz to 0.1Hz, which was reduced stepwise at 10 measurement steps per frequency decade, making a total of forty measurements per full frequency sweep. Frequency steps were of equal increments in logarithmic-space. Each test run output forty resistance values, one at each frequency, with the resistance measured at 1Hz being used to convert resistance to resistivity later in the experimental process. The reason for selecting resistance at 1Hz was because field resistivity equipment also implemented by this project takes electrical measurements at his frequency, thus making a reasoned comparison more achievable. The test was initiated by switching the toggle switch on the board to the right (off to left), waiting a few seconds and then clicking the run button on the IP software. Soil (or saline solution resistance, when calibrating trough) resistance was determined by extracting the decibel noise magnitude measured at 1Hz ($N_{(f_n)}$) and inputting it, along with (Ω_{Ref}) into Equation 5.1.

Laboratory Calibration of Soil Trough

A calibration factor – the geometric factor – for the troughs was determined to permit the conversion between measured resistance, R (Ω), and sample resistivity, ρ_a (Ωm). This geometric factor, k (m), is a function of sample shape and electrode array type and size employed.

$$\rho_a = kR$$

Equation 5.2. Relationship between apparent resistivity (ρ_a), resistance (R) and geometric factor (k)

To determine the geometric factor of each square array size and electrode arrangement a plot of measured electrical resistance versus saline solution resistivity was produced. To establish the relationship, and conversion, between trough resistance and resistivity a number of saline solutions of different molarities and measured electrical conductivities are utilised. The solutions chosen spanned the range of electrical conductivities/resistivities observed during laboratory measurements of resistance. For that reason,

four saline solutions were chosen, whose electrical resistivities ranged between 10.8 and 1130ohm.m.

Saline solutions of various electrical conductivities were made by adding various amounts of sodium chloride (table salt) to de-ionised water. The trough was then filled with each saline solution in turn, until reaching the top of the rubber insert, which corresponds to the upper surface of soil core, the plastic core sleeve must also be placed in position within the trough. Following the filling of the trough with each saline solution the temperature and electrical conductivity of the saline solution was measured using accurate laboratory conductivity and temperature meters. Solution temperature must be measured before every test as temperature affects solution conductivity and is corrected for (Hayley et al., 2007) and covered later in this section.

Once the trough was filled with a saline solution and had its conductivity and temperature measured the electrode guide was fixed to the trough.

Determination of trough geometric factor was achieved by filling a number of empty troughs with saline solutions, one at a time and making a measurement of resistance using the resistance instrument. The reference resistor was set to be the same resistance as the sample resistance. Electrical resistance measurements for each of the four measurement orientations (A, B, E & F) are then used to produce a graph of the solution's electrical resistance versus its electrical resistivity. By repeating this procedure several times (four times) and by making use of several saline solution concentrations linear regression could be used to determine the geometric factor of the trough.

Saline Solution Properties

Several saline solution concentrations were needed because at least three points are needed to constrain the best fit line of the electrical resistance/resistivity graph. The physical properties of the four saline solutions utilised in the geometric factor determination are shown in Table 5.2.

Saline Solution	Solution Concentration (mMol)	Electrical Resistivity (Ωm)
1	12	10.81
2	1	114.28
3	0.5	230.59
4	0.1	1134.74

Table 5.2. Chemical and electrical properties of saline solutions used during trough calibration

Correcting laboratory electrical resistivity measurement for temperature

All measurements of electrical resistance and resistivity, whether field- or laboratory-based, were adjusted for the affect of ambient temperature on the measurement. Therefore, all measurements of resistance/resistivity were normalised to mean air temperature, MAT, at Hollin Hill this temperature is 10.03°C. The assumption that resistivity decreases by 2% per 1°C increase in temperature was followed (Hayley et al., 2007). Subsurface temperature was modelled over a period of two years and is explained in detail in Section 4.3.2.

Electrical resistance measurement of undisturbed samples at various moisture contents

Electrical resistivity of the soil was measured by the same four point measurement as used to determine the trough geometric factor. The first resistance measurements to be made of the soil samples were at the moisture content which the soils were at when extracted from the subsurface, i.e. no water was artificially added or removed. At each soil moisture content resistivity measurements were carried out utilising two square array sizes – 5cm and 1cm – and for each array size four measurement orientations (designated A, B, E and F) were implemented (Fig 5.11). Therefore, at every moisture content a total of 8 resistivity measurements were performed per trough, four utilising the 5cm array and a further four from the 1cm array. Resistances performed at 1 Hz were extracted and used in subsequent analyses.

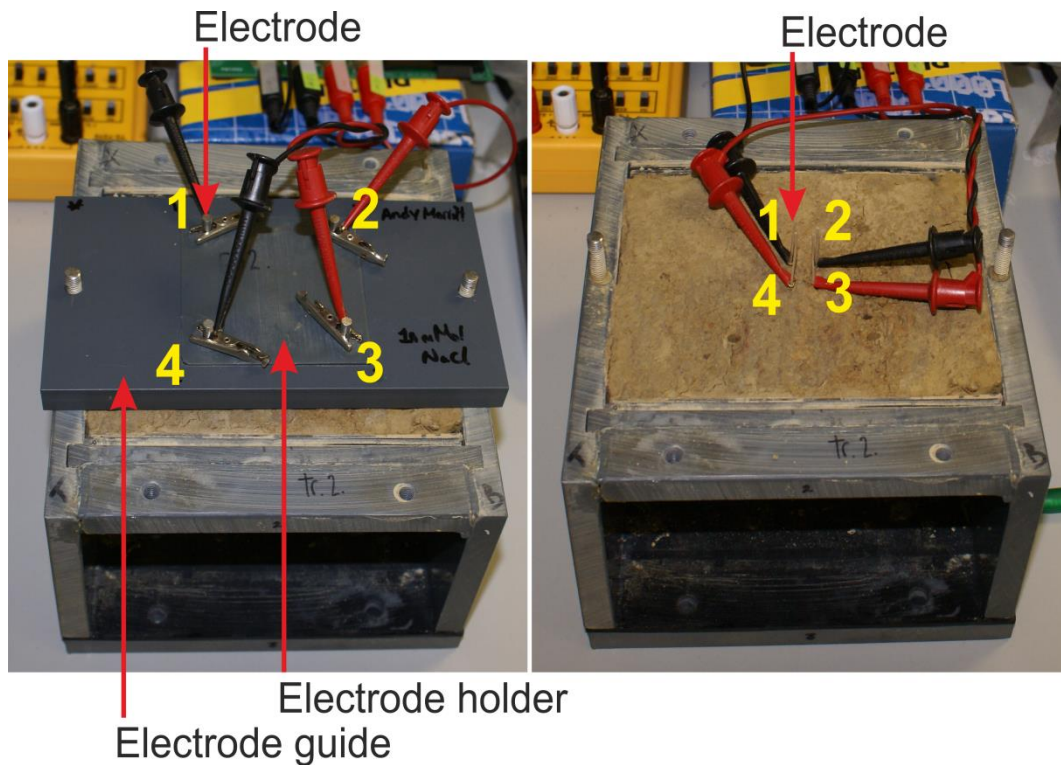


Figure 5.11. a.) Resistance measurements made by 5 cm (left) and b.) 1 cm (right) square array. Yellow numbers, 1-4, represent four electrode sites. 'Electrode' labels point to one of four electrode sites used to perform resistance measurement.

Two resistivity measurement orientations were considered at 90 degrees to one another so as to inform about resistivity directional anisotropy of undisturbed soil samples. Electrical resistance measurements were both orientated parallel (A-E), and perpendicular (B-F) to bedding. These arrangements are illustrated in Figure 5.12.

Measurements of resistance were converted to electrical resistivity – for the given soil sample and moisture content increment – by applying the cell geometric factor and then corrected for temperature effects. Once all the trough resistance measurements were made at their ambient moisture content the troughs were photographed along with information photoplate and images recorded in a photographic log.

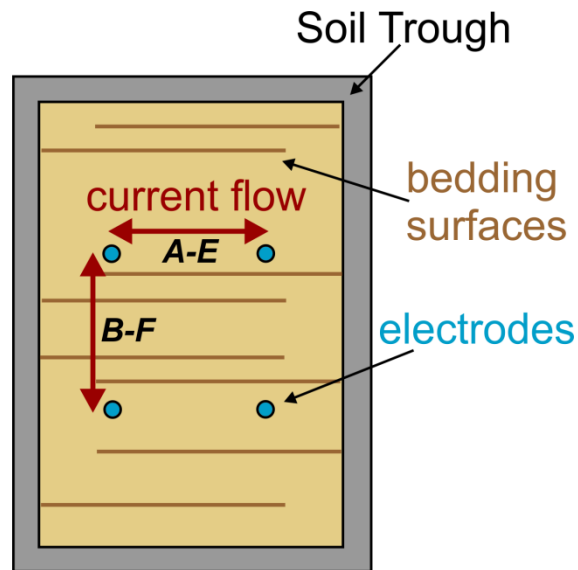


Figure 5.12. Orientation of electrical measurements relative to sample bedding

Each soil trough was then incrementally air-dried in steps of between 2% and 5%, and a further set of resistance measurements performed on all soil troughs at their new moisture content. The gravimetric moisture content of the soil was determined at each drying increment and is determined by:

$$G = \frac{m_w - m_d}{m_d}$$

Equation 5.3. Formula for determining soil gravimetric moisture content, G , where, m_w is the incremental weight of soil and m_d is the dry weight of the soil.

After the troughs reached their lowest dry weight by air-drying the trough samples were progressively re-wetted and resistances measured. Care was taken to perform several resistance measurements at moisture contents within the range already tested during incremental drying, thus highlighting clear reciprocity (and hysteresis present) between resistance measurements. Upon re-wetting beyond ambient moisture content, until water pooled on the sample surfaces, soil samples were oven dried at 50°C until completely dry (no more loss of mass) and soil dry weight measured by precise mass balance. Samples were not oven dried at 105°C as per Head, (2008) as the PVC troughs would have melted. Moisture contents of samples were given approximately 2 weeks between testing in order to give sufficient time for water to seep in to the samples. Samples were periodically

inverted (turned upside down) to prevent a water table developing in samples.

5.2.3 Undisturbed cores resistivity results

Calibration of soil trough

The outcome of trough calibration, through geometric factor determination, for the two electrode arrays is presented in Table 5.3 and Figure 5.13a. The 5 cm array returned electrical resistances at the four solution concentrations of between 27.49 Ω and 4720 Ω . The highest concentration of saline solution (12mMol) is responsible for producing the lowest electrical resistances of between 27.49 Ω and 39.10 Ω . Conversely, the highest electrical resistances are attributed to the lowest concentration of saline solution (0.1mMol) of between 3373 Ω and 4720 Ω . For each electrode arrangement (A, B, E and F) the gradient of the best fit line of resistivity versus resistance corresponds to the geometric factor of that electrical arrangement. Therefore the geometric factor of electrode arrangement A is 0.33m and that of B is 0.24m. As repeat measurements were made for each measurement orientation (A-E, B-F) the two geometric factors were averaged and incorporated into the resistivity/resistance conversion. A plot of resistivity versus resistance for the 5cm array is presented as Figure 5.13a in semi-log space and shows the best fit lines for each electrode arrangement. Measurement orientation A-E produces lower resistances than orientation B-F and as a result orientation A-E has a higher average geometric factor (resistance/resistivity ratio) of 0.335m than B-F, 0.242m.

The 1 cm electrode array produced electrical resistances of between 16.81 Ω and 2800 Ω for the range of four saline solutions. The 12mMol saline solution produced the lowest electrical resistances of between 16.81 Ω and 21.69 Ω and the 0.1mMol solution produced the highest resistances of between 2791 Ω and 2800 Ω . The plot of solution resistivity versus resistance is shown in Figure 5.13b, along with best fit lines. The geometric factors for the 1cm electrode array are higher than those of the 5cm array and are attributed to the reduced edge effects on the 1 cm array measurements.

Measurement orientation A-E produced a higher geometric factor than B-F and is in agreement with the 5cm electrode array. Average geometric factors

for each measurement orientation are 0.501m for orientation A-E and 0.408m for B-F.

5cm Square Array	Electrical Resistivity (Ωm)	Electrical Resistance (Ω)			
		A	B	E	F
12 mMol	10.81	27.49	39.10	27.50	39.06
1.0 mMol	114.28	336.41	472.45	336.07	471.31
0.5 mMol	230.59	669.71	933.21	672.77	936.72
0.1 mMol	1134.74	3403.27	4720.33	3373.60	4660.84
Gradient of Trend line		0.3339	0.2436	0.3366	0.2407

1cm Square Array	Electrical Resistivity (Ωm)	Electrical Resistance (Ω)			
		A	B	E	F
12 mMol	10.81	16.97	20.63	16.81	21.69
1.0 mMol	114.28	203.06	234.72	210.41	240.54
0.5 mMol	230.59	384.69	513.96	377.56	488.78
0.1 mMol	1134.74	2284.00	2791.54	2272.46	2800.00
Gradient of Trend line		0.5001	0.4084	0.5027	0.4077

Table 5.3. Results of geometric factor laboratory measurements. Columns headed with A, B, E and F represent the four orientations of electrode measurements.

The gradients of the trend lines (presented in Table 5.4) of measurement orientation A and E for both of square array sizes were averaged, as were the gradients of trend lines B and F and yielded the following cell geometric factors

	Measurement orientation	Averaged Geometric Factor, k (m)
5 cm Array	A-E	0.335
	B-F	0.242
1 cm Array	A-E	0.501
	B-F	0.408

Table 5.4. Averaged geometric factors applied to laboratory electrical resistance measurements.

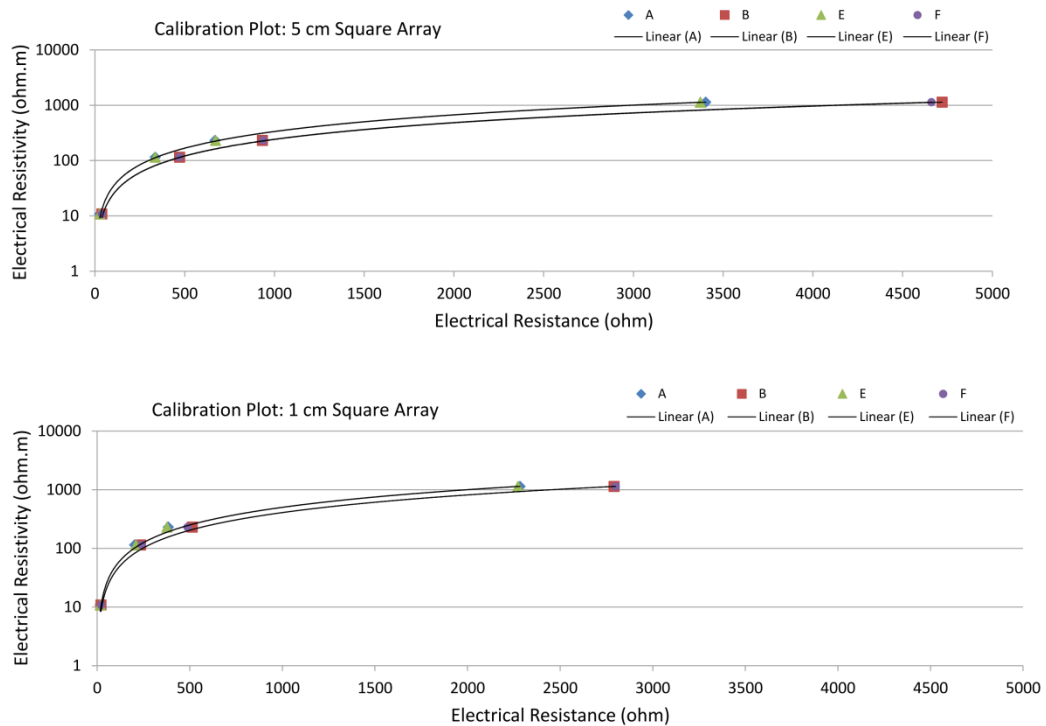


Figure 5.13. a) Cell geometric factor determination for 5 cm and Figure 5.13. b) 1 cm electrode arrays. A, B, E and F represent the four electrode orientations for each resistance measurement along with linear best fit trend line. Plotted in semi-log space.

Results of resistivity – gravimetric moisture content relationship

All of the six troughed soils exhibit similar trends with decreasing gravimetric moisture content and these trends; an increase in soil resistivity (Figures 5.14 to 5.19). This increase in resistivity (resistance measured at 1 Hz) is most profound for the fine sand of trough 3 (Figure 5.14) which shows a resistivity increase of four orders of magnitude with only a 4% moisture content change (1 & 5 % GMC). The clays of trough 1 and 2 (Figures 5.14 & 5.15) show similar increases in soil resistivity with decreasing moisture content, however, the magnitude of resistivity increases, at the lowest MC, are much less abrupt than trough 3, with a 100-150ohm.m increase taking place over a moisture content decrease of 20%. The silt and siltstone of troughs 5 and 6 (Figures 5.18 & 5.19) exhibit a resistivity increase of 2-3 orders of magnitude over a moisture content range of 10% and shows an intermediate $\Delta\rho/G$ relationship, between the sharp increase in the resistivity-GMC curve of the trough 3 sand and the much shallower resistivity increases of the clays of troughs 1 and 2. Troughs 1 and 2 also

have experimentally derived resistivity-GMC points from Gunn et al (*pers comms*). Their electrical measurements performed on Whitby Mudstone Formation utilised a similar method to this investigation and their results compare favourably with those made in this investigation. Their results are very similar to electrical resistivity measurements using orientation B observed in this study.

Two electrode array sizes were considered during soil resistivity measurement and results reveal several apparent trends. Firstly, for the majority of the measurements a range of resistivity values were returned, resistivity variation exists for a specific moisture content, between both array sizes and between measurement orientations. It can be seen throughout that the B-F orientated measurements (perpendicular to bedding) of both the 5cm and 1cm arrays almost consistently return higher resistivity values than measurement orientation A-E (parallel to bedding). The exception to this trend is the silty clay of trough 4 whose results from the 1cm array and oriented B-F return the lowest resistivity values for much of the moisture content range. Trough 3 soil shows divergence of resistivity values between the 5cm and 1cm array sizes at the drier end of the moisture content scale. Resistivities of troughs 1 and 2 for both array sizes and measurement orientations show good correlation throughout the moisture content range except for the driest moisture measurements which show a high degree of scatter.

The relationship between resistivity, electrode orientation and moisture content is less clear for troughs 4, 5 and 6. The silty clay soil of trough 4 (Figure 5.17) exhibits little scatter in resistivity both between measurement orientations and electrode array sizes over the majority of the moisture content range. However, between 4% and 12% moisture content the 1cm, B-F orientated resistivity measurement is lower than might be expected with respect to their surrounding resistivity values. Soil resistivity values from trough 4 show very little divergence (with the exception of the 1cm, B-F orientated resistivities described previously) between values from the two square array sizes.

The clayey, sandy laminated silt of trough 5 shows B-F-orientated resistivity values consistently higher than those orientated A-E. Trough 5 exhibits a hierarchy in terms of resistivity values, array size and measurement orientation which isn't as clear cut in the resistivities of other troughs. Resistivity values for a specific measurement orientation do not show the same degree of coincidence as the other troughs, there is a clear difference between the resistivities measured between the 5cm and 1cm array sizes and this difference is exhibited by all measurements carried out on trough 5. Resistivity measurements utilising the 1cm array produce the highest and lowest values, with the two 5cm array measurements positioned between the two 1 cm derived values.

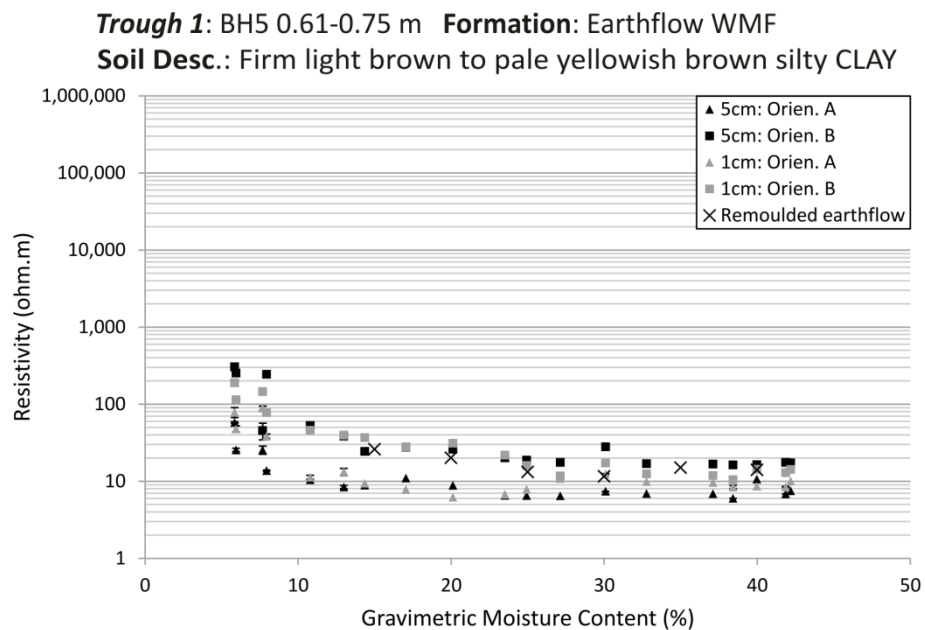


Figure 5.14. Electrical resistivity results at a range of gravimetric moisture contents for trough 1 soil sample. Error bars, see Section 5.2.4.

Conversely, it is the 5cm array which produces the highest and lowest resistivity values of trough 6, here, the 1cm resistivities are positioned between the two 5cm values. This apparent disparity between two lithologically similar samples can be explained in terms of the pervasiveness, scale and range of soil drying processes such as soil desiccation. In terms of electrical resistivity, the silts and siltstones of troughs 5 and 6 plot between the higher resistivities of trough 3 and the lower resistivities of troughs 1, 2 and 4. Trough 5 has a resistivity at the highest moisture content (22%) of

~50ohm.m and resistivity of both the 5 cm and 1 cm array gradually curve upwards to a resistivity at very low moisture content of ~1000ohm.m.

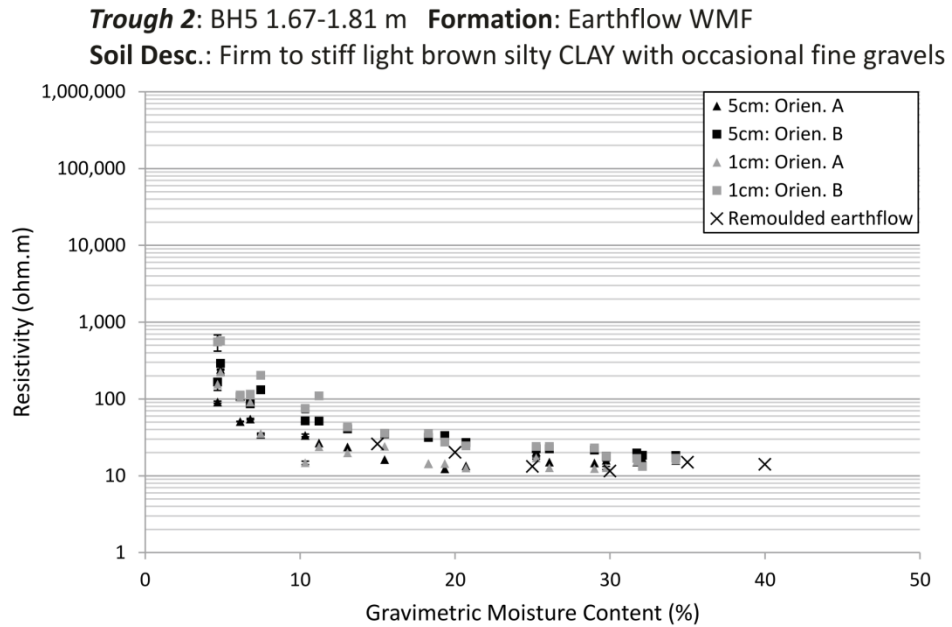


Figure 5.15. Electrical resistivity results at a range of gravimetric moisture contents for trough 2 soil sample. Error bars, see Section 5.2.4

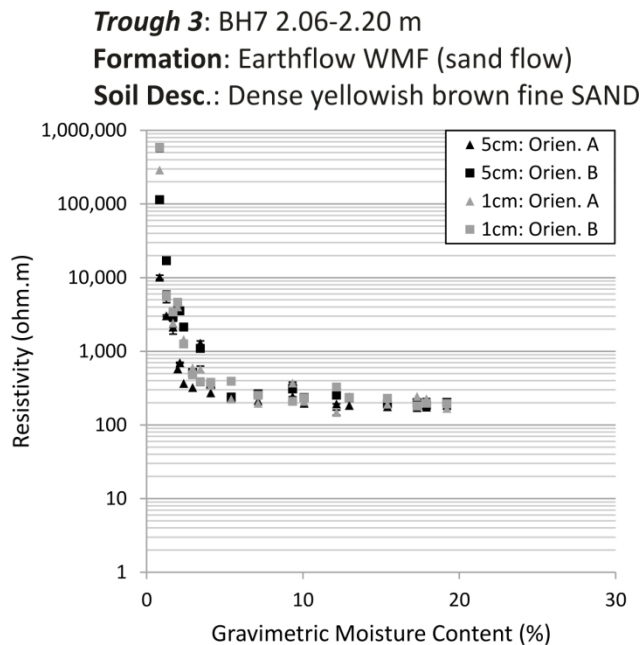


Figure 5.16. Electrical resistivity results at a range of gravimetric moisture contents for trough 3 soil sample. Error bars, see Section 5.2.4

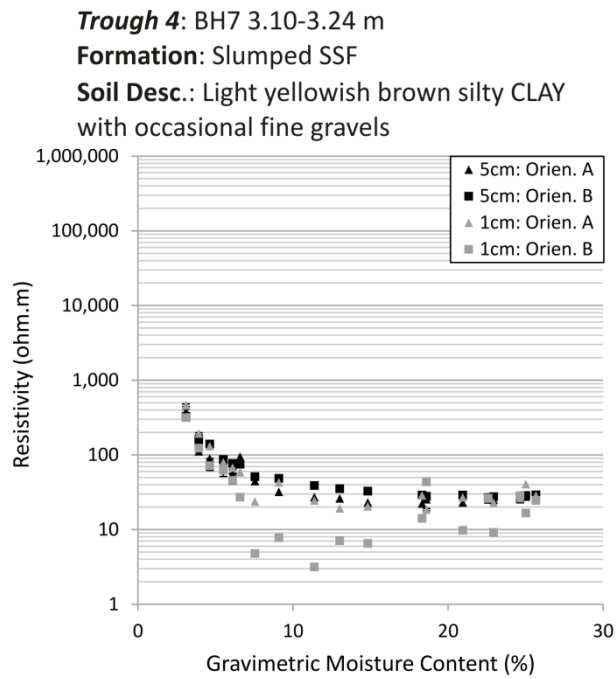


Figure 5.17. Electrical resistivity results at a range of gravimetric moisture contents for trough 4 soil sample. Error bars, see Section 5.2.4

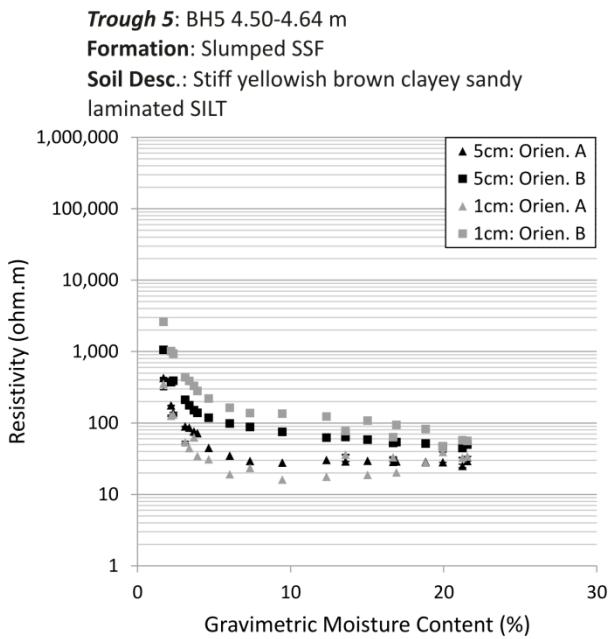


Figure 5.18. Electrical resistivity results at a range of gravimetric moisture contents for trough 5 soil sample. Error bars, see Section 5.2.4

While trough 6 follows a similar trend of increase resistivity with ever decreasing moisture content, the resistivities pertaining to the 5cm square array orientation B increase much more rapidly than the 1cm resistivities,

before reuniting at the lowest moisture contents. The resistivity measurements taken using the 5cm array orientation B increase ahead of the three other measurement orientations, from 14% until 4% GMC, where resistivity measurements of all four orientations and array sizes coincide once again. Over this moisture content range resistivity measurements pertaining to the 5cm orientation B increase by 1000ohm.m whereas the resistivities of the other three measurements increase by a few tens of ohm.m. This seemingly premature and abrupt increase in resistivity from the 5cm orientation B can be linked to macroscopic bedding-parallel cracks forming perpendicular to current flow in this troughed sample. The photographic log of the laboratory resistivity – moisture content experiment shows clear evidence of sample cracking at the moisture content increments associated with abrupt resistivity increase.

The highest moisture content reached for the silt of trough 6 is (19%) and is the lowest of the six troughs tested.

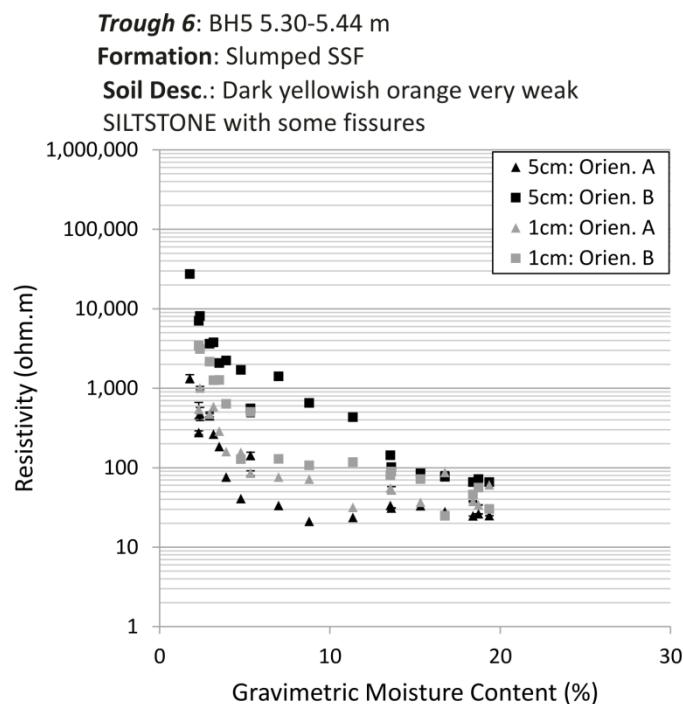


Figure 5.19. Electrical resistivity results at a range of gravimetric moisture contents for trough 6 soil sample. Error bars, see Section 5.2.4

The reason for the range of lowest moisture contents at which resistivity measurements were performed is because soil troughs were air dried at

room temperature until no more water evaporated. The clays of troughs 1,2 and 4 still contained upwards of 5-6% GMC when air dried, however, after being oven dried at 50°C this water was liberated and evaporated away. The sand and silt samples of troughs 3, 5 and 6 released the water they contained much more readily, as a result by air drying only 1% to 2% was retained in the trough.

5.2.4 Measurement quality assessment

As was alluded to in 5.2.2 repeat resistivity measurements were performed to permit assessment of data quality throughout the laboratory resistivity measurement exercise. Repeat measurements were performed at 9 of the 19 or 20 moisture content increments for each of the six soil troughs. Repeat measurements were not initially taken as soils were incrementally dried from their initial, ambient moisture content because measurement errors were not expected to be substantial for near-saturated soils. However, as moisture content decreased the decision was made to catalogue measurement error.

Differences between repeated resistance measurements are graphically presented along in Section 5.2.3 in the form of data point error bars (Figures 5.14 to 5.19) and error was calculated as half the different between initial resistivity and repeat resistivity, hence

$$E_R = \frac{(\rho_f - \rho_r)}{2}$$

Equation 5.4. Repeat error (E_R) of soil trough resistivity measurement. Where, ρ_f is initial resistivity, ρ_r is repeat resistivity.

However, error assessment is more understandable if represented as a percentage of the forward resistivity measurement. Graphs of percentage error in repeated electrical measurements are presented below, with percentage errors calculated by

$$E_{R\%} = \left(\left(\frac{\rho_f - \rho_r}{2} \right) / \rho_f \right) \cdot 100$$

Equation 5.5. Percentage error ($E_{R\%}$) of soil trough resistivity measurement.

Presentation of repeat measurement errors

Generally, results of repeat percentage errors for resistivity measurements, presented as Figures 5.20 to 5.25 below, show that repeat errors are highest for resistivity measurements performed at the lowest moisture contents. Conversely, resistivity measurements at the highest soil moisture contents provide the lowest repeat errors. Looking in more detail at each individual repeat measurement error plot several trends can be identified, firstly, measurements using the 1cm square array (grey-coloured points) almost consistently provide the highest repeat errors throughout the measurement campaign. Errors using the 5cm square array are often up to five times lower than their 1 cm array equivalent. Repeat measurement errors of the 5cm array are consistently lower than those from the 1cm square array which appear to vary much more sporadically with only small changes in moisture content. The 1cm array, A-orientated measurements (grey-coloured diamonds) produce many of the highest repeat errors across the moisture content range tested. Error data from troughs 2 and 4 are the exception to this rule as their highest errors are provided by orientation B of the 1cm square array (grey-coloured triangles). The gap in error data in the gravimetric moisture content mid-range exists because repeat measurements were performed as the soils reached their dry weights and as they were rapidly wetted to near saturation.

Reasons for measurement errors at low moisture contents is attributed to difficulties in getting the current into the soil sample, which is in principle due to the inability of the metal electrodes to make good electrical contact with the soil while electrical measurements are being taken. This issue is most apparent when performing measurements using the 1cm square array, where higher contact resistances were observed relative to the 5cm array. Electrodes for this measurement are composed of 2mm diameter silver alloy, which struggle to make and maintain good electrical contact with the soil due to having a low surface area. The electrodes utilised with the 5cm square array however have a wider diameter and hence have a larger surface area in which to make contact with the soil during electrical measurement.

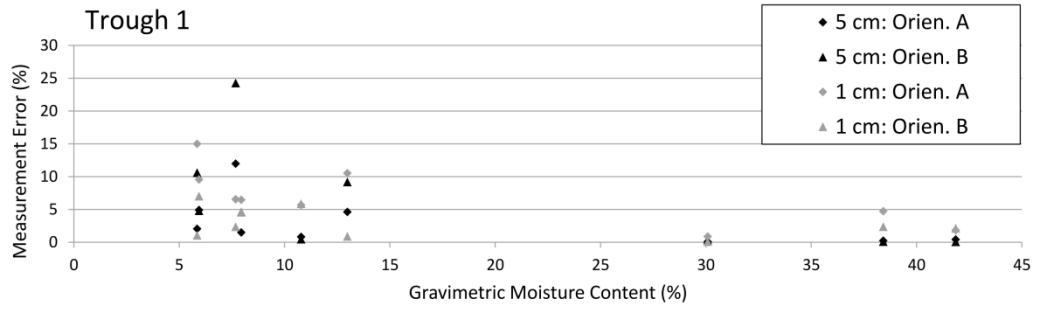


Figure 5.20. Resistivity percentage measurement error performed on Trough 1.

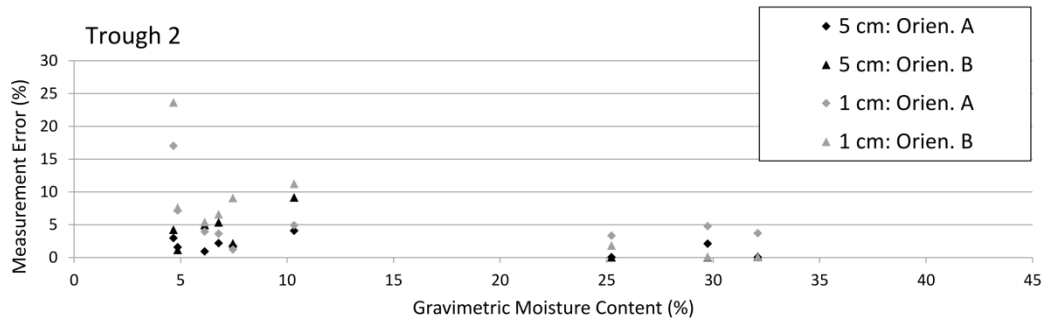


Figure 5.21. Resistivity percentage measurement error performed on Trough 2.

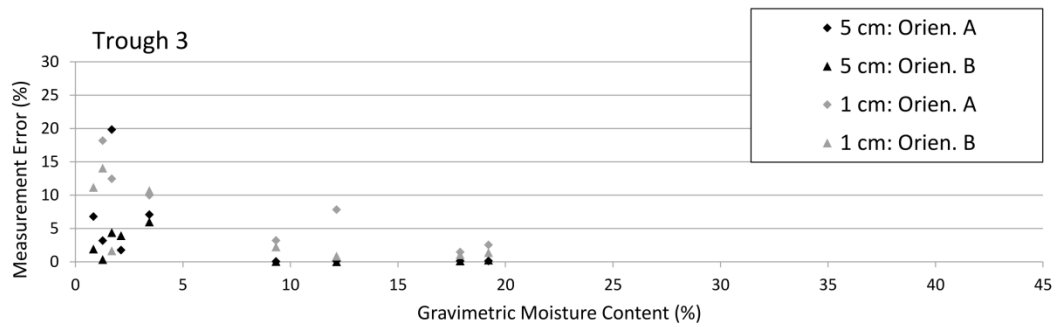


Figure 5.22. Resistivity percentage measurement error performed on Trough 3.

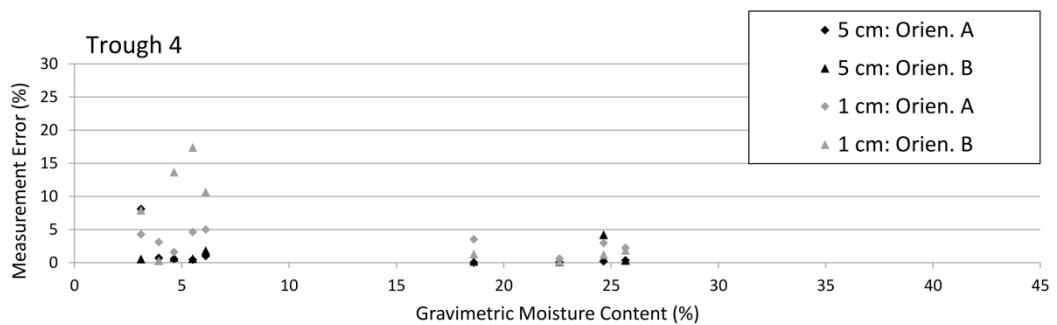


Figure 5.23. Resistivity percentage measurement error performed on Trough 4.

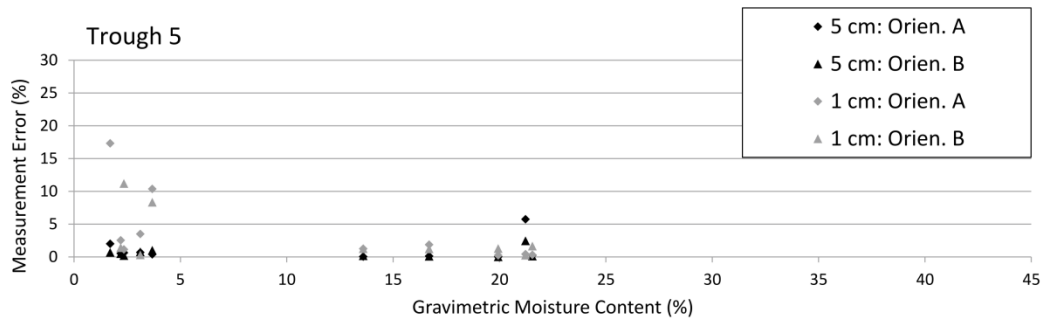


Figure 5.24. Resistivity percentage measurement error performed on Trough 5.

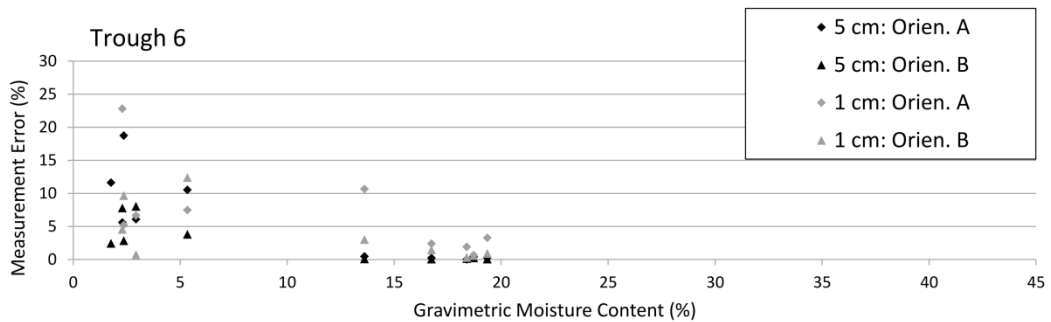


Figure 5.25. Resistivity percentage measurement error performed on Trough 6.

5.3 Modelling of electrical resistivity – moisture content relationship

Several approaches exist for modelling the relationship between resistivity – moisture content of geological materials. Two were considered this project. These are Archie’s Law (Archie, 1942) and the Waxman-Smiths model (Waxman and Smits., 1968), both have benefits and handicaps, and with that in mind the reasons governing the chosen model are justified below.

Archie’s Law is an empirical relationship linking pore volume, pore organisation, moisture content and pore fluid resistivity (Archie, 1942; Brunet et al., 2010; Binley et al., 2002; Schwartz et al., 2008). The original and most basic form of the model describes dc resistivity with moisture content

$$S = \left(\frac{\rho}{\rho_s} \right)^{-\frac{1}{n}}$$

Equation 5.6. Original form of Archie's Law

where saturation is S , ρ is bulk resistivity, ρ_s is bulk resistivity at 100% saturation and n is an empirical constant frequently labelled Archie's saturation exponent. Binley et al (2002) used a least-squares fit to the data and derived a saturation exponent of 1.13.

A more complex form of Archie's Law takes the form (Telford et al, 1990)

$$\rho = a\rho_w\varphi^{-m}S^{-n}$$

Equation 5.7. Modified Archie's Law

where a (cementation exponent), m and n are empirical coefficients, where the saturating fluid is water and where no other calibration data exists, n , the saturation coefficient takes the value of 2 and a is assumed to be 1, where the material in question is unconsolidated and granular (Telford et al, 1990). These formulae are valid for medium- to coarse-grained soils and rocks, where only a single conducting phase is present, thus presenting an issue if applied to Hollin Hill soils. This is because the majority of the geological formations cropping out and therefore of interest at the field site contain considerable fines and clay content, for example, Whitby Mudstone formation has a clay content greater than 60%. Therefore, a different physical model must be applied to link electrical resistivity with moisture content. The model should account for the complex manner in which electrical current flows within a material with appreciable clay/shale content (Section 2.2.2).

Geological materials with non-negligible clay components conduct electrical current by two methods, through the conductive pore fluid – by electrolytic conduction – and in addition within a layer of negatively charged platy clay minerals called the Electrical Double Layer.

Waxman-Smit Equation

The original Waxman and Smits equation (Waxman and Smits, 1968) was developed to account for a two phase conducting formation where electrical conductivity (inverse of electrical resistivity) is due to the combined effect of pore fluid conductivity with the additional electrical conductivity contributed by counter-ions balancing the negatively-charged grain-water interface (Brovelli et al., 2005). This additional mode of electrical conductivity is a result of ionic movement in the electrical double layer of clay-coated grains (described in section 2.2.1). Waxman-Smits model to describe formation conductivity as a function of moisture content does so by representing a porous media as a system of two resistors in parallel. Formation conductivity is therefore the sum of the pore fluid conductivity and the surface conductivity contributed by clay minerals in contact with aqueous pore fluid (Waxman and Smits, 1968). Waxman-Smits equation to describe formation electrical resistivity as a function of water saturation takes the form

$$\rho = \frac{F}{S^n} \left(\frac{1}{\rho_w} + \frac{BQ_v}{S} \right)^{-1}$$

Equation 5.8. Original Waxman-Smits Equation

where ρ is formation resistivity, S is formation saturation, n is the saturation exponent, F is the formation factor, ρ_w is the pore fluid resistivity, B is the average mobility of the ions and Q_v is the cation concentration per unit pore volume of the EDL. The average mobility of the ions, B , is commonly described as the equivalent conductivity of the compensating counterion, ($S \text{ m}^{-1}$) $\text{cm}^3 \text{ meq}^{-1}$. Q_v , or cation concentration per unit pore volume has the units (meq cm^{-3}) and combined with B is assumed that $\sigma_s = BQ_v$, where σ_s is conductivity contributed by surface conductivity in the EDL. Q_v and B are determined by

$$Q_v = (1 - \varphi)\rho_g c / 100\varphi$$

Equation 5.9. Cation concentration per unit pore volume, Q_v .

$$B = 4.6(1 - 0.6\text{Exp}[-\sigma_w/1.3])$$

Equation 5.10. Average mobility of cations, B , SI units of $(\text{S m}^{-1}) \text{cm}^3 \text{meq}^{-1}$ and where units of σ_w is S m^{-1} .

Modified Waxman-Smit Equation

A modified form of Waxman-Smits equation exists which instead of translating resistivity to saturation translates resistivity to gravimetric moisture content (GMC). The modified model takes the form

$$\rho = \frac{F \left(\frac{\varphi \rho_w}{(1 - \varphi) \rho_g G} \right)^n}{\left(\frac{1}{\rho_w} + B \left(\frac{c \rho_w}{100G} \right) \right)}$$

Equation 5.11. Modified Waxman-Smits Equation, where c is cation exchange capacity in meq/100g.

where, φ is the soil porosity ρ_w is the water density, assumed to be 1 gcm^{-3} , ρ_g is the particle density, gcm^{-3} , c is the soil cation exchange capacity, meq/100g, and G is soil gravimetric moisture content, %. Electrical conductivity of pore fluid (groundwater), σ_w , Sm^{-1} , was established using the Solinst LTC Levellogger Junior, a down hole installed piezometer which was installed in the flow region of the Hollin Hill landslide system and an average pore fluid conductivity (0.098 Sm^{-1} , or 10.13 ohm.m) was determined after a 3 month logging period. As is evident, Waxman-Smit equation uses many irregular and non-SI units as a standard SI version of the equation does not exist.

5.4 Waxman-Smit Modelling

This version of the Waxman-Smit equation (Equation 5.11) is more appropriately applied in this research investigation as it models resistivity-GMC curve shape independently of certain soil physical properties which can naturally vary as a result of environment and climate. The original form

of Waxman-Smit equation converts moisture content to saturation using soil porosity. Clay rich soils – such as the Whitby Mudstone Formation investigated at Hollin Hill – exhibit variable porosity with change in moisture content, attributed to the shrink-swell capability of certain clay minerals. Porosity appears as a multiplicative factor that only affects the formation factor which is one of the multiplicative factors used to fit the resistivity-moisture content curve.

The relationship between electrical resistivity and gravimetric moisture content was modelled through application of modified Waxman-Smiths equation (Equation 5.11) instead of the original version which models resistivity in terms of soil saturation. A mathematical modelling software suite called Mathematica was used to fit the resistivity-moisture content curve through parameters, formation factor, F and saturation exponent, n . Where no data is available to constrain the saturation factor an arbitrary value of 2 (Telford, 1990) is often assigned to this parameter. However, this value does vary between models and examples of saturation exponent from literature vary between 1.64 and 2.87 (Keelan et al., 1979).

This procedure was performed a total of 36 times for all troughs. Each of the six troughs had two sets of resistivity measurements modelled, one applying the 5 cm array, the other with the 1 cm array. Each of the two array sizes had two orientations curve-modelled (orientations A and B) as well as their arithmetic average. The input parameters and results of modelling for Waxman-Smit parameters are summarised in Tables 5.5 to 5.11. Geotechnical parameters, c , ϕ and ρ_g were determined through geotechnical testing are input parameters passed to Waxman-Smiths equation to output F and n . The curve was iteratively fitted as the equation cannot be re-arranged in terms of G . The values of the three geotechnical parameters passed to Waxman-Smiths equation were those which were determined from samples closest to the core locations of each soil samples and are therefore most representative. Cation exchange capacity values range between 25.90meq/100g, for the silty clay of trough 1 and 6.40meq/100g for the sand of trough 3. Porosity is seen to vary between 0.47 for the silty clay of trough 1 and 0.32 for the siltstone of trough 6 and particle density varies slightly between 2.69 and 2.74.

Trough 1	5 cm Array			1 cm Array		
	Average	Orient. A	Orient. B	Average	Orient. A	Orient. B
F	21.01	11.98	30.01	19.93	14.23	24.72
n	2.14	1.68	2.24	2.14	1.92	2.26
c , meq/100g	25.90					
φ	0.47					
ρ_g , gcm ⁻³	2.73					

Table 5.5. Waxman-Smiths Equation modelling and fitting parameters for Trough 1.

Trough 2	5 cm Array			1 cm Array		
	Average	Orient. A	Orient. B	Average	Orient. A	Orient. B
F	21.48	17.42	25.14	19.57	16.08	22.22
n	2.09	1.96	2.17	2.44	2.13	2.59
c , meq/100g	19.20					
φ	0.45					
ρ_g , gcm ⁻³	2.69					

Table 5.6. Waxman-Smiths Equation modelling and fitting parameters for Trough 2.

Trough 3	5 cm Array			1 cm Array		
	Average	Orient. A	Orient. B	Average	Orient. A	Orient. B
F	59.84	73.11	58.23	54.28	53.88	53.30
n	2.41	1.97	2.57	2.60	2.56	2.63
c , meq/100g	6.40					
φ	0.36					
ρ_g , gcm ⁻³	2.69					

Table 5.7. Waxman-Smiths Equation modelling and fitting parameters for Trough 3.

Trough 4	5 cm Array			1 cm Array		
	Average	Orient. A	Orient. B	Average	Orient. A	Orient. B
<i>F</i>	22.17	20.35	23.89	16.43	20.26	10.76
<i>n</i>	1.90	1.87	1.91	1.89	1.95	1.84
<i>c</i> , meq/100g	6.60					
φ	0.34					
ρ_g , gcm ⁻³	2.70					

Table 5.8. Waxman-Smits Equation modelling and fitting parameters for Trough 4.

Trough 5	5 cm Array			1 cm Array		
	Average	Orient. A	Orient. B	Average	Orient. A	Orient. B
<i>F</i>	47.35	32.09	62.33	60.10	29.60	86.29
<i>n</i>	1.86	1.78	1.91	2.05	1.60	2.18
<i>c</i> , meq/100g	10.00					
φ	0.32					
ρ_g , gcm ⁻³	2.69					

Table 5.9. Waxman-Smits Equation modelling and fitting parameters for Trough 5.

Trough 6	5 cm Array			1 cm Array		
	Average	Orient. A	Orient. B	Average	Orient. A	Orient. B
<i>F</i>	83.57	30.97	128.99	60.10	58.32	63.00
<i>n</i>	3.14	2.39	3.26	2.05	2.26	2.97
<i>c</i> , meq/100g	12.00					
φ	0.32					
ρ_g , gcm ⁻³	2.74					

Table 5.10. Waxman-Smits Equation modelling and fitting parameters for Trough 6.

Trough 6 (Minus cracking affected measurements)	5 cm Array			1 cm Array		
	Average	Orient. A	Orient. B	Average	Orient. A	Orient. B
<i>F</i>	72.10	30.97	105.59	60.10	58.32	63.00
<i>n</i>	3.18	2.39	3.31	2.05	2.26	2.97
<i>c</i> , meq/100g	12.00					
φ	0.32					
ρ_g , gcm ⁻³	2.74					

Table 5.11. Waxman-Smits Equation modelling and fitting parameters for Trough 6 (resistance measurements affected by sample cracking are removed).

5.4.1 Waxman-Smiths and Porosity

The relationship between porosity was investigated (Figure 5.26) using the model curve fitted to electro-petrophysical data pertaining to Trough 1 and the 5 cm electrode array. An increase in porosity increases resistivity of the whole curve by shifting the whole model curve upwards. This trend is most probably due to higher porosities encouraging electrolytic current flow at the expense of mineral surface conductivity in the EDL. As porosity has such a vital role in curve modelling a robust estimation of porosity is essential.

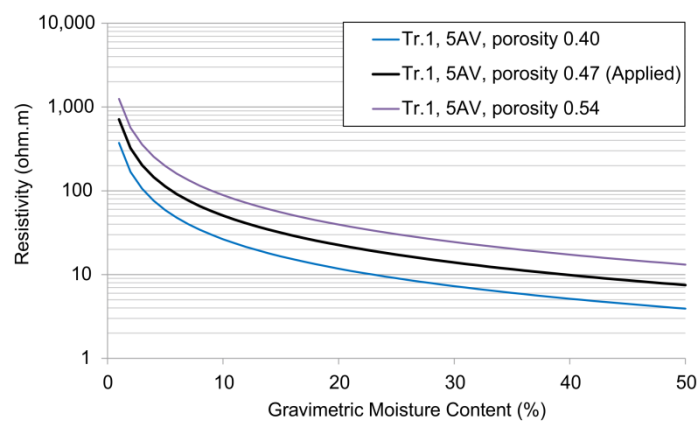


Figure 5.26. Effect of porosity on Waxman-Smiths Model Curves

5.4.2 Waxman-Smiths Modelling Results

Earthflow clays of troughs 1 and 2 (Figures 5.27 & 5.28) both show modelled resistivities of measurement orientation B returning higher resistivities throughout than those modelled resistivities returned from orientation A. Trough 1, 5 cm orientation B produces higher modelled resistivities than 1 cm orientation B, conversely, for the same trough it is the 1 cm square array orientation A which returns higher modelled resistivities than those from the equivalent 5 cm square array. Although modelled resistivities from the two square array sizes of orientation A coincide between 45% and 50% gravimetric moisture content. Modelled resistivities pertaining to orientation B coincide at very low moisture contents, at 2% to 3% GMC. Trough 2 has 1 cm orientation B modelled resistivities returning higher resistivities at low GMC, when compared to those modelled resistivities related to 5 cm orientation B. However, at higher GMC, beyond 22% GMC, the trend swaps

and 5 cm orientation B begins to return higher modelled resistivities, in comparison to modelled resistivities of orientation B utilising the 1 cm square array. Orientation A, 5 cm and 1 cm resistivity models display the same 'resistivity swap' trend occurring at 17% to 18% GMC with the same measurement orientation dominating at relative high and low moisture content for both square array sizes.

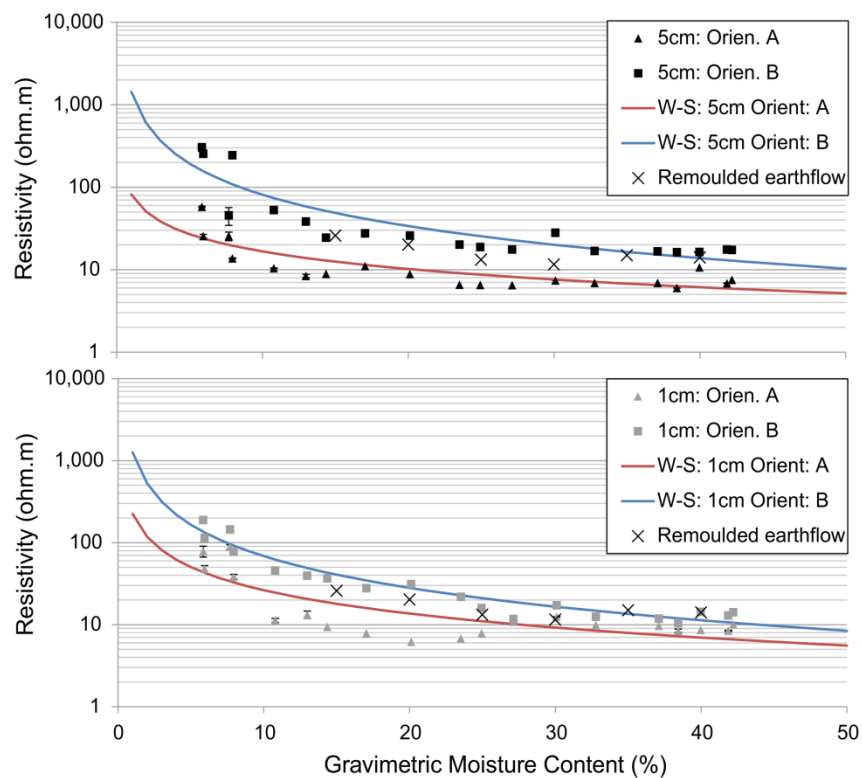


Figure 5.27 a). Trough 1 electrical resistivity – gravimetric moisture content model relationship for 5cm electrode array. b). Trough 1 electrical resistivity – gravimetric moisture content model relationship for 1cm electrode array Modelled by Waxman-Smits Equation.

Troughs 3, 4, 5 & 6 (Figures 5.29 to 5.32) are plotted on lower moisture content range axes, 0% to 30%, as oppose to troughs 1 and 2 whose axes range 0% to 50%. This is because soils of troughs 3, 4, 5 and 6 have lower porosities than those of troughs 1 and 2. Model curves of trough 3 (Figure 5.29) show three which are closely coincident, these are the 5 cm orientation B and both orientations (A & B) making use of the 1cm square array. The 5cm array size, orientation A has a lower resistivity at low GMC and a higher resistivity at high GMC when compared to the three modelled resistivity

curves which coincide. The cross over point where all four model curves meet is at 14% GMC and a resistivity of 140~Ωm.

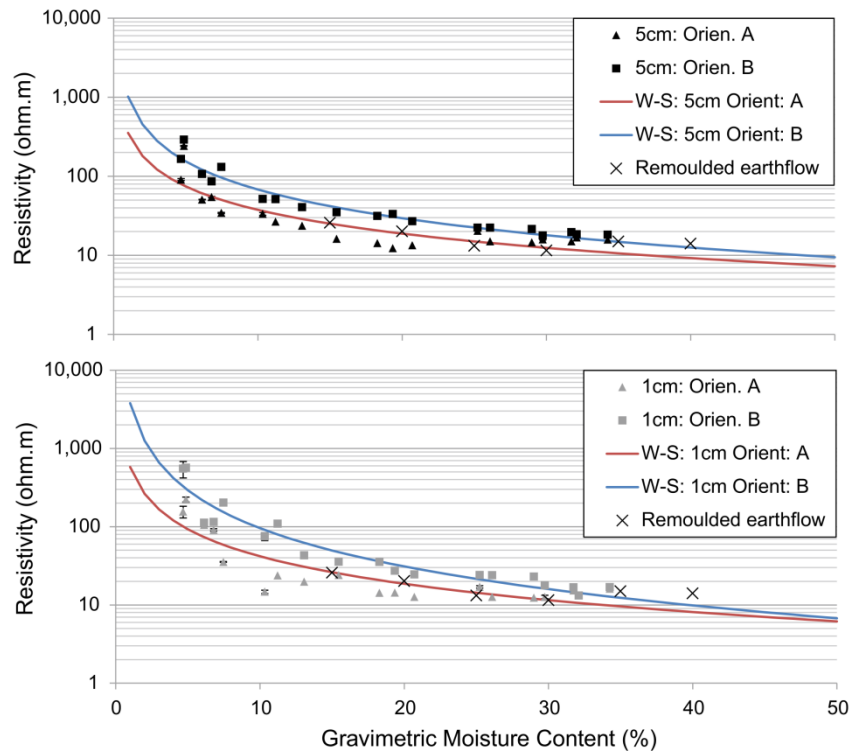


Figure 5.28 a). Trough 2 electrical resistivity – gravimetric moisture content model relationship for 5cm electrode array. b). Trough 2 electrical resistivity – gravimetric moisture content model relationship for 1cm electrode array Modelled by Waxman-Smits Equation.

Modelled resistivities of both orientation A curves for trough 4 (Figure 5.30) display very little difference, however, modelled resistivities of orientation B do not share a similar trend as the 5cm array model plots above the orientation A curves and the 1cm array substantially below. The 1cm orientation B modelled curve plots substantially below the other curves as a result of the resistivity measurements, from which the curves were modelled, showing low measured resistivities over much of the moisture content range.

The curves modelled for slumped Staithes Sandstone Formation (troughs 5 & 6, Figures 5.31 to 5.32) exhibit a wide range of resistivities throughout the moisture content range. Both orientation B curves show higher resistivities than both the orientation A related resistivity curves, with the 1cm square

array returning higher modelled resistivities than the equivalent 5cm modelled resistivities.

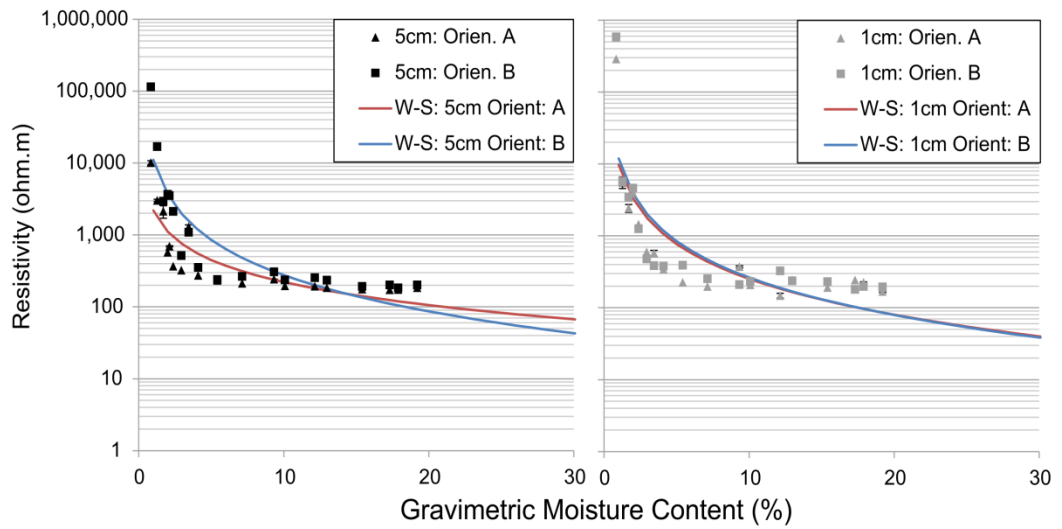


Figure 5.29 a). Trough 3 electrical resistivity – gravimetric moisture content model relationship for 5cm electrode array. b). Trough 3 electrical resistivity – gravimetric moisture content model relationship for 1cm electrode array Modelled by Waxman-Smits Equation.

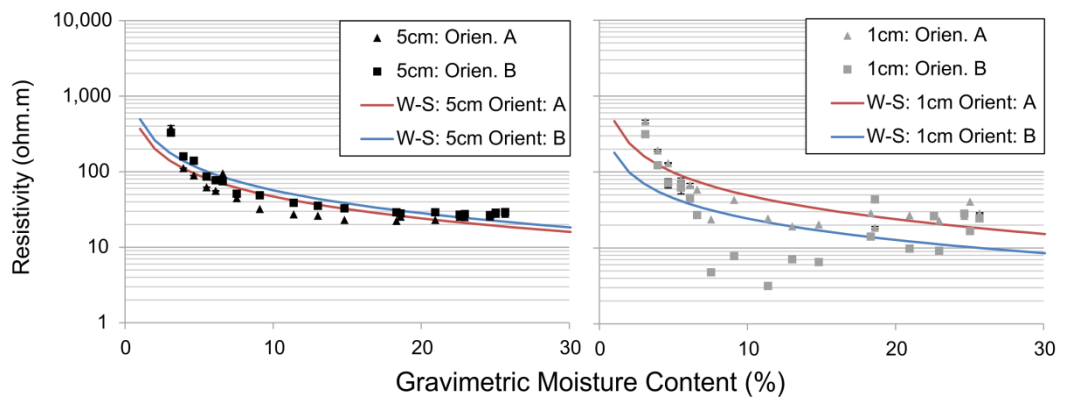


Figure 5.30 a). Trough 4 electrical resistivity – gravimetric moisture content model relationship for 5cm electrode array. b). Trough 4 electrical resistivity – gravimetric moisture content model relationship for 1cm electrode array Modelled by Waxman-Smits Equation.

Models pertaining to orientation A derived measurements of resistivity plot below orientation B models with 5cm square array producing higher

resistivities at low moisture contents before converging with 1cm array models at the highest moisture contents.

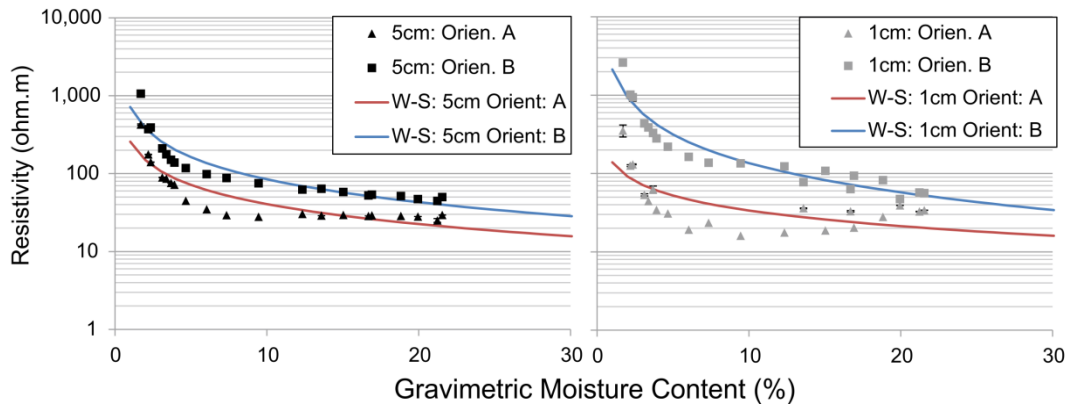


Figure 5.31 a). Trough 5 electrical resistivity – gravimetric moisture content model relationship for 5cm electrode array. b). Trough 5 electrical resistivity – gravimetric moisture content model relationship for 1cm electrode array Modelled by Waxman-Smits Equation.

Trough 6 required its resistivity – moisture content curve be modelled twice as a means of quantifying the affect that cracking affected resistivities have on the outputs of Waxman-Smits modelling (Figure 5.32). The modelled curve which includes the cracking affected resistivity measurements into its data input shows a similar trend to trough 5, also slumped Staithes Sandstone Formation. Both orientation B modelled curves plots above orientation A curves, thus highlighting that resistivities associated with orientation B measurements are higher than those associated with orientation A. However, contrary to trough 5, 5cm orientation B model displays higher modelled resistivities throughout than the 1 cm equivalent. The same can be said for orientation A related models, their modelled curves show the reverse of the trend seen in trough 5, as the 1cm model plots above the 5cm model. The electrical resistivity – moisture content relationship of trough 6, 5cm square array and orientation B was modelled a second time, this time with the cracking related resistivity measurements excluded in the model data input. Comparison between the two sets of model parameter results (Tables 5.10 & 5.11) shows that by excluding the cracking related measurements into the model very slightly lowers the modelled resistivities.

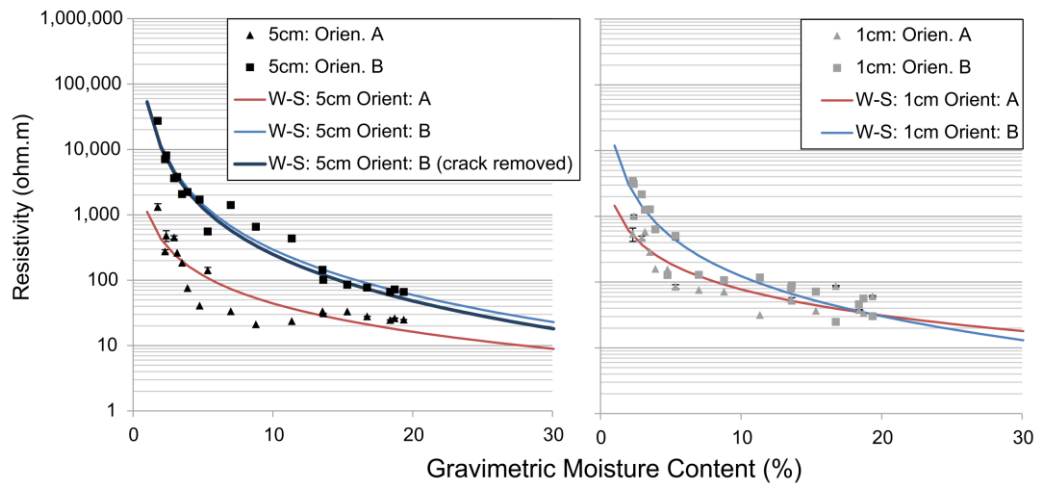


Figure 5.32 a). Trough 6 electrical resistivity – gravimetric moisture content model relationship for 5cm electrode array and including model excluding crack affected measurements. b). Trough 6 electrical resistivity – gravimetric moisture content model relationship for 1cm electrode array Modelled by Waxman-Smits Equation.

5.4.3 Waxman-Smits Modelling Error

Errors associated with fitting Waxman-Smits empirical relationship to actual laboratory observed data are presented in the form of root-mean-square error and percentage root mean square error. Data correlation is also presented as a means of quantifying laboratory data spread away from the model. Table 5.12 displays the error and correlation results of all the Waxman-Smits fitting curves to experimentally derived laboratory data.

Figures 5.33 to 5.35 below presents the percentage RMS errors for the Waxman-Smit models associated with both the 5 cm and 1 cm square array resistivity measurements. Percentage RMS errors associated with orientation A vary between square array size utilised and between soil sample lithology. Troughs 1, 2, 4 and 5 (Fig 5.33) have %RMS errors all less than 60% for both square array sizes of measurements of orientation A. The 1cm square array records %RMS errors almost double those associated with the 5cm array and for trough 1 these are 57.1% and 31.4% respectively. Trough 3 follows suit, its 1cm, A oriented models record %RMS errors higher than their 5 cm counterpart. Errors associated with Trough 3 – both 5cm and

1 cm square arrays – are considerably higher than models for all other troughed soils (Trough 6; 5cm orientation A being the only exception). Percentage RMS errors orientation A of trough 6 trend differently to the other 5 troughs, as it displays %RMS errors higher for the 5cm array than 1cm array.

	5 cm Square Array			1 cm Square Array		
Trough 1	Average	Orient. A	Orient. B	Average	Orient. A	Orient. B
RMS	29.68	8.47	55.65	17.41	16.30	19.45
%RMS	42.60	31.35	50.56	26.80	57.10	23.75
Correlation	0.89	0.77	0.88	0.91	0.83	0.94
Trough 2	Average	Orient. A	Orient. B	Average	Orient. A	Orient. B
RMS	34.17	38.52	31.63	55.01	34.06	84.35
%RMS	21.51	34.72	18.48	30.88	56.68	35.68
Correlation	0.85	0.76	0.90	0.92	0.90	0.91
Trough 3	Average	Orient. A	Orient. B	Average	Orient. A	Orient. B
RMS	12184.1	1755.01	22756.80	99151.3	64858.60	133553.0
%RMS	92.20	68.19	108.24	113.60	104.61	132.78
Correlation	0.90	0.87	0.91	0.87	0.87	0.87
Trough 4	Average	Orient. A	Orient. B	Average	Orient. A	Orient. B
RMS	46.18	56.74	37.02	65.94	73.34	60.36
%RMS	26.97	33.66	22.79	83.47	58.71	205.39
Correlation	0.86	0.80	0.91	0.82	0.84	0.78
Trough 5	Average	Orient. A	Orient. B	Average	Orient. A	Orient. B
RMS	103.03	60.62	145.81	210.81	60.67	347.97
%RMS	26.98	35.01	25.41	32.19	58.92	30.00
Correlation	0.85	0.84	0.85	0.87	0.73	0.89
Trough 6	Average	Orient. A	Orient. B	Average	Orient. A	Orient. B
RMS	1653.11	203.87	2994.26	266.02	144.34	412.00
%RMS	35.81	76.00	41.79	52.38	48.98	84.12
Correlation	0.93	0.88	0.94	0.97	0.89	0.98
Trough 6 w/o cracking	Average	Orient. A	Orient. B	Average	Orient. A	Orient. B
RMS	2008.86	203.87	3725.70	266.02	144.34	412.00
%RMS	31.49	76.00	33.90	52.38	48.98	84.12
Correlation	0.93	0.88	0.94	0.97	0.89	0.98

Table 5.12. Root-mean-square error, percentage root-mean-square error and correlation between laboratory measured resistivity and empirically modelled resistivity by Waxman-Smiths equation. Error and correlation results for measurement orientations A and B for both 5cm and 1cm square arrays. Error and correlation results refer to modelling performed on the average of two orientations (A & B) for each square array.

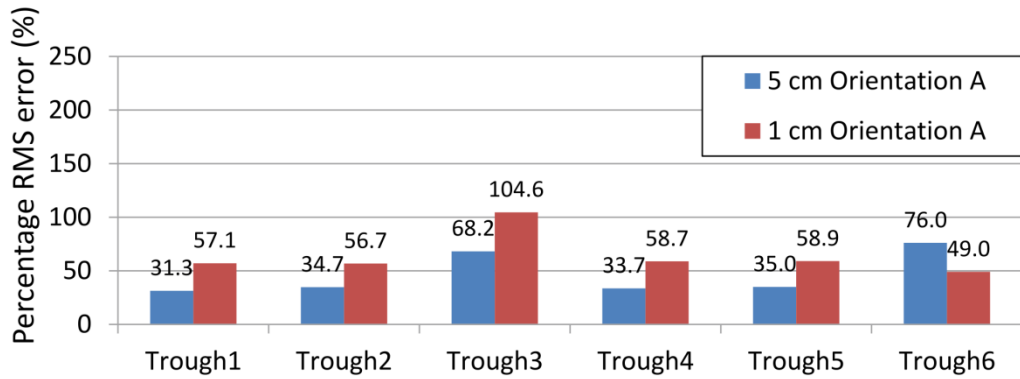


Figure 5.33. Percentage RMS error of modelled results from measured resistivity results using measurement orientation A. Presented are model errors associated with both 5cm and 1cm square arrays.

Percentage RMS errors for models associated with experimental resistivity measurements in orientation B are shown in Figure 5.34. Waxman-Smit models of troughs 1, 2 and 5 show %RMS errors less than 50%, with troughs 2 and 5 recording errors half that. All troughs except trough 1 provide lower %RMS values for the 5cm square array than the 1cm. Trough 1 is the exception, its 5cm value being 50.6% and its 1cm being just under half that value at 23.8% RMS error. Troughs 3 and 4 display seemingly high %RMS errors when compared to those provided by the other troughs. Trough 3 has relatively high %RMS errors at 108.2% and 132.8% for the 5cm and 1cm square arrays respectively. Trough 4 display great variation in the %RMS error values of its two empirical models. The model produced using the 5cm square array has an error of 22.8%, however, the error pertaining to the 1cm array is 205.4%, almost a factor of 10 higher. This could be attributed to processes taking place in the soil that the Waxman-Smit model does not account for such as electronic conduction within ironstone clasts. For example, coarse sand to fine gravel size ironstone clasts were present in the sample of trough 4.

The Waxman-Smit models produced by passing the arithmetic mean of resistivities derived from orientation A and B measurement orientations to the model produce %RMS errors as presented in Figure 5.35. For all but trough 1 it is the model utilising 5cm array resistivities which reports lower %RMS errors than the equivalent 1cm array model.

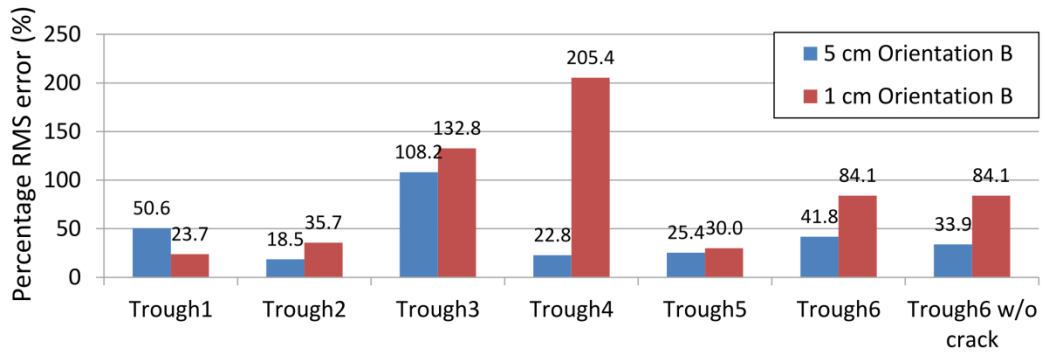


Figure 5.34. Percentage RMS error of modelled results from measured resistivity results using measurement orientation B. Presented are model errors associated with both 5 cm and 1 cm square arrays.

The clean sand of Trough 3 again produces the largest errors with 5cm and 1cm giving errors of 92.2% and 113.6% respectively. Clays of the Whitby Mudstone Formation contained within troughs 1 and 2 offer some of the lowest %RMS errors, all being less than 43%. The greatest variability between models with different array sizes is trough 4 which shows a difference of over 56%. By removing the cracking affected resistivities from the siltstone of trough 6 reduced the 5cm model error by 4.3%.

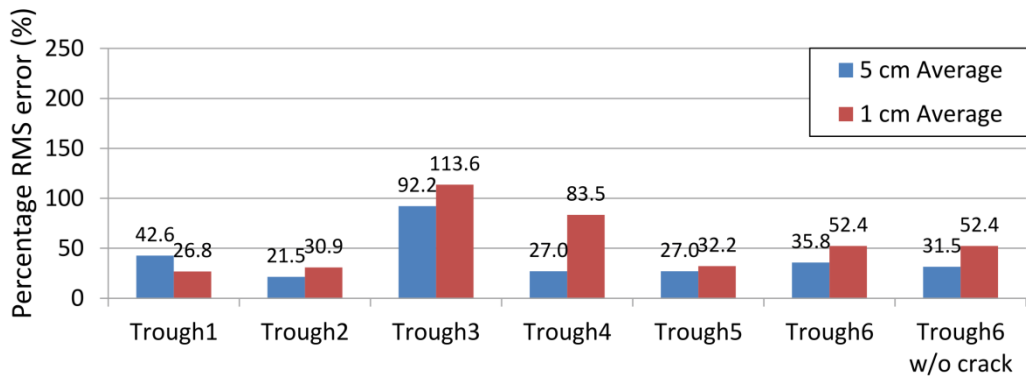


Figure 5.35. Percentage RMS error of modelled results from mean averaged laboratory measured trough resistivity data. Averaged resistivity of the two orientations A and B for each square array size. Presented are model errors associated with both 5 cm and 1 cm square arrays.

Trough 3 %RMS errors appear high (between 68.2% and 132.8%) because Waxman-Smit equation did not produce a successful fit to the laboratory data. Observation of the apparent misfit between laboratory data and the model makes it clear that the model is not appropriately applied in light of trough 3 lithology. This could be due to the Waxman-Smit equation not being

the most appropriate electro-petrophysical equation for this sample. Trough 3 is a fine, clean sand and so Archie's Law may be a more appropriate model to apply to this sample.

5.5 Soil Moisture Content , Matric Suction and Resistivity

In many regions of the world it is rainfall which is the most frequent landslide triggering mechanism (Corominas, 2000). It is widely assumed that landslides are triggered by rainfall (TRB, 1996), i.e. rainfall-induced, and landslides events can often be correlated with rainfall events; however, it is the changes in pore water pressures as a consequence of rainfall infiltration which are the cause of slope activations (Toll et al., 2011). When rainfall infiltrates, the suctional forces, or negative pore water pressures, which under normal conditions act to increase the strength and therefore stabilise the soil reduce the frictional component of the soils strength (Barnes, 2010). This reduction in soil strength can lead to slope instability initiation. Negative pore water pressures can dissipate, i.e. trend towards atmospheric pressure, in direct response to rainfall infiltration, or increase in response to soil drying during intense evapotranspiration. It is these seasonally and temporally transient near surface pore water pressure changes that, if sufficiently large can induce landslides (Toll et al., 2011). It is this transient soil property that is active at the Hollin Hill landslide system, in particular in the basal region of earthflows, and with that in mind quantification of the property through laboratory measurement was performed. It is desirable to investigate this soil property to better improve the understanding of this internal and dynamic landslide property that is a key factor in slope stability.

The soil moisture content retained in a soil under equilibrium at a given matric potential (ψ_m) is commonly expressed as a soil water characteristic curve or water retention curve (Tuller et al., 2005). Soil water retention characteristics are a function of soil structure and texture, including porosity, grain size and pore connectivity of partially saturated soils. Matric potential is attributed to capillary and adsorptive forces acting between three phases, gaseous, liquid and solid. O'Brien et al, (2004) reports that changes in pore

water pressures as a result of seasonal wetting and drying of swelling clays can be up to 500kPa close to the ground surface.

This section lays out an investigation into the relationship between soil moisture contents and subsequent matric suctions for two soil samples from cored samples from the field site. The laboratory method outlined and followed here to determine soil moisture-matric potential relationships works by applying a known positive pressure all around a soil. The porous pressure plate allows water to flow out of the sample until equilibrium exists between the force exerted by air pressure and the force by which moisture is being retained within the sample, the latter being ψ_m . At equilibrium there is an exact but opposite relationship between the air pressure (positive force) in the extractor and the soil suction, or potential (negative force).

This is somewhat different to the way in which moisture content and matric potentials equilibrate in the natural soils of the field site. The geological materials at the field site are subjected to weather and climatic processes such as rainfall and evapotranspiration, which temporally act to vary their moisture contents. As a function of seasonal moisture content variation, moisture retained in the soil must re-equilibrate with ambient pore water pressures (matric potential or, if negative suctions) resulting from capillarity and surface adsorption.

5.5.1 Methodology

Soil gravimetric moisture content and matric suction

Soil water retention curves were determined in terms of gravimetric moisture content via the pressure outflow method using Pressure Plate apparatus. Firstly, samples were selected to be loaded on to the pressure plate and have their water retention curves determined. Two samples of about 1 kg were extracted from the core within active flow material of BH5 and BH7 and their exact locations relative to landslide structure are shown in Figure 5.6, Section 5.2.1. The two samples originated from BH5 0.4m and BH7 1.3m and both were saturated by immersion in water for a week until visibly saturated. Six cylindrical plastic trays (10mm tall and 40mm wide) were weighed and placed on to the surface of the porous pressure plate apparatus. A small square of kitchen roll was placed into the tray to act as a

base for the saturated soil samples and sit between the porous plate and the sample yet still permit hydraulic connectivity between soil and plate. Three of the six trays were filled with the clay flow material of BH5 0.4m, the other three filled with sandier flow material of BH7 1.3m. Each filled tray was weighed and re-placed onto the plate, noting all weights, before closing and sealing the pressure plate apparatus.

Pressure Plate Apparatus

The 15bar pressure plate extractor is made by Soil Moisture Equipment Corp. in the USA and the apparatus is composed of a pressure vessel and lid, pressure plate cells, pressure inlet fitting, outlet ports, clamping bolts, burette and pressure gauges (Figure 5.36a). High pressure air is supplied to the extractor from a compressed air cylinder and not air compressor. Before closing the lid and performing an experiment, a small layer of water (150ml) was poured onto the already mounted plate cell in order to saturate the cell and improve water connectivity between the sample and the cell. The outflow pipe runs from the cell to the outerwall of the vessel, which then feeds into the burette (Figure 5.36c) to measure water outflow volume. The extractor is closed and the air supply is opened (Figure 5.35b) to increase the pressure in the extractor to the desired pressure (up to 15 Bar). Air initially rushed from the outflow pipe as air trapped within the cell plate rushes out under the increased pressure inside the extractor. Air is evacuated from the cell and water contained within the sample then begins to flow through the sample and through the porous cell plate. Upon travelling through the ceramic plate it then flows between the ceramic porous plate and the rubber membrane and out through the outflow pipe to collect in the measuring burette. Equilibrium is reached between the suction within the sample pores and the positive pressure in the extractor when the water level in the measuring burette stops rising. At this point the pressure is released, clamping bolts undone and the vessel opened. Samples are weighed and moisture loss recorded as soil gravimetric moisture content at the given cell pressure.

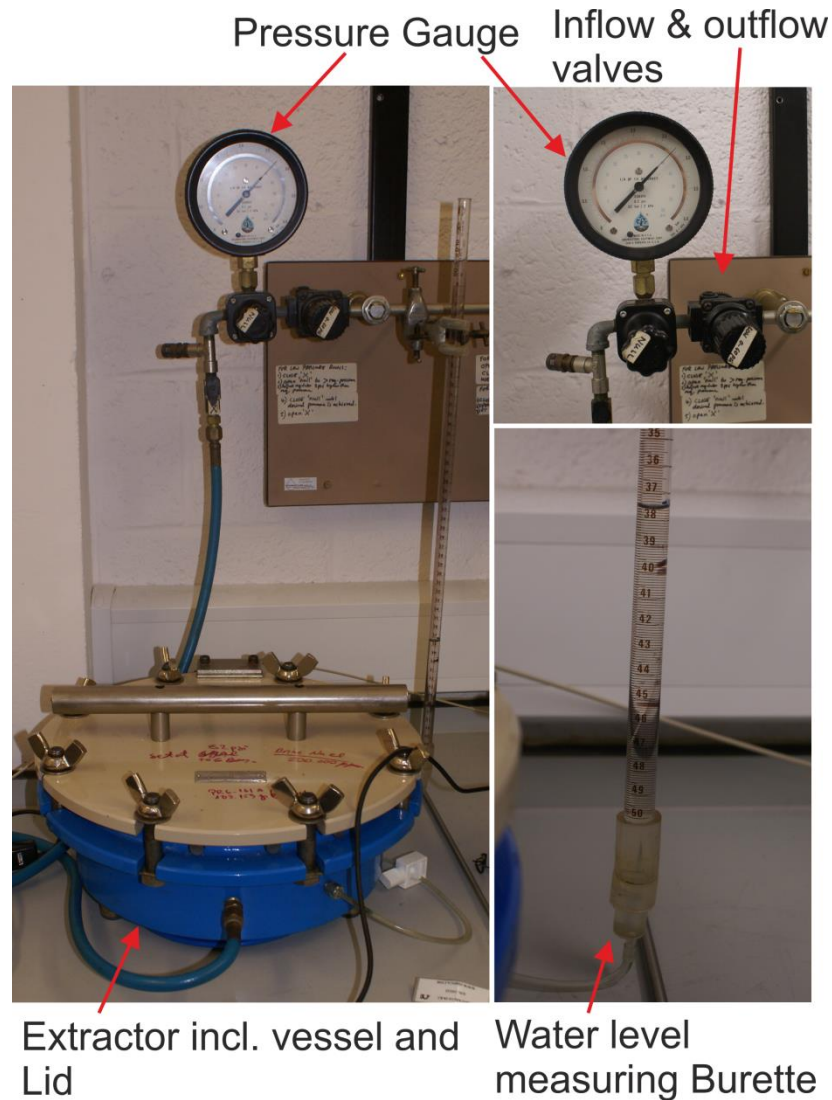


Figure 5.36. a) (left) Pressure plate apparatus as setup during soil moisture retention curve experiments. b) (top right) Pressure regulation gauge reading 40 PSI. c) (bottom right) Water level measuring burette for determining when soil moisture equilibrium is reached. Note: the marker pen lines indicating previous water levels while reaching equilibrium.

Electrical resistivity and matric suction

After determining the relationship between soil moisture and soil matric suction of earthflow materials, over a 1100kPa pressure range, moisture contents were converted to electrical resistivities with the aim of characterising soil matric suction – resistivity relationships. The procedure for determining soil moisture content-suction relationships is explained previously in this section, however, relating soil suctions with resistivities required implementing resistivity-GMC models outlined in Section 5.4 & 5.5.

Waxman-Smit models were produced for both of the soil types tested in the pressure plate. Models from troughs 1 and 3 – 5cm average resistivity data – were applied to convert the gravimetric moisture contents reached during pressure plate testing to electrical resistivity. Waxman-Smit model from trough 1 was applied to BH5 0.4m samples and the trough 3 model applied to BH7 1.3m. The reason for ascertaining the relationship between soil suction and electrical resistivity is to quantify how suctions dissipate or accumulate as water contents of soil samples change, i.e. to use resistivity as a proxy for suction. This process was upscaled and applied to the rainfall-induced landslide system at Hollin Hill, whereby slope soil moisture accumulation and subsequent dissipation of suctions is likely to be the principal cause of instability at the landslide.

5.5.2 Soil Moisture Retention Results

Soil moisture retention curves for two samples of earthflow were determined by pressure plate to ascertain their gravimetric moisture content-matric suction properties. Results of this experiment are presented in Figure 5.37 and the two samples, when compared, show several similarities and differences. Firstly, the clay rich flow material of BH5 has a much higher gravimetric moisture content range than the sand rich flow material of BH7, ranging between 30.51-49.17% and 10.67-18.66% respectively for the pressure range tested. Thus, indicating at the differing abilities to retain soil moisture under transient pressure conditions. Both samples reveal that moisture contents reduce relatively swiftly at low suctions (100-400kPa) but as suctions increase beyond 400-600kPa moisture contents incrementally reduce by much less. Using the sand of BH7 as an example; a suction increase from 100kPa to 300kPa results in a moisture content decrease of 2.41% change in GMC, as oppose to between 900kPa to 1100kPa which saw GMC drop by just 1.15%.

The range of resistivities exhibited throughout the suction measurements is markedly different between the two samples. The clay has relatively low resistivities of between 7.67ohm.m at high GMC to 13.65ohm.m at low GMC. In contrast, the sand of BH7 records much higher resistivities for the same

suction range between 98.38ohm.m at high GMC to 228.36ohm.m at low GMC.

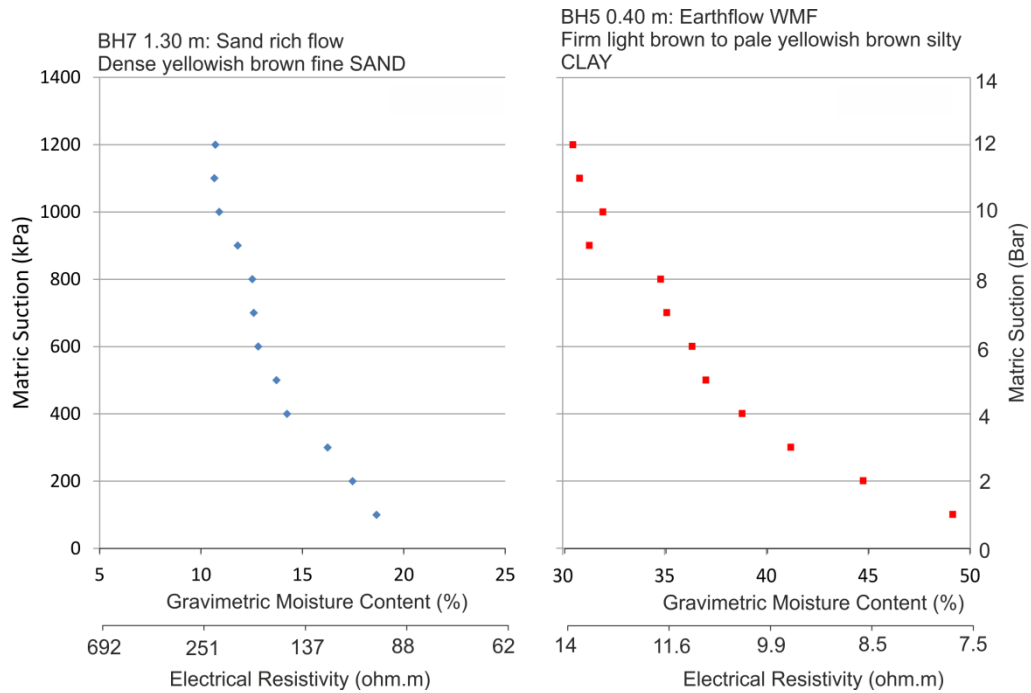


Figure 5.37. Soil moisture retention curve of two earthflow samples, extracted from Hollin Hill soil cores. a) BH7,1.30 m, and b) BH5, 0.40 m.

The results of soil moisture retention measurements reveal that the suctions pertaining to the sand rich flow material (Figure 5.37a) varies over a narrower range of moisture contents and therefore also electrical resistivities. This would in theory make suctions more visible as a field resistivity change in sandy material than clay rich material. Suction ranges within clays occur over a high range of moisture contents but a low range of resistivities. In order to monitor suction using ERT monitoring the system would have to be installed at a high resolution so as to achieve a high enough sensitivity to small resistivity ranges.

5.6 Discussion

Model Parameter Selection

When selecting appropriate Waxman-Smiths models to apply to field-derived model cell resistivity data the following considerations must be addressed:

The soil sample, from which experimental data originated before passing to Waxman-Smiths model must be taken from the lithological formation in

question. Put simply, the laboratory, resistivity-tested soil sample must originate from the same formation as the region of the field resistivity monitoring data to which it will be applied. This was achieved by producing detailed core logs – which included analysis of core electrical properties – and through development of a ground model Chapter 3.

Care must be taken to apply Waxman-Smiths models which have reasonably low percentage root-mean-square errors, as a low %RMS error infers that the empirical model applied is suitable for the task and that experimental resistivity data, which is passed to the model, is both valid and is not affected by other physical processes that the empirical formula implemented does not account for, such as desiccation cracking or electronic conductivity. Laboratory results of resistivity experiments show that several of the soil troughs exhibit evidence to suggest that additional processes, such as sample cracking and potentially electronic conduction, acted during the resistivity experiment.

Laboratory resistivity measurements were performed using two orientations, performed perpendicular to one another, one with current flow parallel to bedding, the other with current flow perpendicular to bedding. In addition to having laboratory results for two measurement orientations, the arithmetic mean of the two measurement orientations was also calculated. Taking into account that resistivity measurements were taken using two square array sizes – 5cm and 1cm – many options exist when deliberating which experimental resistivity dataset to apply the Waxman-Smiths equation to. Resistivity measurements utilising the 5cm square array almost universally produce models with the lower %RMS errors than their 1cm square array equivalent. That fact, coupled with the fact that the 5cm square array samples a greater volume of soil and is therefore more representative of the whole formation led the decision to select models derived from 5cm array resistivity measurements to be applied to field resistivity monitoring data.

In addition to selecting which resistivity measurement square array size to model when modelling resistivity–GMC relationships, the decision as to which resistivity measurement orientation to use, one of either orientations A, B or an arithmetic average of A and B had to be made. Of these three

options the application of orientation A and the average are the most appealing, the former due to field resistivity measurement geometry, the latter because of the inversion process.

It was highlighted earlier that resistivity measurements pertaining to orientation A were lower than orientation B because of preferential current flow parallel to lithological structure such as bedding and lineations. Field resistivity measurements are taken along 5 parallel lines which are installed, to within a few degrees, parallel to the maximum dip of the slope. The dip of lower and middle Lias formations are shallowly dipping by a few degrees to the north, i.e. into the slope. That slope feature combined with the fact that earthflow materials are deposited roughly parallel to the dip of the slope – borne from the fact that flows deposit onto former land surfaces means that when field resistivity surveys are performed injected current is assumed to flow along bedding surfaces and flow slip surfaces. This hypothesis would justify the implementation of resistivity measurements utilising orientation A, however, another argument exists for opting to use the mean averages of resistivities measured by orientations A and B.

Field measurements of electrical resistance are modelled and in doing so converted to electrical resistivity through the inversion process. The inversion process takes a series of surface measurements of current and subsequent potentials and builds a model of the subsurface structure which best-matches a subsurface which could exist based on the raw surface field measurements passed into the model. Inversion software however doesn't take into account inversion anisotropy; that is the resistivity variation due to the orientation of field measurements relative to subsurface structure. The inversion process builds a subsurface resistivity distribution and does not account for measurement orientation relative to features which might alter the measured potential in response to current injection, it models a bulk, average resistivity for each and every model cell. It would therefore not make final plots of model resistivity or gravimetric moisture content more accurate by passing orientationally specific data to an inverse model that does not accommodate the geometric subtleties of such data.

With the aforementioned in mind, the decision was made to apply Waxman-Smits models of experimental resistivity results using average resistivities pertaining to the 5 cm square array. Of the six samples experimentally tested for their electrical resistivity-moisture content properties two were selected to be applied to field resistivity monitoring surveys to convert volumetric domains of model resistivity into domains of gravimetric moisture content. Two models must be applied to field resistivity monitoring surveys, one to convert Whitby Mudstone Formation composed model cells, the other for Staithes Sandstone Formation composed cells.

Whitby Mudstone Formation (WMF) property conversion

The model derived from trough 1, average resistivity measurements from the 5 cm square array was selected to convert resistivity monitoring surveys to moisture content plots. The electropetrophysical model has a low percentage RMS error (42.6%) and is the closest of the experimentally tested samples to both the most active earthflow slip surface and the land surface. The latter signifies that the sample was extracted from temporally active WMF composed flow material and is the main reason for not selecting Trough 2, 5cm average resistivity model which has a lower %RMS error but is extracted from slightly deeper and therefore most probably a less active, if active flow. As the flow which the sample came from is relatively surficial (0.6m depth) the flow itself will be relatively immature and when compared with other, deeper flows is a suitable representation of the WMF as a whole. Waxman-Smits equation can be accurately applied to the selected troughed sample as cation exchange capacity data is available from close to the selected sample.

Staithes Sandstone Formation (SSF) property conversion

The decision as to which trough sample to apply was much more difficult for Staithes Sandstone Formation due to there being three troughs from which to choose from. The model produced from 5cm average resistivity results from trough 5 was selected to convert SSF composed model cells resistivities to GMC as the trough soil sample is silt and is not located near a significant structural boundary. Other troughed samples of Staithes Sandstone Formation were deemed unrepresentative of the formation either

because of lithological heterogeneity or a consequence of uncontrollable processes taking place on soil samples such as desiccation. Soil of trough 4 is particularly clay-rich and as the sample originated close to and a few centimetres below earthflow deposits some leaching and re-deposition of clay minerals may have occurred. Whereas, the siltstone of trough six experienced significant desiccation during the drying phase of resistivity experimentation, rendering much of the resultant resistivity-moisture content curve unworkable.

Trough Calibration

As the geometric factor of both array sizes is higher in the A-E orientation the geometry of the cell, its trough-shape, has less of an effect on current flow through the sample in this orientation than orientation B-F, i.e. current flow is less restricted. The 5cm array records geometric factors lower in both measurement orientations (A-E, B-F) than those of the 1cm array and is again attributed to the geometry of the trough cell. The 1cm array is much less affected by the geometry and proximity of the cell edges to the measurement electrodes.

The four saline solutions utilised during trough calibration possessed electrical resistivities which ranged over 1100Ω (10.8Ω to 1134Ω). This range was deemed sufficient even though the calibration range did not contain some of the more resistive, laboratory-measured soil samples, taken at the drier end of the soil moisture contents investigated. This issue is not believed to be a factor that might influence the validity of the investigation as its principal aim is to investigate the hill slope which activate due to rainfall infiltration. Therefore, the landslide is of most interest to our geophysical investigation when the slope is at or nearing water saturation and is there considerably wet, also, none of the lithological formations are ever dry enough to reach such a high resistivity in the field.

Electrical resistivity–moisture content relationships

The six experimental troughs all show that soil resistivity increases as soil moisture content decreases. This relationship can be accredited to a change in the manner in which electrical current flows through the soil samples as a function of soil moisture content. The geological materials tested here are

soil and weak sedimentary rock. They are granular and exist as a solid mineral assemblage phase with associated pore filled fluid, most commonly air and water. The flow of electrical current is predominantly within the pore fluid as movement of charged ions in the electrolyte. In clay rich soils there will also be a significant component of flow within the EDL of clay mineral surfaces.

At high moisture content, many flow paths exist along which current can flow, the resulting resistance to current flow is therefore relatively low. However, as the moisture content reduces and the number and volume of flow paths diminishes the ability of current to flow is hindered and is therefore accompanied by a relative increase in resistance to current flow.

Variability in soil electrical resistivity–moisture content response between soil samples is explained in terms of lithological diversity which exists between geological formations at Hollin Hill. Trough 3, which contains fine sand soil has the highest resistivity of the troughed samples, likely to be because it's voids drain easily when unsaturated. Sand grains are composed of quartz which is an electrical insulator and acts to inhibit current flow, thus, for a given sandy soil the dominant controlling factor on soil resistivity in a sand-dominated soil is moisture content.

Troughs 1, 2 and 4 contain soils whose principal soil type is clay (predominantly, Whitby Mudstone Formation) with minor constituents such as silt and fine gravels, all display markedly lower resistivities for a particular moisture content compared to the sand of trough 3. This trend is associated with the manner with which electrical current flows through clay. Generally, clays have a low resistivity because their mineralogy and structure permit two modes of electrical conductivity, within the pore fluid (in the same way a sand does) and the additional pathway through the electrical double layer, along the surface of clay minerals such as ilmenite and smectite. This two-phased mode of electrical charge transfer makes clay an efficient electrical conductor, however, at low moisture contents the mode loses efficiency and soil resistance increases. Resistivity measurements were performed on a much wider moisture content range on the clays of troughs 1, 2 and 4 relative to the granular materials (silts and sands) of troughs 3, 5 and 6

(36.3%, 29.6% and 22.6%, compared to 18.4%, 19.8% and 17.6% respectively). There are two reasons for this, firstly, the clay minerals occurring within the Whitby Mudstone Formation at Hollin Hill contain high proportions of swelling clays (approximately 33%, illite-smectite) and are hence capable of accommodating large quantities of fluid – electrically conductive electrolyte – within its network of clay particles. Secondly, clay minerals have a lower bulk density compared to sand, so for a given volume of both materials it is the clay sample which would weigh the least.

Experimental resistivity results show conclusively that resistivity measurements performed in orientation B record higher resistivities than equivalent resistivity measurements pertaining to orientation A. To illustrate the point, measured resistivities of trough 1, the 5cm and 1cm array sizes both exhibit orientation B resistivities substantially higher than 5cm and 1cm orientation A measurements. This difference varies between a factor of 2 at high moisture contents to a factor of 5 at the lowest moisture contents. This trend can be explained in terms of pervasive, natural soil structures such as bedding or laminations existing within the tested soils. The process of sediment deposition and subsequent bedding development can act to align platy minerals, such as clay minerals, and thus act as conduits or channels along which electrical current can flow more easily and with minimal disturbance. This is believed to be the mechanism taking place for measurements in orientation A, which consistently produce lower resistivities than orientation B. For electrical resistivity measurements orientated in orientation B current flow is effectively perpendicular to bedding, i.e. current is having to travel across these aligned platy minerals, rather than flow along them. The process of current flow across bedding acts to restrict current flow and results in much higher orientation B resistivities. Literature contains several examples where the issue of directional anisotropy of resistivity measurement has been encountered, most notably Busby, (2000) identified that rock mass heterogeneities manifested themselves in azimuthal apparent resistivity measurements as variation of apparent resistivity measurement. Apparent resistivity variations occurred with changes in measurement orientation relative to subsurface structure. A landslide monitored by both conventional profiles and by azimuthal resistivity

monitoring found that temporal polar resistivity variations informed about rock mass fractures and in particular how changes in water networks due to extending rock mass cracks manifest themselves (An et al., 2008).

5.7 Conclusion

The reason for performing laboratory resistivity measurements on a series of cored soil samples from the field site was to permit conversion of volumetric, site-scale, field resistivity monitoring data into a more meaningful format. The need to convert field resistivity models to volumetric images of gravimetric moisture content (GMC) came about to advance the understanding of landslide hydrogeological dynamics. In order to convert the field-measured electrical resistivities to GMC the most appropriate Waxman-Smit model must be applied to each of the lithological formations represented at the field site; one model for Whitby Mudstone Formation and one for Staithes Sandstone Formation.

Suitability of Methodology

The methodology utilised to make the laboratory electrical measurements, the board and pre-amplifier connected to the sample through four point measurement was suitable and appropriate for the task in hand. Trough calibration through application of a geometric factor and temperature correction enables a robust estimate of sample resistivity to be made, as field measurements of resistivity also take into account both geometry of electrical measurements during the inversion process and temperature effects post-inversion by normalising all field resistivities to an arbitrary temperature. Therefore the laboratory determined property relationships can be effectively applied to field resistivity results due to the similar ways in which both datasets have been treated.

However, the only obvious problem arose from inserting soil samples into troughs as this resulted in a change in sample stress state compared to *in situ*. Due to the lack of normal stress which effectively prevents cracks from opening within the soil some samples were greatly affected by bedding orientated cracking. This hindered the data collection process and affected the quality and relevance of measured resistivities. If I were to repeat these

experiments I would attempt to maintain the trenched soils in their in situ stress state while carrying out resistivity measurements. Actual field conditions are somewhat different to the laboratory conditions under which samples were experimented. For example, for many of the soils the whole range of soil moisture contents were recreated, from completely dry to approaching saturation.

Chapter 6

Geoelectrical Observation of Landslide Hydrogeological Processes

In this chapter the results from the geophysical monitoring campaign are presented. These results are presented in several formats, from raw transfer resistance data through to soil gravimetric moisture content. The beginning of this chapter contains the results of conventional slope monitoring data including *inter alia* rainfall, estimated evapotranspiration and piezometry. Subsequently, these results are integrated with a series of time-lapse resistivity outputs, each having followed a different processing route, and presented in a number of different interpretative formats. These datasets are integrated, analysed and interpreted together in order to assess critically the effectiveness and suitability of time-lapse 3D ERT as installed at this test site to observe the hydrogeological processes taking place in the slope. Following on from this results chapter is the final chapter which presents guidelines and recommendations for future use of time-lapse ERT in the context of shallow landslide monitoring.

6.1 Rainfall and piezometry monitoring results

Soil moisture input at the field site is measured and monitored by two methods. A rain gauge provides rainfall amount and event intensity and provides a means of quantifying moisture entering the subsurface. The second subsurface soil moisture monitoring method provides data about temporal ground water level variation. It also highlights how water level responds to weather conditions within two periodically active earthflow deposits.

6.1.1 Rainfall

Rainfall was monitored over a period of 4.5 years and data was provided predominantly by a site-installed rain gauge. Where rain gauge data was not available (before rain gauge monitoring began) rain fall information was extracted from hand-written weather logs recorded by the landowner. Rainfall data is presented from 01/01/2008 until 01/05/2013 and goes back

to several months before geophysical monitoring began, so that antecedent rainfall can be considered (Fig.6.1). Rainfall is displayed in several formats including weekly rainfall, effective weekly rainfall (weekly rainfall minus evapotranspiration effects), cumulative weekly rainfall and cumulative effective weekly rainfall.

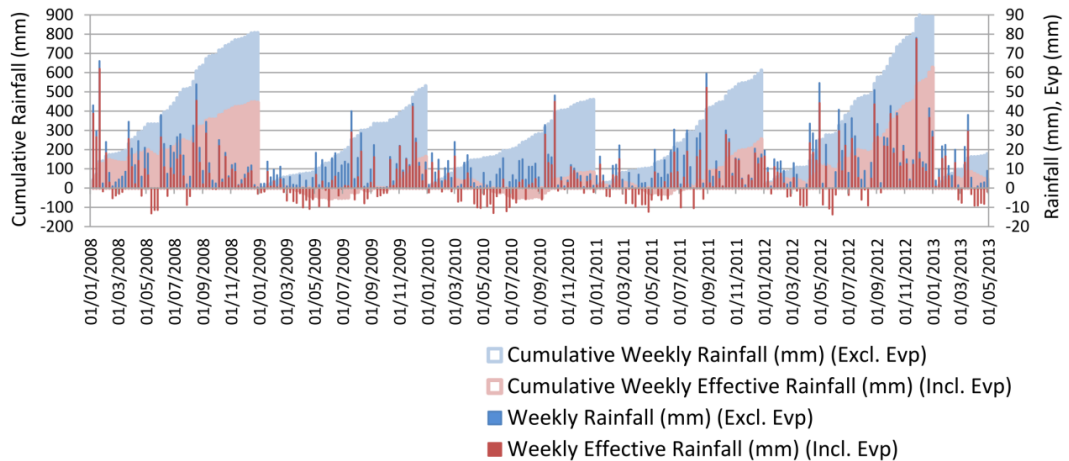


Figure 6.1. Rainfall data for Hollin Hill field site. Presented are both weekly total rainfall and weekly cumulative rainfall. Weekly effective rainfall is presented and was modelled using Hargreaves evapotranspiration model.

The first year of rainfall data, 2008, has several weeks of high rainfall. In particular, January begins with 3 weeks of 100mm of cumulative rainfall. The annual highest weekly rainfall occurs in January with 65mm falling in a single week. January is succeeded by 4 months of lower weekly rainfall, with weekly rainfall ranging between 1mm and 35mm between February and May. June had three weeks of zero rainfall before a period of prolonged weekly rainfall between July and October 2008. Over 350mm of rainfall fell within this four month period. Between October and the end of December rainfall intensity tailed off as ~110mm of rainfall fell during the period with the maximum weekly rainfall recorded as 19mm. Cumulative weekly rainfall over 2008 shows that over 800mm of rainfall fell and just over half of that entered groundwater as 440mm was calculated as cumulative weekly effective rainfall.

The year 2009 began in a similar way to how 2008 terminated, with low weekly rainfall recorded during the first two months of 2009. Only ~70mm of rain fell during this period and was followed by two months (March and April) of even less weekly rainfall, much of which was calculated to be negative

effective rainfall (- ~60mm) as evapotranspiration outpaced actual rainfall. June to September saw a relative increase in weekly rainfall as 240 mm fell but due to intense evapotranspiration during both this period and the two months preceding cumulative effective weekly rainfall remained slightly negative (~-20mm). The last two weeks of September 2009 and the first of October had zero weekly rainfall, this three week dry spell preceded 5 months (October 2009 – February 2010) of relatively high rainfall. 2009 had sufficiently less rainfall than 2008 with 530mm of total rainfall, of which 180mm was effective rainfall during this period. The relatively heavy rainfall during the last 4 months of 2009 contributed sufficient rainfall to cancel out the negative cumulative effective rain that took place in the first 6 months of 2009.

The following year, 2010, began with 3 months of intermediate intensity rainfall, with ~150mm falling. March to August was relatively dry month with 110mm of rain falling, which converted to a negative cumulative effective rainfall change of ~-100mm. The effects of evapotranspiration outpaced rainfall resulting in an overall reduction in cumulative effective rainfall to the point that negative rainfall conditions prevailed, indicating that moisture was being drawn from the soil. The end of Summer was marked by a month long period of high rainfall during September. 100mm of rain fell during this month and due to the reduced efficacy of evapotranspiration later in the year meant that negative cumulative rainfall gave way to positive cumulative effective rainfall. The final 3 months of 2010 were similar to 2009 however consistently less rain fell between October and December. 2010 saw 450mm of total rainfall which translated to only 95 mm of effective rainfall for the year, the annual lowest of the four and a half year monitoring campaign.

The year of 2011 began with two months of intermediate rainfall (between the highest and lowest weekly rainfall) as 90mm fell between January and February, representing a very similar trend to 2009 and 2010. March and April were particularly dry months as less than 10mm of rain fell and due to evapotranspiration effects negative cumulative effective rainfall prevailed once again, taking the value from 40mm to -30mm. May to August were somewhat wetter than the first four months of 2011 however evapotranspiration effects negated the infiltration potential of the majority of

the rainfall. Approximately 250mm of rain fell which equated to only 70mm of effective rainfall. During this period only a single week recorded zero rainfall. The first week of August was subject to substantial intense rainfall as 60mm fell, and is the third highest weekly rainfall of the whole rainfall monitoring period. The trend of intense and prolonged rainfall was continued for the rest of 2011 – and into 2012 – as the final 3 months of 2011 recorded 240mm of rainfall and 190mm of effective rainfall. August 2011 saw the beginning of almost constant high rainfall trend which persevered well into 2012 and only seemed to cease during the spring months of 2013. 2011 saw ~610mm of rain throughout the whole year, of that, 260mm was effective rainfall.

2012 started with a six week period of moderate rainfall with 90mm falling during that period and was succeeded by 6 relatively dry weeks where a tenth of the rainfall of the previous month fell and all was lost of evapotranspiration. April was particularly wet, each week consistently recorded weekly rainfall greater than 25mm and ranging between 25mm and 54mm. 140mm of rain fell during April, much of which contributed to the effective rainfall total (~90mm). May recorded 2 weeks of zero and one week of 22mm rainfall and precedes a very wet, 7 month period from May until the end of 2012. This seven month period saw 620mm of rain and 500mm of effective rainfall, more than the previous three years put together. This period also records the highest weekly rainfall, 78mm, and occurring in late November.

Rainfall monitoring took place until the end of April 2013, these four months started with three months of intermediate amounts of weekly rainfall of between 10mm and 38mm (with 2 weeks of very low rainfall of between 2mm and 6mm). Rainfall monitoring during the month of April showed that very little rain fell, totalling ~20mm, meaning that effective rainfall was negative during the final month of monitoring.

6.1.2 Piezometry

Two piezometers were installed within the Hollin Hill landslide, located geographically within the earth flow region of the system and their installation depths are shown in Figure 4.6, of Chapter 4.

The water table results from the western piezometer are presented in Figure 6.2b below with the piezometer level represented by the thin blue line, and the other lines represent the ground surface and inferred shear surface depth. The piezometric level can be seen to range between lows of 77.0-77.2m, for example between 5/2010 and 12/2010 and highs of 78.7-79.0m as occurred between 10/2009 and 4/2010. The piezometer of the western flow region was installed and began logging hydraulic head in the subsurface on 24th September 2009 and for the first two-months piezometric level was relatively low, fluctuating around 77.0m, relative to AoD. This relative low was followed by 5 months of relative piezometric high, between December 2009 and May 2010, with the level consistently up to 2 meters higher than the relative low of the previous two months. After the piezometric high the level rather sharply reduced over a period of three to four weeks, decreasing rapidly initially before tailing off as piezometric low was once again reached. From June 2010 and late November 2010 a period of low piezometric level at 77.2m prevailed.

Superimposed onto this piezometer low were three piezometer level spikes, both rising by just over a meter to 78.3m and were most probably correlated with sudden, short rain events. The ensuing four months, December 2010 to April 2011, were shown to contain three broad piezometric peaks, each of between 79.1m and 79.3m. Located between these peaks the piezometric level briefly reduced by between 1m and 1.5metres before swiftly spiking back to another piezometric high. Following this period of relative piezometric high and as occurred during May 2011, the piezometric level sharply decreased over a period of a up to a month at the start of the year's warmer months.

For the next twelve months, from May 2011 and April 2012 the piezometric level was very changeable, rising sharply over a period of a day before decreasing suddenly back to baseline level (77.2m) or near that level. This process took place up to 14 times during this one year period, that saw the piezometric level rise to between 78.0m and 78.9m. The next four months, from April 2012 until October 2012 was a period characterised by more flashy, sudden piezometer highs followed by lows, however the highs associated with this period were higher and more sustained, for example the

high of May 2012 lasts a month, rose up to 79.3m and was seemingly composed of three individual peaks superimposed onto one another. There were four of these broad piezometer highs within this period and the piezometer lows did not reach baseline (77.2m), instead they bottomed out at 77.4-77.5m. The final phase of piezometer monitoring, between October 2012 and the end of 2012, was characterised by consistently high piezometric level ranging between 78.8m and 79.4m, and represented some of the highest levels recorded throughout the monitoring period.

The monitoring results from the piezometer installed in the eastern flow deposit region of the landslide system were represented by the red line on Figure 6.2a. As with the western flow piezometer monitoring began 24th September 2009 and the initial piezometer level was lower than the rest of the monitoring period. This initial low piezometer level could be a result of the drilling process interfering with the ground water level or the removal of overburden creating an area under suction (Barnes, 2007). The initial six weeks of monitoring show that the water level slowly but uniformly increased from 76.6m to 77.0m, before suddenly increasing by a metre to 78.0m in the space of a month. Piezometer level then sat at 78.0m for over five months, during that period the water level fluctuated by +/- 0.2m. Beyond April 2010 the water level gradually and uniformly decreased by 0.7m (to 77.3m) until a short period was reached where no data is present, between September and November 2010.

November 2010 saw the level once again gradually and uniformly increase from 77.5m to 78.0m it then remained constant for several winter months, from December 2010 until March 2011. The piezometer level then gradually lowered during the Spring months until the Summer month of June 2011, where the level can be seen to then sit, near constant at 77.5m until September 2011.

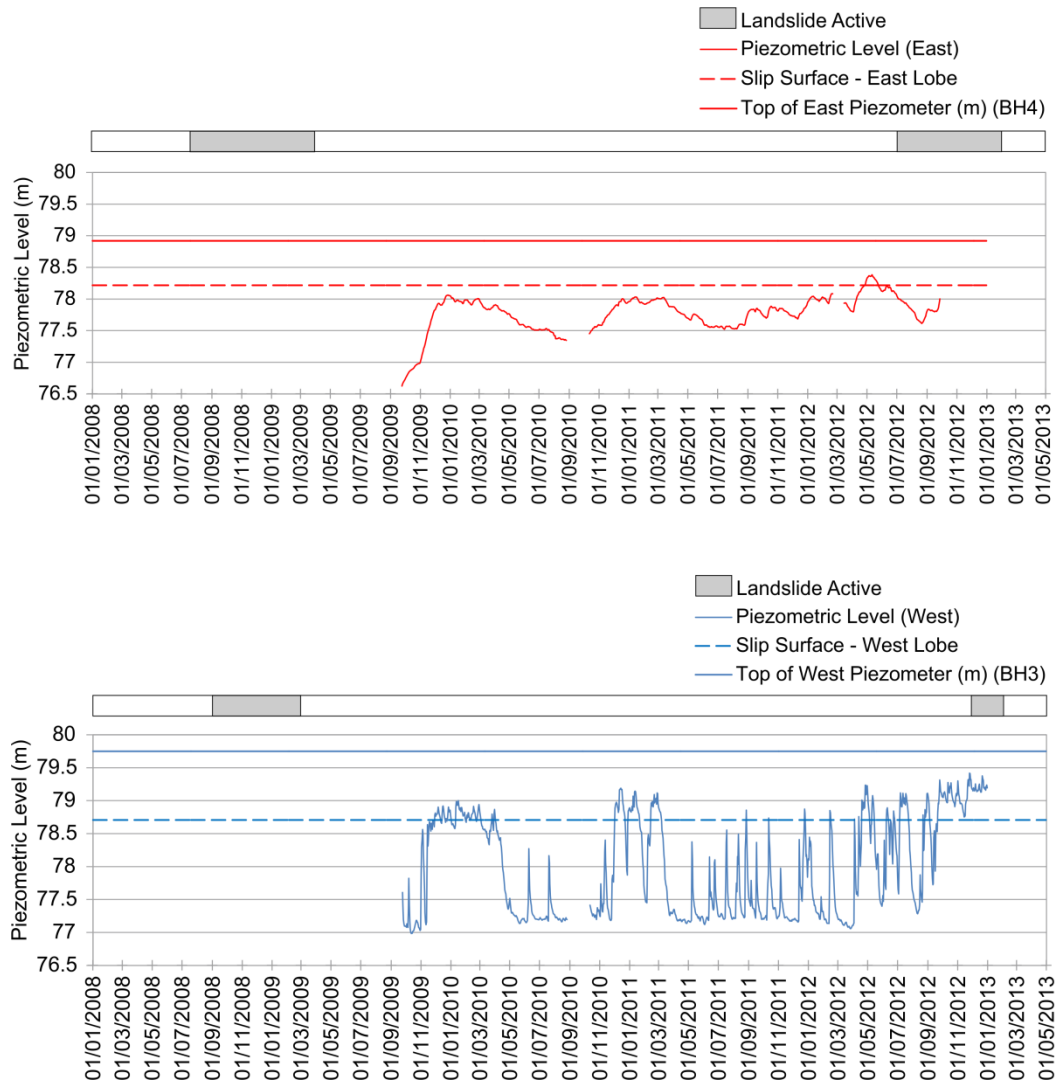


Figure 6.2. a.) Piezometric levels within eastern earth flow deposits throughout monitoring period at Hollin Hill field site. Locations and depths of piezometers are displayed in Chapter 4 and are relative to AoD. b.) Piezometric levels within western earth flow deposits throughout monitoring period at Hollin Hill field site.

For the next 4-5 months the piezometric level rose to a 78.1m, however on this occasion the level rose far more sporadically and non-uniformly, dipping by up to 0.2m for two week periods during October and December 2011. The level remained at 78.0m from January 2012 until the end of March, where the level dipped for a three week period before temporarily rising even higher – April 2012 saw the highest level of the eastern flow deposit throughout the monitoring period – to 78.4m. Following the week long piezometer high the level gradually lowered from May 2012 until mid-August 2012 to 77.7m. Late August to September 2012 saw the level increase by 0.3m to 78.0m, beyond early October the level can be seen to end abruptly.

This is because between 28th September 2012 and 9th January 2013 the flow region of the landslide system activated and sheared the piezometer casing, making it impossible to extract the downhole piezometer from the subsurface to download its monitoring data.

6.1.3 Environmental Input Correlations

In order to analyse the interplay between effective rainfall infiltration and piezometric level response a comparison was made between the two datasets. Figure 6.3 shows the piezometer level response as a result of effective rainfall penetrating the subsurface. As can be seen, considerably more rainfall fell during the last few months of 2009, and between April and the end of 2012. 2011 experienced more rainfall than 2010 which appears to have only one period of considerable rainfall, September to November 2010.

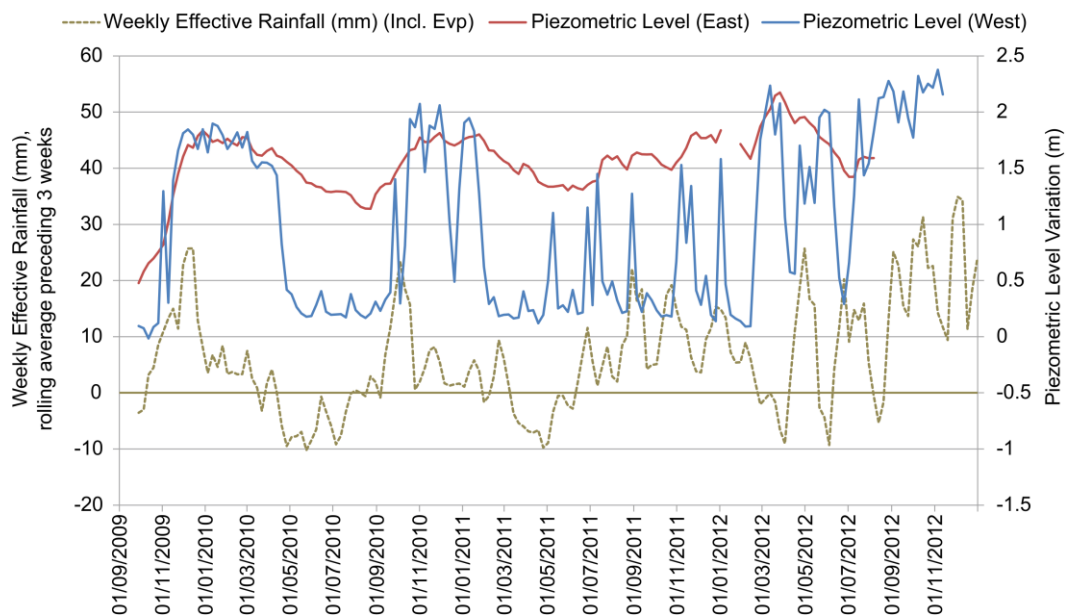


Figure 6.3. Rolling averaged effective rainfall and piezometric levels at Hollin Hill. Correlation coefficients were calculated between east and west piezometric levels and the preceding three week rolling average effective rainfall. Correlation coefficient between effective rainfall and the western piezometric level is 0.18 and the eastern piezometric level is 0.16. These values suggest weak correlation between weekly effective rainfall and piezometric levels.

6.1.4 Weekly averaged air temperature

Raw transfer resistance monitoring results are presented alongside rainfall and weekly averaged air temperature as these datasets can aid interpretation. The months between the temperature peaks record air temperatures between the two extremes. At the field site weekly averaged air temperatures reach a maximum of 15 – 18°C, conversely, the minimum averaged air temperature is between 0 and -2°C.

6.2 Transfer Resistance

This dataset contains raw, unprocessed field transfer resistance measurements spanning from 13th July 2008 until 24th February 2013. A wide variety of measurement geometries were implemented in each ERT survey and along each of the 5 lines. The extracted resistance measurements analysed in this section pertain to the narrowest electrode geometries, i.e. where both potential and both current electrodes are closely located to each other, and are sensitive to near-surface resistance variations. These measurements are termed $a=1, n=1$ where, $n=1$ means that the two potential electrodes (and two current electrodes) are separated by 1 electrode spacing, along the 5 lines the electrode spacing is 5m. The distance between the inner most potential electrode and the innermost current electrode is also 1 electrode spacing. Therefore, the width of the measurement array $a=1, n=1$ is 15m and the medium depth of investigation of $a=1, n=1$ resistance measurements is 1.90m. Resistance measurements pertaining to $a=1, n=1$ were chosen to look at in detail as the landslide processes of interest are taking place within this depth range in the near surface.

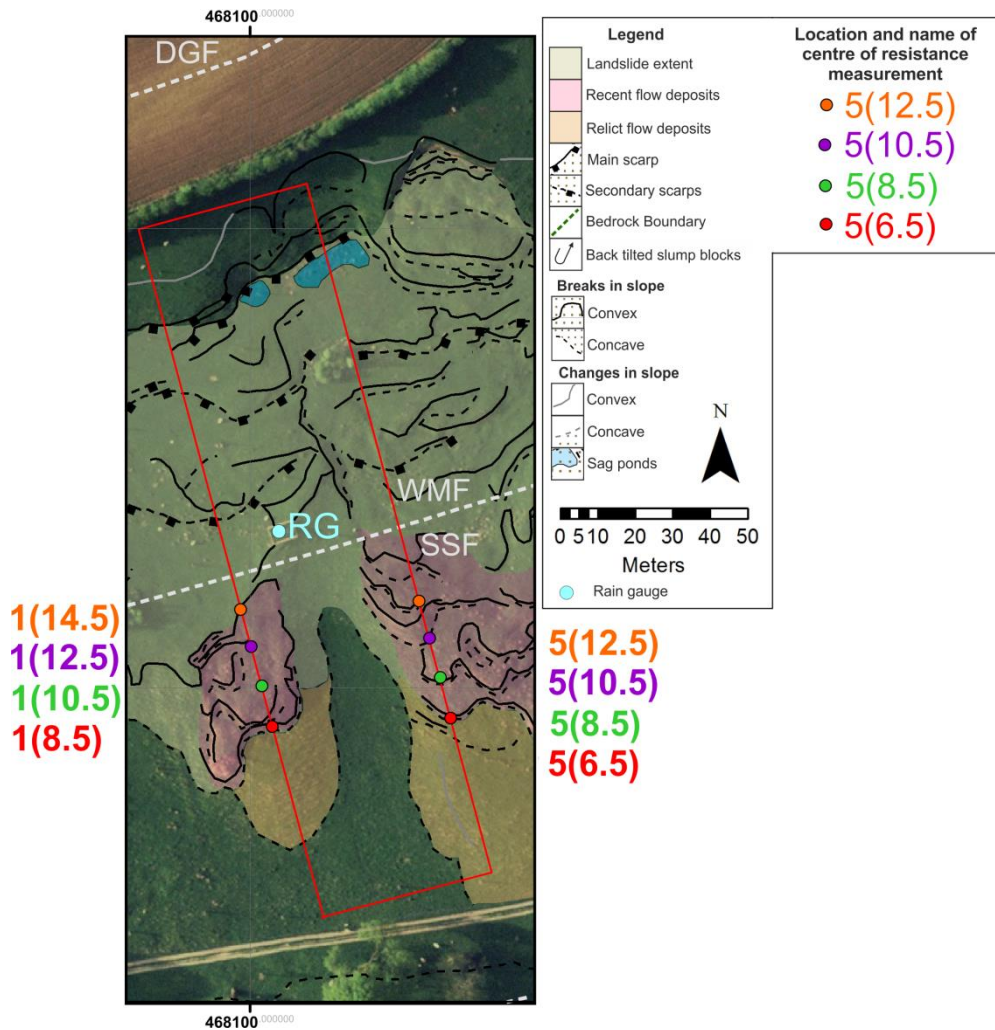


Figure 6.4. Plan of electrode locations and resistance measurement dipole locations. Annotated on the plan are the locations of dipole centres of resistance measurements analysed within this chapter.

6.2.1 Transfer Resistance Results

Resistance measurements relate to measurement dipoles located within the periodically active eastern earthflow region of the landslide system as shown in Figure 6.4.

Resistance monitoring measurements taken at the western earthflow region of the landslide system are displayed in Figure 6.5. Four resistance dipole measurements are presented in the figure and each measurement is colour coordinated, the red points on the transfer resistance graph represent dipole measurement 1(8.5), while the purple points represent dipole measurement 1(12.5). Displayed alongside transfer resistance is daily average air

temperature (central plot) and rainfall. Rainfall is presented in several formats, both total and effective rainfall, as well as annual cumulative rainfall.

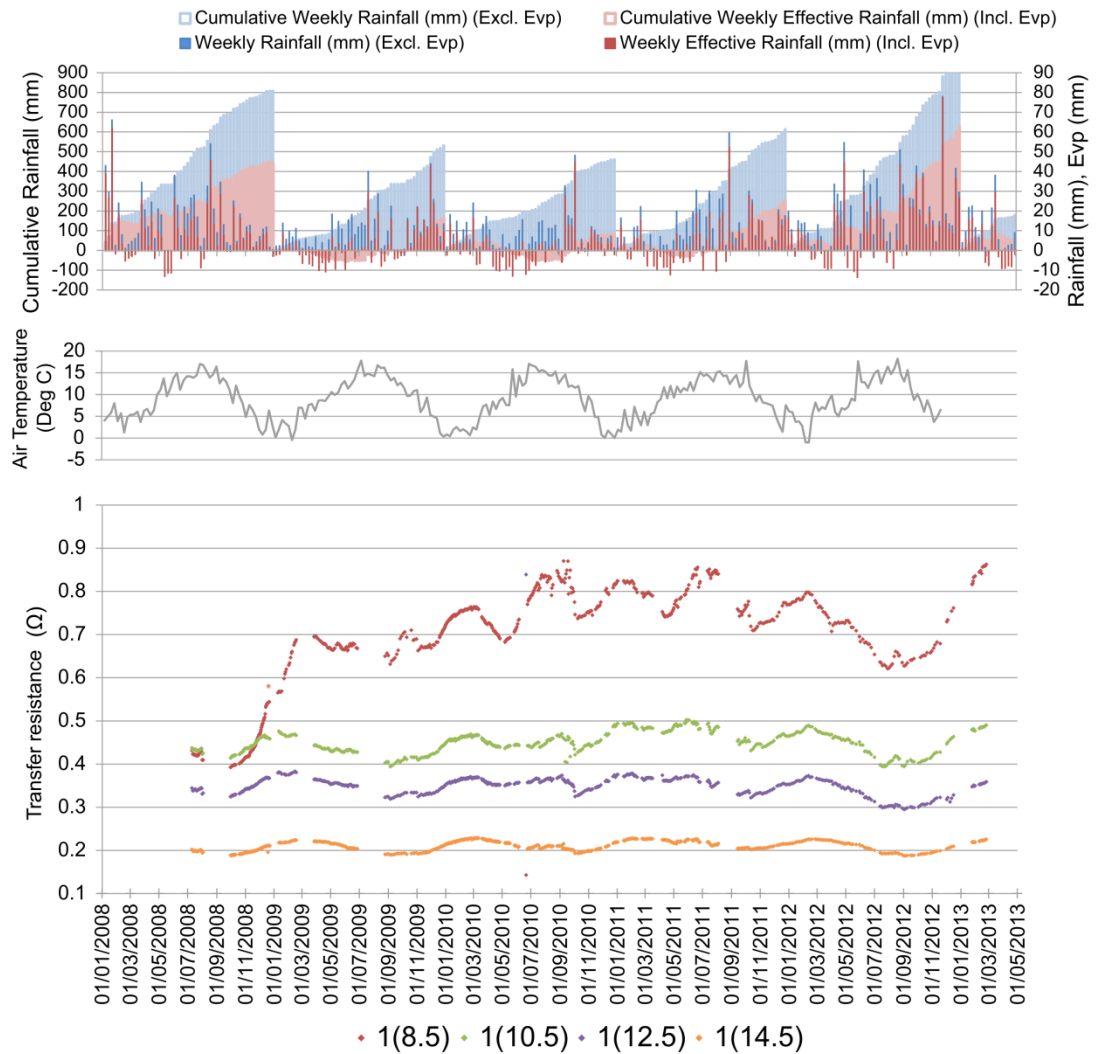


Figure 6.5. Transfer resistances extracted from ALERT monitoring campaign between 07/2008 and 02/2013. Data pertain to Line 1 of monitoring array and are from western earthflow region of landslide system.

In July 2008, dipole measurement 1(8.5) records a resistance of 0.42Ω before reducing to 0.4Ω by October 2008. Over the next 5 months until March 2009 this dipole sees its resistance gradually increase to 0.7Ω where it varies very little until August 2009 where it can be seen to rise and dip again over the period of two months. During the winter 2009 the resistance increases steadily up to 0.77Ω before lowering again to 0.7Ω by April 2010. April to August 2010 is marked by a steady increase in resistance from 0.7Ω to a peak at 0.87Ω . For the next three months between August and

November 2010 resistances decrease to 0.72Ω . The next 6 months – between December 2010 and May 2011 – resistance gradually rises to a peak of 0.82Ω then lowers back to 0.72Ω . The next seven months sees the resistance rise once again by 0.10Ω to 0.87Ω (just as it did the previous year during the same months, May and November). Resistance then steadily increases by 0.07Ω from 0.72Ω to 0.79Ω between November and March 2012. Between March 2012 and August 2012 the resistance decreases from 0.8Ω until reaching a low of 0.62Ω . The next three months sees the resistance slightly rise by 0.04Ω before increasing much more abruptly from November 2012 until the end of the monitoring period early March 2013.

The other three plotted measurement dipoles – 1(10.5), 1(12.5) and 1(14.5) – all show very similar trends throughout the monitoring period. Dipole 1(10.5) has the highest initial resistance of 0.43Ω , measurement 1(12.5) has the next highest resistance at 0.33Ω and 1(14.5) has the lowest at 0.19Ω . All dipoles (green, purple and orange coloured points) initially decrease by $\sim 0.02\Omega$ between July and September 2008. Between October and January 2009 resistance increases and can then be seen to decrease over the next six months until September 2009. Resistances then remain stable for a two month period, from October until November 2009. December 2009 and February 2010 sees resistances pertaining to dipoles 10.5, 12.5 and 14.5 of line 1 rise by up to 0.04Ω before decreasing to just higher than resistances recorded during November 2009.

Resistances again remain relatively constant for four months, between May and September 2010. Resistances decrease abruptly during September 2010 and can be attributed to a four week period of intense rainfall taking place during that month. October 2010 to January 2011 is a period during which resistance increases for all three dipoles, with dipole 1(14.5) showing the smallest resistance increase and dipoles 1(10.5) and 1(12.5) increasing by a similar amount. Resistance values for the period between January and May 2011 remain almost constant with dipoles 1(10.5) and 1(12.5) slightly decreasing before all three dipoles appear to rise and fall again between May and August 2011. A small gap in resistance data exists between the second week of August until the second week of September 2011. The measured resistances then increase almost linearly for the next five months

until March 2012 where resistances begin to decrease at a similar rate until July 2012, with dipole resistances reducing by between 0.1Ω and 0.3Ω . August 2012 until October 2012 sees resistances remain reasonably constant, except dipole 1(10.5), which rises and dips slightly during this period. November 2012 until the end of the monitoring period (March 2013) sees resistances increase, with dipoles 1(10.5) and 1(14.5) increasing by 0.2Ω and 0.9Ω respectively.

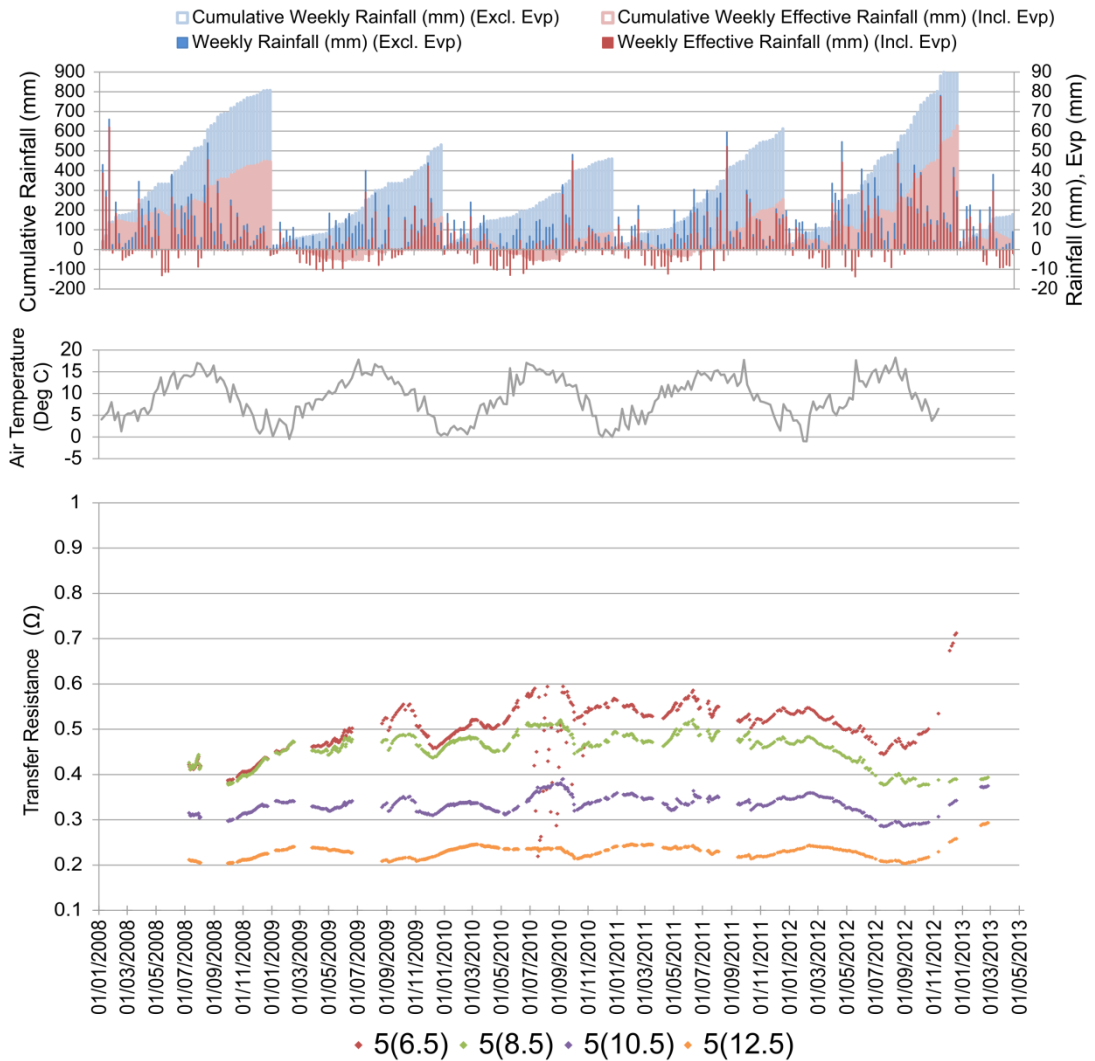


Figure 6.6. Transfer resistances extracted from ALERT monitoring campaign between 07/2008 and 02/2013. Data pertain to Line 5 of monitoring array and are from eastern earthflow region of landslide system.

Transfer resistances pertaining to line 5 of the resistance monitoring array installed at Hollin Hill are presented in Figure 6.6. Each of the four dipole measurements located within periodically active earthflow are colour

coordinated, red, green, purple and orange, and the exact locations of the dipoles is shown in the basemap, Figure 6.4.

Transfer resistances measured by dipoles 5(6.5) and 5(8.5) are both the highest at 0.42Ω and dipoles 5(10.5) and 5(12.5) recorded initial resistances of 0.31 and 0.21 respectively. October 2008 commences with resistances of all four dipoles increasing until late December 2008 and early January 2009. January to May 2009 sees resistances decrease by a small amount ($\sim 0.01\Omega$) before dipoles 5(6.5), 5(8.5) and 5(10.5) begin to rise, peaking between November 2009 and December 2009. A data gap of 9 weeks is present between July and August 2009. Dipole 5(6.5) rises sharply during September and October 2009 to peak resistance values of 0.57Ω . Dipoles 5(8.5), 5(10.5) and 5(12.5) exhibit a similar peak in resistance in October, however, it is much less substantial when compared to 5(6.5).

The resistance peak decreases over a period of 2 months for dipole 5(6.5) and drops by 0.9Ω to 0.46Ω . The other three dipoles see the resistance reduce over a shorter time frame (~ 1 month) however these measurements reduce by a much smaller amount. All four dipoles then rise and fall between December 2009 and May 2010, with dipoles 5(6.5) and 5(8.5) rising and falling sharply by as much as 0.05Ω , however, dipoles 5(10.5) and 5(12.5) rise and fall in a much more subtle manner. The warmer months of 2010 (between May and early September 2010) are met with a resistance rise of three dipoles, 5(6.5), 5(8.5) and 5(10.5), dipole 5(6.5) has seemingly erroneous scatter in resistance values at the height of the summer and could be attributed to electrode contact issues. Dipole measurement 5(12.5) remains constant during these months.

The rainfall event of late September/early October 2010 results in transfer resistances reducing during the duration of the prolonged rainfall event. Dipoles 5(6.5) and 5(8.5) decrease by the most, $\sim 0.08\Omega$, whereas dipole 5(12.5) decreases by only 0.02Ω . Winter 2010 sees resistances of all dipoles increase, peaking early January, where they then steadily decrease once again and reach a low May 2011. Resistance of all dipoles except 5(12.5) increase for the next two months, May and June, and occurs at a time when air temperature is reaching its annual high. While the other three dipole

measurements of the eastern earthflow exhibit increasing resistances, resistance values taken by dipole 5(12.5) remain relatively constant at 0.29Ω . July to early November 2012 is a period where resistances generally decrease, dipole 5(6.5) decreasing by 0.08Ω to 0.51Ω and 5(12.5) decreasing by 0.01Ω to 0.22Ω . May 2012 until August 2012 sees the resistance measured across all four dipoles decrease and occurs at a time when both air temperatures are rising and initiation of a period of high and intense rainfall March 2012.

Resistances measured during September 2012 remain low and constant as dipoles 5(8.5) and 5(10.5) recorded resistances of 0.39Ω and 0.28Ω respectively. The low resistances measured by dipoles 5(8.5) and 5(10.5) are reminiscent of the resistances observed by the system at the start of the monitoring campaign during August and September 2008. Resistances pertaining to dipole 5(12.5) fluctuate less and similar resistance lows are seen on four occasions, September 2008, September 2009, October 2010 and September 2012. Dipole 5(6.5) initially mirrors resistances measured by 5(8.5) until they deviate from one another July 2009. From then on, an almost constant resistance difference exists between the two dipole measurements, and this apparent offset causes the resistances of 5(6.5) to not reduce to the lows observed September 2008.

For the rest of the resistance monitoring campaign resistances of all four dipoles appear to change abruptly, dipole 5(6.5) increases from 0.47Ω to 0.72Ω over a period of four months. Equally, dipoles 5(10.5) and 5(12.5) increase by almost 0.1Ω . This increase in resistance occurs while the earthflow region is active and is attributed to electrode movement and is explained in more detail Section 6.5.

6.3 Temperature Corrected Transfer Resistance

Raw transfer resistance field measurements were corrected for the effects of subsurface temperature distribution. The process of removing temperature effects from resistance data is described in Section 4.3.2. Raw transfer resistances, described in the previous Section (6.2.1) of this chapter are presented as resistance (Ω). However, temperature corrected resistances of

individual measurement dipoles are presented as resistance ratio, relative to a baseline resistivity survey, performed 13/07/2008 (Chambers et al., 2013). The decision to display temperature corrected resistance data normalised to a baseline survey is to make temporal resistance variation trends much more apparent (compared to plotting absolute resistances) and allows effective comparison between adjacent dipole measurements.

6.3.1 Temperature Corrected Transfer Resistance Results

The temperature corrected (TC) monitoring results from line 1 are presented in Figure 6.7. The same dipole measurements plotted in Section 6.2.1 are presented here alongside piezometric level, landslide activity bar and several formats of rainfall. Annotated on to the piezometer plot are active shear surface depth and ground height (AoD).

Analysis of Western earthflow region

Resistance ratios begin – as would be expected – at unity but after a two month data less period between August and September 2008 ratios begin to dip below zero, indicating a decrease in TC resistance relative to baseline TC resistance. This slight reduction in TC resistance comes at a time when the earth flow region is active and after and during a period of high rainfall. After a two week period of negative effective rainfall at the beginning of July are two months (August and September 2008) of intense and prolonged rainfall, with over 140mm of rainfall. The intense rainfall period and the reduction in resistance ratio coincide in the lead up to western earth flow activation during September 2008 (Section 3.4.2, GPS survey of peg array). The lack of piezometer data until installation of piezometer casing and piezometer in October 2009 means that ground water behaviour during earth flow activation cannot be observed for this activation event. The western earth flow toe is active for a five month period, between late September 2008 and March 2009 and dipole 1(8.5), located at the flow toe, shows this activation event as an abrupt increase of resistance ratio (and absolute resistance), from 0.95 to 1.49. This increase resistance ratio trend during activation is attributed to displacement of electrodes utilised in the 1(8.5) resistance measurement.

During the landslide active period TC resistance ratios of the other three dipoles 1(10.5), 1(12.5) and 1(14.5), which are located above the displacing electrodes, increase from ~0.96 to ~1.02. These increases occur at a time when rainfall intensity was less intense, between October 2008 and February 2009. Landslide suspension occurs late February to early March 2009 and coincides with the beginning of a five-month period of predominantly negative effective rainfall during spring and summer months. Between March and May 2009 TC resistance ratios (after a short hiatus in resistance monitoring data) remain constant, except 1(8.5) which decreases from 1.5 to 1.45. Dipoles 1(8.5), 1(10.5) and 1(12.5) display resistance increases between May and mid-June 2009, with dipole 1(14.5) following trend early June.

A gap in resistance data between July and late August 2009 exists making it impossible to continue tracking the aforementioned resistance ratio increases. Late August and September 2009 sees those TC ratios pertaining to dipole 1(8.5) increase by 0.08 to 1.69 while the other three dipoles remain either constant (1(14.5)) or increase by 0.03 (1(10.5)). This period experienced very little rainfall and so negative effective rainfall dominated and piezometric levels are shown to fall. Rainfall intensity is higher for the next three, winter months as over 160mm of effective rain fell and piezometric levels rise by 1.80 m to one of their highest levels during the monitoring period. TC ratios of all dipoles decrease in response to rainfall with dipoles 1(10.5), 1(12.5) and 1(14.5) decreasing by ~0.06 and 1(8.5) decreasing by almost 0.2. It should be noted that resistances pertaining to 1(8.5) do not return to unity after the episode of electrode displacement of 2008.

Piezometer level fall by 0.6m from mid-January 2010 and is in response to less intense rain falling compared to the previous three month period.

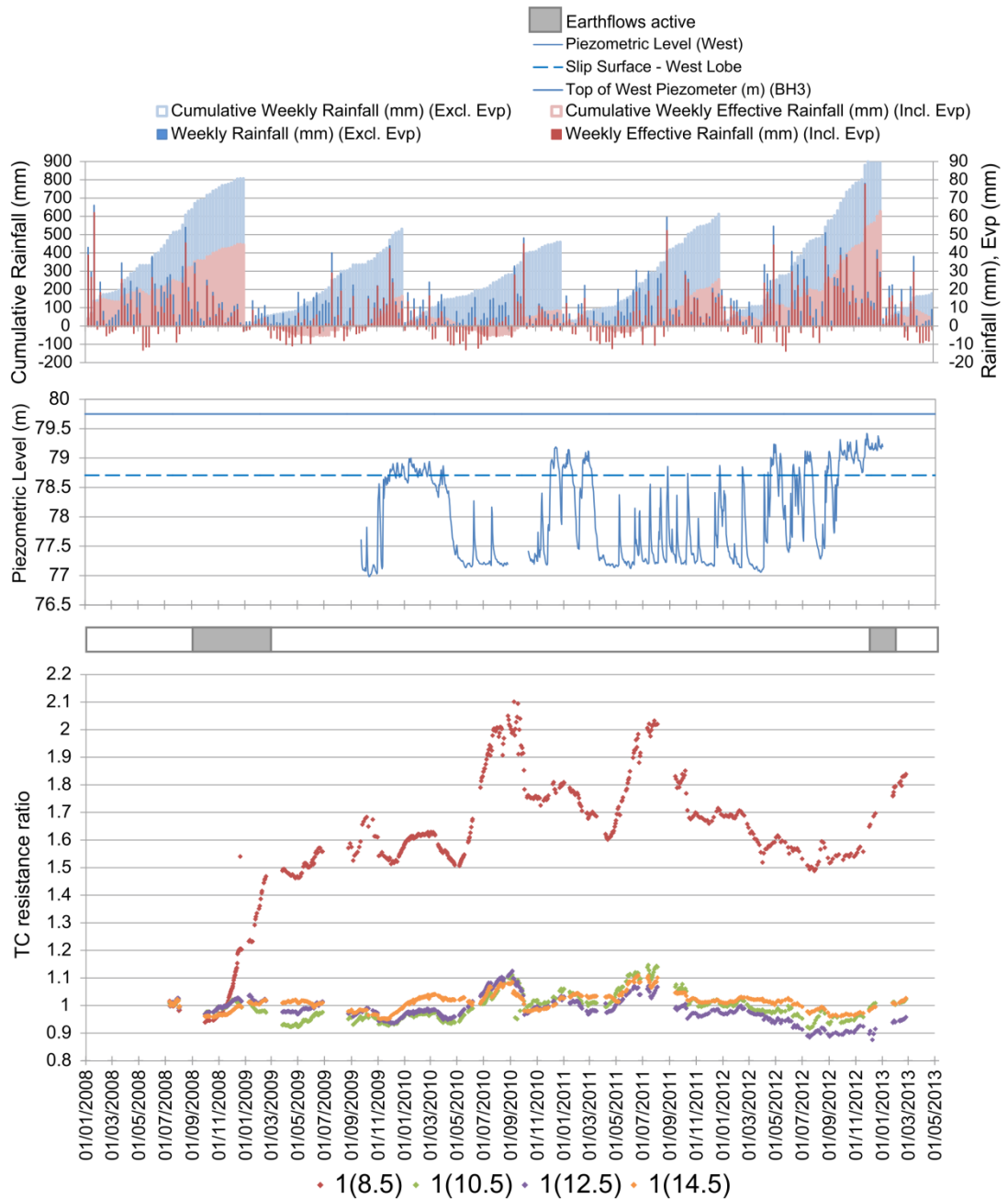


Figure 6.7. Time-lapse temperature corrected transfer resistance ratio measurements of dipoles located within the western earth flow deposits along Line 1. Resistance measurements are normalised to 13/07/2008 baseline survey. Locations of measurement dipoles are shown on Figure 6.4 and resistance results are plotted along with piezometry and rainfall data.

TC resistance ratios increase, reaching a peak at the start of March 2009. Piezometer level peaks once again mid-April and is attributed to two weeks of rainfall where 11mm of rain fell and once again triggers a sharp decrease in TC ratio of 1(8.5) and a more subtle decrease in TC ratio of the three other dipoles. Late-April to September 2010 sees negative effective rainfall dominate and resistance ratios for all four dipoles respond by recording the

largest resistance ratio increases seen during the monitoring campaign. Dipole 1(8.5) increases by 0.6 and dipoles 1(10.5), 1(12.5) and 1(14.5) increase by up to 0.15 during the period in question.

Piezometer level takes 4 weeks to lower to 77.2m where it remains until it begins to rise early December 2010. The piezometer level is punctuated by two piezometer rise events which occur at a time when effective rainfall is positive, the first taking place late May 2010, the second taking place late July 2010, rising by 1.0m and 0.9m respectively. These piezometer level rises tend to fall almost immediately, signifying that the level only remains high for 1-3 days and could represent a single intense rainfall event due to the temporal resolution of installed piezometers. September 2010 is dominated by intense rainfall as ~110mm of effective rainfall was recorded during this month, a dearth in piezometer data exists during this month.

TC resistance ratios values fall rapidly in response to this rainfall period as dipoles 1(10.5), 1(12.5) and 1(14.5) decrease by 0.13 and dipole 1(8.5) by 0.35. Early-December 2010 is met with a large rise in piezometric level, rising on three occasions until March 2011, with the dips in between rises correlating with periods of negative effective rainfall, such as the first week of December 2010 and the second week of January 2011. TC resistance ratios all remain constant during October and November 2010 but increase for 4 weeks from the first week of December 2010. January to April 2011 was a period when resistance ratios decrease and correlates with high piezometric levels and positive effective rainfall events with ~50mm of effective rain falling during this period. Piezometric levels gradually fall during March and take 4 weeks to lower from 78.8m down to 77.3m.

Resistance ratio of dipole 1(8.5) continues to decrease during March while piezometer level is falling, however, dipoles 1(10.5), 1(12.5) and 1(14.5) remain constant during this month. Between May 2011 to April 2012 the piezometric level rises and falls suddenly up to 13 times and this trend appears to be in response to short periods (1-2 weeks) of positive effective rainfall separated by short periods of either very low positive effective rainfall or negative effective rainfall. May 2011 to August 2011 experiences TC resistance ratio increases with dipole 1(8.5) rises by 0.45 and 1(10.5),

1(12.5) and 1(14.5) rise by ~ 0.12 and these rises take place during late spring and summer months dominated by negative effective rainfall events. TC resistance ratios can be seen to fall over the next three months despite a four week gap in resistance data centred on the first week of September 2011. Only two weeks during this three month period (August to late October 2011) had negative effective rainfall, as over 200mm of effective rainfall fell during this period. Despite the high amount of rain falling piezometric levels continue to be flashy, rising and falling over a number of days.

November 2011 to February 2012 is a period when TC resistance ratios remain almost constant, only dipole 1(12.5) increases by ~ 0.02 . All resistances decrease in March 2012 and is believed to be in response to 3 weeks of rainfall (40mm effective rainfall) occurring at the end of February and hints at the presence of lag between rain falling and resistance response. However, this potential lag is not observed extensively throughout the resistance monitoring data. Piezometer levels are less flashy than the previous 5 months and there appear to be three broad peaks from April 2012 until September 2012. These peaks reach 79.2m, 78.6m and 79.1m and both troughs lower to ~ 77.5 m. Effective rainfall data shows that each of these piezometer peaks is associated with an extended period of rainfall of around three to four weeks in duration. Between these rainfall periods are one to four weeks of negative effective rainfall which correlate with the piezometer level troughs.

The resistance ratios in April 2012 remain constant, except 1(8.5) which increases and is potentially in response to the negative effective rainfall period of late March 2012. May 2012 until mid-August 2012 sees resistance ratios taken by all dipoles gradually reduce with dipole 1(12.5) reaching a lowest ratio of the monitoring campaign. Between September and mid-November 2012 dipoles 1(10.5), 1(12.5) and 1(14.5) then remain almost constantly between September and mid-November 2012 at some of the lowest resistance ratio levels observed throughout the entire monitoring campaign and comes at a time when piezometer level is at its highest recorded level of the campaign and ~ 200 mm of effective rainfall was recorded. During the same period of time dipole 1(8.5) – located at the toe of the earth flow region – increases slightly, by ~ 0.03 . Only positive effect rain

fall was recorded between September 2012 and the end of February 2013. The western earthflow region activates early December 2012 and at a time when piezometer levels are sustained at a campaign high (79.3m for 6 weeks) and over 250mm of rain fell during the four months preceding activation.

Piezometer level remains consistently above the periodically active shear surface for 3 months prior to landslide activation. Resistance ratios from dipole 1(8.5) rise very sharply while the earthflow was active and are once again – as it was late 2008 – accompanied by displacement of measurement electrodes. The other three dipoles show a gentle increase in resistance ratio during earthflow activation of the order of 0.03-0.04.

Analysis of Eastern earthflow region

Temperature-corrected resistance measurements pertaining to the eastern earthflow are presented in Figure 6.8. The first three weeks of July 2008 see TC ratios remain reasonably constant except 5(8.5) which rises from 1.0 to ~1.1 most probably in response to 2 weeks of negative effective rainfall. A data gap exists during August and September 2008 and for the three months leading on from the gap ratios steadily rise back to 1, with 5(10.5) and 5(12.5) rising to ~1.02. Dipole 5(12.5) increases by 0.03 during January however all other dipoles remain constant at unity into mid-February where another data gap exists until mid-March 2009. The ratio increase of dipole 5(12.5) could be attributed to three weeks of slightly negative effective rainfall (~8mm), signifying that very little rain is falling and due to evapotranspiration none enters the subsurface. Late-March and April 2009 are represented by reasonably constant resistances but dipole ratios range between 0.97 and 1.03. May 2009 until October 2009 sees resistance ratios increase from 0.97-1.13 up to between 1.14 and 1.35 as displayed by dipoles 5(8.5) and 5(6.5) respectively. It should be noted that dipole 5(12.5), although it shares the arcuate form of resistance ratio with other dipoles its ratio decreases over this period and could be in response to several positive rainfall events taking place within this intense negative effective rainfall dominated period. A resistance datagap between late July and September 2009 means that the whole resistance trend was not recorded during this

period and as a result interpretation is difficult to muster. The other three dipoles also react to these positive effective rainfall events by decreasing resistance ratios by ~ 0.04 but immediately return to increasing resistance very soon after (3-4 days). When resistance monitoring was back online in September 2009 resistance ratios had substantially diverged and it can be seen that resistance ratios measured by dipole 5(6.5) would never re-align with the other three dipoles during the monitoring campaign.

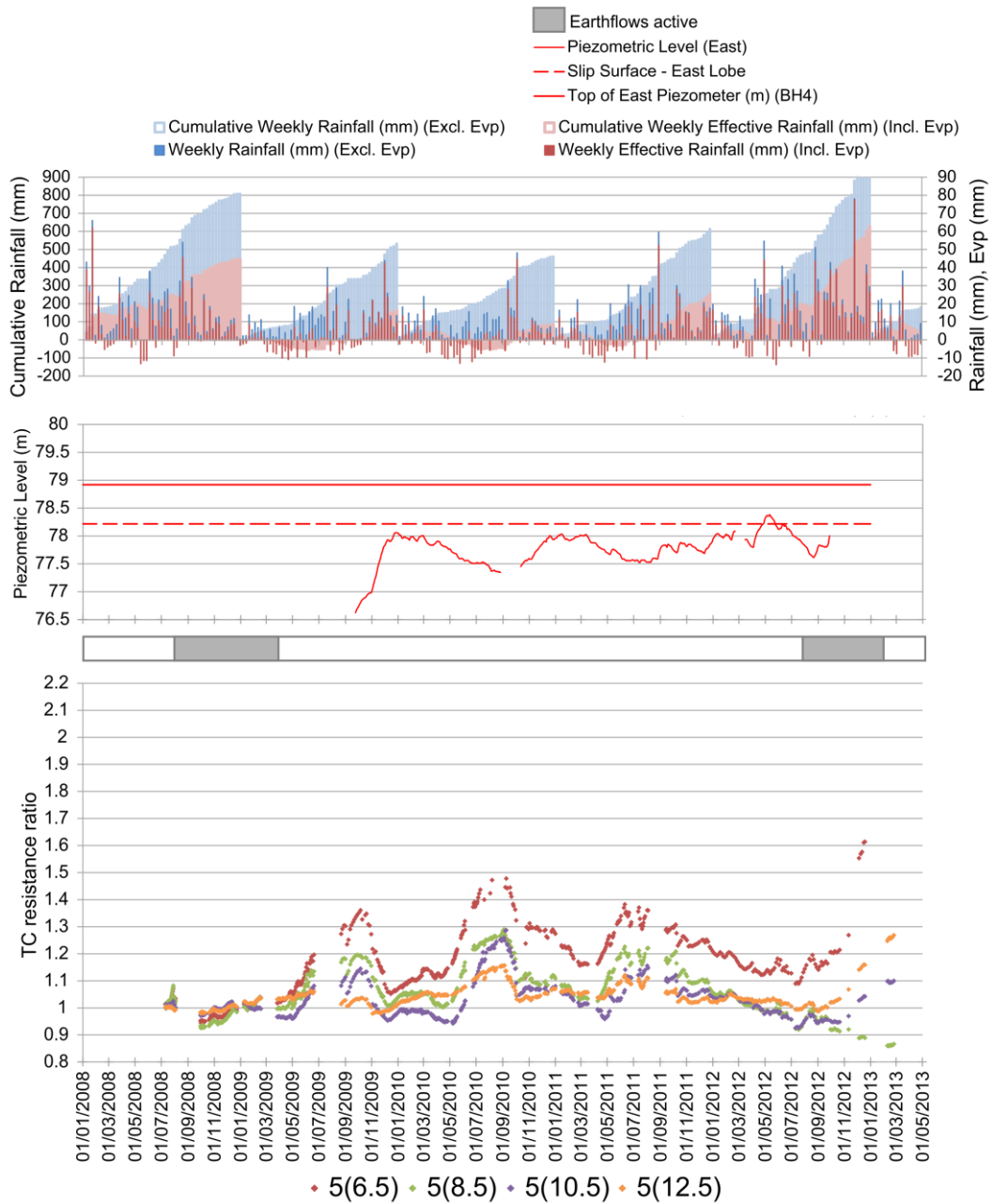


Figure 6.8. Time-lapse temperature corrected transfer resistance measurements of dipoles located within eastern earth flow deposits along Line 5. Locations of

measurement dipoles are shown on Figure 6.4.

Late-October commences as the last of the negative effective rainfall events passes and 3 months of intense positive effective rainfall begins. Over 160mm of effective rainfall is recorded during this period and piezometer levels can be seen to rise steadily from a low of 77.0m to ~78.0m, reaching a peak during December 2009. The first 6 weeks of piezometer data are discounted as during this time the level appears to rise by 0.5m at the end of Summer 2009 and during a period of negative rainfall. This piezometer level rise is attributed to the disruption of ground water flow as a result of piezometer casing installation and recovery back to a steady flow state.

In response to high rainfall taking place between late-October and early-December 2009 resistance ratios pertaining to dipoles 5(6.5), 5(8.5) and 5(10.5) decrease by up to 0.3, however, 5(12.5) falls by 0.04 to 0.98 within the first 4 weeks. The dipole then begins to increase almost uniformly for the next nine months until September 2010. Dipole 5(12.5) was already close to unity and therefore at a similar moisture content to baseline, which was while the slope was particularly wet, evident from the fact the eastern earthflow was active during this time. Whereas the ground around other dipoles is drier and perhaps more capable of further wetting up, which is why their resistance ratios continue to decrease after 5(12.5) has begun to increase. The final 3 weeks of December 2009, January, February and early-March are characterised by a piezometric level that is high, but gently falling and by less intense rainfall, with weeks of positive effective rainfall interspersed by weeks of slight negative effective rainfall. During this period dipoles 5(6.5) and 5(12.5) display resistance ratio increases of 0.05, 5(8.5) and 5(10.5) increase by ~0.02. The second half of March and April 2010 sees resistance ratios drop in response to three weeks of positive effective rainfall before continuing to increase again following the rainfall – as it did before March/April – and occurs at a time when negative effective rainfall and falling piezometric levels are prevalent.

Resistance ratios rise during the Summer 2010 during the months of May until August, with ratios increasing less sharply from July onwards due to the occurrence of several positive effective rainfall periods which act to slow resistance ratio increase. Both piezometric level and resistance ratio reach

their lowest values of the entire monitoring campaign during August 2010. As was observed in the resistance ratio results from line 1 of the eastern earthflow region, the intense rainfall event of October 2010 causes resistances to drop sharply as dipole 5(8.5) and 5(10.5) reduce by 0.18 and 0.2 respectively. Despite the gap in piezometer data the piezometric level only rose by ~0.1m as a result of this rainy period. Between November and December 2010 piezometric level rises uniformly from 77.5m to 78.0m and however during the same time frame the resistance ratios either remain constant or increase by ~0.04, hinting at a disconnect between piezometric level rising and resistance ratio response. September 2010 to March 2011 is a period with very little negative effective rainfall and ~100mm of positive effective rainfall. The second half of this period, between January and March 2011 exhibits a constantly high piezometric level (~78.0m) and falling resistance ratio values.

Resistance ratio values continue to fall during April, a month after piezometric levels begin to fall in response to a period of mostly negative effective rainfall, highlighting once again at the lag in the system between change in piezometric level and resistance response. From May until late-June 2011 resistances rise as piezometric level fall by 0.5m to 77.5m. The following two months are characterised by several weeks of moderate effective rainfall interspersed with negative effective rainfall events. Piezometer levels during these two months remain low despite moderate rainfall and resistance ratio is high but fluctuates as a result of rainfall events. Dipoles show a range of resistance ratios during this period and typically range between 0.04 and 0.09, and with 5(12.5) and 5(10.5) exhibiting the lowest ratio and 5(6.5) the highest.

September 2011 sees TC resistances gradually decrease from the highs of Summer 2011 to the lows in the lead up to eastern earthflow activation in July 2012. During this 10 month period over 300mm of effective rainfall fell and with it piezometric level rose from its lowest level (77.5m) to its highest of the campaign (78.4m), in July 2012, a month before flow activation. Piezometric level does not rise with a uniform gradient, it is punctuated by piezometric level falls in response to reduced rainfall intensity and negative effective rainfall. Examples of this process can be seen late-December 2011

and early-April 2012. Dipole 5(10.5) decreases to its lowest resistance ratio of the monitoring campaign during the first week of July 2012 as the earth flow activates, and dipole 5(8.5) decreases to the ratio exhibited when the eastern earthflow activated in late-2008.

For the two months post-activation, the TC resistance ratios of all dipoles subtly increase. These increases are coincident with falling piezometric levels despite high rainfall. September 2012 until the end of piezometer level monitoring in October 2012 sees the level rise from 77.6m to 78.0m. All four dipoles exhibit a sudden jump in resistance ratio values in the last week of September and could be attributed to electrodes beginning to mobilise. From November 2012 until the end of the resistance monitoring campaign sees TC resistance ratios either curve upwards or downwards. Dipole 5(6.5) exhibits TC resistance ratio increases from 1.28 to 1.55 in less than a month. While dipole 5(8.5) decreases by a 0.05 in 5 weeks and both of these resistance trend events are interpreted as being an artefact of electrode mobilisation during eastern earthflow activation.

6.3.2 Temperature Corrected Transfer Resistance of 2012 Landslide Activation

In order to draw detailed conclusions about the efficacy of 3D ERT monitoring as a means of observing hydrogeological precursors to landslide activation it is essential to look at the monitoring results for the months leading up to one such activation event. The only activation event we have the monitoring data during the period leading up to failure is the event taking place from ~August 2012.

Temperature corrected resistance monitoring results during the period leading up to the 2012 earthflow activations are presented here in two formats; as resistance maps (Figures 6.9 & 6.10) and as plots of individual dipoles (Figure 6.11 & 6.12). Resistance maps of twelve surveys of the time period between 26/06/2008 and 12/12/2012 are presented. Each map displays resistance difference relative to a baseline survey, performed 13/07/2008. Resistance maps are graphical plan view representations of $a=1$, $n=1$ resistance measurements and characterise the resistance distribution of the shallowest 1.9 m of the subsurface. Figure 6.9 shows the

region of the landslide system which is encompassed in the temperature corrected resistance maps and is displayed alongside the baseline map (right-hand side of Figure 6.9)

Individual dipole resistances are plotted as TC resistance ratios, relative to the same baseline as was used in both Section 6.3.1 and the resistance maps mentioned previously. Individual dipole results focus on the time between 01/06/2011 and 27/02/2013.

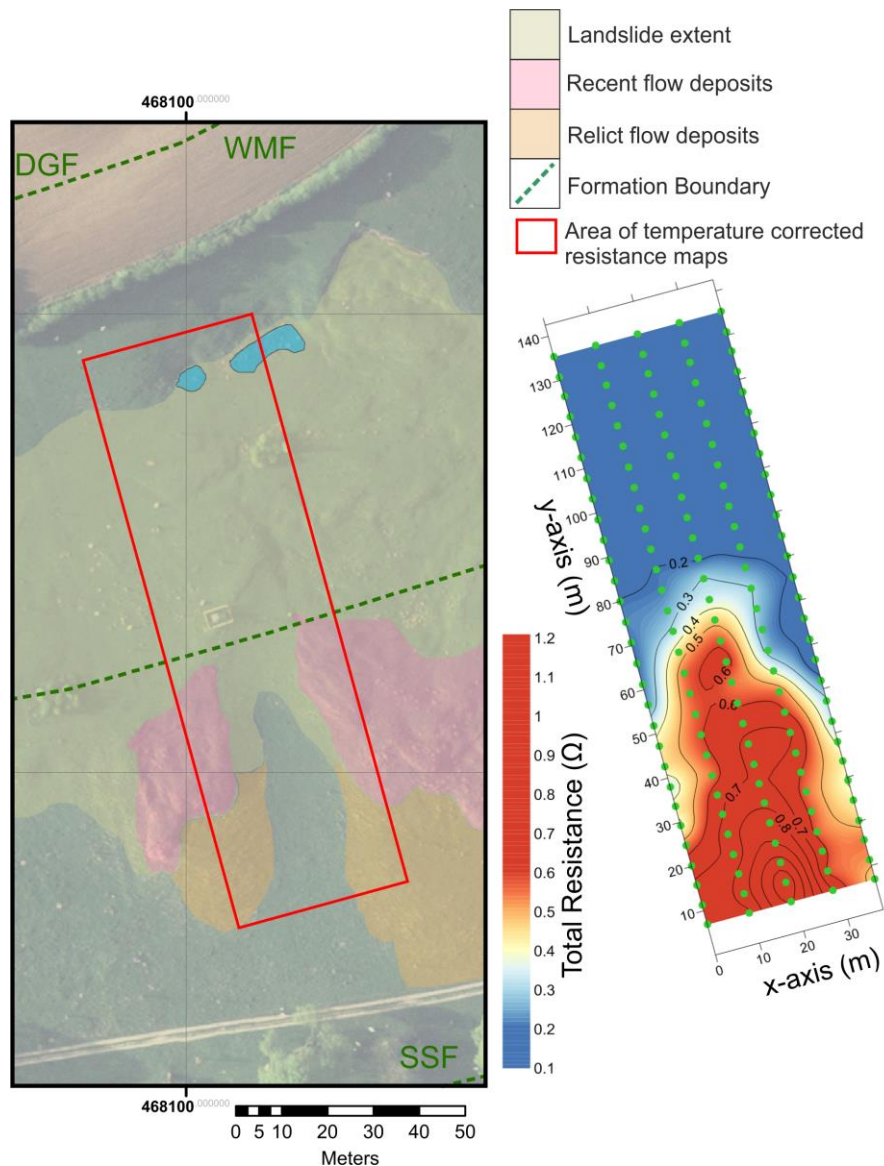


Figure 6.9. Geographic location of resistance maps (left). Outline of survey area indicated by red rectangle and to the right of geographic map is the baseline resistance map to scale.

Temperature Corrected Resistance Maps of 2012 Landslide Activation

Temperature corrected resistance maps are displayed (Figure 6.10) as resistance difference ($\Delta\Omega$) between resistance at date (Ω_n) relative to a baseline resistance (Ω_{BL}), i.e. $\Delta\Omega = (\Omega_n - \Omega_{BL})$.

The first resistance map is from the ERT survey performed 26/06/2011 and is dominated by negative resistances relative to baseline, indicating that this survey is mostly more resistive than baseline survey. A high negative resistance difference feature exists centred around $X=0.0\text{m}$, $Y=34.0\text{m}$ and is attributed to an electrode displacing as a result of landslide activation between baseline and 26/06/2011 survey. This feature exists at the toes of the western earth flow and was active late-2008, and so this feature is an electrical artefact of this activation event. Below the electrical anomaly and centred on $X=0.0\text{m}$, $Y=18.0\text{m}$ is a negative resistance difference region, located within relict earthflow deposits. North of the electrical anomaly, between $X=0.0\text{m}$, $Y=38.0\text{m}$ and $X=0.0\text{m}$, $Y=86.0\text{m}$ the ground is slightly more resistive than baseline and displays a resistance difference of $\sim -0.03\Omega$. Further east, and in the central region is a more resistive region centred on $X=10.0\text{m}$ and $Y=60.0\text{m}$ and this feature becomes less resistive until it no longer exists at survey 02/05/2012.

The northern half of the survey is more resistive than baseline with some regions of equal resistivity at the edges of the survey area, for example $X=110.0\text{m}$ and $Y=0.0\text{m}$. This region becomes less resistive and more similar to baseline until 01/01/2012 and reaches a least resistive peak at the 02/11/2011 survey. A small positive resistivity difference region exists at $X=20.0\text{m}$, $Y=10.0\text{m}$ and has a resistance difference of 0.06 and is not present at the next survey 14/09/2011. The lower eastern region of the survey area, between $X=38.0\text{m}$, $Y=0.0\text{m}$ and $X=38.0\text{m}$, $Y=40.0\text{m}$ is entirely negative resistance difference and ranges between -0.04Ω and -0.1Ω .

Resistance differences within this region also become less negative until reaching a lowest resistance difference at the 02/05/2012 survey. Another artefact of electrode mobilisation exists at $X=38.0\text{m}$, $Y=23.0\text{m}$ and is visible in all resistance difference maps, however it becomes more apparent from the 29/08/2012 survey as the electrodes re-mobilise in response to the 2012

earth flow activation event. A negative resistance difference between earthflows, initially at X=19.0m, Y=0.0m on the 14/09/2011 survey can be seen to grow until reaching a maximum area at 15/03/2012 survey before increasing and being non-existent by the 02/05/2012 survey. The 02/05/2012 survey almost consistently records a resistance difference of -0.01Ω with the exception of a region in the south east of the area which has a higher negative resistance difference of -0.04Ω . A very small region of positive resistance difference (0.03Ω) daylight at X=19.0m, Y= ~9m. By 02/06/2012 survey the uniform resistance difference seen at 02/05/2012 has altered to a region of greater negative resistance difference, reference to baseline survey, with large regions in the south (below Y=80.0m) recording differences between -0.02Ω and -0.1Ω . A region of positive resistance difference exists (X=19.0m, Y=5.0m to Y=30.0m) between the two extremely negative resistance difference regions associated with relict earthflow material. This feature is present in the 02/06/2012 and 25/06/2012 surveys, however, it is much more subtle in the latter, indicating a relative increase in resistance between the former and latter surveys in the area outlined. The main body region of the landslide, above Y=80.0m can be seen to increase in resistance between the 25/06/2012 survey and the 02/06/2012 survey.

The next survey was performed 13/07/2012 and at first glance appears considerably different to the previous eight resistance maps. Below Y=90.0m almost the entire region is either at the same resistance as baseline – indicated by a zero resistance different – or a positive resistance difference of between 0.03–0.06. Thus, indicating that this region of the survey area is wetter than baseline. Both earthflow regions display a positive resistance difference and so have a lower resistance than baseline. The western earthflow region (X=0.0m, Y= 38.0m to Y=60.0m) which activated 08/2012 records a lower resistance relative to baseline, as does the eastern earthflow region (X=38.0m, Y=24.0m to Y=~60.0m) at the 13/07/2012 survey.

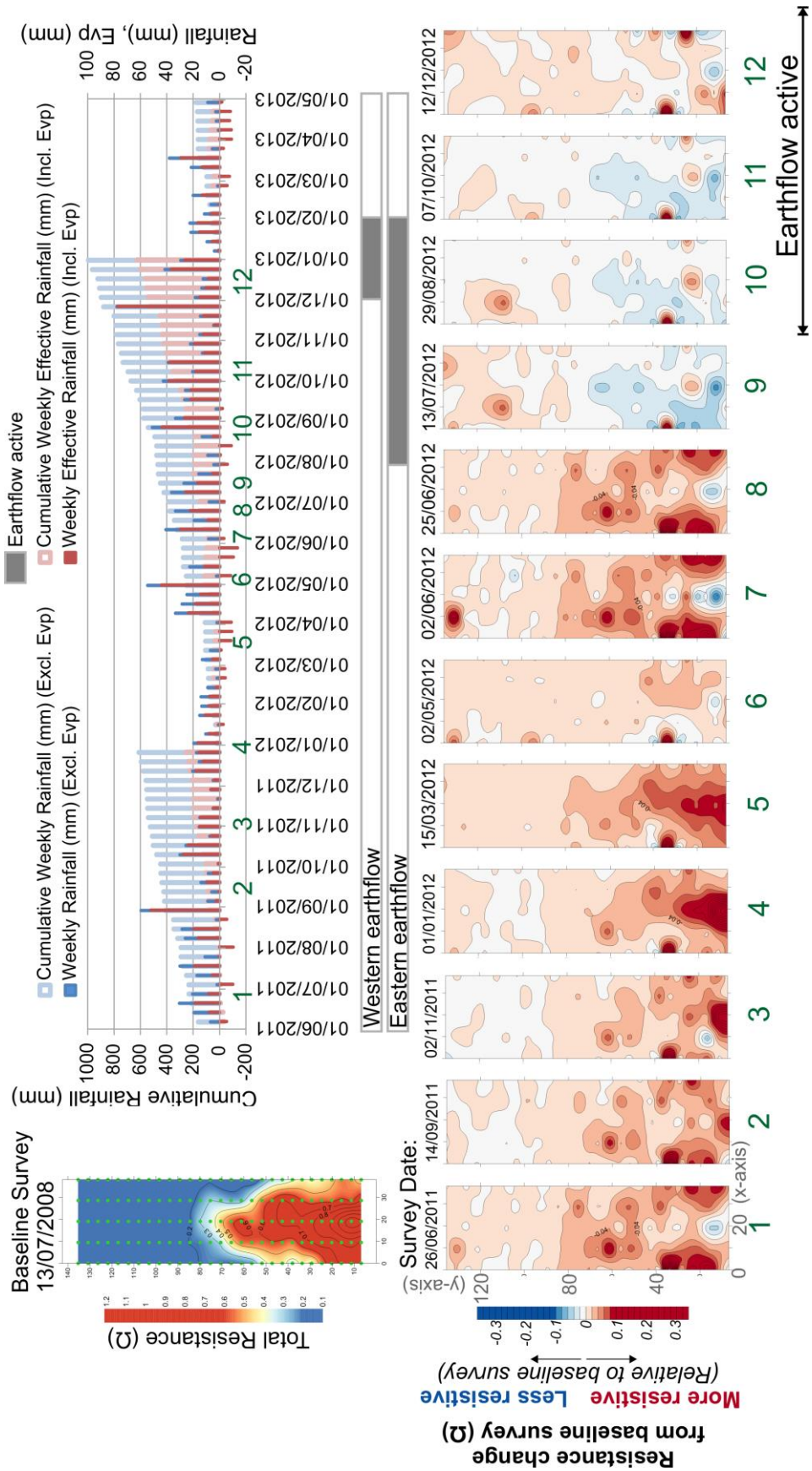


Figure 6.10. Time-lapse temperature corrected transfer resistance measurements of dipoles plotted as resistance map. Locations of measurement dipoles are

shown on initial survey.

The toes area of the eastern earthflow region (centred on $X=38.0\text{m}$, $Y=35.0\text{m}$) has a lower resistance relative to baseline, however the majority of the earthflow region is at a similar resistance ± 0.01 , evident from the white coloured region between ($X=38.0\text{m}$, $Y=35.0\text{m}$ to $Y\sim 60.0\text{m}$). At this survey the region above $Y=90.0\text{m}$ is dominated by resistance difference of 0.02Ω along with approximately a third of the region at a similar resistance to baseline and one small region showing a positive resistance difference ($X=9.5\text{m}$, $Y=110.0\text{m}$). This small positive region existed into late August as it is visible in the 29/08/2012 survey.

Staying with the upper region of the survey area, above $Y=90.0\text{m}$, the resistance of this region lowers further compared to 13/07/2012 as the majority of the area is now at a similar resistance to baseline. The lower region of the map, below $Y=90.0\text{m}$, remains dominated by positive resistance difference and therefore continues to have a lower resistance than baseline. The eastern earthflow activated around the August 2012 and so between the 13/07/2012 survey and the 29/08/2012 survey the landslide became active. An artefact of landslide activation is evident in the eastern earthflow region of the map area between $X=38.0\text{m}$, $Y=24.0\text{m}$ and $Y=54.0\text{m}$. The artefact manifests as a series of high resistance 'concentric-ringed' anomalies with low resistance anomalies located between and is attributed to electrode mobilisation occurring during landslide activation. It should be noted that electrode mobilisation acts to overprint the resistance variations and thus make further observation of resistance in the vicinity of electrode mobilisation practically impossible.

Two months after the 07/10/2012 survey the map area once again dominated by negative resistance difference and has a resistance greater than the resistance of the baseline survey. The artefacts of electrode movement are distinct and well developed on the eastern earthflow region, indicative of several mobile electrodes practically running the length of the earthflow region.

Western earthflow activation occurs at December 2012 at a time when resistance differences are zero and therefore very close to the resistance

recorded at baseline when the western earth flow was active. One small region of positive resistance centred at Y=50.0m, X=0.0m, within active earthflow. Electrical resistance maps using an average of all resistance measurements (from 2010) pertaining to a period of landslide stability is presented as Appendix D. This figure displays many of the environmental trends in resistance data present in Figure 6.10, thus revealing that valuable interpretations can be drawn whether using a single resistance value or an average as the baseline.

Temperature Corrected Transfer Resistance Ratios of 2012 Landslide Activation

Temperature corrected resistance ratio results from individual measurement dipoles located within active earthflow and for the timeframe leading up to and during earthflow activation are analysed herein. The focussing of attention on the lead up to landslide activation and by altering the resistance ratio scale it is possible to identify small property variations which were not apparent in previous plots and may lead to more informed interpretations about landslide activation precursors. Figure 6.11 displays resistance ratios pertaining to the western earthflow region located along line 1. The resistance ratio axis has been altered and in doing so dipole 1(8.5) is not presented on the figure. Resistance ratios during June 2011 are initially high after three months of almost only negative effective rainfall during late Spring/early Summer, with dipoles 1(10.5), 1(12.5) and 1(14.5) varying between ~1.05, ~1.08 and ~1.11 during the second week of July 2011.

The following five months – July 2011 to December 2011 – is a period of weather fluctuation and this trend is reflected in both the piezometry (sudden rises and falls of up to 1.5m) and subsequent resistance ratio response. Weekly effective rainfall varies between 1-2mm and 56mm during this period. Resistance ratio decreases during this period and does so by dropping sharply after a rainfall event and associated piezometer rise. The second week of November 2011 is an example of this process, conversely, periods of low rainfall and piezometric level fall trigger a rise in resistance ratio.

A key observation is that resistance decrease, due to rainfall events, occurs much more rapidly than resistance increase because of a lack of rainfall and resulting piezometer low. This relationship causes resistance ratios to steadily decrease throughout this five month period, reaching a low between August and September but remaining low until December 2011.

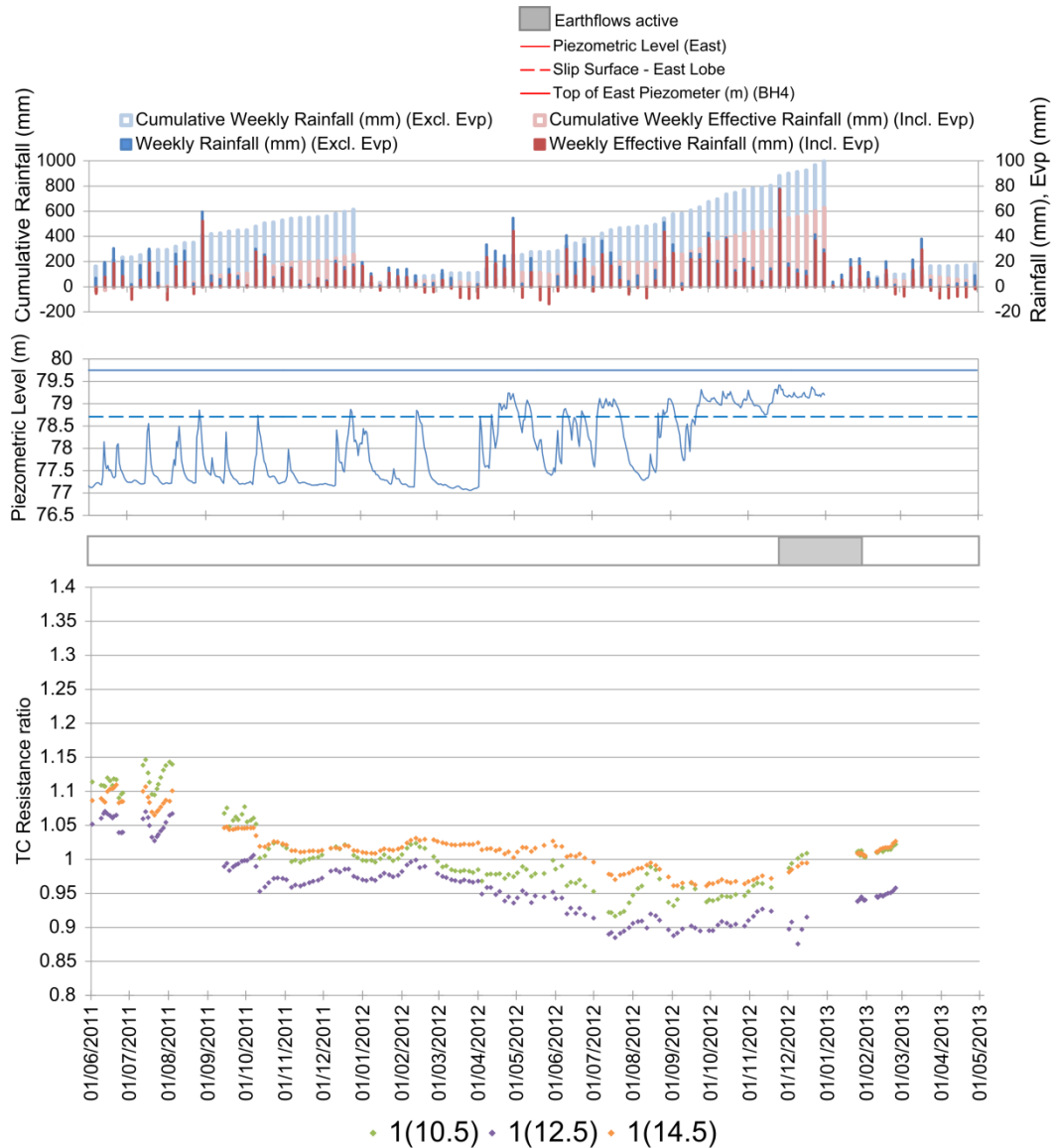


Figure 6.11. Time-lapse temperature corrected transfer resistance measurements of dipoles located within western earth flow deposits along Line 1. Time period between 06/2011 and 02/2013 plotted as lead up to earthflow activation at 08/2012. Locations of measurement dipoles are shown on Figure 6.4.

Between December 2011 and April 2012 similar climatic uncertainty exist however, resistance ratios seem to have plateaued and with the exception of two small resistance peaks remain steady. An example of the small

deviation in resistance ratio occurs mid-February 2012. Mid-April to mid-July 2012 experienced relatively high piezometric level compared to the previous year and is attributed to high rainfall, for example the month of April 2012 saw ~100mm of effective rainfall. Piezometric levels between mid-April and July 2012 remain consistently above 78.5m and above the flow slip surface. Resistance ratio levels during this time decrease, dipole 1(10.5) decreases by 0.06 to 0.92, whereas 1(12.5) decreases by 0.07 to 0.88. By the end of this period dipole 1(12.5) has decreased to its lowest level of the monitoring campaign, however, dipoles 1(10.5) and 1(14.5) had decreased to lower levels during the campaign and at a time when the landslide was suspended.

Piezometric levels rise even further and remain at just over 79.0m for six weeks from mid-September 2012, during this time resistance ratios remain constantly low at 0.94 (rising slightly), 0.9 and 0.96 for dipoles 1(10.5), 1(12.5) and 1(14.5) respectively. The western earthflow region activates December 2012 at a time when piezometric levels reach a maximum of the campaign and comes to within 0.4m of the ground surface. Despite the high rainfall and highest piezometric levels of the monitoring campaign resistance ratios increase from December 2012 onwards and the trend is coincident with eastern earthflow activation. Dipole 1(12.5) produced a small cluster of lower resistance ratio measurements during early December as resistance ratios appear to decrease to 0.87 before rising abruptly back up to ~0.92 and then increase further in the final few days of the monitoring period (27/02/2013).

Looking at individual dipoles from the earthflow of line 5 (Figure 6.12) in the 14 months leading up to earthflow activation, from 01/06/2011, dipole 5(6.5) can be seen to be significantly higher than the other dipoles at 1.35. Dipoles 5(8.5), 5(10.5) and 5(12.5) have resistance ratios of 1.2, 1.04 and 1.1 respectively. Resistances subtly fluctuate between 06/2011 and 08/2011 and decrease in response to rainfall events and increase by a similar amount due to periods where rainfall is outpaced by evapotranspiration. A datagap of 6 weeks is present between 08/2011 and mid-09/2011 and during this period a week with 56mm of effective rainfall fell, raising the piezometric surface by 0.3m to 77.8m. Resistance ratios are lower than before the

datagap but rise during the second half of September 2011 just as piezometer level falls by 0.1m and effective rainfall intensity settles post last week of August 2011. Between 10/2011 and 05/2012 piezometric level gradually increases from 77.7m until reaching a peak at 78.4m, during this period, three of the four dipoles recorded a resistance decrease with dipole 5(12.5) reaching a ratio minimum late 2011 of 1.03 where it remained almost constantly until 05/2012. Dipoles 5(6.5), 5(8.5) and 5(10.5) reduce during this seven month period by 0.2, 0.25 and 0.13 respectively. Piezometer level reached its peak after a four week period of intense effective rainfall. Resistance ratios continue to fall despite piezometric level lowering for the next 3.5 months between May and August 2012. Resistance levels fall until mid-July 2012 as all four dipoles record their lowest values during the lead up to the August 2012 activation and during this time over 100mm of effective rainfall falls. Mid-May sees the resistance ratio of 5(6.5) increase from 1.12 to 1.18 before decreasing in line with all other dipoles. The decrease of resistance ratio in the lead up to earthflow activation could be attributed to landslide related processes and is addressed in the discussion section.

During the first week of July 2012 all four dipole measurements appear to jump downwards and could potentially be an artefact of earthflow activation and occurred approximately two weeks before the GPS survey of pegs recorded movement. Immediately after this apparent resistance jump resistances again start to increase at a time when piezometer levels are further falling. Effective rainfall during this period wains, as several weeks of negative effective rainfall were recorded and by the second week of August 2012 piezometer levels have almost fallen back to their original June 2011 level of 77.6m. The eastern earthflow activates August 2012 and resistance ratio uniformly increases during the active phase, except for the second two weeks of August. These two weeks are characterised by all four dipoles recording a decrease in resistance ratio in response to 65mm of effective rainfall occurring. Another resistance jump can be seen to take place late-September while the earthflows are active and from November onwards it is clear that resistances are increasing (5(6.5), 5(10.5) & 5(12.5)) and decreasing (5(8.5)) because of electrode mobilisation. Piezometer data is

not present from November 2012 onwards as the piezometer became trapped downhole because earthflow activation broke the plastic casing.

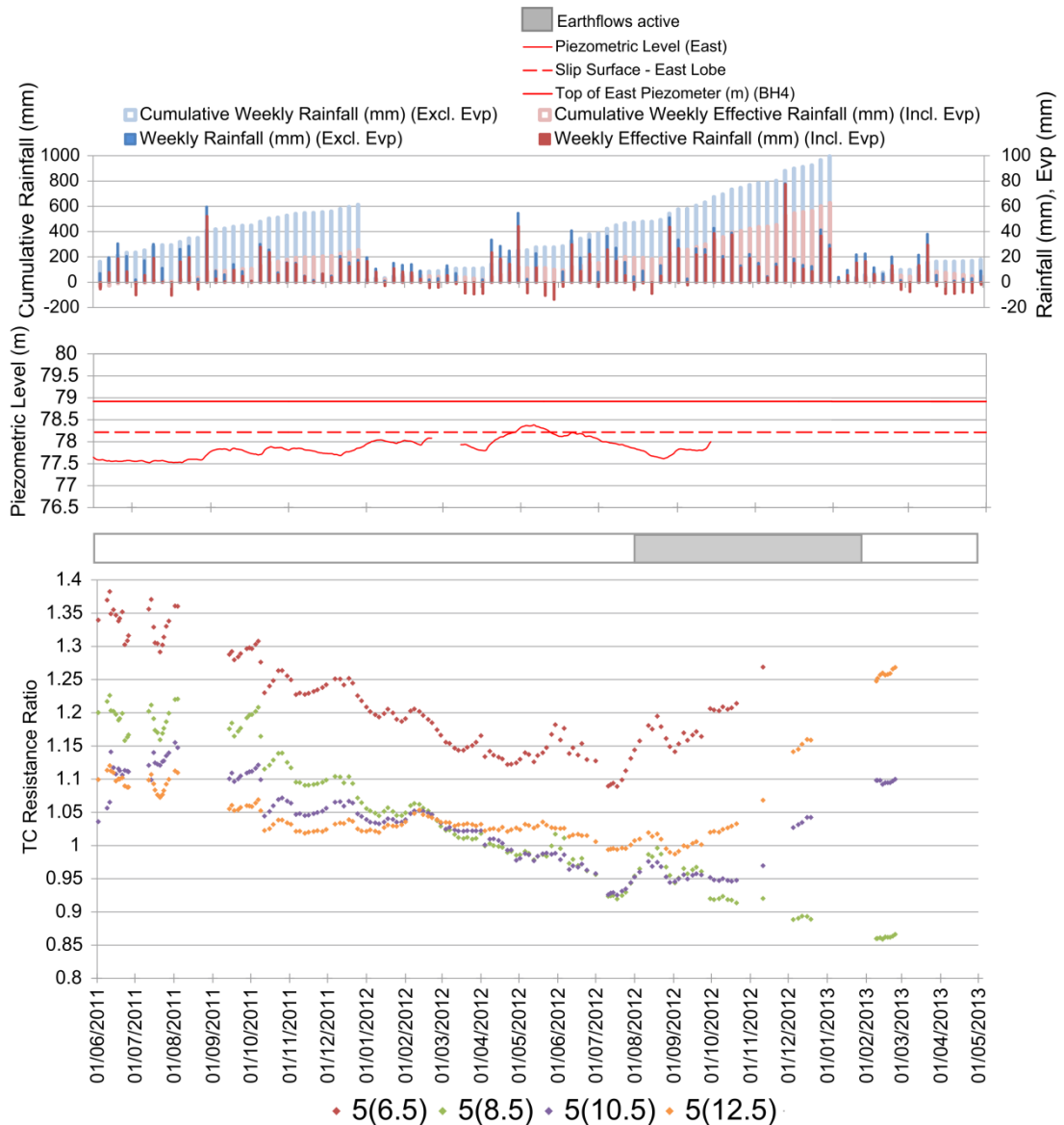


Figure 6.12. Time-lapse temperature corrected transfer resistance measurements of dipoles located within western earth flow deposits along Line 5. Time period between 06/2011 and 02/2013 plotted as lead up to earthflow activation at 08/2012. Locations of measurement dipoles are shown on Figure 6.4.

Summary of Temperature Corrected Resistance Observations

The main trends observed in temperature corrected resistance data include; TC resistance ratio highs during periods of low water table levels, and conversely, resistance ratio lows when piezometer levels are high.

Resistance maps are particularly useful at identifying abrupt increases or decreases in resistance ratio during periods of earthflow activation which are a result of electrode mobilisation. In the build up to the 2012 earthflow activation resistances gradually decrease to some of their lowest levels of the monitoring campaign however, the low resistance ratios also occur when the slope is inactive. Resistance maps reveal that resistances decrease throughout the area in advance of earthflow activation but increase while the flows are active. The eastern earthflow resistances reveal that some small rainfall events are not picked up by piezometry but are responsible for small changes in resistance. Piezometer level fluctuations in the lead up to flow activation are observed by resistance monitoring and highlight water level decrease in the eastern earthflow in the two months leading up to activation.

6.3.3 Temperature Corrected Resistance and Piezometry Correlations

Resistance monitoring results were compared with piezometry measurements of the eastern earthflow region. Correlation coefficients between the two datasets (Figure 6.13) suggest strong negative correlation (-0.65) between piezometry and electrical resistance response. Therefore, as piezometric level rises due to rainfall infiltration the electrical resistances actively reduce.

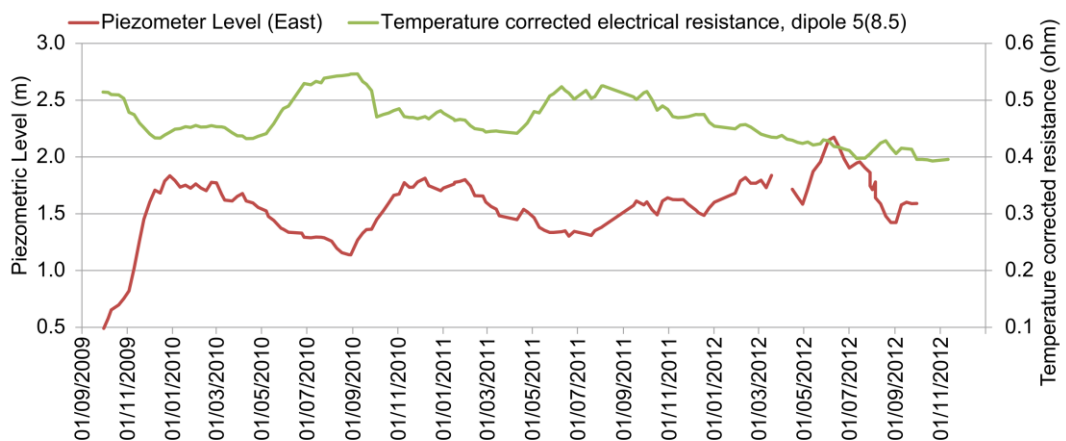


Figure 6.13. Comparison between temperature corrected resistance and western piezometer level

6.4 Time-lapse tomography results

The details of the inversion process carried out on ~65 ERT surveys is provided in Chapter 4 and include two methods of inversion, the first, used independent inversions and interpolated electrode positions. The second method applies time-lapse constraints to resistance data during the inversion process which acts to minimise resistance differences between inversions. In this section results are presented and each of the products of each inversion route are analysed. Sixty five inversions were carried out on movement corrected ERT survey data and fifty inversions were performed of ERT survey data utilising time-lapse model constraints. The reason that fewer time-lapse constrained inversions (L1 smooth inversion, 0.2 time-lapse constraint damping factor) were performed is due to the inability to incorporate electrode displacement into these inversions (L1 smooth inversion). With this in mind ERT surveys performed while the landslide was active were not inverted with time-lapse constraints applied.

Depths of centres of model cells of uppermost cell layers is 0.6 m.

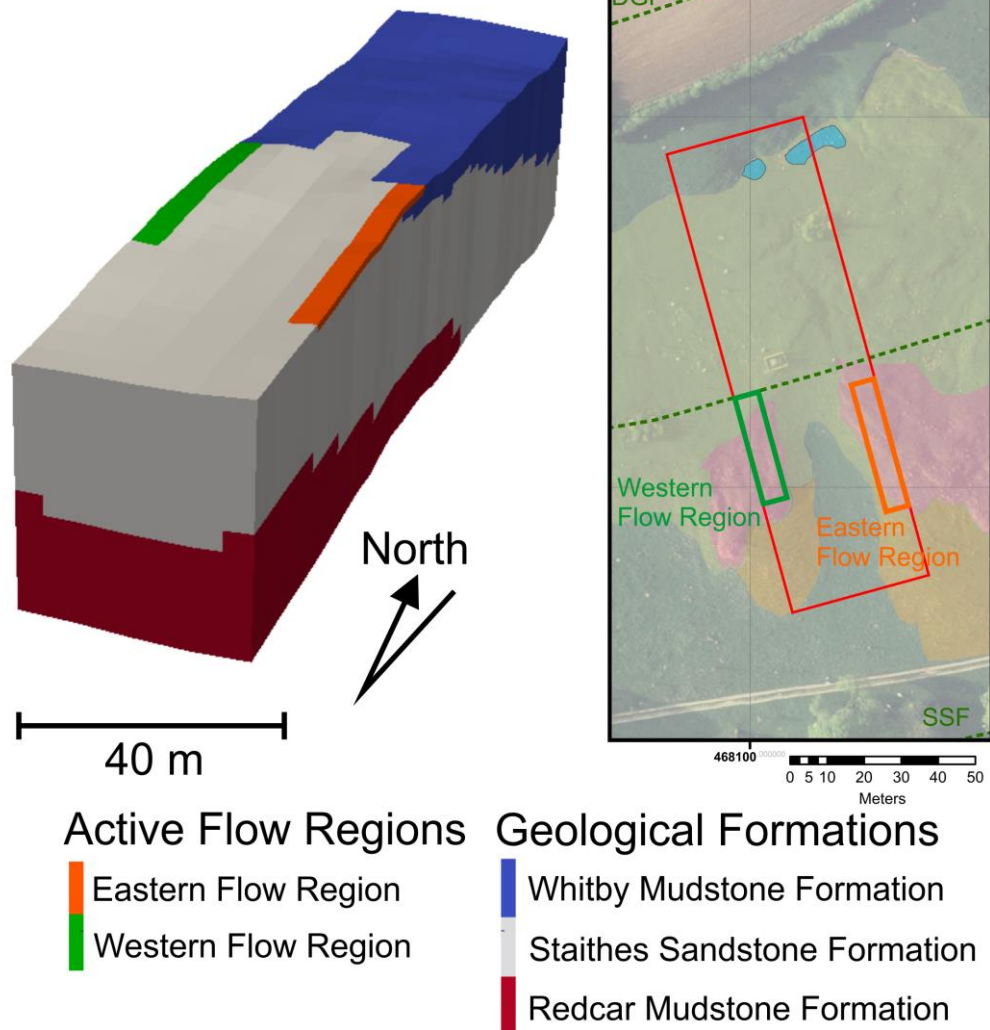


Figure 6.14. a) (left) Block diagram showing model partitioning of the low resolution resistivity model domain. Shown are the three geological formations present, WMF, SSF and RMF, as well as three landslide regions examined in detail, Slump, eastern and western flow deposits. The area imaged is shown in 6.13b, right.

6.4.1 Time-Lapse Model Resistivity & GMC Results

The cells interpreted as being composed of western earthflow deposit are represented in Figure 6.14 by cells coloured green and model resistivity results are shown in Figure 6.15 alongside rainfall and piezometry data. The blue coloured diamonds of the model resistivity and gravimetric moisture content plots (lowermost two plots) represents electrode movement corrected model resistivity (herein abbreviated to mov-cor resistivity) and the maroon squares represent time lapse constrained model resistivity (abbreviated to T-LC resistivity) pertaining to western earthflow. Results

pertaining to the cluster of eastern earthflow model cells are presented in Figure 6.16 and follow the same format as Figure 6.15. Model resistivity results are arithmetic averages of all model cells spatially located on earthflow material. Centres of model cells are located at 0.6m depth.

Figure 6.14 displays the model cells interpreted as containing active earthflow, these cells were grouped together and the mean resistivity of these cells calculated. Two lines, one grey, the other black are marked on each model resistivity graph (Figures 6.15 & 6.16) and they indicate two important geotechnical properties of the WMF earthflow material; resistivity at their plastic limit and saturation.

Model Resistivity & GMC of Western Earthflow

The first clear trend visible in model cell data is the apparent disparity between cell resistivity from electrode movement corrected inversions and time-lapse constrained inversions, with the former plotting almost consistently between $1\Omega\text{m}$ and $7\Omega\text{m}$ above the latter (described in Discussion, Section 6.5). The second clear observation that can be made is the degree of scatter between adjacent movement corrected resistivity measurements when compared with time-lapse constrained resistivity which shows smooth variation throughout the monitoring period. Movement corrected resistivities are plotted from January 2009 until February 2013. Time-lapse resistivity is plotted from the cessation of the 2008/2009 earthflow activation period and the onset of the 2012 activation. It is therefore plotted between 05/2009 and 06/2012.

Mov-cor resistivity initially plots at $21\Omega\text{m}$ (21% GMC) but begins to fall between May 2009 and late November 2009, decreasing from $21\Omega\text{m}$ to $14.5\Omega\text{m}$ (28% GMC) and occurs during a period where both negative effective rainfall is met by occasional weeks of high positive effective rainfall events, such as the 29 mm of the third week of July 2009. Between May 2009 and late November 2009 time-lapse resistivity decreases from $14\Omega\text{m}$ down to $12.5\Omega\text{m}$, a much smaller decrease than displayed by mov-cor resistivity.

As piezometric level rises and remains high for a 6 month period between December 2009 and mid-May 2010 both mov-cor and T-LC resistivity

increase due to December 2009 recording several snow days, January 2010 recording more than 0.37m of snowfall and February and March 2010 both experienced 15 frost days.

During April 2010 resistivity plateaus until piezometric level falls sharply during May in response to warmer months and onset of 5 months of strong evapotranspiration restricting rainfall infiltration. June to late-August 2010 sees T-LC resistivity increase from $14\Omega\text{m}$ to $17\Omega\text{m}$ (24% to 26% GMC), at the same time mov-cor resistivity falls by $2\Omega\text{m}$ to $17\Omega\text{m}$ (29% to 26%). Mov-cor resistivity jumps upwards from $17\Omega\text{m}$ to $22\Omega\text{m}$ (26% to 22% GMC) during September 2010 and both sets of model resistivities fall in response to the ~100mm of effective rainfall which fell during November 2010, with T-LC resistivity decreasing from $17\Omega\text{m}$ to $14\Omega\text{m}$ (26% to 30% GMC) and mov-cor resistivity falling more subtly from $22\Omega\text{m}$ to $17\Omega\text{m}$ (22% to 27% GMC) by March 2011 and in response to three distinct rises and falls in water table level. However, this reduction in mov-cor resistivity is punctuated by data scatter.

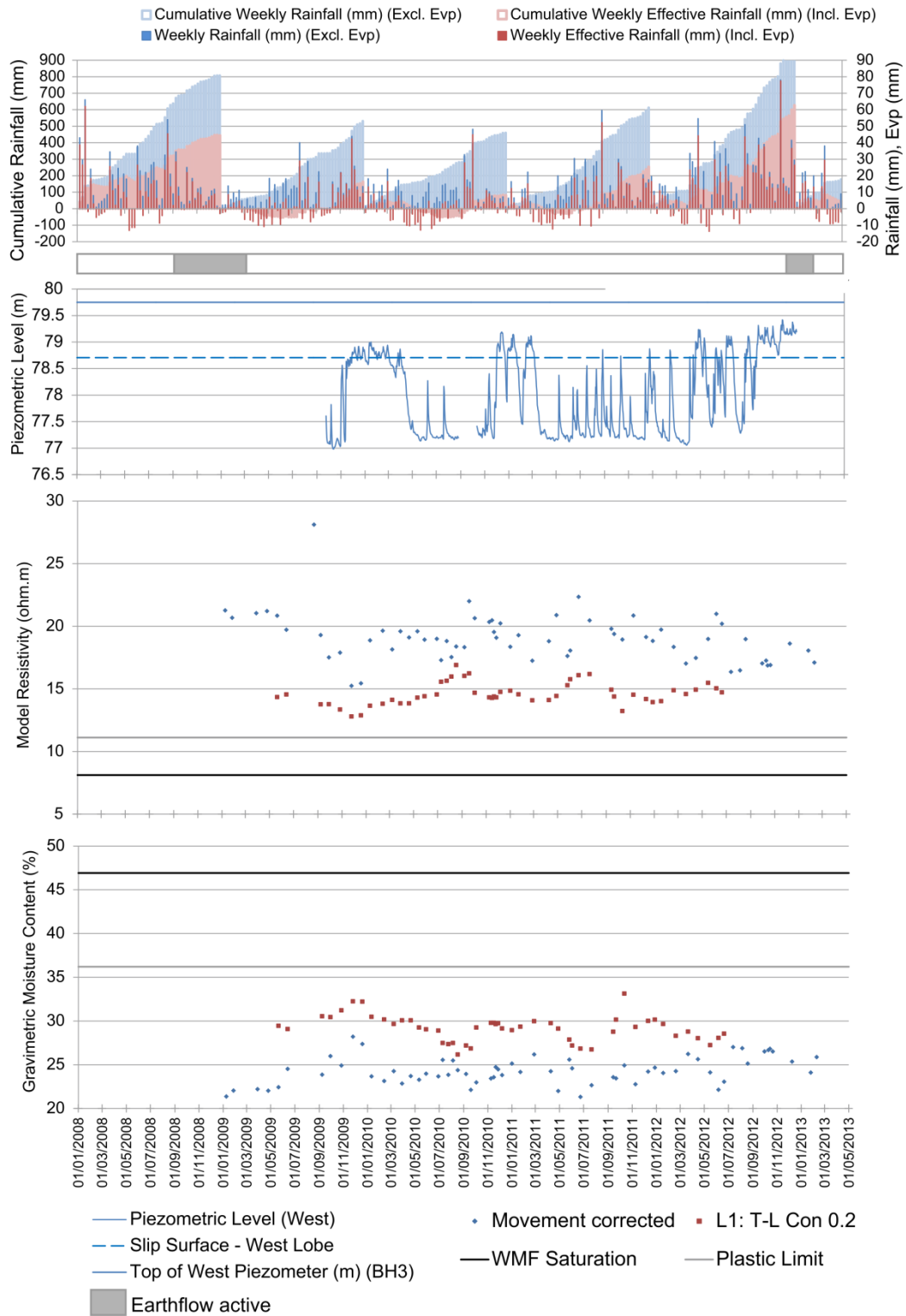


Figure 6.15. Time lapse model resistivity results from the western earth flow region of the landslide system (green region in Figure 6.14)

May to August 2011 is a period of time-lapse resistance rise as piezometric levels fall by 1.9m but fluctuate wildly during this period in response to alternating weeks of positive and negative effective rainfall. Mov-cor resistivities during this four month period show high degrees of scatter and

no apparent trend is observed. September 2011 commences with an abrupt decrease in resistivity from $15\Omega\text{m}$ to $12\Omega\text{m}$ (27% to 30% GMC) in time-lapse data and a similar decrease is also shown by mov-cor resistivity, however resistivity is initially considerably higher. A small increase in resistivity is observed by both sets of resistivity during October 2011 from $12\Omega\text{m}$ to $14\Omega\text{m}$ (33% to 29% GMC) and from $17.5\Omega\text{m}$ to $21\Omega\text{m}$ (25% to 23% GMC) of T-LC and mov-cor resistivities respectively. A particular strong piezometer level rise lasting from mid-December 2011 until the end of January 2012 sees T-LC resistivity slightly decrease before remaining constant for January.

For the following four months T-LC and mov-cor resistivity increases in line with negative effective rainfall and low piezometric level and decreases at times of high positive effective rainfall. Mov-cor resistivity data follows a similar trend, however, it varies over a wider resistivity range between December 2011 and the end of monitoring at the end of February 2013. June 2012 sees T-LC resistivity fall from $\sim 15.5\Omega\text{m}$ to $\sim 14.5\Omega\text{m}$ (27% to 28.5% GMC) until time-lapse data ceases due to activation of the eastern earthflow region in August 2012. According to mov-cor resistivity data, resistivity decreases in the two months leading up to earthflow activation in August 2012 and continues to fall until October 2012 where it rises from $17\Omega\text{m}$ by $2\text{--}3\Omega\text{m}$ (27% to 25% GMC) in December 2012 and then gradually falls by $2\Omega\text{m}$ towards the end of monitoring in February 2013 (24% to 26% GMC).

Model Resistivity & GMC of Eastern Earthflow

Time-lapse constrained and movement corrected model resistivity from the cluster of orange coloured model cells (domain partition diagram, Figure 6.14) of the eastern earthflow region are presented in Figure 6.16.

As was seen in model resistivity data of the western earthflow there is a disparity between mov-cor resistivity and T-LC resistivity of $\sim 4\text{--}5\Omega\text{m}$. Mov-cor resistivity fluctuates slightly from $17.5\Omega\text{m}$ (26% GMC) for the first nine months of resistivity monitoring results and between 01/2009 and 09/2009. Time-lapse resistivity results begin 05/2009 and initiate with a small increase in resistivity of $2\Omega\text{m}$ (up to 28% GMC) before encountering a data gap of

three months between July and September 2009. September 2009 commences with T-LC resistivity increasing by $2\Omega\text{m}$ from $12.5\Omega\text{m}$ (from 34% to 33% GMC) before falling to less than $12\Omega\text{m}$ (34.5% GMC) by January 2010. During the same period, mov-cor resistivity decreases gradually from $17.5\Omega\text{m}$ down to $15.5\Omega\text{m}$ (25.5% to 29% GMC).

This downward resistivity trend occurs in the winter, when rainfall is high and piezometer levels rise by over 1 m in two months. Piezometer levels gradually fall over the next nine months between January and late-August 2010. Time-lapse resistivity increases uniformly during this time from $12.5\Omega\text{m}$ to $16.5\Omega\text{m}$ (34.5% to 27% GMC) and mov-cor resistivities emulate this trend albeit in a much more dispersed manner, increasing from $\sim 16\Omega\text{m}$ to $21.5\Omega\text{m}$ (or, 29% to 22% GMC). The sharp decrease in resistivity in line with four weeks of intense rainfall during October 2010 is also present in model resistivity of the eastern flow region. Comparison with piezometer data during this event is not possible due to a data gap, although immediately after the rainfall intense month piezometer level gradually rises from $\sim 77.4\text{m}$ to reach a peak of 78m during December 2010. November 2010 to February 2011 sees both time-lapse and mov-cor resistivities rise and fall back to their original values at a time when piezometer levels are at a peak. The slight rise in resistivity could be in response to a two week period of negative effective rainfall in late January 2011. Spring 2011 commences with high negative effective rainfall causing a fall on piezometric level between March and June 2011. Mov-cor resistivity increases from $17\Omega\text{m}$ to $\sim 21\Omega\text{m}$ (26% to 23% GMC) and T-LC resistivity also increases, by $2\Omega\text{m}$, to $14\Omega\text{m}$ (33% to 31% GMC).

Piezometric level then rises by 0.3m to 77.8m in response to $\sim 80\text{mm}$ of effective rainfall falling during August 2011 and both resistivity types decrease until the end of 2011, time-lapse and mov-cor decreasing to $12.5\Omega\text{m}$ (34% GMC) and $15\Omega\text{m}$ (27.5% GMC) respectively. January 2012 commences with piezometric level rising from 77.8m to its highest level of the monitoring campaign, 78.4m at the last week of May 2012. The rise in piezometric level is interrupted by small decreases in piezometric level as two to three week periods of negative effective rainfall occur, as can be seen late-March and early-April 2012.

During the same period – January to May 2012 – T-LC resistivity increases uniformly from 12.5Ωm to 14Ωm (32% to 34% GMC), mov-cor resistivity rises and falls in almost exactly the same manner as the piezometric level, and ranging between 16Ωm and 18.5Ωm (29% to 25% GMC).

June to late September experiences gradual piezometric level lowering at a time when rainfall is very high, over 100 mm of effective rainfall fell in the preceding five months and since the start of 2012. T-LC resistivity remains near-constant (32.5% GMC) in the lead up to earthflow activation in August 2012 and mov-cor resistivity decreases from 19Ωm to 16Ωm (25% to 27.5% GMC). While eastern earthflow was active piezometric level continued to fall reaching a low at late-August 2012. Mov-cor resistivity drops after earthflow activation from 19.5Ωm to ~13.5Ωm (23.5% to 34% GMC) by the end of 2012. The last two inversions show that movement corrected resistivity had risen to over 22Ωm (25.5% GMC) by February 2013.

Summary of Model Resistivity & GMC Observations

The following behaviours were identified from analysis of model resistivity datasets and include; time-lapse inverted data varies much more smoothly than movement corrected data which at times varies very abruptly. Model resistivity decreases in response to intense rainfall events and in response to piezometer level rises. Model resistivity reduces in the build up to activation, although there is considerable scatter in movement corrected resistivity results. Mov-cor resistivity is higher during the 2008/2009 earthflow activation period than it was during the 2012 earthflow activation. Resistivity is higher during the summer months when negative effective rainfall is prevalent and conversely, falls during the wetter, winter months.

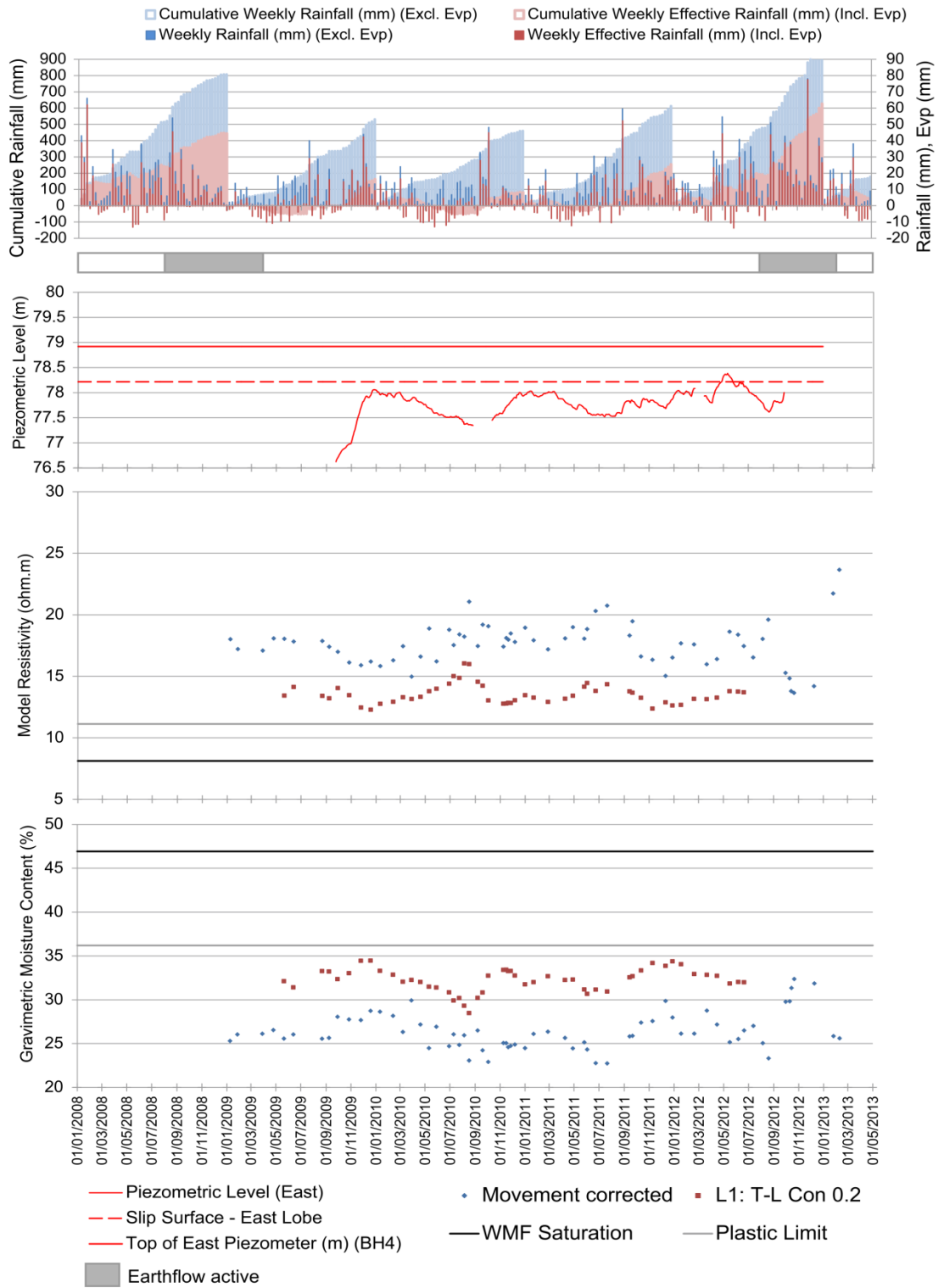


Figure 6.16. Time lapse model resistivity results from the eastern flow region of the landslide system (orange region in Figure 6.14)

6.4.2 Time-lapse Volumetric Images of Gravimetric Moisture

Content

The geophysical method of investigating landslides hydrogeological processes that required the most processing and is therefore furthest from the original, raw, transfer resistance measurements is time-lapse volumetric imaging of gravimetric moisture content. Figure 6.17 displays a selection of these GMC volumetric images during the period leading up to earthflow activation in late 2012. For these images, 3D model inversion was used with applied time-lapse constraints and the images show subtle changes in GMC during the 14 months before activation.

In the 02/06/2011 GMC image, earthflow regions have moisture contents ranging between 15% and 25% and consist of wet regions separated by drier regions. This survey was performed during the summer and at the end of a dry 18 months between 01/2010 and 07/2011, beyond which substantial rainfall takes place. As a wet winter takes hold and after several months of substantial rainfall moisture contents of each earthflow begin to increase further and by 19/02/2012 also appear to be much more amalgamated. summer months do not permit moisture contents within earthflows to decrease as each earthflow remains above 25% GMC and still amalgamated at the 20/06/2012 survey, approximately 6 weeks before earthflow activation.

Looking at the 3D volumetric images of GMC at depths greater than the earthflow deposits there is a red-coloured, high moisture content region, centred at $y=40\text{m}$, $z=60\text{m}$. This feature is relatively small at 02/06/2011 but gradually becomes larger and by 20/06/2012 is arguably at its largest and shows a clear connection between itself and the Redcar Mudstone Formation lithologically located below. This feature highlights the lithological variability of the Staithes Sandstone Formation as the lithologies surrounding this feature consistently have a lower GMC. There could be a hydrogeological flow path between this high GMC region in the SSF and the RMF beneath which becomes a significant flow pathway when the water table is high.

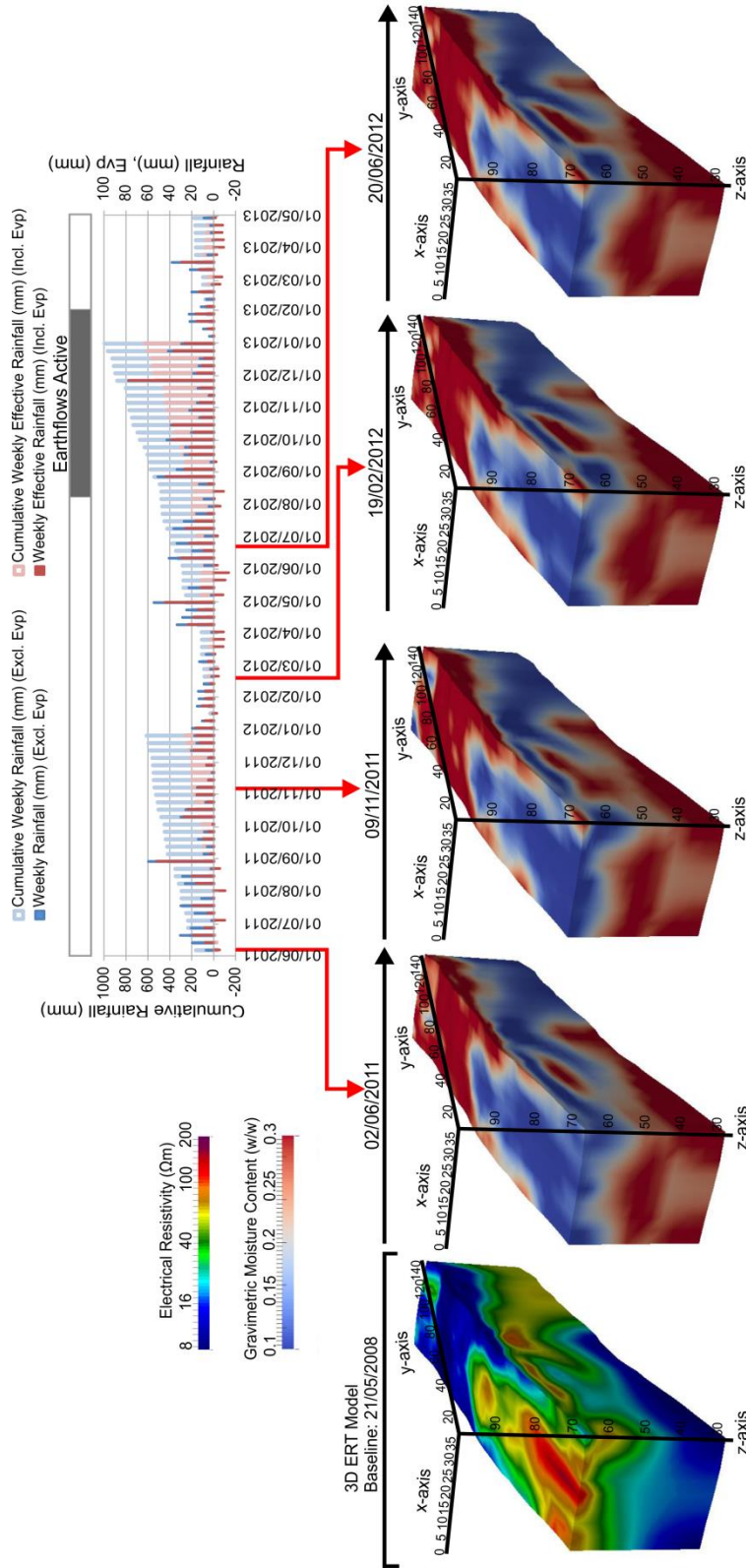


Figure 6.17. Selection of volumetric images of gravimetric moisture content for the period between 06/2011 and 05/2013 and leading up to earth flow activation 08/2012.

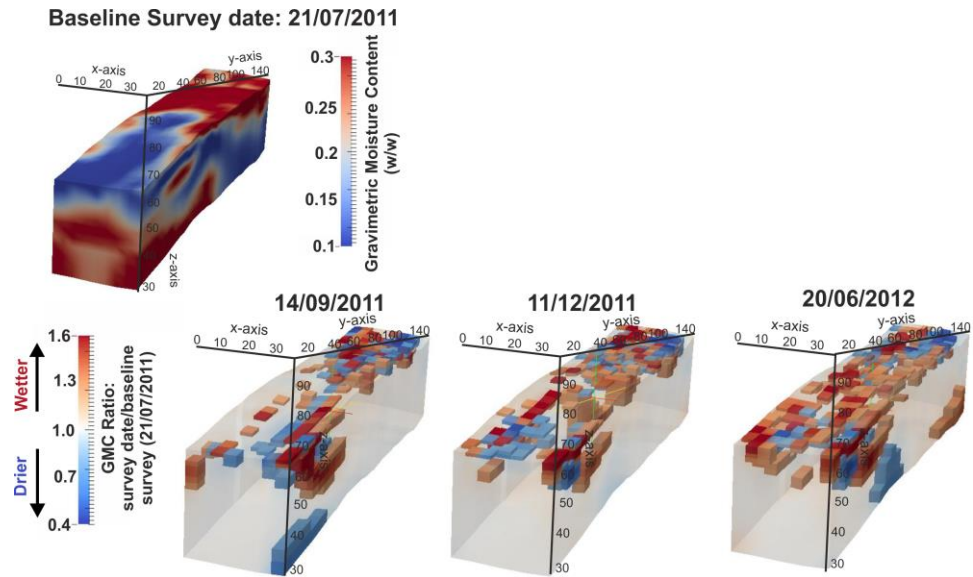


Figure 6.18. Four-dimensional volumetric image of gravimetric moisture content ratio of the low resolution array. Originated from time-lapse constrained model inversions.

Gravimetric moisture content was converted to a ratio by dividing each model cell GMC by model cell values from a reference, baseline survey model. Figure 6.18 shows the results of three volumetric images of GMC ratio from the twelve months leading up to the 2012 activation. Between the baseline survey and 14/09/2011 the domain is seen to several regions which are drier (blue cubes) and wetter (red cubes), and the wetter regions are likely to have developed in response to ~90 mm of rainfall during August 2011. Three months later and after a period of sustained rainfall the 11/12/2011 GMC ratio model shows that considerable, pervasive wetting took place. Pervasive wetting is indicated by larger regions of both surface and deeper red cubes. The final volumetric image of GMC ratio reveals that the subsurface moisture accumulation trend continued for the first six-months of 2012, as the majority of the surface of the model domain is wetter than the baseline image. Drier regions exist near the back scarp, to the north of the domain but has reduced in area from the 14/09/2011 survey. One month after the 20/06/2012 ERT survey the earthflow region of the landslide activated. Thus, the three volumetric images presented in Figure 6.18 show the ability of GMC ratios to monitoring site-scale soil moisture dynamics at the field site, in the lead up to activation.

6.4.3 Matric Suctions

A laboratory investigation into the three way relationship between soil moisture content, soil matric suctions and soil electrical resistivity response was performed and described in Chapter 5. This relationship was then to be used to suggest changes of soil suctions as soil moisture content changed in response to precipitation and water table variation, which would be evident in time-lapse model resistivity monitoring data. However, due to the range of model resistivities and gravimetric moisture contents observed in time-lapse ERT data it is apparent that the range of gravimetric moisture contents, over which soil suctions were determined, are not sufficient to cover the soil moisture content range observed in resistivity monitoring data. Gravimetric moisture content monitoring results converted from time-lapse model resistivity data displayed lower moisture contents than the 12 bar (1200kPa) soil suction plate could reach in the laboratory (Fig 5.37). The range of moisture contents produced by suction plate laboratory testing of earthflow silty clay material (from BH5 0.40m) was 31% (at 1200kPa) and 49% (at 100kPa), which equates to a model resistivity of 7.5 Ω m and 14 Ω m. The reason for the discrepancy between field geophysics-derived GMC and laboratory-derived GMC is because of the model resistivity values being affected by the more resistive SSF formation beneath. This acts to increase resistivity and hence decrease the field geophysics-derived GMC. Field suctions are likely to approach zero after infiltration which signifies that field geophysics-derived GMC is lower than actual field GMC.

6.5 Discussion

Analysis of monitoring results has produced a number of features related to each monitoring method and these features are described herein. The discussion section describes the features observed in each of the monitoring data sets, starting with conventional ground monitoring methods such as piezometry and ending with monitoring gravimetric moisture content. The Discussion section is brought to a close by summarising the processes taking place within the Hollin Hill field slope and assesses the suitability of the implemented monitoring methods for slow-moving, shallow earthflows.

Piezometer

The piezometric record pertaining to the western piezometer – installed within earth flow deposits – has a very distinct form, piezometric levels vary very sharply and abruptly in response to rainfall events. Water levels commonly respond to rainfall in a matter of days and can rise by over a metre during this time period and this process is particularly apparent between May 2011 and April 2012. Water levels lower after a sudden rise. This reduction is almost an exponential decline, reducing rapidly initially before tailing off as the lowest, baseline water level is approached. When analysed in conjunction with rainfall data, in particular effective rainfall plots, there is correlation between periods of negative effective rainfall and piezometer level lows. Conversely, periods of sustained positive effective rainfall see the piezometric level rise in response to substantial weekly rainfall.

An example of the former scenario is evident between March 2011 and June 2011, and the latter scenario between November 2009 and February 2010. Although periods of prolonged and intense effective rainfall do cause the piezometric level to rise sharply and remain high as is visible late 2009, also, periods of sustained but lower intensity rainfall have the effect of raising the piezometric water level in the eastern flow region, however these events are followed by a fall in water level shortly after the rainfall episode has terminated (See mid-November 2010 to mid-March 2011). Prolonged rainfall events taking place between August 2011 and January 2012 do not show this trend of sustained piezometric level rise in response to intense and prolonged effective rainfall as is evident in 2009 and 2010. This could be due to summer of 2011 being particularly dry, drawing moisture from the soils and creating capacity for the autumnal and winter rain events of 2011. This process is feasible because the wet period extends well into 2012 and the piezometric water level can be seen to begin to remain high between March 2012 and September 2012. The summer of 2012 shows very few periods of negative effective rainfall, where soil moisture could be removed from the subsurface, as a result the overall moisture content of the slope was probably consistently increasing during this period. In accordance with the process outlined this could explain the sustained piezometric high recorded

in November 2009 and May 2010, the previous year, 2008 shows considerable annual cumulative effective rainfall which would have drawn the soil closer to saturation. The rainfall event of the six month period just outlined would act to top-up the already nearing saturated soil, resulting in the piezometer level remaining high due to ineffective soil water drainage.

The seemingly flashy nature of the piezometric level within the western flow region can be explained in terms of the presence of a sandy layer located below the Whitby Mudstone Formation composed earth flow deposits of the eastern flow region. This sandy layer acts as a drainage pathway for soil moisture which travels downwards through the predominantly clay-composed Whitby Mudstone Formation flows, maybe through cracks or fissures formed by desiccation during the Summer months. The sustained high piezometric levels described above can only occur when the clay-composed WMF flows release their soil moisture at a rate higher than the sandy layer below permits drainage.

The piezometer positioned on the eastern earthflow region is markedly different to the western earthflow region. The eastern piezometer builds up much more gradually over a longer period of time relative to the western piezometer. Piezometer levels build up gradually because of the impermeable nature of the earthflow deposits and due to the lack of sandy earthflow present in the western earthflow region. The range over which piezometer level varies is considerably less for the eastern piezometer compared to the western piezometer, which have a range of 0.8 m and 2 m respectively. It is thought that the eastern piezometer is less able to respond to sudden intense rainfall events because the water flow network isn't as well developed most probably due to the lack of sand-dominated earthflow and less well developed crack network.

Observation of water level trends in the lead up to earthflow activation suggests that east and west flows respond differently to pore pressure variation. Pore pressure of the eastern earthflow increases by 3-5kPa between April and May 2012 before reducing to level of the of active slip surface in the month before activation begins. Piezometric levels continue to fall by 0.5m (~5kPa) while the landslide is active. The western earthflow

behaves differently as it activates after a 0.1-0.2m rise on piezometer level (1-2kPa increase in pore water pressure) and remains relatively high and stable while the flow is active.

Piezometer levels are a function of rainfall infiltration, as described by the hydrology model (reference), but in addition to infiltration, rainfall can also runoff the surface of a hillslope when rainfall intensity is greater than the rate of infiltration in to the soil (Fookes et al., 2007) or when soil is saturated. Therefore, effective rainfall, total rainfall minus evapotranspiration, alone may not sufficiently describe the quantity of rainfall infiltrating to the groundwater.

Runoff can occur in two scenarios, the first is referred to as Hortonian and the second, Dunne runoff (Kollet et al., 2005). Hortonian runoff (infiltration excess overland flow) occurs when rainfall rate exceeds the hydraulic conductivity of the land, thus preventing rainfall from infiltrating. Infiltration excess overland flow begins to occur in the lowest permeability and wettest materials (Beven., 2012). Dunne runoff, or saturation excess overland flow, occurs when the rainfall rate is less than the hydraulic conductivity of the land surface. In this scenario, ponding and surface flow occur when the soil is completely saturated. This process tends to occur in valley bottoms and where soil moisture deficit is small.

The geological units at Hollin Hill were not sufficiently studied to make a conclusive interpretation as to whether, if at all, either Hortonian or Dunne were taking place. However, it is likely that both processes were taking place at various regions of the landslide system and slope as a whole. Piezometer levels never quite reach the ground surface as the eastern piezometer level reaches a high of 0.5m below the ground surface. Some rainfall events were sufficiently heavy that rainfall rate outpaced hydraulic conductivity and therefore infiltration rate. Thus inferring that any runoff is most probably due to Hortonian processes.

The uppermost tens of centimetres of the hillslope may become saturated during extended periods of rainfall and, therefore on occasions, Dunne runoff may also be taking place. However, it should be noted that rainfall

very rarely exceeds infiltration rate unless the surface is completely saturated (Beven., 2012).

Runoff was estimated for Hollin Hill using the *US Soil Conservation Service Method* (USSCS, 1972) and the three largest rainfall events which took place during the four and a half year monitoring programme modelled runoff values of:

Date of Rainfall Event	Rainfall (mm)	Evapotran. (mm)	Effective Rainfall (mm)	Runoff, Q (mm)	Runoff Percentage of Eff Rainfall (%)
25/09/2012	38.4	1.8	36.6	6.0	16.4
29/11/2009	30.2	0.0	30.2	4.0	13.2
06/07/2012	29.8	2.2	27.6	2.0	7.3

Table. 6.1. Calculations of hillslope runoff modelled from US Soil Conservation Service Method (1972).

The results presented in Table 6.1 reveal that even the most intense of rainfall events and using the USSCS model for estimating runoff only 16% of rainfall is converted to overland runoff.

GPS Survey of Peg Displacement

Repeat surveying of an array of survey pegs located in a grid throughout the landslide system informs about when pegs have displaced which in turn is inferred as being due to landslide deposits re-activating. The frequency of repeat GPS surveys dictates the temporal resolution of the monitoring method. Therefore, exact date of landslide activation is only possible if pegs are surveyed on a daily basis, which did not take place. Landslide activation date can only be narrowed down to having occurred between the date of the previous survey and the survey which shows displacement, in this investigation peg surveys were performed every two to four months.

Transfer Resistance

Plotting of raw transfer resistance monitoring data – without any form of processing – showed many of the large scale trends, such as sudden resistance decrease in response to summer rainfall events (August 2010) but subtle resistance changes are masked by seasonal air temperature variations which penetrate the subsurface. The sinusoidal nature of transfer

resistance variation in response to air temperature acts to reduce resistance in the summer months when air temperature is higher than the annual average temperature and increases resistance in the winter months when air temperature is lower than the annual average. This process is affecting all resistance measurements but is particularly visible in dipole measurement 1(12.5) of line 1.

Measured transfer resistances are systematically higher at the toe of earthflows when compared to the top. This is due to low resistance WMF-composed flows being thinner at the toe and therefore resistance measurements are sensitive to more of the underlying SSF. Earthflows become considerably thicker upslope (30-40 m upslope of earthflow toe) and so for a given dipole size (here, $n=1$, $a=1$ gives a median depth of investigation of 1.9m for a 4.75m electrode spacing) each measurement encompasses less underlying SSF and more WMF-composed earthflow. For example, dipoles 5(6.5) and 5(8.5) both recorded first resistance measurements of 0.4Ω , whereas, heading upslope dipoles 5(10.5) and 5(12.5) measure 0.3Ω and 0.2Ω respectively.

Periods of landslide activity cause electrodes to mobilise, resulting in geometries of individual resistance measurements changing. This process manifests itself in resistance monitoring data as an immediate and steep increase or decrease in resistance. These resistance jumps during phases of landslide activity are demonstrated by dipoles 1(8.5) between October 2008 and March 2009 and by all dipoles of line 1 between January and February 2013. Analysis of resistance data can therefore be used to 'date' periods of landslide activation which manifest because of variations in electrode measurement geometries.

Another intriguing trend spotted while analysing raw transfer resistance results is the interplay between increased rainfall infiltration during winter months and the effects of seasonal temperature variation, which overprints the rainfall-induced fall in resistance with a cold-induced resistance increase. This has been termed a 'double resistance dip' by myself and colleagues at the British Geological Survey and is displayed by dipoles 5(8.5) and 5(10.5) between October 2009 and May 2010.

Temperature corrected transfer resistance

The sensitivity of the ERT monitoring system to soil moisture accumulation and water table level variation highlights an interesting process taking place in the months preceding earthflow activation (highlighted in Figure 6.19). The system successfully identified the fall in piezometric levels, which manifested as an increase in resistance in the lead up to earthflow activation. This feature can be explained due to drainage occurring along the slip surface as the surface progressively activates and, partially/completely, drains the earthflow. The western earthflow experiences a small decrease in water level in the 3-4 weeks leading up to flow activation, and lowers to the level of the slip surface before rising again as the earthflow is active. Resistance can be seen to increase during the slight decrease in water level.

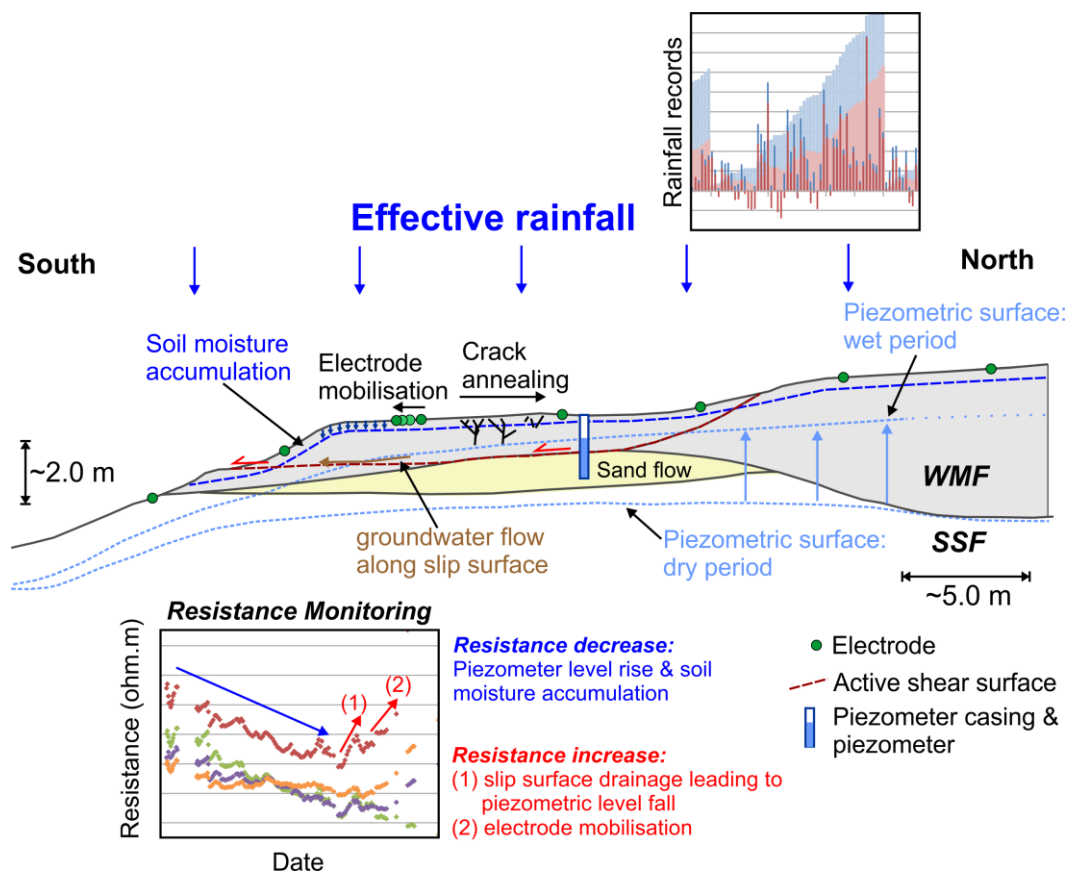


Figure 6.19. Response of electrical resistivity monitoring results to both subsurface processes and landslide activation. Sand flow exists within western earthflow.

The eastern earthflow experiences a fall in water level in the two months leading up to flow activation and is associated with an increase in resistance and is attributed to slip surface drainage. A month into earthflow activation (September 2012) rainfall begins to top-up the water level once again as resistances briefly fall during September and October 2012. November onwards marks a time when electrodes are mobilising and is represented on temperature corrected plots as divergence and jumps in resistance values.

Figure 6.18 also depicts an additional feature of the eastern earthflow resistance results, that, when piezometric levels are not at their lowest, they almost perfectly mirror piezometer level, thus indicating that the most surficial measurement dipoles are imaging bulk changes in hill slope water table level which for the vast majority of the monitoring period is below the active surface of each earthflow. When piezometric levels are very low small rainfall events cause rapid resistance decreases. However, some small rainfall events are not picked up by piezometry and result in small changes of resistance, indicating the sensitivity of the system to moisture infiltrating only the uppermost few centimetres of earthflows. This process is seen in Figure 6.12 of the 'Analysis of 2012 landslide activation' section during the 3rd week of July 2011. Thus indicating the sensitivity of the monitoring system to resistance changes are a hybrid of bulk hill slope hydrogeology, which are overprinted by less obvious, parasitic resistance changes associated with more surficial rainfall infiltration processes. Therefore the ERT monitoring system is versatile enough to image two separate hydrogeological subsurface processes taking place.

Several natural processes also take place in the near surface and are outlined herein. When looking at temperature corrected resistances from individual measurement dipoles it is apparent that dipoles located within the toe of earthflows demonstrate a greater range of resistance ratios (and resistances) when compared to dipoles located within thicker successions of earthflows.

For example, the difference in the manner in which resistance measurements taken by dipole 5(6.5) responds to changing environmental inputs, such as rainfall, compared to resistance measurements taken by

dipole 5(12.5) in Figure 6.8. Pervasive and deep cracking hinders subsurface current flow, by presenting obstacles to flow, and increases resistances taken in the vicinity of cracking. This trend of more elaborate resistance responses to environmental factors is attributed to thin earthflow regions being more susceptible to pervasive desiccation during dry summer months. They are more susceptible because the shear surfaces between individual flows act both as a conduit for water drainage, assisting flow through and out to underlying formation, and as an aid to joining up desiccation cracks and encouraging their development. The opening of cracks is thought become more effective as the dry spell progresses, as cracks open up the ground to further drying and causes resistances to continue increasing. A point is reached where resistances reach a summer peak at around August/September as further desiccation is cut short by the onset of increased rainfall events.

During rainfall events it is at the cracked regions where run-off enters the subsurface, where it can accumulate within earthflow and flow through cracks into the SSF below. Dipoles located within thick earthflow successions seem more able to retain moisture and as a result are less susceptible to pervasive and deep cracking. Thick successions of earthflows are more able to retain water because they have fewer water drainage paths and are often located on less steep slopes, reduced run off therefore provide more time for surface water to penetrate the ground. Desiccated earthflow toes may permit more fluid to enter the subsurface when compared to less desiccated thick successions of earthflows, however, very little soil moisture is retained by these cracked regions and as a result resistances made in these regions rise and fall sharply.

Laboratory calibration of soil moisture – resistivity relationships has identified an electropetrophysical factor that could make the conversion of electrical resistivity to GMC for clay slopes potentially non-trivial. From Figure 6.19 and the outcome of laboratory experimentation (Chapter 5) it is apparent that at higher moisture contents resistance plots appear less responsive to rainfall and wetting up events, due to the shape of the electrical resistivity-moisture content curve. Electrical resistivity varies much less profoundly with increasing moisture content, and could make field resistivity systems less

sensitive to the subtle differences in resistivity when the slope is wet that landslide imaging is focussed on. Therefore, with resistivity varying by very little at high GMC any additional outside influences could have substantial effects on field measured electrical resistivities. Conversely, resistances respond rapidly and abruptly to decreases in soil moisture content and in addition with cracking effects.

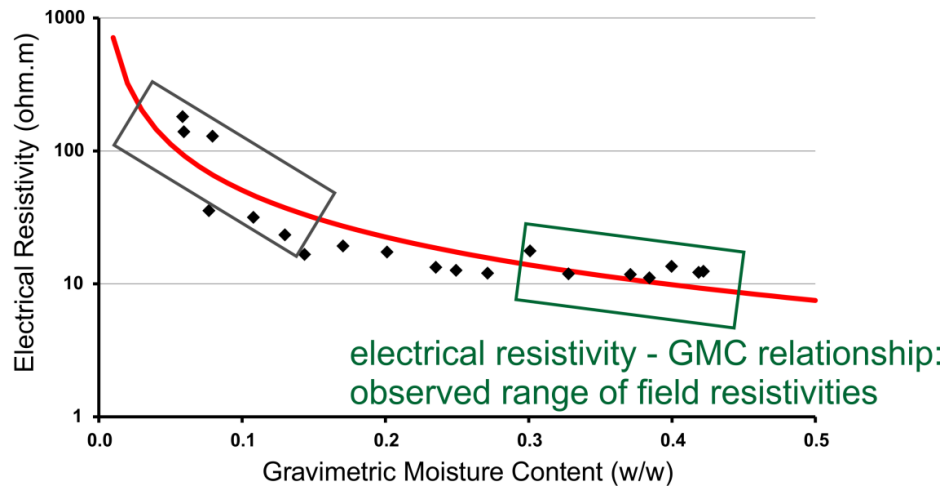


Figure 6.20. Schematic describing less responsive nature of resistivity measurements at higher gravimetric moisture contents.

Resistances decrease to their lowest levels both during periods of landslide activation and inactivity. For example, Figure 6.8 of temperature corrected transfer resistances from line 5 are at their lowest values on three occasions; 09-12/2008, 12/2009-05/2010 and 07-11/2012. Earthflows are active at two of these three low resistance periods, indicating that the presence of resistance/resistivity thresholds, below which landslides activate, are either not applicable at this landslide type or that the array is not successfully imaging the desired slope property.

Resistances from dipoles located further up slope react less suddenly and abruptly to negative effective rainfall as a result of less pervasive cracks existing within the slumped regions of the landslide. The slumped region dips less steeply than earthflow regions, precipitation therefore has the time to penetrate the subsurface and not run off. The region of the survey area where resistances vary the least is in the North East of the survey area, slumps in this region are back rotated and allow moisture to accumulate and

penetrate almost constantly, thus maintaining low resistances throughout the year.

Temperature correcting raw resistance monitoring results using Hayley et al (2010) makes interpretation of resistance results much more straightforward as one major external process which seasonally affects resistance has been estimated and removed. Resistance trends from individual measurement dipoles are more informative about the processes that lead to landslide activation. By altering the procedure outlined by Hayley et al (2010) to model a correction ratio for every transfer resistance dipole measurement, as oppose to modelling a single correction factor and applying it to all transfer resistances, the method was adapted to be more applicable to monitoring landslides, because dipole geometries change when activated.

Inverted Model Resistivity

As can be seen in model resistivity results in Figures 6.15 & 6.16 a consistent difference in time-lapse and movement corrected model resistivity is present and is created during the inversion modelling process. This offset is most probably introduced by the time-lapse constraints function in Res3DINV modelling software, which acts to smooth the resistivity changes between resistivity surveys. By inverting resistance measurements again and maintaining a constant mesh (i.e. not accounting for electrode movement) and without applying time-lapse constraints would most probably produce inversion results similar to the movement corrected inversion results. Another explanation – although less likely to have an effect as inversion settings were standardised between models – is that the mesh is different between inversion methods (time-lapse and standard inversion). Whatever the cause, the offset between model inversion results has ramifications for this investigation as resistivity is converted into estimates of moisture content which are reliant on accurate model resistivity data.

Movement corrected resistivity show a high degree of scatter in outputted model data. This scatter is attributed to the model cell mesh geometries, and hence the volume over which resistance is averaged, which are allowed to change between surveys, thus model cells change shape as the landslide system evolves temporally.

Time-lapse constraints incorporated during the inversion process act to dampen the resistance difference between cells in adjacent surveys and so produce a smooth transition between resistivities between similar cells in adjacent surveys. However, applying time-lapse constraints on data could reduce the accuracy of actual model resistivity, and hence cell moisture content, by applying an artificial, arbitrary dampening factor to raw resistance data during the modelling process. Any further advances in time-lapse constraints should take into account actual field and laboratory calibration so as to avoid losing accuracy at the expense of artificially reducing scatter. The application of dampening factors such as time-lapse constraints acting to minimise time-lapse resistivity development is a strange concept; to dampen the most interesting and relevant part of the investigation could seem a strange concept to some. However where scatter exists within movement corrected model resistivity data time-lapse constraints make data trends much easier to identify.

As was observed in resistance results, inverted resistivity respond to snow and frost in both eastern earthflow region and western earthflow region as a rise in resistivity of 2-3 Ω m. Frost at Hollin Hill would not penetrate deep, up to 0.1-0.2m, therefore the resistivity rise is caused by contact resistances at the electrode-soil boundary.

Model resistivity monitoring results show that earthflow soils do not reach plastic limit at any time during the monitoring campaign, let alone during periods of landslide activation. This could be due to one of two reasons; firstly, internal earthflow consistency may not be an important factor in earthflow activation processes because of the dominance of shear displacement along basal shear surfaces. Slow moving earthflow movement is triggered along wet and weak shear surfaces, therefore the bulk of the earthflow material could possess a moisture content lower than the shear zone and still the flow would activate.

The second reason could be that the imaging technique is incorporating the higher-resistivity SSF into its computation of cell resistivity of earthflow located model cells, and artificially making the flows appear to have lower moisture contents. A soil sample extracted from an earthflow shear surface

during a site visit in October 2012 and subjected to plasticity index testing revealed that the sample had a moisture content of 46%, very close to the liquid limit of the soil. As ground truth information suggests that shear surface material is ~1% GMC less than liquid limit suggests that estimates of GMC by inverted resistivity conversion under estimates soil GMC and is again most probably due to the influence of more resistive underlying Staithes Sandstone Formation. This issue has been remedied by the installation of a higher resolution ERT array at the western earthflow area.

Model resistivities pertaining to western earthflows are consistently higher than those pertaining to the eastern earthflow and are caused by the influence of the sand earthflow increasing the bulk model cell resistivity of the western flow region.

The reason for model resistivity rising between February and June 2012 despite high rainfall and associated piezometric level rising to a four year high is unknown. Plots of temperature corrected resistance from individual dipoles of the earthflow regions are all decreasing during this timeframe and in theory should follow suit.

Gravimetric Moisture Content & Matric Suctions

Producing plots pertaining to clusters of earthflow model cells and also volumetric images of GMC show much promise if the purpose of imaging is to observe landslide hydrogeological processes. For example, Figures 6.15 and 6.16 show a rise in GMC followed by a fall in GMC in the lead up to earthflow activation and is consistent with trends seen in piezometry measurements (and temp. corr. resistance). Comparison between Figures 6.17 and 6.18 highlight the progressive wetting up of the near surface of the hill slope during the 12-month build up to the 2012 activation. Plotting GMC ratio appears to be successful at clearly displaying general hill slope dynamics, whereas 'absolute' GMC can mask the subtle variations in GMC. Although, time-lapse images of 'absolute' volumetric GMC were difficult to analyse and interpret, when plotted as GMC ratios, relative to a baseline survey, soil moisture accumulation trends became much easier to identify. It is therefore highly recommended to make use of GMC ratio if observing temporal soil moisture dynamics is the property of interested.

However, due to the nature of the electro-petrophysical relationship between soil electrical resistivity and moisture content – as described by Archie's law and Waxman-Smits Equation – an increase in model resistivity transforms to a decrease in soil/rock moisture content.

At the highest moisture contents and approaching a saturation of 1, electrical resistivity varies very little with large changes in moisture content. With this in mind, the suitability of utilising electrical resistivity as a proxy for moisture content is called into question. This is not an issue that only affects this investigation but will likely hinder all electrical resistivity monitoring investigations of clay slopes.

The GMC range produced by conversion of model resistivity monitoring data and Waxman-Smits calibration was 35% and 21%. The reason for GMC results not falling within the range of moisture contents produced by the 12bar pressure plate is due to the way in which GMC is derived from model resistivity monitoring results. Model resistivity monitoring data are converted to gravimetric moisture content via the application of a laboratory calibrated petrophysical formula called Waxman-Smits equation. When upscaling this relationship to field ERT measurements other factors come into play, such as cracking, and the influence of higher resistivity underlying formations, such as Staithe Sandstone Formation.

None of those are taken into account by Waxman-Smits, therefore, any increase in resistivity due to these factors would result in a lower GMC than if the cracks/more resistive formation were not an influencing factor. This technique of converting subsurface electrical resistivity to moisture content, and then to a soil matric suction would be more effective if earthflow model cells were smaller and were unaffected by cracking or underlying more resistive units could be avoided. Despite the influence on data by the underlying formation, monitoring results are still very informative. Plotting and analysing ratio data, i.e. resistivity-ratio or GMC-ratio this problem can be largely eradicated.

Any processes which affect raw transfer resistance will also be carried through the processing streams and affect both model resistivity and

gravimetric moisture data also. The key factor is to take quality and meaningful raw resistance data.

6.6 Suitability of ERT monitoring of slow-moving earthflows

The ERT monitoring system responds very well to piezometric level variation, as resistance/resistivity are low during piezometric highs (and vice-versa). Piezometer levels in the eastern earthflow region reach a peak two months before earthflow activation and continue to lower after activation. The ERT system observed that water table levels might begin to reduce before earthflow activation because the shear surface is beginning to act as a conduit for fluid flow and therefore drainage. The fall of piezometric level in the lead up to landslide activation was observed by Dixon et al (2002) within the London Clay coastal cliffs of the south-east coast of the UK. The electrical resistivity monitoring system observed the increase of resistivity in the lead up to earthflow activation, which occurred coincident with falling water level. The usually very flashy and responsive piezometric level in the western earthflow must only remain high in the lead up to and after activation because soil moisture input is greater than the soil moisture outflow rate.

The system responds to rainfall events and soil moisture accumulation in the subsurface, however, determination of whether it is piezometric rise or moisture accumulation in subsurface that causes a resistance/resistivity decrease is very difficult to decide. Using a resistivity tomography array that contains several model layers between the surface (Figure 6.21) and the periodically active shear surface would go a long way towards understanding which hydrogeological process contributes to resistance/resistivity changes. A higher resolution ERT array could be implemented to observe rainfall infiltrating through the earthflow region and to the water table and also show moisture content accumulation within earthflow lobes themselves. Surficial regions might show more clearly the effects of crack formation during drier spells and crack annealing during wetter periods. The effects of cracking are believed to be identifiable in monitoring results of this investigation but a higher resolution array would shed more light on crack depth and lateral extent within earthflows.

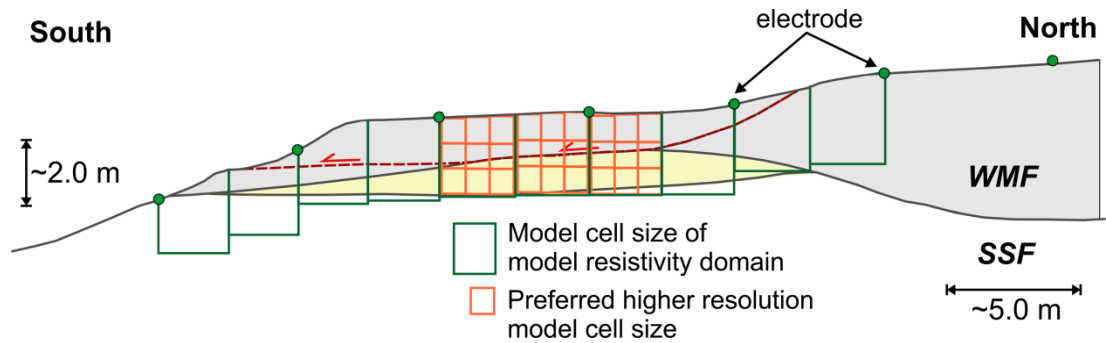


Figure 6.21. 2D ground model describing recommended relationship between dimensions of flows and resolution and size of model cells.

As lowest resistances/resistivities occur during periods of slope inactivity this brings into question the suitability of the use of threshold values, below which the slope will activate, at the Hollin Hill landslide, purely due to the complex nature of the landslide system.

The plotting of individual measurement dipoles is successful at providing detailed information, at a high temporal resolution about subsurface changes in electrical properties but is limited by the relatively small region of the subsurface 'sampled' by each measurement. Increasing the volume of subsurface imaged can of course be increased by changing the dipole geometry, i.e. increasing the distance between the two current and two potential electrodes (the n-number), This is believed to not be beneficial to this investigation as the aim is to observe hydrogeological processes taking place within landslide, increasing n-number would image more stable material on which the earthflows overly.

On the other hand, temperature corrected resistance maps are much more informative at revealing spatial, near-surface, resistance variation within a resistance survey. When several adjacent surveys are presented side by side lateral resistance trends are easily visible. Instead of plotting total temperature corrected resistance, resistance difference relative to a baseline survey makes small resistance changes much more apparent. A caveat of resistance maps is the inability to present results at high temporal resolution. Each individual dipole plot is composed of ~650 survey points for each dipole measurement, To get a similar resolution using maps would fill approximately 60 pages of A4-sized paper. Resistance maps are beneficial

at showing small degrees of resistance variation within slope material. For example, the 'un-reworked' slump region of the landslide, located between the top of the earthflows and the back scarp at the top of each resistance map. This small resistance variation could be attributed to the soil moisture varying very little throughout the year. Its small resistance variation and lack of rainfall infiltration and flow pathways potentially indicates that the slump region of the landslide holds on to its moisture and doesn't freely release it like the heavily cracked earthflow region.

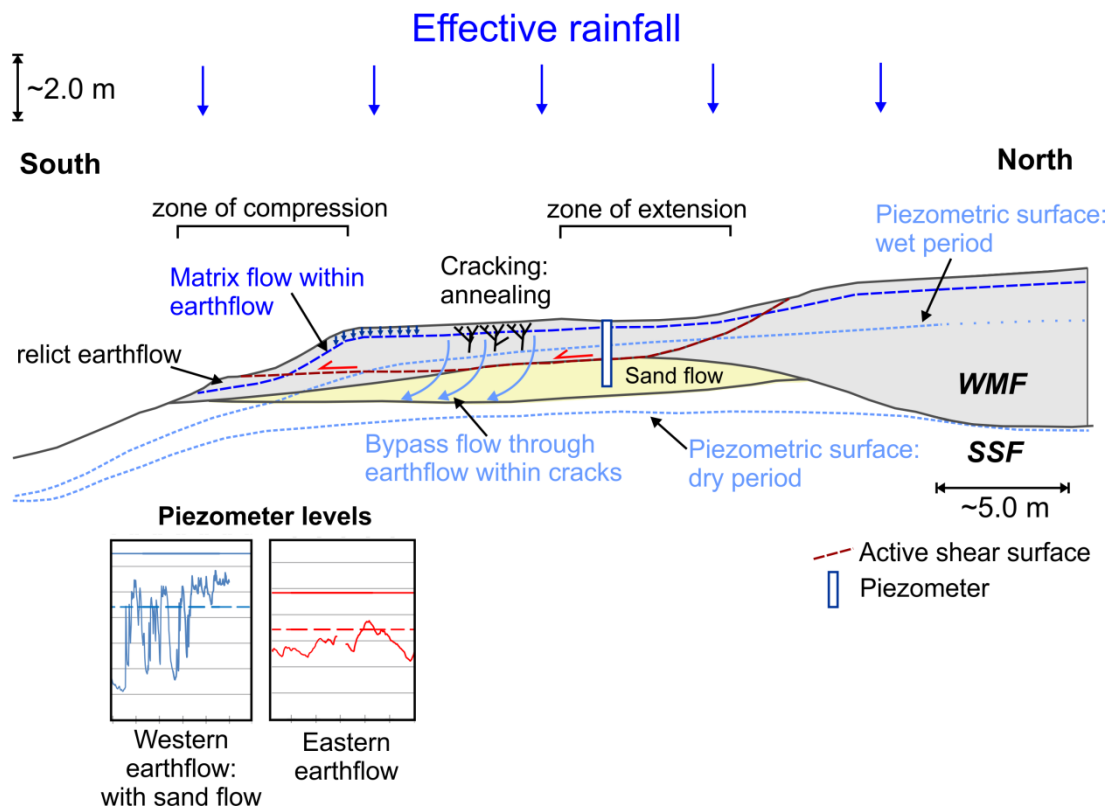


Figure 6.22. 2D ground model describing activation mechanism of slow-moving, shallow earthflows of the Hollin Hill landslide system, North Yorkshire.

It should be reiterated at this point the principal cause of slow moving earthflow movement, which is along a basal shear surface and as a result of a decrease in basal shear strength along that slip plane (see Chapter 2 for details). The effective shear strength along this shear plane decreases as a consequence of approaching water saturation and the associated pore water pressure change. The ERT monitoring system is capable of observing this

principal mechanism of landslide activation, which is, in response to high and sustained piezometric level. This leads to soil moisture suctions dissipating and weakening along principal shear surfaces. Figure 6.22 displays the subsurface response to rainfall events and the processes which lead to earthflow activation.

Soil water saturation within earthflow region can rise because of two processes taking place, these are:

- 1) Rainfall infiltration during periods of high effective rainfall leading to wetting up from the ground surface downwards
- 2) Rainfall preferentially infiltrating the phreatic zone via bypass flow through desiccation cracks, with minimal wetting up of earthflow, until reaching the water table, causing it to rise.

Earthflow activation is principally associated with high water table levels which saturate shear zone material, reduce shearing resistance (resisting forces) of shear zone material and earthflow activation ensues. Minimal earthflow displacement is attributed to internal deformation and so, although soil moisture accumulation will take place within earthflow deposits, if effective stress conditions are assumed, this accumulation will only contribute to the driving forces (promoting shear failure) because of the increase weight of that rainfall contributes to the sliding mass.

6.7 Conclusion

When applied in the context of observing landslide processes, time-lapse 3D ERT makes use of its sensitivity to variation in moisture content in the subsurface. ERT monitoring only informs about the manner in which the slope responds to rainfall infiltration and soil moisture accumulation, and not about the response of the landslide itself. Landslides respond to changing ground conditions, i.e. rising water table or soil moisture content reaching plastic limits, which can bring about a change in internal physical properties, such as soil strength.

This investigation confirms the suitability of ERT monitoring for observing landslide hydrogeological precursors, however, the sensitivity of the system must be harnessed in the right way, and must image the area of interest at a

high enough resolution, to observe the features of interest. Many environmental and physical processes are taking place in the near subsurface that take place alongside one another and act to emphasise or nullify the processes of interest. If observing landslide hydrogeological precursors then soil moisture content accumulation is the target process to observe, seasonal temperature variation and electrode displacement are the processes which need to be accounted for.

This investigation has shown that electrical resistivity monitoring as a technique for observing hydrogeological precursors to landslide activation has a definite future being used to observe soil moisture infiltration and movement at high resolution. Presently, the current system does not allow direct measurement of the principal driving mechanism of shallow earthflows i.e. the reduction in effective normal stress due to increasing pore water pressures. However, the capability of observing increased moisture content with time is a powerful tool for landslide forecasting when combined with additional *a priori* geotechnical data.

The final chapter (Chapter 7) draws this thesis to a close by stating the 'lessons learned' from the project and also potential hypotheses to progress the research area in the future.

Chapter 7

Recommendations & Guidelines for geoelectrical monitoring of landslides

A comprehensive ground model including ground displacement information is useful for directing the positioning of electrical resistivity monitoring equipment. When using three-dimensional ERT methods, it is advised to install the array to allow the active region of the landslide to be observed and monitored in all three-dimensions.

Resolution of geophysical images must be sufficient to permit the observation of the processes of interest. Sacrificing overall areal coverage in favour of concentrating resolution on the most active regions of the landslide is advisable because a geographically focussed monitoring campaign provides data more capable of being comprehensively analysed. The model cell size of the most interesting region of this investigation is thicker than the thickness of the feature of interest, thus only allowing interpretation on bulk earthflow properties. Bulk properties can mask the finer details of subsurface processes and can limit their interpretation. A focussed investigation would allow *intra*-earthflow features and processes to be observed, such as the interplay between matrix and bypass flow, seasonality and depth of cracking effects.

Brunet et al (2010) and Friedel et al (2006) imaged at a resolution ten times greater than that utilised in this investigation, a 0.5 m spacing as opposed to 5.0 m. Higher resolution would permit more informative observation of the two-tier hydrogeological system; effects of surface cracking allowing piezometric levels to rise rapidly and the increase in surface moisture content which acts to close those conduits to flow (as outlined in Section 6.5). High resolution ERT monitoring of the Hollin Hill landslide would shed more light on falling water table level as the earthflow activates by observing moisture content increases in the slip surface region.

There is no doubt that the Hollin Hill landslide system is complex, with many phases of activity most probably dating back several millennia, perhaps even

to the last glacial maximum, which ended c.10,000 years ago. Testing the suitability of ERT monitoring of hydrogeological precursors to landslide activation on a more classical, more homogeneous landslide (such as the Higher Sea Lane landslide, Dorset, or the Blackgang Chine landslide on the Isle of Wight), rather than a complex, potentially glacial-process formed landslide such as Hollin Hill. Very slow moving earthflow-debris-flow type landslides are rare in nature, as the majority of flow type landslides occur as intense, rainfall-induced rapid debris flows within highly weathered soils in tropical climates (Iverson, 2000).

An interesting way to take this research forward would be through a combination of high resolution resistivity monitoring of earthflows, installed alongside an array of tensiometers. Tensiometers should be installed vertically between the surface and beyond the periodically active shear surface and would inform about the evolution of slip surface pore pressures, or dissipation of matric suctions in clays, in the lead up to landslide activation. The upwards migration of the water table could be monitored by tensiometers installed at depths greater than the shear surface. This installation would aid understanding of suction dissipation and evolution during slope wetting up and eventual landslide activation. This method permits direct field measurement of suction and is therefore preferable to laboratory pressure plate measurement of suctions and estimation of suction evolution from field resistivity derived GMC variation. This investigation has shown the sensitivity of ERT to observing hydrogeological precursors to earthflow activation which manifest as a fall in water level pre-activation. High resolution ERT monitoring would be used to observe and confirm the characteristic fall of piezometer level in advance of activation and also corroborate tensiometer data.

In addition, ERT monitoring has highlighted the complex interplay between hill slope soil moisture dynamics, such as soil moisture accumulation or dissipation and resulting crack formation/annealing.

Ascertaining electrode positions could be made much more straight forward and made less time-consuming if every electrode had a surface reference, for example, a survey peg. This would negate the need to extrapolate

electrode locations and in doing so removes a processing step and along with it a potential source of error. During periods of landslide activity multi-core cables become stretched under tension and can either tear or detach at the join with the electrode. Repairing and preventing this type of damage would be made easier if multi-core cables were located within a narrow gantry (such as narrow, flexible piping) with plenty of excess cable, that can be spooled out when electrodes displace.

Incorporating electrode displacement into model domains introduces the issue of not being able to compare like-with-like in terms of model cell geometries and therefore their assigned model parameters. In this investigation the geometry of each ERT survey domain was corrected for electrode displacement and following that was individually inverted. Loke's Res3DINV does not possess the capacity to run a time-lapse constrained inversion model along with developing domain geometries. A valid addition to current inversion code that would assist imaging dynamic systems – such as a landslide – would be a means of accounting for domain geometry development with time-constraint capability.

To overcome the challenge of modelling electrode movement from a sparse array of reference points and potentially eradicate some of the scatter associated with the movement corrected model resistivity monitoring dataset, it is recommended to use a small surface-located, coloured survey peg at each electrode position. For this investigation that would require the installation of 160 pegs.

On several occasions at Hollin Hill the landslide activation caused either electrodes to come away from the cable, or caused the connecting wire to split. One way to get around this issue could be to provide plenty of slack in the cables, that way, should the landslide displace cables are less likely to tear. Using armoured cables or laying cables within a gantry will get around the issue of livestock or rabbits chewing through exposed wires.

A powerful addition to ERT monitoring of shallow landslide systems such as the one at Hollin Hill would be Spontaneous Potential imaging (SP). This would contribute to the understanding of subsurface water flow both in time of activity and suspension (Jongmans et al., (2010); Robert et al., (2011)).

Studying streaming potentials (Telford et al., 1990), generated when a solution flows through a porous medium resulting from pressure gradients may shed some light on why piezometric levels generally fall during landslide activity, i.e. where the water is flowing to.

The laboratory phase of the project successfully defined the character of the resistivity – GMC relationship, however, it could have been performed in a more economic manner. Electrical measurements at fewer moisture contents but which define a similar range of moisture contents would be a reasonable trade-off between quantity and usability of data. Repeat measurements were used as the measure of laboratory data quality and this highlighted the trend of increased error at the very lowest soil moisture contents. However, reciprocal measurements are a more scientifically rigorous method of error management, if not yet commonplace in laboratory electrical experiments.

An exciting outcome of this project is the observation of landslide precursor hydrogeological behaviour using electrical resistivity monitoring. This technique is capable of observing an apparent rise in resistance (and resistivity) in the two months preceding earthflow activation at the field site. Correlation between piezometric level fall and associated temperature corrected resistance rise highlight the sensitivity of the geophysical monitoring system to interesting hydrogeological precursory processes to landslide activation.

Acronyms & Abbreviations

2D – two-dimensional

3D – three-dimensional

ALERT – automated time-lapse electrical resistivity tomography

AGI – Advanced Geophysical Inc. (Manufacturer)

AoD – Above Ordnance Datum

BGS – British Geological Survey

BNG – British National Grid

BUFI – British University Funding Initiative

CEC – Cation exchange capacity

DEM – Digital elevation model

DF – Dogger Formation

EDL – Electrical Double Layer

ERT – electrical resistivity tomography

GT – Geophysical Tomography Research Group (BGS)

GMC – Gravimetric moisture content

GPS – Global Positioning System

InSAR – Interferometric Synthetic Aperture Radar

LiDAR – Light Detection and Ranging

NERC – Natural Environment Research Council

RTK-GPS – Real-time Kinematic GPS

RMF – Redcar Mudstone Formation

SP – spontaneous potential imaging

SSF – Staithes Sandstone Formation

USGS – United States Geological Survey

WMF – Whitby Mudstone Formation

XRD – X-ray diffraction imaging

References

Archie, G.E. 1942, The electrical resistivity log as an aid in determining some reservoir characteristics, *Petroleum Transactions of AIME.*, 146: 54–62

Barnes, G. 2010, Soil Mechanics Principles and Practice 3rd Edition, *Palgrave Macmillan*, Hampshire

Baum, R.L., and Johnson, A.M., 1993, Steady movement of landslides in fine-grained soils--A model for sliding over an irregular slip surface. *U.S. Geological Survey Bulletin 1842*, p. D1-D28.

Bell, F.G. 2007, Engineering Geology, *Butterworth-Heinemann*, 2nd Edition, 581 p

Beven, K.J., (2012), Rainfall-runoff modelling: the primer, Wiley and Sons, ISBN 978-0-470-71459-1

Bichler, A., Bobrowsky, P., Best, M., Douma, M., Hunter, J., Calvert, T. and Burns, R. 2004, Three-dimensional mapping of a landslide using a multi-geophysical approach: the Quesnel Forks Landslide. *Landslides* 1: 29-40.

Binley, A., P. Winship, L.J. West, M. Pokar and R.Middleton, 2002, Seasonal Variation of Moisture Content in Unsaturated Sandstone Inferred from Borehole Radar and Resistivity Profiles, *J. Hydrol.*, 267(3 - 4), 160-172

Bovis, M.J. and Jones, P. 1992, Holocene history of earthflow mass movements in south-central British Columbia: the influence of hydroclimatic changes, *Canadian Journal of Earth Sciences* 1992;29:1746–55.

Bovis, M.J., 1985, Earthflows in the Interior Plateau, southwest British Columbia. *Can.Geotech. J.* 22:313–334.

BS5930, 1990, The Code of practice for site investigations, HMSO, London, 206 p.

BS1377, 1990, Methods of testing for soils for civil engineering purposes, HMSO, London.

Brovelli, A., Cassiani, G., Dalla, E., Bergamini, F., Pitea, D., Binley, A.M., 2005, Electrical properties of partially saturated sandstones: novel computational approach with hydrogeophysical applications. *Water Resources* 41:W08411. doi:10.1029/2004WR003628

Brunet, P., Clement, R. and Bouvier, C., 2010, Monitoring soil water content and deficit using Electrical Resistivity Tomography (ERT) – A case study in the Cevennes area, France. – *Journal of Hydrology*, 380, 146-153.

Busby, J.P., 2000, The effectiveness of azimuthal apparent-resistivity measurements as a method for determining fracture strike orientations. *Geophys. Prospec.* 48, 677–695.

Cassiani, G., Godio, A., Stocco, S., Villa, A., Deiana, R., Frattini, P., Rossi, M., (2009), Monitoring the hydrologic behaviour of a mountain slope via time-lapse electrical resistivity tomography. *Near Surface Geophysics*. 7(5-6): 475-486.

Chambers, J.E., Gunn, D.A., Wilkinson, P.B., Meldrum, P.I., Haslam, E., Holyoake, S., Kirkham, M., Kuras, O., Merritt, A., Wragg, J.. (2013), 4D Electrical Resistivity Tomography monitoring of soil moisture dynamics in an operational railway embankment. *Near Surface Geophysics*, doi:10.3997/1873-0604.2013002

Chambers, J.E., Wilkinson, P.B., Kuras, O., Ford, J.R., Gunn, D.A., Meldrum, P.I., Pennington, C.V.L., Weller, A.L., Hobbs, P.R.N., and Ogilvy, R.D., (2011), Three-dimensional geophysical anatomy of an active landslide in Lias Group mudrocks, Cleveland Basin, UK. *Geomorphology*, Vol. 125, 472-484.

Chambers, J.E, Ogilvy, R., Kuras, O., Cripps, J., Meldrum, P., 2002, 3D electrical imaging of known targets at a controlled environmental test site. *Environmental Geology*, 41 (6). 690-704. 10.1007/s00254-001-0452-4

Coe, J.A., Godt, J.W., Parise, M, and Moscariello, A., (2003), Estimating debris-flow probability using debris-fan stratigraphy, historic records, and drainage-basin morphology, Interstate 70 Highway Corridor, Central Colorado: In, Rickenmann, D.and Chen, C., eds., *Debris flow hazards mitigation: mechanics, prediction, and assessment*, Proceedings of the Third International Conference on Debris-Flow Hazards Mitigation, Davos, Switzerland, September 10-12, Millpress, Rotterdam, pp. 1085-1096.

Colangelo, G., Lapenna, V., Loperte, A., Perrone, A., Telesca, L. (2008) 2D electrical resistivity tomographies for investigating recent activation landslides in Basilicata Region (Southern Italy). *Ann Geophys* 51:275–285

Corominas, J., (2000) Landslides and climate. Keynote lecture- In: Proceedings 8th International Symposium on Landslides, (Bromhead E, Dixon N, Ibsen ML, eds). Cardiff: A.A. Balkema, 4: 1–33

Cruden, D M (1991) A simple definition of a landslide. Bulletin International Association for Engineering Geology, 43: 27–29.

Cruden, D.M. and Varnes, D.J., (1996), Landslide types and processes. In Special Report 247: Landslides: Investigation and Mitigation, *Transportation Research Board*, Washington D.C..

Day-Lewis, F.D., Harris, J.M. and Gorelick, S.M., (2002), Time-lapse inversion of crosswell radar data, *Geophysics*, 67, 1740 – 1752.

Descloitres, M., Ruiz, L., Sekhar, M., Legchenko, A., Braun, J., Kumar, M., Subramanian, S., (2008) Characterization of seasonal local recharge using electrical resistivity tomography and magnetic resonance sounding. *Hydrological Processes*, 22(3): 384-394.

Dey, A. and Morrison, H.F., (1979), Resistivity modelling for arbitrarily shaped two-dimensional structures: *Geophys. Prosp.*, 27, no. 1, 106-136.

Di Maio R., Piegari E., (2011): Water storage mapping of pyroclastic covers through electrical resistivity measurements. *Journal of Applied Geophysics*, 75, 196-202, doi:10.1016/j.jappgeo.2011.07.009

DI Maio, R. and Piegari, E., (2012), A study of stability analysis of pyroclastic covers based on electrical resistivity measurements, *Journal of Geophysics and Engineering*, 9(2), 191.

Dixon, N., and Bromhead, E.N., (2002) Landsliding in London Clay coastal cliffs, *Quarterly Journal of Engineering Geology and Hydrogeology*, 35(4), pp.327-343, ISSN: 1470-9236. DOI: 10.1144/1470-9236/2000-53

Edwards, L.S., 1977, A modified pseudosection for resistivity and IP: *Geophysics*, v. 42, no. 5, p. 1020-1036.

Fleming, R.W., and Johnson, A.M., (1989). Structures associated with strike-slip faults that bound landslide elements. *Engineering Geology*, v. 27, pp. 39-114.

Fleming, R.W., Baum, R.L., and Johnson, A.M., (1993), Deformation of landslide surfaces as indicators of movement processes, in *Proceedings of the 2nd Seminar on Landslide Hazards, Cosenza, Italy, March 5-6, 1990*. Geografic

Ford, J.R., in press. Geological Map of the High Stittenham Area (Sheet SE66NE). *British Geological Survey*, Nottingham, UK.

Foster, C., Jenkins, G.O., and Gibson, A.D. (2007), Landslides and mass movement processes and their distribution in the York District (Sheet 63). *British Geological Survey Open Report*, OR/07/004. 49pp.

Friedel, S., Thielen, A., Springman, S.M., (2006), Investigation of a slope endangered by rainfall-induced landslides using 3D resistivity tomography and geotechnical testing, *Journal of Applied Geophysics*. 60, pp 100-114

Gharibi, M. and Bentley, L. (2005). "Resolution of 3-D Electrical Resistivity Images from Inversions of 2-D Orthogonal Lines." *JEEG*, 10(4), 339–349

Glover, P.W.J., Hole, P.J., and Pous, J., (2000a), A modified Archie's law for two conducting phases, *Earth and Planetary Science Letters*, 180, no. 3–4, 369–383, doi: 10.1016/S0012-821X 0000168-0.

Godio, A., Strobbia, C., and De Bacco, G., (2006) Geophysical characterization of a rockslide in an alpine region. *Eng. Geol.*, 83: 273-286. DOI:10.1016/j.enggeo.2005.06.034

Gunn., D.G., (2013) Personal Communications

Haneberg, W.C. and Onder Gocke, A., (1994), Rapid water level fluctuations in a thin colluvium landslide west of Cincinnati, Ohio. *US Geol. Surv. Bull.*, 2059 C (1994), pp. 1–16

Hargreaves G.H., and Samani Z.A., (1985), Reference crop evapotranspiration from temperature. *Appl Engine Agric.* 1(2):96–99.

Hayley, K., Bentley, L.R., Gharibi, M. and Nightingale, M., (2007), Low temperature dependence of electrical resistivity: Implications for near surface geophysical monitoring. *Geophysical Research Letters.* 34 : L18402.

Hayley, K., Bentley, L.R. & Pidlisecky, A., (2010), Compensating for temperature variations in time-lapse electrical resistivity difference imaging, *Geophysics*, 75(4), WA51–WA59.

Head, K.H., (2006) Manual of Soil Laboratory Testing: soil classification and compaction tests. *Whittles*, Caithness

Heincke, B., Günther, T., Dalsegg, E., Rønning, J.S., Ganerød, G.V., Elvebakk, H., (2010), Combined three-dimensional electric and seismic tomography study on the Åknes rockslide in western Norway. *J Appl Geophys* 70(4):292–306

Hutchinson, J.R., and Bhandari, R.K., (1971). Undrained loading, a fundamental mechanism of mudflows and other mass movements: *Geotechnique*. v. 21, pp. 353-358.

Ingeman-Nielsen, T. and Baumgartner, F., (2006), CR1Dmod: A Matlab program to model 1D complex resistivity effects in electrical and EM surveys, *Computers and Geosciences*, 32, 1411–1419.

Iverson, R.M., (2000), Landslide triggering by rain infiltration. *Water Resources Research*, v. 36, pp. 1897-1910.

Jenkins, G.O., Foster, C. And Price, S.J., (2006) Landslide Survey of North Yorkshire: Reconnaissance Report. BGS Internal Report No. IR/06/036

Jomard, H., Lebourg, T., Binet, S., Tric, E. and Hernandez, M., (2007), Characterization of an internal slope movement structure by hydrogeophysical surveying. *Terra Nova*, 19: 48–57. doi: 10.1111/j.1365-121.2006.00712.x

Jomard H., Lebourg T., and Tric E., (2006), Identification of the gravitational discontinuity in weathered gneiss by geophysical survey: La Clapiere landslide (France). *J. Applied Geophysics*, vol. 62, issue 1, pp. 47-57.

Jones, D.K.C. and Lee, E.M., (1994), Landsliding in Great Britain. *Department of the Environment*, London, 390 p

Jongmans, D. and Garambois, S., (2007), Geophysical investigation of landslides: a review. *Bulletin De La Societe Geologique De France*. 178(2): 101-112.

Jordan, C., Bateson, L., Bow, J., Newell, A., Napier, B., Sabine, R.J., (2009) Geovisionary TM software for 3D visualisation and petroleum exploration in southern Tajikistan. Paper presented at the RSPSoc 2009: New Dimensions in Earth Observation, Leicester, UK

Karlsrud, K., Aas, G., and Gregerson, O., (1985), Can we predict landslide hazards in soft sensitive clays? Summary of Norwegian practice and experiences. *Norwegian Geotechnical Institute*, Publication 158, pp. 1-24.

Kearey, P. and Brooks, M., (1984) An Introduction to Geophysical Exploration, *Blackwell*, Oxford, 296 pp

Keefer, D.K., (1984), Landslides caused by earthquakes. *Geol. Soc. Am. Bull.* 95:406–421

Keelan, D.K. and McGinley, D.C. (1979). Application of Cation Exchange Capacity in a Study of the Shannon Sand of Wyoming. Paper KK presented at the 1979 SPWLA Annual Symposium

Keller, G. and Frischknecht, F.C., (1966) Electrical Methods in Geophysics. *McGrawHill*, New York

Kelsey, H. M., (1978), Earthflow in Franciscan melange, Van Duzen River basin, California: *Geology*, v. 6, p. 361-364.

Kim, J.H., (2005), Four dimensional inversion of dc resistivity monitoring data. Proceedings of Near Surface 2005, the 11th European Meeting of Environmental and Engineering Geophysics. European Association of Geoscientists and Engineers, p. A006.

Kim, J.H., Yi, M.J., Park, S.G. and Kim, J.G., (2009), 4-D inversion of DC resistivity monitoring data acquired over a dynamically changing earth model, *Journal of Applied Geophysics*, 68, 522-532.

Kollet, S.J., Maxwell, R.M., (2006), Integrated surface-groundwater flow modelling: A free-surface overland flow boundary condition parallel groundwater flow model. *Advances in Water Resources*, DOI: 10.1016/j.advwatres.2005.08.006

Kuras, O., Pritchard, J.D., Meldrum, P.I., Chambers, J.E., Wilkinson P.B., Ogilvy R.D., Wealthall G.P., (2009) Monitoring hydraulic processes with automated time-lapse electrical resistivity tomography (ALERT). *Comptes Rendus Geoscience*. 341(10-11): 868-885.

Lapenna, V., Lorenzo, P., Perrone, A., Piscitelli, S., Sdao, F., Rizzo, E., (2003), High-resolution geoelectrical tomographies in the study of Giarrossa landslide (southern Italy). *Bulletin of Engineering Geology and Environment* 62, 259–268.

Lebourg. T., Binet, S., Tric, E., Jomard, H., El Bedoui, S., (2005) Geophysical survey to estimate the 3D sliding surface and the 4D evolution of the water pressure on part of a deep seated landslide. *Terra Nova*. 17(5): 399-406

LeFebvre, G., (1996), Soft sensitive clays. In Turner, A.K. and Schuster, R.L. (eds.), *Landslides-Investigation and mitigation*. Washington D.C: National

Academy Press, *Transportation Research Board Special Report 247*, pp. 607-619.

Leroy, P. and Revil, A., (2004) A triple-layer model of the surface electrochemical properties of clay minerals, *Journal of Colloid and Interface Science*, Volume 270, Issue 2, ISSN 0021-9797, <http://dx.doi.org/10.1016/j.jcis.2003.08.007>

Loke, M.H., (1997), Rapid 2D resistivity inversion using the least-squares method. RES2DINV Program manual, Penang, Malaysia.

Loke, M.H., and Dahlin, T., (2002), A comparison of Gauss-Newton and quasi-Newton methods in resistivity imaging inversion. *Journal of Applied Geophysics* 49:149–162. DOI: 10.1016/S0926-9851(01)00106-9

Loke, M.H., Acworth, I. and Dahlin, T., (2003), A comparison of smooth and blocky inversion methods in 2D electrical imaging surveys. *Exploration Geophysics*, 34, 182-187.

Loke, M.H., Wilkinson, P.B., and Chambers, J.E., (2010), Fast computation of optimized electrode arrays for 2D resistivity surveys. *Computers and Geosciences*, Vol. 36, pp.1414-1426.

Loke, M.H., (2011), Electrical resistivity surveys and data interpretation. in Gupta, H (ed.), *Solid Earth Geophysics Encyclopaedia* (2nd Edition)

Lourenco, S., Gallipoli, D., Toll, D., Augarde, C., Evans, F., (2011), A new procedure for the determination of soil-water retention curves by continuous drying using high-suction tensiometers, *Canadian Geotechnical Journal*. 48. 327-335.

Mackey, B.H., Roering, J.J., and McKean, J.A., (2009), Long-term kinematics and sediment flux of an active earthflow, Eel River, California: *Geology*, v. 37, no. 9, p. 803–806, doi: 10.1130/G30136A.1.

Mackey, B.H., Roering, J.J., (2011), Sediment yield, spatial characteristics, and the long-term evolution of active earthflows determined from airborne LiDAR and historical aerial photographs, Eel River, California. *Geological Society of America Bulletin*. DOI.10.1130/B30306.1.1

Merritt, A.J., Chambers, J.E., Murphy, W., Wilkinson, P.B., West, L.J., Gunn, D., Dixon, N. (2013). 3D ground model development for an active landslide in Lias mudrocks using geophysical, remote sensing and geotechnical methods. *Landslides*. DOI: 10.1007/s10346-013-0409-1

Monteith, J.L., (1965). Evaporation and environment. pp. 205-234. In G.E. Fogg (ed.) *Symposium of the Society for Experimental Biology, The State and Movement of Water in Living Organisms*, Vol. 19, *Academic Press, Inc.*, NY.

Montgomery, D.R., Dietrich, W.E., (1994), A physically based model for the topographic control on shallow landsliding *Water Resources Research*, 30, pp. 1153–1171

O'Brien A, Ellis EA and Russell D (2004) Old railway embankment fill: laboratory experiments, numerical modelling and field behaviour. In *Advances in Geotechnical Engineering: Proceedings of the Skempton Memorial Conference*, Hindhead, UK (Jardine RJ, Potts DM and Higgins KG (eds)). Thomas Telford, London, UK, vol. 2, pp. 911–921.

Ogilvy, R.D., Kuras, O., Meldrum, P.I., Wilkinson, P.B., Chambers, J.E., Sen, M., Pulido-Bosch, A., Gisbert, J., Jorreto, S., Frances, I. and Tsourlos, P., (2009), Automated Monitoring of Coastal Aquifers with Electrical Resistivity Tomography. *Near Surface Geophysics*, Vol. 7, 367-375.

Penman, H.L. (1948) Natural evaporation from open water, bare soil, and grass. *Proc. Roy. Soc. London A*193:120-146

Perrone, A., Iannuzzi, A., Lapenna, V., Lorenzo, P., Piscitelli, S., Rizzo, E., and Sdao, F., (2004), High-resolution electrical imaging of the Varco d'Izzo earthflow (southern Italy): *Journal of Applied Geophysics*, v. 56, 17-29.

Picarelli, L., Leroueil, S., Delisle, M.C., Urciuoli, G., and Guerriero, G., (1998), Occurrence and features of shear zones in clay. In *Localization and bifurcation theory for soils and rocks*, Adachi, Oka, and Yashima, A. (eds.), Balkema, Rotterdam, p. 259-268.

Powell, J., (1984), Lithostratigraphical nomenclature of the Lias Group in the Yorkshire Basin. In: *Proceedings of the Yorkshire Geological and Polytechnic Society. Geological Society of London*, 45, pp 51–57. doi:10.1144/pygs.45.1-2.51

Pride, S., (1994) Governing equations for the coupled electromagnetics and acoustics of porous media, *Phys. Rev. B*, 50, 15678–15696.

Putman, W. (1940) and R. Sharp. Landslides and Earthflows near Ventura, Southern California, *Geographical Review* , Vol. 30, No. 4 (Oct., 1940) , pp. 591-600

Rawson P.F., Wright, J.K., (1995), Field geology of the British Jurassic. In: Taylor PD (ed) Jurassic of the Cleveland basin, North Yorkshire. *Geological Society of London*, London, pp 173–208

Revil, A.P., and Glover, W.J., (1997) Theory of ionic surface electrical conduction in porous media, *Phys. Rev. B*, 55, 1757–1773, 1997

Reynolds, J.M., (2011). An Introduction to Applied and Environmental Geophysics, *Wiley, Blackwell*, UK.

Robert, T., Dassargues, A., Brouyère, S., Kaufmann, O., Hallet, V., Nguyen, F., (2011), Assessing the contribution of electrical resistivity tomography (ERT) and self-potential (SP) methods for a water well drilling program in fractured/karstified limestones, *Journal of Applied Geophysics*, Vol.75, 42–53.

Russell, E.J.F, and Barker, R.D., (2010), Electrical properties of clay in relation to moisture loss, *Near Surface Geophysics*, 8,172-180, DOI:10.3997/1873-0604.2010001

Rosqvist, H., Leroux, V., Dahlin,, T., Johansson, S. and Svensson, M., (2010), An evaluation of the potential of the geoelectrical resistivity method for mapping gas migration in landfills. *SAGEEP 2010 Proceedings*, Keystone, Colorado.

Sass, O., Bell, R. & Glade, T. (2008), Comparison of GPR, 2D-resistivity and traditional techniques for the subsurface exploration of the Öschingen landslide, Swabian Alb (Germany). *Geomorphology* 93: 89-103

Savage, W.Z., and Smith, W.K., (1986), A model for the plastic flow of landslides. *U.S. Geological Survey Professional Paper* 1385, 32 p.

Scheingross, J.S., Minchew, B.M., Mackey, B.H., Simons, M., Lamb, M.P., and S. Hensley, (2013), Fault-zone controls on the spatial distribution of slow-moving landslides, *GSA Bulletin*, V. 125, no. 3/4, p. 473–489; doi:10.1130/B30719.1

Schmidt, K.M., Roering, J.J., Stock, J.D., Dietrich, W.E., Montgomery, D.R., Schaub, T., (2001) The variability of root cohesion as an influence on shallow landslide susceptibility in the Oregon Coast Range, *Canadian Geotechnical Journal*, 38(5): 995-1024, 10.1139/t01-031

Schmutz, M., Guerin, R., Andrieux, P., Maquaire, O., (2009). Determination of the 3D structure of an earthflow by geophysical methods The case of Super Sauze, in the French southern Alps. *Journal of Applied Geophysics* 68(4), 500-507.

Schwartz, B. F., Schreiber, M. E., & Yan, T. (2008). Quantifying field-scale soil moisture using electrical resistivity imaging. *Journal of Hydrology*, 362, 234-246.

Silvester, P.P. and Ferrari, R.L., (1990), *Finite Elements for Electrical Engineers*, second ed., *Cambridge University Press*, Cambridge

Skempton, A.W., (1985), Residual strength of clays in landslides, folded strata and the laboratory. *Géotechnique*, v. 35, pp. 3-18.

Slater, L., Binley, A.M., Daily, W., Johnson, R., (2000), Cross-hole electrical imaging of a controlled saline tracer injection. *Journal of Applied Geophysics* 44, 85-102.

Telford, W.M., Geldert, L.P., and Sheriff, R.E., (1991) Applied geophysics. *Cambridge Univ, New York*

Terlien, M.J.M., (1996). Modelling spatial and temporal variations in rainfall-triggered landslides. International Institute for Aerospace and Earth Sciences (ITC). Pub. No. 32. Enschede, 254 pp.

Terzaghi, K., and R.B. Peck. (1948). Soil Mechanics in Engineering Practice. John Wiley & Sons, New York, 566 pp

Toll, D.G., Lourenço, S.D.N. Mendes, J. Gallipoli, D. Evans, F.D., Augarde, C.E. , Cui, Y.J. Tang, A.M. Rojas Vidovic, J.C. Pagano, L. Mancuso, C. Zingariello, C. & Tarantino, A. (2011). Soil suction monitoring for landslides and slopes, *QJEGH*, 44: 23-33.

Tu, X.B., Kwong, A.K.L., Dai, F.C., Tham, L.G., Min, H., (2008) Field monitoring of rainfall infiltration in a loess slope and analysis of failure mechanism of rainfall-induced landslides, *Engineering Geology*, Volume 105, Issues 1–2, ISSN 0013-7952.

Tuller, M. and Or, D., (2005) Water films and scaling of soil characteristic curves at low water contents, *Water Resour. Res.*, 41, W09403, doi:10.1029/2005WR004142.

Turner, K.A., and Schuster, R.L., (1996), Landslides—Investigation and mitigation: *Transportation Research Board*, National Research Council, National Academy Press.

Udphuay, S., Günther, T., Everett, M.E., Warden, R.R., Briaud, J-L, (2011) Three-dimensional resistivity tomography in extreme coastal terrain amidst dense cultural signals: application to cliff stability assessment at the historic D-Day site. *Geophys J Int* 185(1):201–220. doi:10.1111/j.1365-246x.2010.04915.x

Uhlemann, S., Chambers, J.E., Wilkinson, P.B., Merritt, A.J., Gunn, D., Meldrum, P., Maurer, H., (in press) Estimation of electrode movement for 4D geoelectrical monitoring of an active landslide.

Uhlemann, S.S., Wilkinson, P.B., Chambers, J.E., Meldrum, P.I., Kuras, O., and Oxby, L., 2013, Estimation of electrode movements from sparsely distributed reference points for time-lapse ERT, Near Surface Geophysics, Conference paper.

US Soil Conservation Service, (1972), National Engineering Handbook; Section 4 Hydrology. US Department of Agriculture, Washington DC.

Van Asch, Th. W.J., Buma, J., and Van Beek, L.H. (1999) A view on some hydrological triggering systems in landslides, *geomorphology* 30, 25–32.

Varnes, D.J. (1978), Slope movement types and processes. In: Special Report 176: Landslides: Analysis and Control (Eds: Schuster, R. L. & Krizek, R. J.). *Transportation and Road Research Board*, National Academy of Science, Washington D. C., 11-33

Waxman, M.H., and Smits, L.J.M., (1968), Electrical conductivities in oil bearing sands. *Journal of the society of Petroleum Engineering* 8:107–122

Wilkinson, P.B., Chambers, J.E., Meldrum, P.I., Gunn, D.A., Ogilvy, R.D., and Kuras, O., (2010), Predicting the movements of permanently installed electrodes on an active landslide using time-lapse geoelectrical resistivity data only. *Geophysical Journal International*, Vol. 183, 543-556

Appendix A Data Processing Performance

<i>Operation Description</i>	<i>Performed by:</i>	
	<i>Student</i>	<i>BGS Staff</i>
4.1.1		
Installed surveyors peg array		x
Performed GPS peg survey	x	x
Tidied GPS dataset & converted into usable dataset	x	
Converted GPS peg data to local grid	x	
4.1.2		
Installed temperature sensors		x
Maintained temperature sensors and downloaded data	x	
Concatenated temperature data to be modelled	x	
Modelled subsurface temperature distribution by Heat Equation		x
Temperature plots produced and interpreted by	x	
4.1.3 & 4.1.4		
Rainfall data downloaded	x	x
Rainfall data processed and converted to effective rainfall	x	
Evapotranspiration modelling	x	
4.1.5		
Piezometer wells installation		x
Piezometer data downloaded	x	x
Piezometer data processed and interpreted	x	
4.3		
ALERT system installed and managed remotely		x
Resistivity monitoring data extracted form server	x	
Raw resistivity data processed and interpreted	x	
Code written to temperature correct resistivity data		x
Temperature correction of resistivity monitoring data	x	
temperature correction code implementation	x	
Code to interpolate electrode positions		x
Implementation of code to movement correct resistivity data	x	x
Inversion of monitoring data		x
Electropetrophysical relationships measured	x	
Electropetrophysical relationships modelled		x
Resistivity - GMC code written		x
Resistivity - GMC code utilisation	x	
5		

Extraction of soil core samples and placement in troughs	x	
Laboratory electro-petrophysical experimentation campaign	x	
Curve modelling by Waxman-Smit Equation		x
Analysis and interpretation of results	x	
Geotechnical laboratory testing (porosity, particle density)	x	

Appendix A. Which member of the collaboration performed each of the major data processing tasks.

Appendix B Standardised Model Inversion Parameters

Inversion Setting	Movement Corrected	Time-lapse constrained
Initial damping factor	0.15	0.15
Minimum damping factor	0.005	0.005
Line search option	1	1
Convergence limit	0.1	0.1
Minimum change in RMS error	0.2	0.2
Number of iterations	7	7
Number of iterations to recalculate Jacobian matrix	10	10
Vertical to horizontal flatness filter ratio	1	1
X horizontal flatness filter weight	1	1
Y horizontal flatness filter weight	1	1
Flatness filter weight for half-size layers	1	1
Number of nodes between adjacent electrodes	2	2
Normalise potentials	0	0
Flatness filter type, Include smoothing of model resistivity	1	1
Increase of damping factor with depth	1.05	1.05
Type of topographical modeling	0	0
Factor for damped topography model	0.5	0.5
Type of topography trend removal	0	0
Robust data constrain?	1	1
Cutoff factor for data constrain	0.05	0.05
Robust model constrain?	0	0
Cutoff factor for model constrain	0.01	0.01
Reduce effect of side blocks?	0	0
Optimise damping factor?	0	0
Thickness of first layer	0.2686	0.28
Factor to increase thickness layer with depth	1.1	1.1
Number of half-size layers	0	0
Divide half-size layers vertically (1=YES,0=NO)	0	0
Factor to increase model depth range	1.2	1
USE FINITE ELEMENT METHOD (YES=1,NO=0)	1	1
RMS CONVERGENCE LIMIT (IN PERCENT)	5	5
USE LOGARITHM OF APPARENT RESISTIVITY (0=LOG OF APP. RESIS., 1=RESISTANCE, 2=APP. RESIS.)	1	0
LIMIT RESISTIVITY VALUES(0=No,1=Yes)	1	1
Upper limit factor (10-50)	50	50

Lower limit factor (0.02 to 0.1)	0.02	0.02
Type of reference resistivity (0=average,1=first iteration)	0	0
Type of optimisation method (0=Gauss-Newton,2=Incomplete GN)	2	2
Convergence limit for Incomplete Gauss-Newton method	0.01	0.01
Use data compression with Incomplete Gauss-Newton (0=No,1=Yes)	0	1
Use reference model in inversion (0=No,1=Yes)	0	0
Damping factor for reference model	0.2	0.2
Type of initial model (0=Homogeneous,1=approx.inverse)	0	0
Time-lapse inversion constrain	0	2
Type of time-lapse inversion method	NA	0
Type of time reference model,0=first,1=preceding	NA	0
Reduce effect of side blocks? (0=No,1=Yes)	0	0
Use higher damping for first layer? (0=No,1=Yes)	0	0
Extra damping factor for first layer	1	1
Automatically re-sort data points (0=No,1=Yes)	1	1
Type of scaling for Incomplete Gauss-Newton method (1=First, 1=Second 3=Third order)	1	1
Use uniform filter weights (0=No, 1=Yes)	0	0
Type of data compression (0=Simple, 1=Aggressive)	0	0
Reference model resistivity multiplication factor (0.1 to 10)	1	1
Try to optimise model at each iteration (0=No, 1=Yes)	1	1

Appendix B. Model Inversion parameters as applied for all model cell inversions of Hollin Hill ERT surveys.

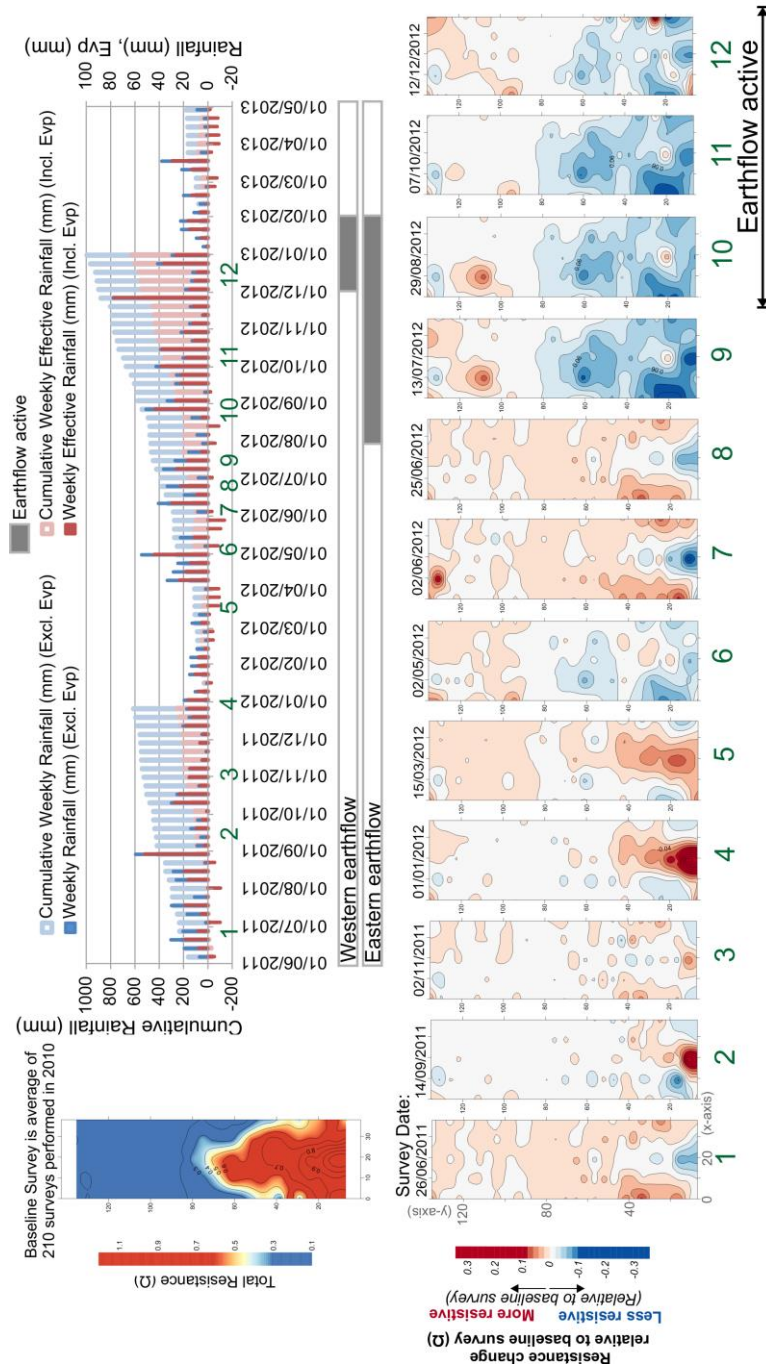
Appendix C Resistivity Model Inversion Misfit Errors

Resistivity Inversion Model Misfit Error	
Survey Date	Electrode movement corrected inversion
09/01/2009	1.91
27/01/2009	1.73
15/02/2009	1.92
29/03/2009	1.58
25/04/2009	1.68
21/05/2009	1.59
13/06/2009	1.61
22/08/2009	1.61
08/09/2009	1.64
29/09/2009	1.70
27/10/2009	1.81
25/11/2009	1.79
19/12/2009	1.66
11/01/2010	1.93
12/02/2010	1.57
08/03/2010	1.93
29/03/2010	1.74
20/04/2010	1.60
11/05/2010	1.51
29/05/2010	1.54
29/06/2010	2.10
10/07/2010	2.40
24/07/2010	2.10
05/08/2010	2.91
17/08/2010	3.10
07/09/2010	2.20
19/09/2010	2.00
03/10/2010	1.80
09/11/2010	2.30
16/11/2010	1.87
21/11/2010	1.86
27/11/2010	1.94
07/12/2010	1.70
01/01/2011	1.59
22/01/2011	1.65
26/02/2011	1.73
09/04/2011	1.58
28/04/2011	1.62

26/05/2011	2.36
02/06/2011	2.03
23/06/2011	1.77
21/07/2011	1.77
14/09/2011	1.61
21/09/2011	1.56
12/10/2011	2.10
09/11/2011	1.88
11/12/2011	2.04
28/12/2011	2.04
18/01/2012	2.25
19/02/2012	2.08
21/03/2012	2.21
15/04/2012	2.49
16/05/2012	2.61
06/06/2012	2.33
20/06/2012	2.42
13/07/2012	3.03
05/08/2012	1.95
19/08/2012	2.31
30/09/2012	2.42
10/10/2012	2.74
14/10/2012	3.06
21/10/2012	3.28
09/12/2012	5.84
25/01/2013	5.64
09/02/2013	3.57

Appendix C. Model Inversion Misfit Errors for Movement Corrected ERT Inversions

Appendix D Time-Lapse Temperature Corrected Resistance Maps using Baseline Average of 2010 Surveys



Appendix D. Time-Lapse Temperature Corrected Resistance Maps using Baseline Average of 2010 Surveys